Special Issue "Sediment Transport in Coastal Waters"

A special issue of *Water* (/journal/water) (ISSN 2073-4441).

Deadline for manuscript submissions: **closed (30 June 2017)**

Special Issue Editor

Guest Editor

Dr. Sylvain Ouillon

Institut de Recherche Pour le Développement (IRD), LEGOS, Université de Toulouse, 14 av. Edouard Belin, 31400 Toulouse, France

Website (http://www.legos.obs-mip.fr/ouillon) | E-Mail ()

Interests: sediment dynamics, sediment processes; watershed; estuaries; coastal oceanography; effects of climate change and human activity on sediment budget; ocean color in coastal waters and applications; numerical modeling

Special Issue Information

Dear Colleagues,

Globally, while land erosion has increased in the last decades, sediment input to the ocean has decreased. Sediment transport and distribution at the land-ocean interface has huge impacts on morphodynamics of estuaries, deltas and coastal zones, on water quality (and related issues such as aquaculture), on navigation and harbor capability, on recreation areas, *etc*. Scientific objectives must be achieved to deepen our knowledge on processes based on field surveys, modeling, space observation or experiments in laboratory, to refine the sediment budget (bedload and suspension) between compartments, and to improve our observation and modelling capacities. Sediment transport which is mainly driven by varying dynamical forcings (currents, tides, wind, waves, turbulence, stratification, density currents, *etc*.) in the estuary, in the ROFI zone, on the shelf or in canyons may also be affected by chemical and biological processes. In this Special Issue, we invite scientists working on different aspects of sediment transport, in muddy, sandy or mixed environments, to share their most recent results and give reviews or examples encompassing different aspects of sediment transport in coastal zones at different scales. Papers may deal with water and sediment analysis (including Particle Size Distribution), modeling, and remote sensing.

Dr. Sylvain Ouillon
Guest Editor

Keywords

- sediment transport processes
- sediment budget
- suspension
- bed load
- estuaries
- coastal zones
- river plume
- nearshore processes
- numerical modeling
- remote sensing

Published Papers (8 papers)

Download All Papers (/journal/water/special_issues/coastal_waters/download)

Research

Open Access Article

Beach Response to Wave Forcing from Event to Inter-Annual Time Scales at Grand Popo, Benin (Gulf of Guinea)

by Grégoire Abessolo Ondoa, Frédéric Bonou, Folly Serge Tomety,Yves du Penhoat, Clément Perret, Cossi Georges Epiphane Degbe and Rafael Almar

Water **2017**, *9*(6), 447; doi:10.3390/w9060447

Received: 31 March 2017 / Revised: 14 June 2017 / Accepted: 16 June 2017 / Published: 21 June 2017

PDF Full-text (/2073-4441/9/6/447/pdf) (2637 KB) | HTML Full-text (/2073-4441/9/6/447/htm) | XML Full-text (/2073-4441/9/6/447/xml)

Open Access Feature Paper Article

Shoreline Response to a Sequence of Typhoon and Monsoon Events

by Rafael Almar, Patrick Marchesiello, Luis Pedro Almeida, Duong Hai Thuan, Hitoshi Tanaka and Nguyen Trung Viet

Water **2017**, *9*(6), 364; doi:10.3390/w9060364 (http://dx.doi.org/10.3390/w9060364)

Received: 11 April 2017 / Revised: 16 May 2017 / Accepted: 18 May 2017 / Published: 23 May 2017

PDF Full-text (/2073-4441/9/6/364/pdf) (658 KB) | HTML Full-text (/2073-4441/9/6/364/htm) | XML Full-text (/2073-4441/9/6/364/xml)

Open Access Feature Paper Article

Shoreline Changes on the Wave-Influenced Senegal River Delta, West Africa: The Roles of Natural Processes and Human Interventions

by Mamadou Sadio, Edward J. Anthony,Amadou Tahirou Diaw, Philippe Dussouillez, Jules T. Fleury, Alioune Kane,Rafael Almar and Elodie Kestenare

Water **2017**, *9*(5), 357; doi:10.3390/w9050357 (http://dx.doi.org/10.3390/w9050357)

Received: 24 December 2016 / Revised: 10 April 2017 / Accepted: 12 May 2017 / Published: 19 May 2017

PDF Full-text (/2073-4441/9/5/357/pdf) (6100 KB) | HTML Full-text (/2073-4441/9/5/357/htm) | XML Full-text (/2073-4441/9/5/357/xml)

Open Access Feature Paper Article

Dynamics of Suspended Sediments during a Dry Season and Their Consequences on Metal Transportation in a Coral Reef Lagoon Impacted by Mining Activities, New Caledonia

by Jean-Michel Fernandez, Jean-Dominique Meunier, Sylvain Ouillon, Benjamin Moreton, Pascal Douillet and Olivier Grauby

Water **2017**, *9*(5), 338; doi:10.3390/w9050338

Received: 30 March 2017 / Revised: 8 May 2017 / Accepted: 8 May 2017 / Published: 10 May 2017

PDF Full-text (/2073-4441/9/5/338/pdf) (9969 KB) | HTML Full-text (/2073-4441/9/5/338/htm) | XML Full-text (/2073-4441/9/5/338/xml)

Open Access Article

Modelling Hydrology and Sediment Transport in a Semi-Arid and Anthropized Catchment Using the SWAT Model: The Case of the Tafna River (Northwest Algeria)

by Amin Zettam, Amina Taleb, Sabine Sauvage, Laurie Boithias, Nouria Belaidi and José Miguel Sánchez-Pérez

Water **2017**, *9*(3), 216; doi:10.3390/w9030216 (http://dx.doi.org/10.3390/w9030216)

Received: 15 December 2016 / Revised: 6 March 2017 / Accepted: 7 March 2017 / Published: 14 March 2017

Cited by 1 (/2073-4441/9/3/216#citedby) | PDF Full-text (/2073-4441/9/3/216/pdf) (5409 KB) | HTML Full-text (/2073-4441 /9/3/216/htm) | XML Full-text (/2073-4441/9/3/216/xml)

Open Access Article

The June 2016 Australian East Coast Low: Importance of Wave Direction for Coastal Erosion Assessment

by Thomas R. Mortlock, Ian D. Goodwin, John K. McAneney and Kevin Roche

Water **2017**, *9*(2), 121; doi:10.3390/w9020121 (http://dx.doi.org/10.3390/w9020121)

Received: 5 December 2016 / Revised: 24 January 2017 / Accepted: 6 February 2017 / Published: 14 February 2017 Cited by 1 (/2073-4441/9/2/121#citedby) | PDF Full-text (/2073-4441/9/2/121/pdf) (16394 KB) | HTML Full-text (/2073-4441 /9/2/121/htm) | XML Full-text (/2073-4441/9/2/121/xml)

Open Access Article

Statistical Analysis of the Spatial Distribution of Multi-Elements in an Island Arc Region: Complicating Factors and Transfer by Water Currents

by Atsuyuki Ohta, Noboru Imai, Yoshiko Tachibana and Ken Ikehara

Water **2017**, *9*(1), 37; doi:10.3390/w9010037 (http://dx.doi.org/10.3390/w9010037)
Received: 13 October 2016 / Revised: 23 December 2016 / Accepted: 5 January 2017 / Published: 10 January 2017

Open Access Article

Numerical Simulations of Suspended Sediment Dynamics Due to Seasonal Forcing in the Mekong Coastal Area

by Vu Duy Vinh, Sylvain Ouillon, Nguyen Van Thao and Nguyen Ngoc Tien

Water **2016**, *8*(6), 255; doi:10.3390/w8060255 (http://dx.doi.org/10.3390/w8060255)
Received: 27 April 2016 / Revised: 6 June 2016 / Accepted: 9 June 2016 / Published: 16 June 2016

Journal Contact

MDPI AG
Water Editorial Office (/journal/water/editorial_office)
St. Alban-Anlage 66, 4052 Basel, Switzerland
E-Mail: (mailto:water)
Tel. +41 61 683 77 34
Fax: +41 61 302 89 18
Editorial Board (/journal/water/editors)
Contact Details (/about/contact/)

water

MDPI

Article

Beach Response to Wave Forcing from Event to Inter-Annual Time Scales at Grand Popo, Benin (Gulf of Guinea)

Grégoire Abessolo Ondoa [1,2,*], Frédéric Bonou [2,3,4], Folly Serge Tomety [2,3,4], Yves du Penhoat [2,3,4], Clément Perret [2,3,4], Cossi Georges Epiphane Degbe [3] and Rafael Almar [2]

1 Fishery Resources Laboratory, University of Douala, BP 2701 Douala, Cameroon
2 LEGOS (Université Paul Sabatier de Toulouse/CNRS/CNES/IRD), 31400 Toulouse, France; fredericbonou@yahoo.fr (F.B.); sertom1@hotmail.fr (F.S.T.); yves.du-penhoat@ird.fr (Y.d.P.); clement.perret@outlook.com (C.P.); rafael.almar@ird.fr (R.A.)
3 Institut de Recherches Halieutiques et Océanologiques du Bénin, 03 BP 1665 Cotonou, Benin; gdegbe@yahoo.fr
4 International Chair in Mathematical Physics and Applications/Unesco Chair, University of Abomey-Calavi, 01 BP 526 Cotonou, Benin
* Correspondence: gregsolo55@yahoo.fr; Tel.: +237-699-76-73-34

Received: 31 March 2017; Accepted: 16 June 2017; Published: 21 June 2017

Abstract: This paper assesses the morphological storm-event impact, seasonal cycles, trends of wave forcing, and beach's response at the coastal area of Grand Popo, Benin. Three and a half years' worth of data were collected from 2013 to 2016, using a video system calibrated with field data collected during a 10 day experiment. A comparison was carried out with Wavewatch III IOWAGA wave hindcast data. The along-shore-averaged shoreline position exhibited a seasonal pattern, which was related more to the average wave height than the average storm intensity. Storms occur in austral winter (June, July, August, and September). Based on 12 storms, the results revealed that the average storm duration was 1.6 days, with a mean erosion of 3.1 m. The average post-storm beach recovery duration was 15 days, and the average recovery rate was 0.4 m/day. The impact of storms was more or less amplified depending on the eroding and accreting periods of the wave climate. There was an inter-annual eroding trend of about −1.6 m/year, but the causes of this trend could not be explained.

Keywords: shoreline; waves forcing; storms; resilience; post-storm recovery; Bight of Benin; seasonal cycle; trend

1. Introduction

The coastal zone of West Africa is under increasing pressure of overpopulation, as it is a zone of economic interest. Human settlements and livelihood activities have been developing on the shores of the Atlantic Ocean, where the beach evolution varies according to a wide range of different temporal and spatial scales. In this region, beaches are microtidal and swell-dominated environments, where waves and tides are the main drivers of nearshore dynamics [1]. Several findings suggest that along wave-dominated coastlines, regionally-varying wave climates will have an increasing impact on the shoreline in the coming decades, and cannot be ignored in forecasting shoreline variability [2–4]. This highly dynamic behaviour is essentially due to the fact that sandy coasts can undergo adjustments in form and processes, which can change rapidly. Periods of accretion and erosion are generally associated with low- and high-energy wave conditions, respectively, but they also exhibit strong site-specific variations [5]. For many coastal regions, both sea-level rise and changes in the storm-wave climate would result in coastal erosion and an increased frequency with a high intensity of coastal flooding. Storm-events represent a major factor of modulating short- and medium-term morphological

evolutions of many sandy shorelines. In the event of changing storm regimes associated with climate change [6], it is important to understand the potential effects of storms on beaches, and how they recover after these high-energy events. Many studies have been carried out on assessing the impact of storms, beaches' responses, and post-storm morphological adjustments in storm-dominated coastlines [6–12]. Managing erosion-induced problems will depend on the resilience of the beach to extreme events, and universal threshold conditions are not likely to be found [5]. Establishing storm thresholds is difficult, especially because they are generally site-specific [11,13]; this is as well as the beach recovery period [7], which has not yet been clearly addressed in the literature. Available literature regarding beaches' responses to storms on tropical microtidal coastlines and the potential impacts of climate change remains scarce.

Along the wave-dominated coastlines of the Gulf of Guinea, the influence of South Atlantic high-energy swells drives strong, eastward longshore sediment transport [14,15]. This littoral drift in the Bight of Benin is one of the largest in the world, with estimations of approximatively 400,000–1,000,000 m^3/year [16]. This transport is mostly driven by swell waves due to the Southern Annular Mode (SAM), rather than wind waves due to the Inter-Tropical Convergence Zone (ITCZ) [15]. This equatorial fluctuation presents a large seasonal and inter-annual variability as well as wave climate [14]. This implies a high seasonal variability in the beaches' responses to equatorial Atlantic forcing, given that seasonal processes dominate the shoreline changes due to seasonal variations of the wave height at several specific sites [5,17]. These findings need to be confirmed, but few measurements are available on the high-frequency evolution of shoreline and beach states in the West and Central African regions.

This study assesses different time scales of beach responses to wave forcing at Grand Popo Coast, Benin, using video-derived shoreline and wave evolution data over a 3.5 year observation period (February 2013 to August 2016). We first investigate an average beach response during and after storm-events. Secondly, we evaluate the impact of storm durations and recurrence with seasonal variability. And finally, we estimate the inter-annual trends.

2. Data and Methods

2.1. Study Area

Located in the Gulf of Guinea, Benin, near the border with Togo, Grand Popo Beach is an ocean-open, sandy stretch of coast facing the South Atlantic Ocean [18]. The beach is far enough from the influence of the major cities: Cotonou (80 km away), and Lome (60 km away). In the last three years, some fields of groynes have been constructed near the town of Anèho, 20 km updrift [19] (see Figure 1b).

The beach dynamics are dominated by the influence of oblique waves (South/Southwest) of moderate energy (mean significant wave height Hs = 1.36 m; mean peak period Tp = 9.4 s). The longshore sediment transport is primarily driven by swell waves (South/Southwest and South/Southeast) generated in the Southern Hemisphere trade-wind region (30–35° S and 45–60° S), rather than wind waves (Southwest) generated locally in the Gulf of Guinea [14–16,20], as shown in Figure 1a. Tides are semi-diurnal with a microtidal range from 0.8 to 1.8 m for neap and spring tides, respectively. The sediment size is medium-to-coarse: 0.4 to 1 mm (median grain size $D50$ = 0.6 mm). Grand Popo Beach is an intermediate low tide terrace (LTT) to reflective beach [14,18,20], according to the classification proposed in [21].

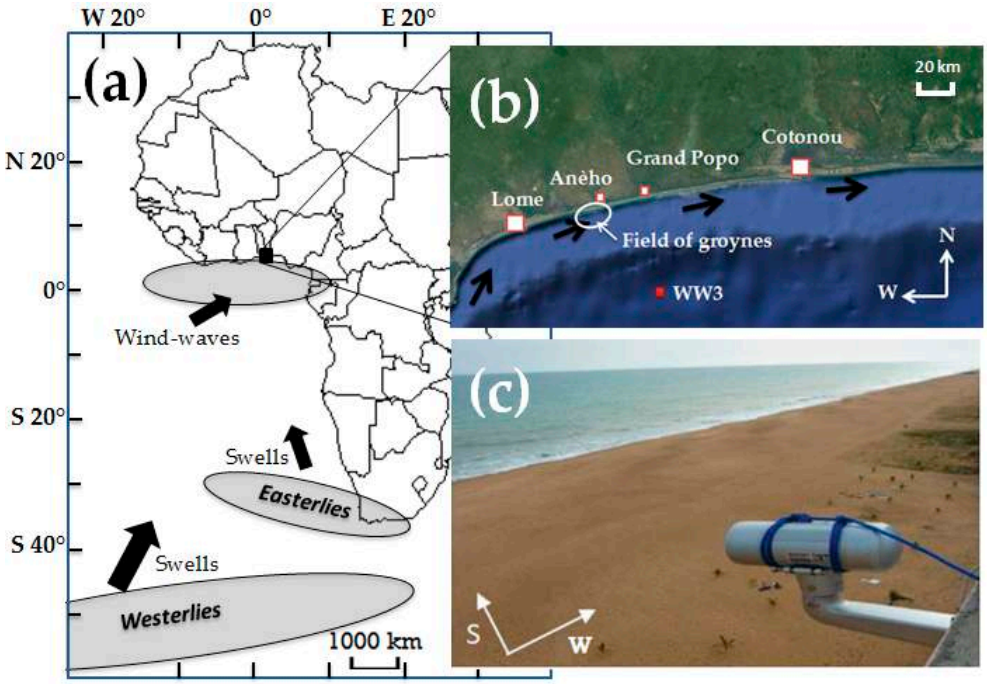

Figure 1. Study site: (**a**) The regions of major generations of swells and wind waves impinging on the Gulf of Guinea are indicated by grey ovals, and their major directions of propagation by the black arrows. (**b**) Focus in the Bight of Benin, with major cities of Cotonou and Lomé. Black arrows represent the longshore sediment transport directions. The red point (2.0° E, 5.5° N) gives the location of the WW3 model output. (**c**) Permanent video camera on a 15 m high semaphore at Grand Popo Beach, Benin.

2.2. Video System and Data

In February 2013, a low-cost video system was installed on the top of a tower of the Navy Forces of Benin in Grand Popo, about 70 m from the shoreline [22]. The system was composed of a VIVOTEK IP 7361 camera (1600 × 728 pixels), which collected data continuously at 2 Hz. An on-site computer processed the raw images and stored three types of secondary images every 15 min: snapshots, cross-shore time-stacks, and 15 min time exposure (or timex) images (Figure 2) [22]. Twenty ground control points were taken with GPS to process image geo-rectification [23], by applying the method of direct linear transformation [24]. This consists of a matrix, which gives the relation between image pixels and control points by taking into account the position of the camera and the correction due to the camera lens distortion [25].

Several recent methods were used to extract hydrodynamic and morphologic parameters. *Hs* video estimations were obtained from the time-stack images [26]. Following the wave signature induced by breaking, wave heights were detected from the pixel intensity threshold $Ipix = 40$. The intensity of breaking pixels was significantly larger ($Ipix > 80$) than that of non-breaking pixels ($Ipix \sim 10$). The pixel intensity peak, which appeared at the wave crests, was calculated by the standard deviation δ of the pixel intensity of each time series. The width of the peak of δ marked the horizontal projection of the wave face covered by the roller (L), which was subsequently projected into the vertical direction for a simple rough estimation: $H_b = L \cdot \tan(\beta)$, where β was the camera view angle. The fact that the wave-front slope (α_b) at breaking differed significantly from the vertical direction was taken into account. The common value $\alpha_b \approx 30°$ is used as a breaking criterion in numerical breaking parameterizations, according to [26]. The wave height could therefore be estimated from the equation [26]:

$$H_b = (L - Cor)\tan(\beta) \quad (1)$$

Cor being a geometrical correction defined as [26]:

$$Cor = \frac{L}{\tan(\alpha_b)} \tan(\beta) \quad (2)$$

The mean wave period T_m was computed from the offshore pixel intensity time series using the mean zero-crossing method on the time-stack images [27]. Wave direction was estimated from the snapshots and 15 min averaged images. The technique consisted of, firstly, subtracting the average image from the snapshot (removing the background, which does not move); secondly, highlighting the wave crests (the time-varying part); then rectifying on a regular grid; and finally, recovering the angle of the crest of the waves by the Radon transform [28].

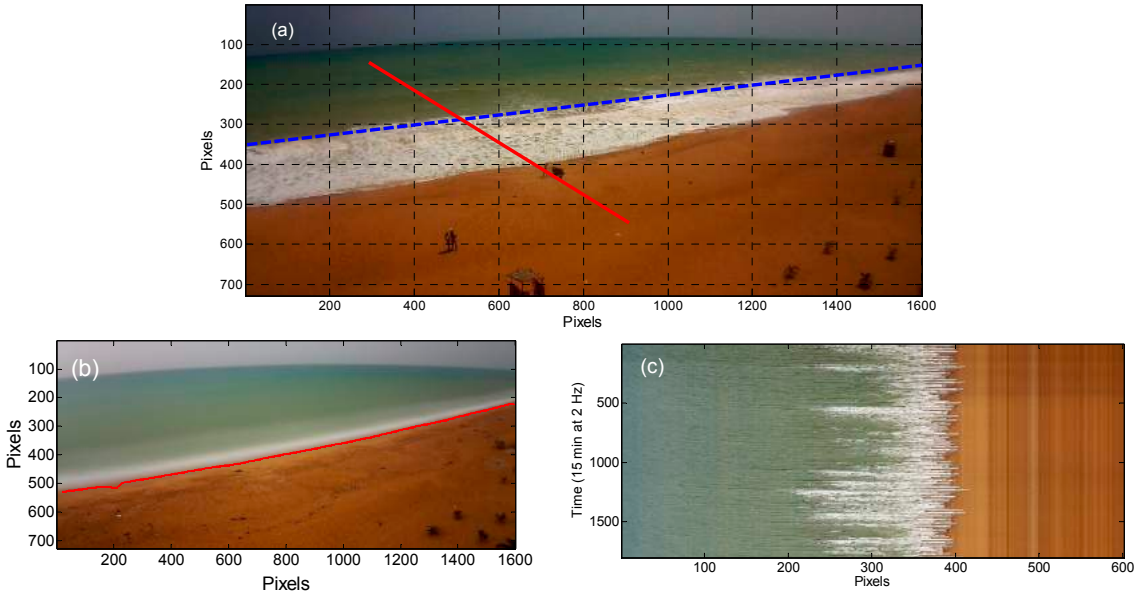

Figure 2. Video image types: (**a**) Snapshot with cross-shore time-stack profile as a red line, and along-shore time-stack profile as a blue dashed line. (**b**) 15 min averaged image; shoreline is shown as a red line. (**c**) Cross-shore time-stacked image (vertical is time: 15 min at 2 Hz).

A 10 day field experiment was conducted at Grand Popo Beach, Benin, in March 2014 [22]. The measurements included both topographic and bathymetric morphological surveys with differential GPS (DGPS) and bathymetric sonar, while offshore forcing (waves and tide) was characterized using an Acoustic Doppler Current Profiler (ADCP) moored at a 10 m depth. *Hs* video data were regressed with 10 days of ACDP field data, with an acceptable root-mean-square error (RMSE) of 0.14 m [18].

Due to technical malfunctions in the video acquisition system, missing video data could be estimated with linear regression between existing video data and Wavewatch III (WW3), model version 4.10 (IOWAGA wave hindcast database [29]) output at the nearest available point, 2.0° E, 5.5° N (Figure 1b), propagated to breakpoint using an empirical predictor formula [30]. This formula was used in a recent study [15] focusing on wave climate variability in the Bight of Benin. This formula directly provides the breaking wave height h_b and angle θ_b, given deep water wave height h_0, period T, and direction θ_0:

$$h_b = \lambda \cdot C^2 / g \quad (3)$$

$$\theta_b = a \sin\left(\sin(\theta_0) \cdot \sqrt{\lambda}\right) \quad (4)$$

with a correction factor λ computed by:

$$\lambda = \Delta \cdot \lambda_a \quad (5)$$

where:

$$\Delta = 1 + 0.1649\xi + 0.5948\xi^2 - 1.6787\xi^3 + 2.8573\xi^4 \quad (6)$$

$$\xi = \lambda_a \cdot (\sin\theta_0)^2 \quad (7)$$

$$\lambda_a = [\cos(\theta_0)/\varphi]^{\frac{2}{5}} \quad (8)$$

$$\varphi = \left(\frac{C}{\sqrt{gh_b}}\right)^4 \left(\frac{C}{C_g}\right)\gamma^2 \quad (9)$$

where the phase celerity is given by $C = 1.6T$, group celerity $C_g = \frac{C}{2}$ and breaker depth index $\gamma = 0.78$.

The shoreline location was calculated from timex images as the maximum gradient in the ratio red/green-blue [31]. Beach pixels display high red-channel values and low green values, whereas water pixels exhibit strong green-channel values and low red values [25,32]. The ratio red/green-blue was computed for all pixels and its local minimum stood for the transition between water and beach, namely, the shoreline. The overall error in video detection of the shoreline location owing to water level uncertainties, due to wave breaking or atmospheric pressure variations, or incorrect shoreline detection, was about 0.5 m [12]. Shoreline migration was estimated via the along-shore-averaged location <*X*> to reduce error data due to the along-shore-digitized shoreline. Determination of the intertidal beach profile and beach slope involved the delineation of the shoreline at different tidal levels [32], and interpolation between daily low and high tides. Tidal levels for the study period 2013–2016 were extracted from the WXTide32 model, version 4.7. As there was no tide gauge at the study site, the tidal subordinate at Lomé, Togo (1°14′ E, 6°07′ N) was referred to the nearest tide gauge station, Takoradi, Ghana (~350 km). The root-mean-square and mean errors in the intertidal profile computed between 7 day DGPS (Grand Popo experiment, 2014) and video data were 0.28 and 0.23 m, respectively [18].

2.3. Event Scale: Storms

The definition of storm-event is site-specific [5,9], and the *Hs* threshold used to define storm conditions or extreme events is selected to produce clear and identifiable storm-events. Three-hourly *Hs* time series were used, and the 5% exceedance probability of the wave height time series over the study period ($H_{S_{5\%}} = 1.85\ m$) was considered as the threshold for storm-events. A single storm is defined as a continuous period of *Hs* exceeding this threshold and lasting at least one tidal cycle (12 h), following [5,12]. The overall impact of storm-events is assessed through the daily-averaging maximum shoreline moving during the storm. Storm intensity I ($m^2 \cdot h$) is computed as the integration of time-varying *Hs* over the storm duration:

$$I = \int_{t_1}^{t_2} H_S(t)^2 \cdot dt \quad (10)$$

where t_1 and t_2 are times corresponding to the beginning and the end of the storm [12].

There are several ways to define the recovery duration after each storm. It can be defined as the time taken by the nearshore morphology to evolve from a post-storm state (e.g., dissipative/longshore bar and trough) to its modal state (i.e., the most frequently occurring beach state, e.g., rhythmic bar and beach or transverse bar and rip) [9–11]. In this study, the time duration taken to reach the first maximum recovery value of the along-shore-averaged shoreline location <*X*> after each storm was accepted as the recovery duration [10,12]. This duration referred to the post-storm period of continuous accretion towards its equilibrium pre-storm state (*Tr*), and did not depend on any forcing parameter. The overall recovery duration for the study period was computed as the time for daily-averaging post-storm evolution of continuous accretion [5].

2.4. Seasonal Signal and Trends

To obtain the seasonal signal, monthly nearshore estimations were computed. The test of Mann Kendall was used to check if the time series showed substantial trends [33]. The null hypothesis of trend absence in a time series was tested, against the alternative of having a trend. Each time series was reorganized as a matrix M_{ij} where $1 \leq i \leq N_y$ with N_y representing the number of years of video observation, and $1 \leq j \leq 12$. The seasonal signal S_j was obtained as follows:

$$S_j = \frac{1}{N_y} \cdot \sum_{i=1}^{N_y} M_{ij} \tag{11}$$

The monthly residual or anomaly signal R_{ij} of each parameter was estimated by removing the seasonal monthly value from each monthly-averaged value computed over the three and a half years. The annual anomaly or trend R_a was computed by averaging monthly anomaly values R_{ij}.

3. Results

3.1. Hydrodynamic and Morphological Variability

Figure 3a–c provides an overview of monthly video and WW3 data [29] over the study period. The same *Hs* seasonality for the two sets of data was observed (Figure 3a), with more energetic waves during the April–October period and less energetic waves during the November–March period. These observations are consistent with the wave climate of the area because of northward migration, by a few degrees, of the wave-generating zone in the high latitudes of the South Atlantic (~40° to 60° S) during the summer period [14,15]. Table 1 gives correlations and errors between the WW3 video and model data on the time series of *Hs*, *Tm*, and the wave direction. There is strong correlation between the two time series of *Hs* ($R^2 = 0.80$). Direction and *Tm* are less correlated ($R^2 = 0.44$ and $R^2 = 0.19$; Figure 3b,c), with a low observed variability.

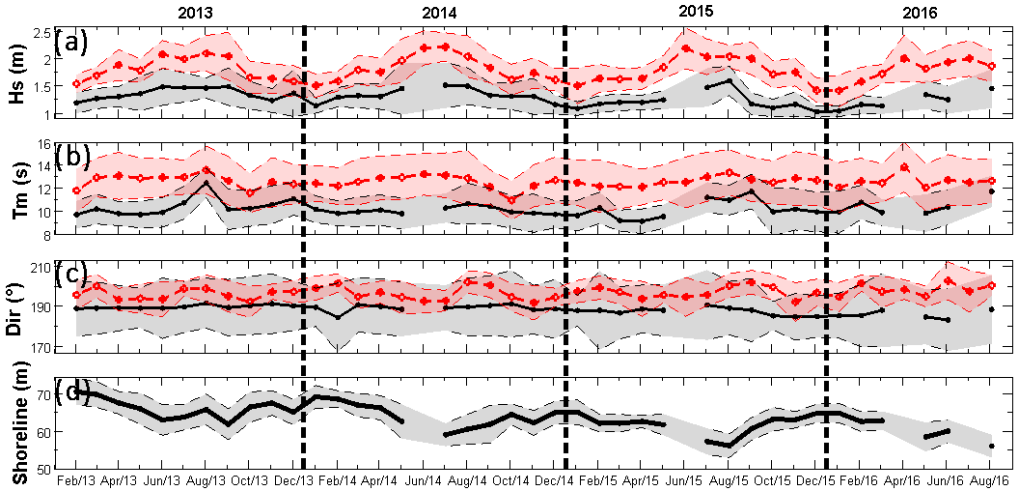

Figure 3. Monthly-averaged video estimates (black) and Wavewatch III data (red): (**a**) wave significant height *Hs*; (**b**) wave mean period *Tm*; (**c**) wave direction *Dir*; and (**d**) shoreline location. Shaded zones stand for day-to-day dispersion (standard deviation).

It should be noted here that the IOWAGA WW3 ocean wave hindcast had not been assimilated with any observations (satellite or buoy). For the previous versions of WW3, random averaged errors between *Hs* model outputs (WW3) and satellite data ranged from 0.3 to 0.4 m for low wave heights (<2 m), and 0.15 m for higher waves [34]. An improvement was made on the recent version used in this work, integrating new parameterizations for the wind–sea and wave dissipation. However, the

normalized RMSE for *Hs* remained ~20%, compared to the satellite data in our study area, with biases of more than 0.1 m [29]. This was consistent with the overestimation observed in the model outputs (Figure 3), which were likely amplified due to local unresolved effects of bathymetry for the wave propagation from deep water to breaking point. However, WW3 results were improved even more from linear regression correction than from bias correction, as shown in [35]. Gaps in *Hs* video data could therefore be estimated using a linear regression between the two sets of data.

Table 1. Comparison of daily hydrodynamic video data and WW3 model outputs. WW3 data were propagated from deep water to breakpoint using an empirical direct formula [30]. The root-mean-square error (RMSE) and the mean error (ME) were computed between the two sets of data.

Video–WW3	*Hs* (m)	*Tm* (s)	*Dir* (°)
Correlation	0.8	0.4	0.2
RMSE	0.3	2.4	9.4
ME	0.3	2.3	8.5

3.2. Storms and Morphological Impact

3.2.1. Detection and Statistics of Individual Storms

Thirty-two storms were identified over the study period (Figure 4a). The mean peak storm wave height was 2.05 m (standard deviation $\sigma = 0.05$ m) and the mean wave height throughout the storms was 1.99 m ($\sigma = 0.12$ m). The average duration of a storm was 1.8 days and storms were recorded from April to September, corresponding to austral winter. With the threshold value of $H_{S_{5\%}} = 1.85$ m, no storm with a duration longer than 12 h was recorded from the November to March period, due to less energetic wave conditions. Only 12 storms (average duration of 1.6 days) were further considered for analyses of shoreline responses due to gaps in shoreline data. Individual storms resulted in a wide range of shoreline impacts (Figure 4b), from no change on 2 July 2013 (1 day storm), to significant erosion (−8.7 m) during a 4 day storm (21–25 September 2013). The maximum number of storm-events was recorded in July. In 2014 for example, 12 storms were counted, with four in July. The strongest storm impacts were recorded at the end of austral fall (in May) with an average onshore migration of −3.7 m during a storm of less than 1 day. This impact decreased with the increase of storm numbers until the beginning of austral winter (June and July).

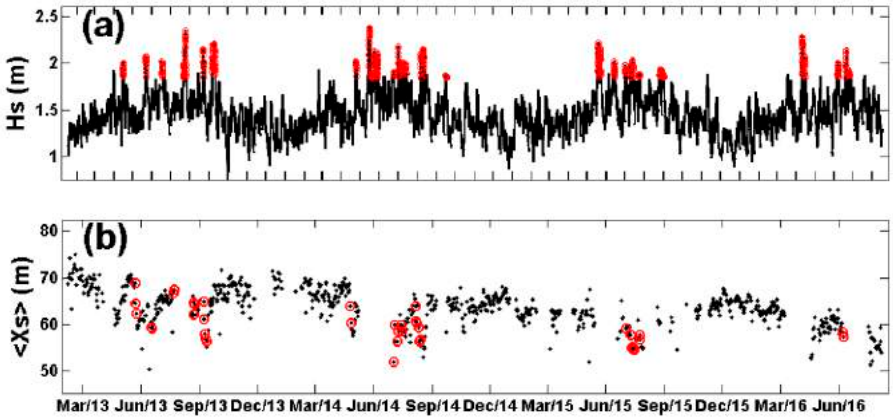

Figure 4. Time series of: (**a**) significant wave height, and (**b**) along-shore-averaged location <*Xs*> from the tower of camera location. Storm periods are marked in red.

3.2.2. Beach Response to Storms and Resilience

Figure 5 shows an ensemble-averaged analysis of the shoreline evolution during the storm and post-storm recovery period, with this period referring to the post-storm period of continuous accretion,

at the end of which the beach was assumed to be stabilized [5,9,12]. The day "0" stands for the beginning of the storm, according to the 5% exceedance (1.85 m) of *Hs*. The average storm intensity was 155 m^2·h and induced an average beach erosion of 3.1 m. After the end of the storm, the beach attempted to recover during a continuous accretive phase: the shoreline moved offshore (0.46 m/day) and the time needed to reach stabilization was ~15 days. This time was considered as the post-storm recovery duration *Tr*.

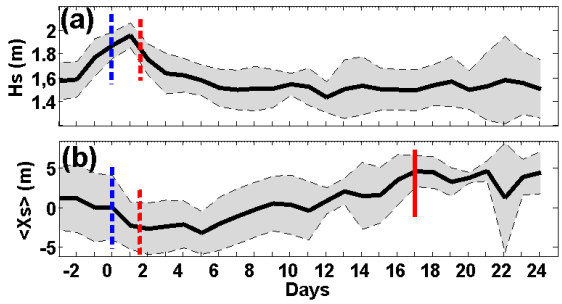

Figure 5. Ensemble-averaged evolution during the storm and post-storm recovery period for: (**a**) *Hs*, and (**b**) shoreline location <*Xs*>. Blue dashed lines stand for the beginning of the averaged-storm, red dashed lines for the end of the storm (1.6 day storm duration), and the solid red line stands for the post-storm recovery duration for beach stabilization (15 days).

3.3. Seasonal Cycle

Figures 6 and 7 present the seasonal cycle of several monthly nearshore forcing parameters and beach morphology. The maximum monthly-averaged *Hs* (1.51 m) was obtained in July, corresponding to the maximum monthly-averaged wave flux (15400 J/m·s). The seasonal pattern was highlighted in the along-shore-averaged shoreline position, which was strongly correlated to the monthly *Hs* seasonal cycle ($R^2 = -0.94$), and in contrast, less correlated to the monthly-averaged beach slope ($R^2 = -0.25$). The maximum beach slope was 0.14 rad at the end of April. For the 32 identified storms, the greatest number of storms was recorded in July, but these were shorter (average duration of 1.34 days), leading to a lesser average intensity compared to the other months. Figure 6a,d and Figure 7a show that the beach response (shoreline location) was most related to the monthly-averaged *Hs* rather than the intensity of storm-events.

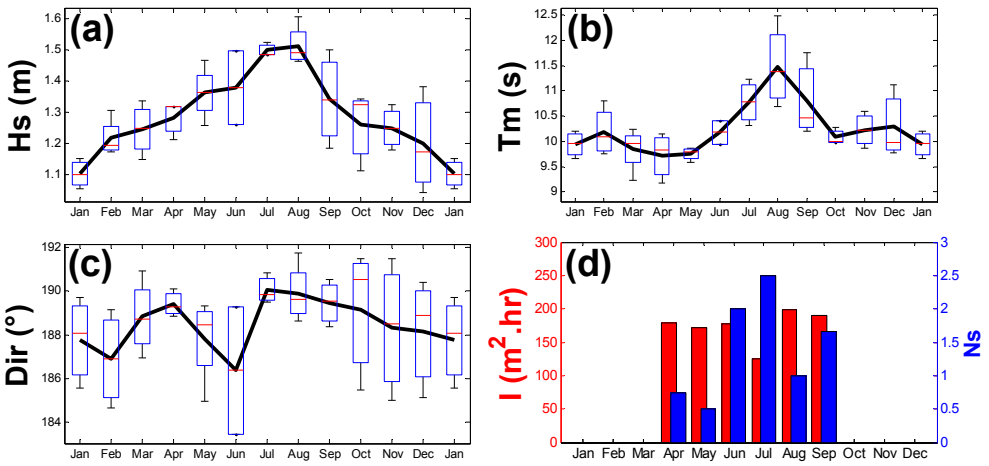

Figure 6. Seasonal variability (monthly average) of: (**a**) *Hs*, (**b**) *Tm*, (**c**) wave direction (*Dir*), and (**d**) storm intensity in m^2·h (red) and storm number *Ns* (blue). For each box, the central mark (red line) is the median, the edges of the box (blue) are the 25th and 75th percentiles, and the whiskers extend to the most extreme data points not considered outliers.

The seasonal cycle of the shoreline presented two main different phases, the erosive phase (January to August) and the accretive phase (August to December), due to the changes of *Hs* (Figure 6a) and *Tm* (Figure 6b), which were driven by swell waves. The standard deviation of the beach slope variation was smaller during the eroding period, reflecting the low variability of the beach slope according to low-energy waves.

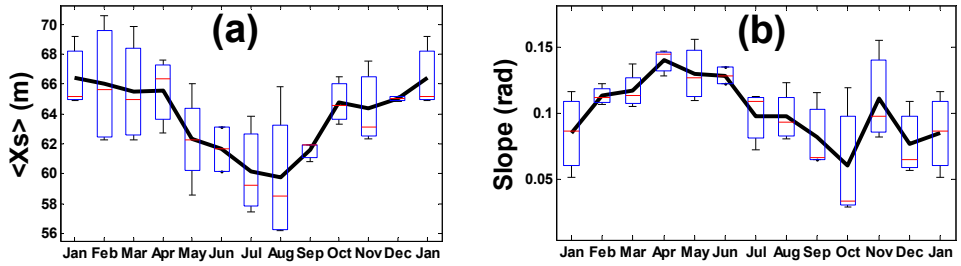

Figure 7. Monthly average seasonal variability: (**a**) mean shoreline location <*Xs*> from video camera location, and (**b**) beach slope. For each box, the central mark (red line) is the median, the edges of the box (blue) are the 25th and 75th percentiles, and the whiskers extend to the most extreme data points not considered outliers.

Storms occurred at the end of the eroding period (April to July) and at the beginning of the accreting period (August to September). The beach exhibited particular responses to storm-events, depending on the concerned period, as shown in Figure 8, where only 12 storms were considered with their corresponding shoreline data. During this eroding period, the recovery duration seemed to be shorter (~10 days). In contrast, in the accreting period, the time recovery duration seemed to be longer and the storm impact increased with the storm duration, consistent with [17]. The post-storm recovery was more significant in the accreting period than in the eroding period. In August, the beach experienced an onshore migration of 2.4 m during a 1.4 day averaged-duration storm, while in September, a 3.7 day averaged-duration storm caused an erosion of −5.4 m. The beach response was therefore influenced by the erosive or accretive period of the wave climate oscillation.

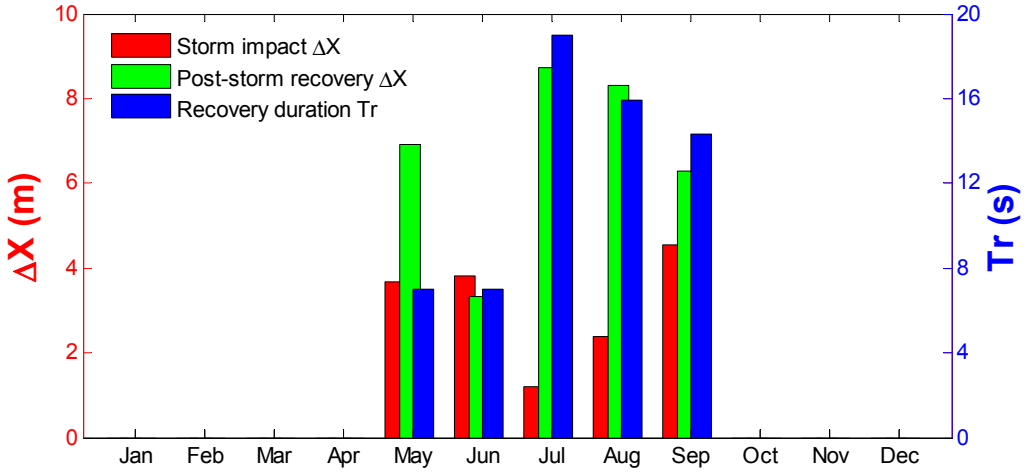

Figure 8. Ensemble-averaged shoreline variation <ΔX_j> during and after storm-events: storm impact (red), beach recovery (green), and recovery duration (blue) per month.

3.4. Trends and Inter-Annual Evolution

Trends of waves and the shoreline were investigated using the test of Mann Kendall [33]. The results showed that the shoreline position *Hs* and wave direction data presented substantial

trends. A failure to reject the null hypothesis (absence of trend) at 95% significance level was obtained for the wave period and energy, and the beach slope. The residual signal reflected trends over the study period and was obtained by removing the seasonal cycle from the daily data. Table 2 shows the annual average and residuals of each studied parameter. During the 3.5 year study period, the shoreline migrated 6 m onshore. The annual anomaly or residual of the shoreline decreased from +2.8 m in 2013 to −2.9 m in 2016, while the annual residual of the beach slope did not change. A decrease of 3° in the wave direction was observed during the study period.

Table 2. Annual averaged values and anomalies (R_a) for the study period.

Study Period	2013		2014		2015		2016 (January–August)	
	Mean	R_a	Mean	R_a	Mean	R_a	Mean	R_a
Hs (m)	1.35	+0.05	1.34	+0.04	1.23	−0.07	1.28	−0.06
Tm (s)	10.4	+0.2	10.1	−0.2	10.2	−0.1	10.6	+0.3
Dir (°)	188.9	+1.4	188.2	+0.5	186.4	−1.3	185.2	−1.8
Shoreline position (m)	66.4	+2.8	63.9	+0.2	61.8	−1.9	60.1	−2.9
Beach slope (rad)	0.098	−0.006	0.101	0	0.109	+0.008	0.113	−0.04

4. Discussion

Perhaps more than other survey techniques (e.g., DGPS, LIght Detection And Ranging LIDAR) used in coastal science, the video system remains less costly. However, video measurements are subject to large uncertainties [10]. In particular, the shoreline-detection methods are sensitive to waves, lighting conditions, and water levels, which can scale the effects of both the setup and run-up, and reduce the colour signal strength [32]. Previous works on video error detection [18,23,36] compared shorelines measured by video to topographic surveys, and the results suggested a reasonable error (about 0.23 m at Grand Popo, Benin, following [18]). In this work, tidal heights were estimated using the WXTide2 model, to compute the shoreline location. This did not take into account all regional and coastal components of the sea level (including wave-induced setup and run-up) and nearshore bathymetry that were measured by the video [18].

The results presented here are consistent with the wave climate observations in the studied area [14,15]. A seasonal pattern was clearly observed in the shoreline position, beach slope, and wave characteristics. Data exhibited two specific periods: an accreting period (August to December), where *Hs* and *Tm* decreased; and an eroding period, where *Hs* and *Tm* increased (January to July). This was consistent with the oscillation of the Southern Annular Mode (SAM), which has a predominant influence on transport induced by swell waves [15]. The low values of the beach slope standard deviation observed during February to April reflected a stabilization reached during low wave-energy conditions. Computing the beach slope variability could lead to an understanding of the nature of the waves breaking, as the beach slope is connected to the surf-similarity parameter. A recent finding [20] suggested that the wave reflection is mostly governed by swash dynamics, whereby the reflected spectrum essentially depends on the swash slope.

The 3.5 years of video of the shoreline location suggests that beach dynamics observed at Grand Popo Beach are affected by storm-events. This study revealed that the impact on shoreline migration can be significant: −8.7 m on 21 September 2013, during a 4 day sequence of storms. The mean duration of the 12 observed storms was 1.6 days, with an average storm-erosion of −3.1 m. At the end of the storm, the shoreline migrated offshore at an average distance of 6 m within 15 days. However, the storm impact and post-storm recovery were very dependent on the observed seasonal pattern, consistent with [17]. The recovery duration in the eroding period was shorter (~10 days) than in the accreting period (>15 days). The end of the period of stabilization observed between February and April was marked by short storms of an average duration of less than 1 day, which caused significant erosion on the beach, averaging 3.7 m. During the accreting period, it took longer storms to observe a

significant impact (mean of 3.7 days for −5.4 m). The beach's response was therefore mostly related to the energy of average wave conditions, rather than to the energy of extreme wave conditions.

The study of inter-annual trends in this work demonstrated a gradual decline of the shoreline cross-shore location during the period 2013–2016. However, the length of the data set was not enough to assess the inter-annual variability. A field of nine groins of 100 m lengths and 20 m widths was constructed between 2012 and 2014 over a distance of 3.5 km, near the city of Anèho (Togo), about 20 km from the video system at Grand Popo Beach. This field could reduce the sediment supply of the eastward coastal drift in the direction of Grand Popo. A recent study [19] investigated the coastline evolution between Grand Popo (Benin) and Anèho (Togo) from 1984 to 2011, using Landsat TM (Thematic Mapper) and ETM+ (Enhanced Thematic Mapper Plus) images. This study showed that the locality of Grand Popo was in dynamic equilibrium from 1984 to 2000, while a significant accretion occurred with +0.4 m/year between 2000 and 2011. The impact of the field of groins was also investigated, but no clear conclusions were drawn on its impacts on the coastal area of Grand Popo; although immediately downstream from the groynes, the region is experiencing significant visual erosion.

The trend of oceanic forcing (wave direction of −3° for the period 2013–2015) is another possible factor of the observed erosion. The diminution of the wave direction from 188.9° to 185.2° during the study period increased the importance of cross-shore processes compared to along-shore processes, resulting in a decrease in the along-shore sediment transport (~5% per year), computed with an empirical formula [30] presented in [15], in our study area. The longshore sediment transport is very dependent on the shore's normal wave direction, and the resulting littoral drift in the Bight of Benin is one of the largest in the world, following [14,15]. Nevertheless, the video estimates of the wave direction had uncertainties. A comparison of video and WW3 wave direction outputs showed that the video data presented a larger standard deviation than the model output, respectively 13.4° (video) and 6.4° (WW3), and the video wave direction trend was not observed in the WW3 data. A previous study estimated the RMSE with field ADCP measurements to be about 9.25°, and the mean error (ME) to be 2.25°, within the range of observed variation from 2013 to 2016 (−3°).

5. Conclusions

Three and a half years of video-derived shoreline and wave evolution data at Grand Popo Beach was used to investigate the beach's response to wave forcing from event to inter-annual time scales in the coastal area of Grand Popo Beach, Benin. The beach exhibited a seasonal pattern in wave conditions and the along-shore-averaged shoreline position was most related to the monthly-averaged wave height rather than the average storm intensity. The seasonal pattern of the shoreline indicated an eroding period and an accreting period, corresponding to austral and winter periods, respectively. Thirty-two storms were identified for the period 2013–2016. The mean storm duration was 1.6 days for the 12 observed storms due to gaps in video data, and the average storm erosion was −3.1 m. Ensemble-averaged storm recovery conditions showed that the beach recovered within 15 days, and the average recovery rate was 0.4m/day. This study underlines that the impact of storms is more or less amplified depending on the eroding and accreting periods of the wave climate: (i) the recovery duration is longer in the accreting period than in the eroding period, (ii) the storm-impact is more significant in the eroding period than in the accreting period, (iii) storms are longer in the accreting period than in the eroding period, and (iv) storm numbers are high during the transition from the eroding to accretive phases. A trend on the along-shore-averaged shoreline location was observed (−1.6 m/year), however our data were not enough to draw conclusions at inter-annual time scales.

Acknowledgments: This publication was made possible through support provided by the IRD. We acknowledge the use of the WW3 dataset (IOWAGA wave hindcast database; http://tds1.ifremer.fr/thredds/IOWAGA-WW3-HINDCAST). We would like to express our gratitude to IRD/JEAI-RELIFOME (Jeune Equipe Associée à l'IRD) for its financial support and to support the three months stay at Gao in Benin. Thanks are due to Gaël ALory for his technical support in maintaining the video system. The Grand Popo experiment was supported by the French INSU/CNRS EC2CO-LEFE/IRD, UNESCO Co-Chair ICMPA/UAC. We are indebted to the "Forces Navales"

of Benin at Grand Popo for their logistic support during field experiments and for allowing the installation of the permanent video system on the semaphore. This work was supported by French ANR project COASTVAR (ANR-14-ASTR-0019).

Author Contributions: All authors were implicated in maintaining the video system at Grand Popo and analysis of data.

Conflicts of Interest: The authors declare no conflict of interest.

References

1. Stive, M.J.F.; Aarninkhof, S.G.J.; Hamm, L.; Hanson, H.; Larson, M.; Wijnberg, K.M.; Nicholls, R.J.; Capobianco, M. Variability of shore and shoreline evolution. *Coast. Eng.* **2002**, *47*, 211–235. [CrossRef]
2. Ranasinghe, R.; Callaghan, D.; Stive, M.J.F. Estimating coastal recession due to sea level rise: Beyond the Bruun rule. *Clim. Chang.* **2012**, *110*, 561–574. [CrossRef]
3. Ruggiero, P.; Cote, J.; Kaminsky, G.; Gelfenbaum, G. Scales of variability along the Columbia River littoral cell. In Proceedings of the Coastal Sediments '99: The 4th International Symposium on Coastal Engineering and Science of Coastal Sediment Processes, Hauppauge, NY, USA, 21–23 June 1999; pp. 1692–1707.
4. Brunel, C.; Sabatier, F. Potential influence of sea-level rise in controlling shoreline position on the French Mediterranean Coast. *Geomorphology* **2009**, *107*, 47–57. [CrossRef]
5. Senechal, N.; Coco, G.; Castelle, B.; Marieu, V. Storm impact on the seasonal shoreline dynamics of a meso-to macrotidal open sandy beach (Biscarrosse, France). *Geomorphology* **2015**, *228*, 448–461. [CrossRef]
6. Zhang, K.; Douglas, B.; Leatherman, S. Do storms cause long-term beach erosion along the U.S. East Barrier Coast? *J. Geol.* **2002**, *110*, 493–502. [CrossRef]
7. Morton, R.A.; Paine, J.G.; Gibeaut, J.G. Stages and durations of post-storm beach recovery, southeastern Texas coast, USA. *J. Coast. Res.* **1994**, *10*, 884–908.
8. Morton, R.A.; Gibeaut, J.C.; Paine, J.G. Meso-scale transfer of sand during and after storms: Implications for prediction of shoreline movement. *Mar. Geol.* **1995**, *126*, 161–179. [CrossRef]
9. Castelle, B.; Marieu, V.; Bujan, S.; Splinter, K.D.; Robinet, A.; Senechal, N.J.; Ferreira, S. Impact of the winter 2013–2014 series of severe Western Europe storms on a double-barred sandy coast: Beach and dune erosion and megacusp embayments. *Geomorphology* **2015**, *238*, 135–148. [CrossRef]
10. Masselink, G.; Scott, T.; Russel, P.; Davidson, M.A.; Conley, D.C. The extreme 2013/2014 winter storms: Hydrodynamic forcing and coastal response along the southwest coast of England. *Earth Surf. Process. Landf.* **2015**, *41*, 378–391. [CrossRef]
11. Almeida, L.P.; Vousdoukas, M.V.; Ferreira, Ó.; Rodrigues, B.A.; Matias, A. Thresholds for storm impacts on an exposed sandy coastal area in southern Portugal. *Geomorphology* **2012**, *143*, 3–12. [CrossRef]
12. Angnuureng, D.B.; Almar, R.; Senechal, N.; Castelle, B.; Addo, K.A.; Marieu, V.; Ranasinghe, R. Shoreline resilience to individual storms and storm clusters on a meso-macrotidal barred beach. *Geomorphology* **2017**, *290*, 265–276. [CrossRef]
13. Ba, A.; Senechal, N. Extreme winter storm versus summer storm: Morphological impact on a sandy beach. *J. Coast. Res.* **2013**, *1*, 648–653. [CrossRef]
14. Laibi, R.; Anthony, E.; Almar, R.; Castelle, B.; Senechal, N.; Kestenare, E. Longshore drift cell development on the human-impacted Bight of Benin sand barrier coast, West Africa. *J. Coast. Res.* **2014**, *70*, 78–83. [CrossRef]
15. Almar, R.; Kestenare, E.; Reyns, J.; Jouanno, J.; Anthony, E.J.; Laibi, R.; Hemer, M.; Du Penhoat, Y.; Ranasinghe, R. Response of the Bight of Benin (Gulf of Guinea, West Africa) coastline to anthropogenic and natural forcing, Part1: Wave climate variability and impacts on the longshore sediment transport. *Cont. Shelf Res.* **2015**, *110*, 48–59. [CrossRef]
16. Anthony, E.J.; Blivi, A.B. Morphosedimentary evolution of a delta-sourced, drift-aligned sand barrier–lagoon complex, western Bight of Benin western Bight of Benin. *Mar. Geol.* **1999**, *158*, 161–176. [CrossRef]
17. Yates, M.L.; Guza, R.T.; O'Reilly, W.C. Equilibrium shoreline response: Observations and modeling. *Geophys. Res.* **2009**, *114*. [CrossRef]
18. Abessolo, O.G.; Almar, R.; Kestenare, E.; Bahini, A.; Houngue, G.H.; Jouanno, J.; Du Penhoat, Y.; Castelle, B.; Melet, A.; Meyssignac, B.; et al. Potential of video cameras in assessing event and seasonal coastline behaviour: Grand Popo, Benin (Gulf of Guinea). *J. Coast. Res.* **2016**, 442–446. [CrossRef]

19. Degbe, C.G.E.; Laibi, R.; Sohou, Z.; Oyede, M.L.; Du Penhoat, Y.; Djara, M.B. Diachronic analysis of coastline evolution between Grand-Popo and Hillacondji (Benin), from 1984 to 2011. *Water* **2016**, submitted.
20. Almar, R.; Ibaceta, R.; Blenkinsopp, C.; Catalan, P.; Cienfuegos, R.; Viet, N.T.; Duong Hai, T.; Uu, D.V.; Lefebvre, J.P.; Laryea, W.S.; et al. Swash-based wave energy reflection on natural Beaches. In Proceedings of the Coastal Sediments 2015, San Diego, CA, USA, 11–15 May 2015.
21. Wright, L.D.; Short, A.D. Morphodynamic variability of surf zones and beaches: A synthesis. *Mar. Geol.* **1984**, *56*, 93–118. [CrossRef]
22. Almar, R.; Honkonnou, N.; Anthony, E.J.; Castelle, B.; Senechal, N.; Laibi, R.; Mensah-Senoo, T.; Degbe, G.; Quenum, M.; Dorel, M.; et al. The Grand Popo beach 2013 experiment, Benin, West Africa: From short timescale processes to their integrated impact over long-term coastal evolution. *J. Coast. Res.* **2014**, 651–656. [CrossRef]
23. Angnuureng, D.B.; Almar, R.; Addo, K.A.; Castelle, B.; Senechal, N.; Laryea, S.W.; Wiafe, G. Video observation of waves and shoreline change on the Microtidal James Town Beach in Ghana. *J. Coast. Res.* **2016**, 1022–1026. [CrossRef]
24. Holland, K.T.; Holman, R.A.; Lippmann, T.C. Practical use of video imagery in near-shore oceanographic field studies. *IEEE J. Ocean. Eng.* **1997**, *22*, 81–92. [CrossRef]
25. Almar, R.; Ranasinghe, R.; Senechal, N.; Bonneton, P.; Roelvink, D.; Bryan, K.; Marieu, V.; Parisot, J.P. Video-based detection of shorelines at Complex Meso–Macro Tidal Beaches. *J. Coast. Res.* **2012**, *28*, 1040–1048. [CrossRef]
26. Almar, R.; Cienfuegos, R.; Catalán, P.A.; Michallet, H.; Castelle, B.; Bonneton, P.; Marieu, V. A new breaking wave height direct estimator from video imagery. *Coast. Eng.* **2012**, *61*, 42–48. [CrossRef]
27. Almar, R.; Senechal, N.; Bonneton, P.; Roelvink, D. Wave celerity from video imaging: A new method. Proceedings of Coastal Engineering 2008, Hamburg, Germany, 31 August–5 September 2008; pp. 661–673.
28. Almar, R.; Michallet, H.; Cienfuegos, R.; Bonneton, P.; Ruessink, B.G.; Tissier, M. On the use of the radon transform in studying nearshore wave dynamics. *Coast. Eng.* **2014**, *92*, 24–30. [CrossRef]
29. Rascle, N.; Ardhuin, F. Global wave parameter data base for geophysical applications. Part II: Model validation with improves source term parameterization. *Ocean Model.* **2013**, *70*, 145–151. [CrossRef]
30. Larson, M.; Hoan, L.X.; Hanson, H. Direct formula to compute wave height and angle at incipient breaking. *J. Waterw. Port Coast. Ocean Eng.* **2010**, *136*, 119–122. [CrossRef]
31. Boak, E.H.; Turner, I.L. Shoreline definition and detection: A review. *J. Coast. Res.* **2005**, *21*, 688–703. [CrossRef]
32. Aarninkhof, S.G.J.; Turner, I.L.; Dronkers, D.T.; Caljouw, M.; Nipius, L. A video-based technique for mapping intertidal beach bathymetry. *Coast. Eng.* **2003**, *49*, 275–289. [CrossRef]
33. Hamed, K.H.; Rao, A.R. A modified Mann-Kendall trend test for autocorrelated data. *J. Hydrol.* **1998**, *204*, 182–196. [CrossRef]
34. Tolman, H.L. Limiters in third-generation wind wave models. *Glob. Atmos. Ocean Syst.* **2002**, *8*, 67–83. [CrossRef]
35. Woodcock, F.; Greenslade, D.J.M. Consensus of numerical model forecasts of significant wave heights. *Weather Forecast.* **2007**, *22*, 792–803. [CrossRef]
36. Ranasinghe, R.; Holman, R.; de Schipper, M.A.; Lippmann, T.; Wehof, J.; Minh Duong, T.; Roelvink, D.; Stive, M.J.F. Quantification of nearshore morphological recovery time scales using Argus video imaging: Palm Beach, Sydney and Duck, NC. *Coast. Eng. Proc.* **2012**, *1*, 24.

water

MDPI

Article

Shoreline Response to a Sequence of Typhoon and Monsoon Events

Rafael Almar [1,*], Patrick Marchesiello [1], Luis Pedro Almeida [1], Duong Hai Thuan [1,2], Hitoshi Tanaka [3] and Nguyen Trung Viet [2]

1 LEGOS (Université de Toulouse/CNRS/CNES/IRD), 31400 Toulouse, France; Patrick.Marchesiello@legos.obs-mip.fr (P.M.); luis.pedro.almeida@legos.obs-mip.fr (L.P.A.); duonghaithuan@tlu.edu.vn (D.H.T.)
2 Faculty of Marine and Coastal Engineering, Thuyloi University, Hanoi, Vietnam; nguyentrungviet@tlu.edu.vn
3 Department of Civil and Environmental Engineering, Tohoku University, Sendai 980-8576, Japan; hitoshi.tanaka.b7@tohoku.ac.jp
* Correspondence: rafael.almar@ird.fr; Tel.: +33-05-6133-3006

Academic Editor: Maurizio Barbieri
Received: 11 April 2017; Accepted: 18 May 2017; Published: 23 May 2017

Abstract: Shoreline continuously adapts to changing multi-scale wave forcing. This study investigates the shoreline evolution of tropical beaches exposed to monsoon events and storms with a case study in Vietnam, facing the South China Sea, over the particularly active 2013–2014 season, including the Cat-5 Haiyan typhoon. Our continuous video observations show for the first time that long-lasting monsoon events have more persistent impact (longer beach recovery phase) than typhoons. Using a shoreline equilibrium model, we estimate that the seasonal shoreline behavior is driven by the envelope of intra-seasonal events rather than monthly-averaged waves. Finally, the study suggests that the interplay between intra-seasonal event intensity and duration on the one hand and recovery conditions on the other might be of key significance. Their evolution in a variable or changing climate should be considered.

Keywords: Vietnam; South China Sea; erosion; recovery; storminess; winter monsoon; typhoons

1. Introduction

It would be a mistake to consider the vulnerability of coastal regions as a simple response to sea level change, assuming static coastal morphology [1,2]. On the contrary, coastal morphology is in a constant process of equilibration at various timescales. It is generally assumed that waves are the main driver of coastal evolution but their role is strongly non-linear, and the coastal response to unsteady forcing is unclear [3].

Beach recovery to extreme events is also still debated as there is not even agreement on their transient or persistent impacts [4,5]. For isolated events, departure from equilibrium is related to the event's intensity and duration [2,6,7]. However, no clear conclusion can be drawn when considering a sequence of events, since both enhanced [8] and weakened effects are observed [9–11], e.g., during the particularly stormy winter of 2013–2014 in Europe, e.g., [12]. The timescales' interplay between recurring events and recovery conditions appears determinant.

Existing shoreline equilibrium models (among others: [2,13,14]) show appreciable skills in predicting shoreline location from wave energy at monthly or longer time-scales for mid-latitude, storm-dominated coasts. However, these skills may be at fault in a so-called low-energy environment as often encountered in the tropics. There, the beach is mostly active during occasional events and is generally found in equilibrium with the preceding energetic event rather than current conditions [15].

Existing equilibrium models might not be able to describe such behavior, in particular when energetic wave events do not occur concomitantly with the seasonal peak of wave energy.

Tropical beaches are exposed to infrequent short (1–3 days) but paroxysmal storms such as cyclones (typhoons in the western Pacific) and can rapidly adapt to these very energetic conditions [16]. They slowly recover under persisting low to moderate waves during the rest of the year. However, all the tropical environments are not strictly low-energy, and this is particularly true in Southeast Asia as it is affected by monsoons [17]. Typical winter monsoon events last from three days to three weeks and can bring strong persistent swells of somewhat lower energy but longer duration than tropical storms. There is substantial literature on the atmospheric cold intrusion affecting the Southeast Asian coastal states every winter, e.g., [18] but the role of these energetic events on shoreline evolution has not been investigated. Clearly, they are active processes for shoreline erosion and must be compared with the effect of short-term storms. Their particularly long duration may be a crucial element of their beach response as the beach may have sufficient time to adjust to the energetic conditions and reach equilibrium.

In this paper, we investigate the video-derived shoreline evolution of Nha Trang beach, Vietnam, over the particularly active 2013–2014 season, with numerous winter monsoon events and storms, including the Cat-5 Haiyan typhoon. We first investigate the role of monsoon events on shoreline evolution compared with storms, and secondly the seasonal behavior of the beach in response to both monthly-averaged wave forcing and wave events using a shoreline equilibrium model [2].

2. Study Site

Nha Trang is an embayed beach located in southeastern Vietnam coast, facing the South China Sea (Figure 1, upper panel). This 6 km bay is oriented north–south and is partially sheltered from waves by a group of islands at its southern end. This medium-sized (D_{50} = 0.4 mm) sandy beach is rather uniform along the shore, and is characterized by a steep (slope ~ 0.1) upper face and a flat low-tide terrace (~40 m wide). The tide is a mix of diurnal and semi-diurnal, with a small tidal range (<1.6 m).

2.1. Typhoons

The Northwest Pacific is the most cyclogenetic region on earth. Of the 16 tropical storms that turn into typhoons (JTWC 2013) annually, about one-third propagate westward to South China Sea [19]. Every year, 4–6 typhoons hit Vietnam [20], typically between August and December, but the risk of landfall varies strongly at seasonal and interannual scales, e.g., [19,21]. The year 2013 came after two years of La Niña conditions, resulting in strong sea surface temperatures, which favored cyclone generation [22]. As a consequence, 2013 was observed to be the most active typhoon season since 2004, and the one with most casualties since 1975. Among the 10 typhoons landing in Vietnam in 2013, Cat. 5 Haiyan in early November turned into one of the world strongest recorded tropical cyclones [23].

2.2. Monsoons

Summer monsoons (May to September) drive relatively weak, short-period southwesterly waves in the South China Sea. The inception of winter monsoon (October to April), caused by high-pressure systems in Siberia, drives strong northeast winds. Because these pressure systems form every three days to three weeks, wind pulses occur at these timescales. As a result, the winter monsoon generates energetic waves larger than 2.5 m off the Vietnamese coast [24], reaching values up to 4 m, which stands for the 10% exceedance level of wave climate [25].

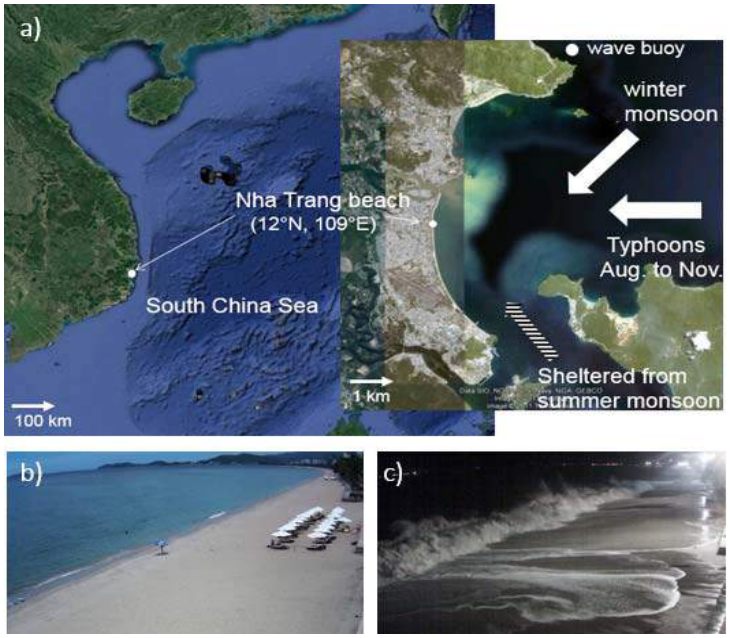

Figure 1. Study site, (**a**) Nha Trang each, Vietnam, facing the South China Sea. Images from the video system during (**b**) calm summer season and (**c**) Cat. 5 Haiyan typhoon.

From its orientation, Nha Trang region is mainly sheltered from summer monsoon which consists in very calm conditions. It can be considered that this stretch of coast is under the influence of winter monsoons and typhoons only [26,27].

3. Methods and Data

A video station was installed in May 2013 [26] in the central part of Nha Trang Bay, is considered far enough from the influence of the edges of the bay and is predominantly influenced by cross-shore rather than by longshore dynamics [27,28]. Hydrodynamic (waves, currents, tides) and morphology (intertidal and submerged bathymetry and shoreline) can be extracted from secondary images, timestack, and average images [27,29]. In this study, the shoreline was extracted manually at a single cross-shore section of the beach. It is estimated as the video-based average between maximum and minimum runup excursions over 15-min images and during daylight and night hours. Hourly tidal modulation of the shoreline location was averaged out using daily means. Wave fields were extracted from ERA-interim global reanalysis provided by the European Centre for Medium-Range Weather Forecasts (resolution of 0.5°, every 6 h [30]) at the closest node off Nha Trang, and validated over a two month period using a local wave gauge. This validation was successful (coefficient of determination R^2 = 0.87, RMSE = 0.26 m) down to event scale, which made it possible to extend our study over a full annual period, from 1 August 2013 to 1 August 2014. The period starts from summer monsoon conditions until October, and then winter monsoon lasts until April when a new summer monsoon begins.

Observations of waves and shoreline changes were used to calibrate the parametrical model of equilibrium shoreline position ShoreFor [2,31] accounting for cross-shore transport processes. This model was chosen as it was applied successfully at various sites for predicting the daily to seasonal shoreline response to waves compared to other models more dedicated to long-term interannual evolution [32]. This one-dimensional shoreline prediction model has the form

$$\frac{dx}{dt} = b + c\left(F^+ + rF^-\right) \quad (1)$$

where b and c are calibrated coefficients, r the ratio between erosive and accretive shoreline change, and $F^{\pm}$ is the shoreline forcing, which depends on disequilibrium with anteceding wave conditions

$$F^{\pm} = P^{0.5}(\Omega_{eq} - \Omega) \quad (2)$$

where P is wave power ($\propto Hs^2Tp$), with Hs and Tp as the deep water significant wave height and peak period, Ω and Ω_{eq} are the instant and time-varying dimensionless fall velocity such as

$$\Omega_{eq} = \left[\sum_{i=1}^{2\phi} \Omega_{eq} 10^{-i/\phi}\right] \quad (3)$$

with Ω defined as $\Omega = H_s/wT_p$, where w is the settling velocity and is a function of the site-specific median grain size (D_{50}). In Equation (3), i is the day prior to present, ϕ the number of past days where the decaying exponential function reaches 10% (more details in [2,14]).

4. Results

The offshore wave forcing for the one year study period is presented in Figure 2a. The southeast coast of Vietnam is partly sheltered from summer monsoon low-energy wind-waves ($Hs < 1$ m, $Tp < 4$s). The winter season presents more energetic swell ($Hs \sim 1.7$ m, $Tp = 7$–8 s) and larger variability, with largest values ($Hs \sim 3$ m, $Tp = 10$ s) during monsoon events. Waves during typhoon events have similar magnitude but shorter duration (<3 days). The shoreline (Figure 2a) is stable or even slightly in accretion till the end of summer monsoon in October, and then begins an erosive phase during winter monsoon until February when it reaches its most landward location, before migrating seaward again.

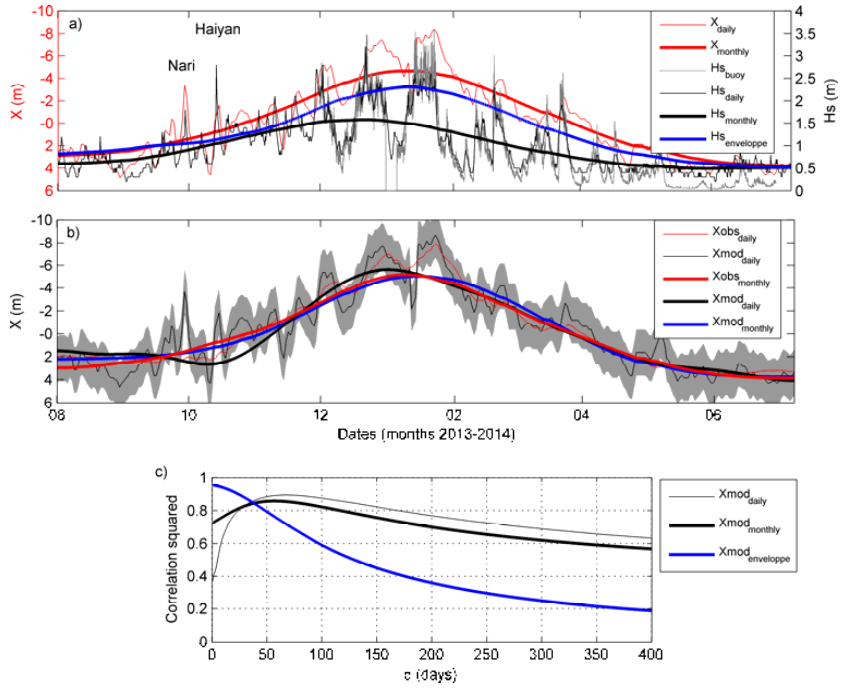

Figure 2. (**a**) Video-derived shoreline location X (red), wave height Hs from Era-Interim (black) and from buoy (gray) off Nha Trang, with the monthly envelope of intra-seasonal Hs (from 3 to 30 days) in blue. (**b**) Results from the shoreline equilibrium model ShoreFor (black, with uncertainty as shaded area), compared with the observed daily shoreline position (red) and in (**c**) the respective correlations squared for different ϕ values. In panels a,b, negative and positive X values stand for erosion and accretion from the mean, respectively. In a–c, thin and thick lines are daily and monthly data respectively.

This seasonal pattern (duration > 30 days) hides important intra-seasonal (or synoptic scale, i.e., winter monsoon events) variability with shoreline variations reaching 10 m during typhoon events and during long-lasting winter-monsoon events with durations from three days to three weeks. Even though the magnitude of shoreline retreat of these events is similar, Figure 2a shows that monsoon events have a more persistent impact with longer recovery (i.e., 10 to 20 days) than typhoons which takes a few days at most (sometimes within less than a day). While typhoon events were frequent at the beginning of the winter season, from October to December 2013, the magnitude of monsoon events increased and peaked in January to February of 2014. This coincided with already decreasing monthly-mean wave height but, surprisingly, the monthly-mean shoreline still eroded.

To investigate this two-month lag between monthly-mean waves and shoreline, the empirical shoreline equilibrium model ShoreFor (Equation (1)) was applied on daily wave and shoreline data. In Figure 2b the model shows good skills (R^2 = 0.8, RMS = 1.2 m) at intra-seasonal (larger than three days) and seasonal scales but miss short-lived storm impacts. The best correlation appears for a lag ϕ of 50 days (Figure 2c), which is much larger than the actual morphological response time of a few days observed at this beach. To investigate this point further, the model was forced with monthly-averaged waves and with the monthly envelop of intra-seasonal events (Figure 2b). The latter is done by means of the Hilbert transform, already applied successfully to study wave groupiness [33,34], $\left| Hs^{hf}(t) + \mathrm{H}\left\{ Hs^{hf}(t) \right\} \right|^{lf}$ where H denotes the Hilbert transform operator and $|\,|^{\mathrm{lf}}$ a low-pass filter operator, taking 30 days as the cutoff period separating short term (*hf*) and monthly (*lf*) timescales. Both monthly estimates well predict the seasonal shoreline behavior (Figure 2b), although that using the envelope gives more accuracy (R^2 = 0.8 and R^2 = 0.9, RMS = 0.5 and RMS = 0.3 m for monthly-averaged and envelope cases, respectively). Interestingly, the main difference rises from ϕ value in Figure 2c, which is similar (52 days) for monthly-averaged and daily data, but 0 for the envelope, indicating that the shoreline is in phase with the monthly envelope of energetic intra-seasonal events. Therefore, the shoreline is in better equilibrium with wave intra-seasonal events than monthly mean wave energy.

5. Discussion

One of the most striking points of this study is the wave energy provided by monsoon events and their dominant role on shoreline evolution. In contrast, while typhoons have large ephemeral impacts, our results show that the shoreline recovers rapidly. There is no evidence for a persistent influence, as suggested for short-lived storms by [35] and [36]. This is confirmed here using the ShoreFor model that presents good skills at predicting intra-seasonal and seasonal scales but poorly describes short-term typhoon-induced dynamics (see Figure 2b, October to November). Recurrence of typhoons is more than 10 days so that they can be considered isolated and without cumulative effect [5]. Winter monsoon events have impacts of similar magnitude to typhoons but with longer recovery, which is close to their observed recurrence period. Therefore, they can be considered as a sequence, as the beach cannot fully recover between events and is constantly moving towards a high energetic equilibrium. Note that the ratio of erosion and accretion rates for typhoons is nearly constant over time, but not so for winter monsoons: while the erosion rate is constant, the accretion rate decreases after each new event. This result highlights the importance of the wave event duration, to the extent that the erosive potential will be satisfied only if the event lasts the necessary time for the beach to establish a new equilibrium [6]. Thus for short-lived typhoons, the full erosion potential is not achieved. Despite the significant shoreline retreat, the beach profile is likely to be far from a new equilibrium. As a consequence, the shoreline recovery to its previous state (and shoreline position) occurs within a few days and does not affect longer term evolution [37]. On the other hand, winter monsoon events have enough duration to achieve their full erosion potential, thus modifying the beach to a fully new equilibrium. The return of the shoreline to its previous position takes longer, leaving the beach more vulnerable and for longer.

It was previously observed that Nha Trang's embayed beach has a seasonal rotation with modulation of waves incidence [27], from northward summer to winter southward transport: the north end of the beach enlarges in summer and erodes in winter, the center of rotation being localized in the central part of the beach [38]. It is noteworthy that, even if summer monsoon has only a weak influence compared to the energetic winter monsoon, locally generated wind-waves induce this northward transport [26]. The shoreline at the central part of the beach close to the video system mainly experiences translation due to cross-shore dynamics and is rather dominated by event scale. This is similar to what has been observed elsewhere [39] where rotation and translation of the shoreline were quantified separately.

A main outcome of this study is the long lag (50–60 days) observed between monthly waves and shoreline location, while the envelope (Hilbert transform) of intra-seasonal monsoon events is in closer phase with the shoreline. This suggests that, contrarily to shoreline equilibrium model paradigms [2,13], the Nha Trang shoreline is actually in equilibrium with energetic wave conditions. This is in line with observations by [15] at low-energy environments where the beach is assumed to be in equilibrium with previous energetic wave events rather than with current conditions. The beach is considered inactive the rest of the time. Here, it is the particularly long duration of winter monsoon events that presumably drives most of the shoreline changes, with very gentle wave conditions in between which limit the recovery potential, as observed elsewhere by [10]. In this sense, the phase-lag observed here between seasonal means and the intra-seasonal envelope is crucial for shoreline equilibrium.

6. Conclusions

In this paper, we addressed the shoreline evolution of the tropical Nha Trang beach, Vietnam, over the particularly active 2013–2014 season. Our results show for the first time that long-lasting (3–10 days) monsoon events have more persistent impact than typhoons (less than 3 days), of similar amplitude but rather transient with fast recovery. The ShoreFor shoreline equilibrium model shows good skills in predicting seasonal shoreline behavior. The seasonal shoreline appears driven by the intra-seasonal event envelope (from Hilbert transform) rather than monthly-averaged waves. Finally, this paper suggests that the interplay between intra-seasonal event intensity and duration, on the one hand, and recovery conditions, on the other, might be of key significance. Therefore, their evolution in a variable or changing climate should be considered.

Acknowledgments: This work was supported by Vietnamese grant (MOST2/216/QD/BKHCN-No2994) and French ANR project COASTVAR (ANR-14-ASTR-0019). We acknowledge use of the ECMWF ERAInterim dataset (www.ECMWF.Int/research/Era). DHT PhD supported by ARTS-IRD program.

Author Contributions: Rafael Almar, Patrick Marchesiello, Nguyen Trung Viet and Luis Pedro Almeida designed the project and conducted analyses. Duong Hai Thuan analyzed the video images and Hitoshi Tanaka provided expertise on shoreline dynamics. All authors wrote the paper.

Conflicts of Interest: The authors declare no conflict of interest.

References

1. Ashton, A.D.; Evans, R.L.; Donnelly, J.P. Discussion of the Potential Impacts of Climate Change on the Shorelines of the Northeastern USA. *Mitig. Adapt. Strateg. Glob. Chang.* **2008**, *13*, 719–743. [CrossRef]
2. Davidson, M.A.; Splinter, K.D.; Turner, I.L. A simple equilibrium model for predicting shoreline change. *Coast. Eng.* **2013**, *73*, 191–202. [CrossRef]
3. Cooper, J.A.G.; Pilkey, O.H. Sea-level rise and shoreline retreat: Time to abandon the Bruun Rule. *Glob. Planet. Chang.* **2004**, *43*, 157–171. [CrossRef]
4. Anderson, T.R.; Frazer, L.N.; Fletcher, C.H. Transient and persistent shoreline change from a storm. *Geophys. Res. Lett.* **2010**, *37*. [CrossRef]
5. Ranasinghe, R.; Holman, R.; de Schipper, M.A.; Lippmann, T.; Wehof, J.; Minh Duong, T.; Roelvink, D.; Stive, M.J.F. Quantification of nearshore morphological recovery time scales using Argus video imaging: Palm Beach, Sydney and Duck, NC. *Coast. Eng. Proc.* **2012**, *1*, 24.

6. Kriebel, D.L.; Dean, R.G. Convolution method for time dependent beach profile response. *J. Waterw. Port. Coast. Ocean Eng.* **1993**, *119*, 204–226. [CrossRef]
7. Frazer, L.N.; Anderson, T.R.; Fletcher, C.H. Modeling storms improves estimates of long-term shoreline change. *Geophys. Res. Lett.* **2009**, *36*. [CrossRef]
8. Ferreira, Ó. Storm groups versus extreme single storms: Predicted erosion and management consequences. *J. Coast. Res.* **2005**, *21*, 221–227.
9. Coco, G.; Senechal, N.; Rejas, A.; Bryan, K.R.; Capo, S.; Parisot, J.P.; Brown, J.A.; MacMahan, J.H.M. Beach response to a sequence of extreme storms. *Geomorphology* **2014**, *204*, 493–501. [CrossRef]
10. Karunarathna, H.; Pender, D.; Ranasinghe, R.; Short, A.D.; Reeve, D.E. The effects of storm clustering on beach profile variability. *Mar. Geo.* **2014**, *348*, 103–112. [CrossRef]
11. Splinter, K.D.; Carley, J.T.; Golshani, A.; Tomlinson, R. A relationship to describe the cumulative impact of storm clusters on beach erosion. *Coast. Eng.* **2014**, *83*, 49–55. [CrossRef]
12. Masselink, G.; Scott, T.; Poate, T.; Russell, P.; Davidson, M.; Conley, D. The extreme 2013/14 winter storms: Hydrodynamic forcing and coastal response along the southwest coast of England. *Earth Surf. Proc. Landf.* **2016**, *41*, 378–391. [CrossRef]
13. Yates, M.L.; Guza, R.T.; O'Reilly, W.C. Equilibrium shoreline response: Observations and modeling. *Geophys. Res.* **2009**, *114*. [CrossRef]
14. Splinter, K.D.; Turner, I.L.; Davidson, M.A.; Barnard, P.; Castelle, B.; Oltman-Shay, J. A generalized equilibrium model for predicting daily to interannual shoreline response. *J. Geophys. Res. Earth Surf.* **2014**, *119*, 1936–1958. [CrossRef]
15. Jackson, N.L.; Nordstrom, K.F.; Eliot, I.; Masselink, G. "Low energy" sandy beaches in marine and estuarine environments: A review. *Geomorphology* **2002**, *48*, 147–162. [CrossRef]
16. Chen, S.S.; Curcic, M. Ocean surface waves in Hurricane Ike (2008) and Superstorm Sandy (2012): Coupled modeling and observations. *Ocean Mod.* **2016**, *103*, 161–176. [CrossRef]
17. Chang, C.-P.; Wang, Z.; Hendon, H. *The Asian Monsoon*; Springer: Heidelberg, Germany, 2006; pp. 89–128.
18. Wu, M.C.; Chan, J.C.L. Surface features of winter monsoon surges over South China. *Mon. Wea. Rev.* **1995**, *123*, 662–680. [CrossRef]
19. Camargo, S.J.; Robertson, A.W.; Gaffney, S.J.; Smyth, P.; Ghil, M. Cluster analysis of typhoon tracks, Part I: General properties. *J. Clim.* **2007**, *20*, 3635–3653. [CrossRef]
20. Nicholls, R.J.; Hoozemans, F.M.; Marchand, M. Increasing flood risk and wetland losses due to global sea-level rise: Regional and global analyses. In *Global Environmental Change*; Elsevier: Amsterdam, The Netherlands, 1999; Volume 9, pp. 69–87.
21. Chan, J.C.L. Tropical cyclone activity in the northwest Pacific in relation to El Niño/Southern Oscillation phenomenon. *Mon. Weather Rev.* **1985**, *113*, 599–606. [CrossRef]
22. Nakamura, T.; Yamazaki, K.; Iwamoto, K.; Honda, M.; Miyoshi, Y.; Ogawa, Y.; Tomikawa, Y.; Ukita, J. The stratospheric pathway for Arctic impacts on midlatitude climate. *Geophys. Res. Lett.* **2016**, *43*, 3494–3501. [CrossRef]
23. Nakamura, R.; Shibayama, T.; Esteban, M.; Iwamoto, T. Future typhoon and storm surges under different global warming scenarios: Case study of typhoon Haiyan (2013). *Nat. Hazards* **2016**, *82*, 1645–1681. [CrossRef]
24. Chu, P.C.; Qi, Y.; Chen, Y.; Shi, P.; Mao, Q. South China Sea wind- wave characteristics. Part I: validation of Wavewatch-III using TOPEX/Poseidon data. *J. Atmos. Ocean Technol.* **2004**, *21*, 1718–1733. [CrossRef]
25. Mirzaei, A.; Tangang, F.; Juneng, L.; Mustapha, M. A.; Husain, M. L.; Akhir, M. F. Wave climate simulation for southern region of the South China Sea. *Ocean Dyn.* **2013**, *63*, 961–977. [CrossRef]
26. Lefebvre, J.-P.; Almar, R.; Viet, N.T.; Uu, D.V.; Thuan, D.H.; Binh, L.T.; Ibaceta, R.; Duc, N.V. Contribution of swash processes generated by low energy wind waves in the recovery of a beach impacted by extreme events: Nha Trang, Vietnam. *J. Coast. Res.* **2014**, *70*, 663–668. [CrossRef]
27. Duong, H.T.; Binh, L.T.; Viet, N.T.; Hanh, K.D.; Almar, R.; Marchesiello, P. Typhoon impact and shoreline recovery from continuous video monitoring: a case study from Nha Trang beach, Vietnam. Proceedings of the 14th International Coastal Symposium (Sydney, Australia). *J. Coast. Res.* **2016**, *75*, 263–267.
28. Almeida, L.P.; Almar, R.; Marchesiello, P.; Blenkinsopp, C.; Martins, K.; Sénéchal, N.; Floc'H, F.; Bergsma, E.; Benshila, R.; Caulet, C.; et al. Swash zone dynamics of a reflective beach with a low tide terrace. *Mar. Geol.* **2017**, submitted for publication.

29. Abessolo, O.G.; Almar, R.; Kestenare, E.; Bahini, A.; Houngue, G.H.; Jouanno, J.; Du, P.Y.; Castelle, B.; Melet, A.; Messignac, B.; et al. Potential of video cameras in assessing event and seasonal coastline behaviour: Grand Popo, Benin (Gulf of Guinea). *J. Coast. Res.* **2016**, *75*, 442–446. [CrossRef]
30. Dee, D.P.; Uppala, S.M.; Simmons, A.J.; Berrisford, P.; Poli, P.; Kobayashi, S.; Andrae, U.; Balsamo, G.; Bauer, P.; Bechtold, P. The ERA-Interim reanalysis: Configuration and performance of the data assimilation system. *Q. J. R. Meteorol. Soc.* **2011**, *137*, 553–597. [CrossRef]
31. Davidson, M.A.; Turner, I.L. A behavioral template beach profile model for predicting seasonal to interannual shoreline. *J. Geophys. Res.* **2009**, *114*, F01020. [CrossRef]
32. Ruggiero, P.; Buijsman, M.; Kaminsky, G.M.; Gelfenbaum, G. Modeling the effects of wave climate and sediment supply variability on large-scale shoreline change. *Mar. Geol.* **2010**, *273*, 127–140.
33. Veltcheva, A.D. Wave and group transformation by a Hilbert spectrum. *Coast. Eng. J.* **2002**, *44*, 283–300. [CrossRef]
34. Ortega, J.; Smith, G.H. Hilbert-Huang transform analysis of storm waves. *Appl. Ocean Res.* **2009**, *31*, 212–219. [CrossRef]
35. Douglas, B.C.; Crowell, M. Long-Term Shoreline Position Pre diction and Error Propagation. *J. Coast. Res.* **2000**, *16*, 145–152.
36. Zhang, K.; Douglas, B.C.; Leatherman, S.P. Do Storms Cause Long-Term Beach Erosion along the U.S. East Barrier Coast? *J. Geol.* **2002**, *110*, 493–502. [CrossRef]
37. Hansen, J.E.; Barnard, P.L. Sub-weekly to interannual variability of a high-energy shoreline. *Coast. Eng.* **2010**, *57*, 959–972. [CrossRef]
38. Thanh, T.M.; Tanaka, H.; Viet, N.T.; Mitobe, Y.; Hoang, V.C. Evaluation of longshore sendiment transport on Nha Trang coast considering influence of Northeast monsoon waves. *J. Jpn. Soc. Civ. Eng.* **2015**, *71*, 1681–1686.
39. Turki, I.; Medina, R.; Gonzalez, M.; Coco, G. Natural variability of shoreline position: Observations at three pocket beaches. *Mar. Geol.* **2013**, *338*, 76–89. [CrossRef]

water

MDPI

Article

Shoreline Changes on the Wave-Influenced Senegal River Delta, West Africa: The Roles of Natural Processes and Human Interventions

Mamadou Sadio [1,2], Edward J. Anthony [1,*], Amadou Tahirou Diaw [2], Philippe Dussouillez [1], Jules T. Fleury [1], Alioune Kane [3], Rafael Almar [4] and Elodie Kestenare [4]

1 Aix-Marseille University, CEREGE UM 34, Europôle de l'Arbois, 13545 Aix en Provence Cedex 04, France; sadio@cerege.fr (M.S.); dussou@cerege.fr (P.D.); fleury@cerege.fr (J.T.F.)
2 Laboratoire d'Enseignement et de Recherche en Géomatique, Ecole Supérieure Polytechnique, Université Cheikh Anta Diop, Dakar, Sénégal; guede1914@gmail.com
3 Laboratoire de Morphologie et d'Hydrologie, Université Cheikh Anta Diop, Dakar, Sénégal; akane@ucad.sn
4 LEGOS (CNRS-IRD-CNES-University of Toulouse), 31400 Toulouse, France; rafael.almar@ird.fr (R.A.); Elodie.Kestenare@legos.obs-mip.fr (E.K.)
* Correspondence: anthony@cerege.fr

Academic Editors: Sylvain Ouillon and John W. Day
Received: 24 December 2016; Accepted: 12 May 2017; Published: 19 May 2017

Abstract: The Senegal River delta in West Africa, one of the finest examples of "wave-influenced" deltas, is bounded by a spit periodically breached by waves, each breach then acting as a shifting mouth of the Senegal River. Using European Re-Analysis (ERA) hindcast wave data from 1984 to 2015 generated by the Wave Atmospheric Model (WAM) of the European Centre for Medium-Range Weather Forecasts (ECMWF), we calculated longshore sediment transport rates along the spit. We also analysed spit width, spit migration rates, and changes in the position and width of the river mouth from aerial photographs and satellite images between 1954 and 2015. In 2003, an artificial breach was cut through the spit to prevent river flooding of the historic city of St. Louis. Analysis of past spit growth rates and of the breaching length scale associated with maximum spit elongation, and a reported increase in the frequency of high flood water levels between 1994 and 2003, suggest, together, that an impending natural breach was likely to have occurred close to the time frame of the artificial 2003 breach. Following this breach, the new river mouth was widened rapidly by flood discharge evacuation, but stabilised to its usual hydraulic width of <2 km. In 2012, severe erosion of the residual spit downdrift of the mouth may have been due to a significant drop (~15%) in the longshore sand transport volume and to a lower sediment bypassing fraction across the river mouth. This wave erosion of the residual spit led to rapid exceptional widening of the mouth to ~5 km that has not been compensated by updrift spit elongation. This wider mouth may now be acting as a large depocentre for sand transported alongshore from updrift, and has contributed to an increase in the tidal influence affecting the lower delta. Wave erosion of the residual spit has led to the destruction of villages, tourist facilities and infrastructure. This erosion of the spit has also exposed part of the delta plain directly to waves, and reinforced the saline intrusion within the Senegal delta. Understanding the mechanisms and processes behind these changes is important in planning of future shoreline management and decision-making regarding the articulations between coastal protection offered by the wave-built spit and flooding of the lower delta plain of the Senegal River.

Keywords: Senegal River delta; Langue de Barbarie spit; delta vulnerability; river-mouth migration; spit breaching; ERA hindcast waves; longshore sediment transport

1. Introduction

The impacts of human activities on coasts are often accompanied by a lack of understanding of the consequences of these activities on the hydrodynamic and sediment redistribution processes that shape coasts [1,2]. Alongshore sediment transport, gradients in transport, and interception of drifting sediment by natural or artificial (man-made) boundaries, including river mouths and inlets, are, from a coastal management point of view, very important, as these processes are significant drivers of short-term to medium-term (days to years) shoreline change. Much of the West African coast (Figure 1) is wave-dominated, and is classified as a cyclone- and storm-free "West Coast Swell Environment" in the global wave classification scheme of Davies [3], with a subsidiary contribution from shorter-period trade-wind waves from the Atlantic. In Figure 1, continental shelf width (clearer hue along the coast) is a fine indicator of the distribution of long stretches of wave-dominated coast (narrow shelf) and the much more limited, predominantly tidal, estuarine sector between Sierra Leone and Guinea-Bissau (broad, low-gradient shelf), subject to significant wave energy dissipation [4,5]. The West African coast is also characterised by a plethora of river deltas, the largest of which are those of the Niger, Senegal and Volta (Figure 1). Abundant sand supplies and strong wave-induced longshore drift have favoured the construction of numerous sand barriers, including at the mouths of these three deltas. These barriers are major settlement sites on the coast as they provide higher-lying areas above lagoons and wetlands, while acting as valuable aquifers. On the coast of Senegal, the barriers are generally elongate to curvilinear spits formed at the mouths of tidal or fluvial ria-like embayments. These spits are commonly capped by dunes, but individual beach ridges are visible in some of the more southern ones. These spits have a protective role on the back-barrier wetlands and lagoons by buffering wave energy. By forming alongshore barriers, they are also important in the regulation of the freshwater-saltwater balance and ecology of these lagoons and back-barrier wetlands, both of which can be considerably altered by breaches in the spits or by spit erosion [6,7]. This is particularly the case of the largest of the Senegal wetland systems, that of the lower Senegal River and delta plain (Figure 2).

The Senegal River delta is an iconic example of a delta subject to strong wave action [8–12]. This delta is often represented in the ternary (river-wave-tide) classification of Galloway [13] at the wave apex. Using a fluvial dominance ratio—defined as river sediment input versus the potential maximum alongshore sediment transport away from the delta mouth—to quantify the balance between river inputs and the ability of waves to spread sediments along the coast, Nienhuis et al. [12] computed a value of 0.04 for the Senegal, which highlights the strong role of wave-induced longshore transport along this delta's shoreline. A manifestation of this strong longshore transport potential is a long narrow sand spit presently fronting the delta plain, the Langue de Barbarie [10]. This spit has historically played an important role not only in the protection of the lower Senegal delta plain but also in regulating saltwater intrusion by diverting the mouth of the river several kilometres southwards. Of particular significance, in terms of long-term flood-risk and coastal management, is the historic and picturesque city of St. Louis (population in 2013: 300,000), a UNESCO world heritage site located in the proximal part of the delta (Figure 2). The cultural attractiveness of St. Louis, a French colonial city, and the biodiversity of the deltaic wetlands and lagoon bound by the Langue de Barbarie spit have also generated a substantial rise in tourism. Much of St. Louis, which has undergone a rapid growth in population over the last 50 years, lies at an elevation of less than 2.5 m above sea level [14], and the city has, therefore, been prone to the flooding that affects the lower Senegal valley in the rainy season (May to October).

In October 2003, to avoid flooding of St. Louis in the wake of a massive rise in the water discharge of the Senegal River, an artificial breach was hastily cut through the Langue de Barbarie, generating rapid reworking of the spit. In the present paper, we describe the recent dynamics of the spit within the framework of development of the Senegal delta and specifically aim at disentangling processes of natural forcing from those of the impact of this breach. Two approaches are used in the study: (1) clearly define the wave climate and longshore sediment transport potential along the Langue de Barbarie; and (2) compare spit behaviour patterns prior to, and following the October 2003 artificial

breach. Both of these approaches are important in understanding the current dynamics prevailing along this deltaic coast. They should also be of use in planning of future shoreline management and decision-making regarding the articulations between coastal protection offered by the wave-built spit and flooding of the lower delta plain of the Senegal River.

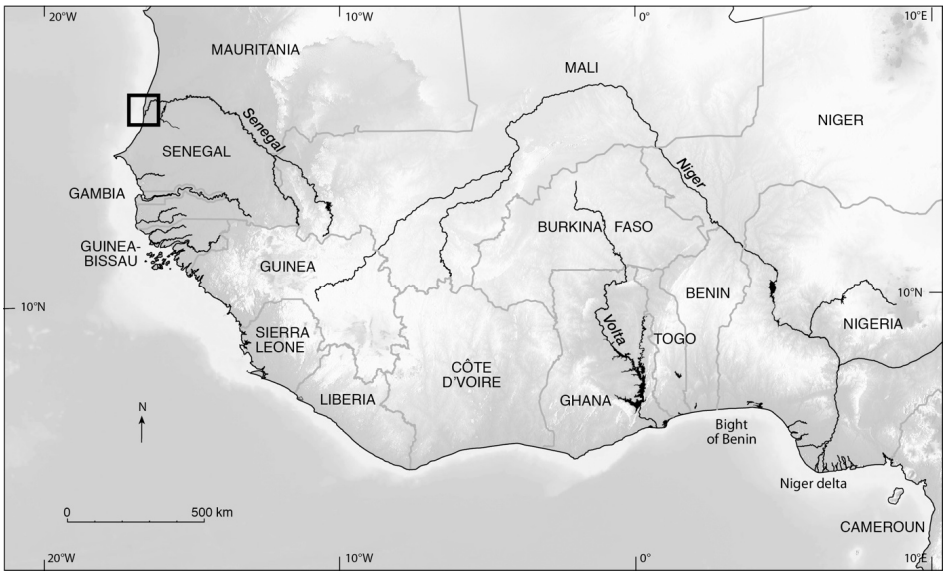

Figure 1. The coast of West Africa, showing the Senegal (box) and other major river deltas. Much of this coast is wave-dominated, and is characterised by beach-ridge sand barriers and spits.

Figure 2. The Senegal River delta, a fine example of a wave-dominated delta characterised by the Langue de Barbarie spit and a river-mouth system subject to strong north-south longshore drift.

2. The Senegal River and Delta

The Senegal River is about 1800 km long, and is the second longest river in West Africa after the Niger. The catchment size has been estimated at 345,000 km^2 [15], much of it covering the arid western Sahel. The river's discharge has been particularly affected by Sahelian droughts since the 1970s [16]. The mean annual water discharge at Bakel, the reference station of the Senegal River, situated 557 km upstream of St. Louis, is 676 m^3/s, and varies from a mean low dry season value of 10 m^3/s in May, to a mean maximum flood value of 3320 m^3/s in September at the height of the rainy season [17]. The interannual variability is extremely high, with a mean annual discharge ranging from 250 to

1400 m^3/s. Little is known of the solid discharge of the Senegal. This solid load has been estimated at 0.9 to 1 $\times$ 10^6 tonnes a year [18], a rather low figure when viewed against the size of the river's catchment and when compared to other tropical rivers. The solid discharge is largely dominated by suspended load transport [19]. The lower Senegal delta is characterised by high biological productivity and by rich agricultural and fishing sectors. In November 1985, the Diama dam (Figure 2) was built in the lower river valley 23 km upstream from St. Louis. The dam was commissioned with the twin aims of preventing saltwater intrusion, which, hitherto, penetrated up to 350 km upstream in the lower Senegal valley, and regulating the river's rainy season discharge in order to improve irrigation of agricultural lands [15]. The delta plain provides 8% of the arable land of Senegal [20].

The Senegal delta coast is fronted by a relatively narrow continental shelf only 15–20 km wide. The dominant waves are from the northwest, and this direction is especially prevalent during the dry season from November to June. One of the objectives of this study is to highlight the salient characteristics of this "West Coast" wave setting (see Results). The tidal regime along the Langue de Barbarie is semi-diurnal and the range microtidal, comprised between 0.5 m at neap tides and 1.6 m at spring tides. The relatively moderate river discharge, including during the flood season, the permanence of moderately energetic waves propagating across a relatively narrow shelf, and the microtidal regime, are three conditions that have been forwarded to explain the wave-dominated character of the Senegal River delta [10].

The stratigraphy and patterns of Holocene geomorphic development of the Senegal delta have been highlighted from borehole data, limited radiocarbon dating, and analysis of plan-view sand barrier and longshore drift patterns in relation to the courses of the river [21,22]. The delta plain prograded as a bayhead delta within a confined setting rich in Late Pleistocene aeolian deposits (Ogolian dunes) that extended as subaerial forms over the then exposed shelf during the last lowstand that peaked at 19,000 year B.P. [21,22]. Mud supplied by the river and fine sand derived from reworking of dunes inland by river-channel meandering have generated up to 8.5 km of essentially fine-grained delta-plain progradation within this bayhead setting. Although the delta plain does not protrude significantly into the Atlantic Ocean (Figure 2), probably because of the combination of this embayed setting and the relatively steep narrow shelf, the Senegal has, nevertheless, formed quite a large delta with an area of about 4254 km^2, much of which is subaerial, the ratio of the subaerial to subaqueous delta being 2:1 [9]. This mud-rich delta plain is bound by massive sandy barriers [21] built by waves propagating over loose aeolian deposits on the submerged narrow shelf. These coarse-grained barriers are separated by swales comprising abandoned river courses. Efficient trapping of river-borne sediments by the aggrading delta plain behind these wave-built sand barriers probably explains the high subaerial-subaqueous ratio of this delta, which is also consistent with the limited delta bulge compared to the more cuspate form commonly evinced by wave-dominated deltas. Remnants of these degraded barriers with beach ridges are discernible within the outer margins of the delta plain south of St. Louis. These spits are ancestral to the present Langue de Barbarie spit. Michel [21] dated the formation of these barriers at between 4000 and 1900 B.P. In essence, therefore, much of the Holocene development of the Senegal delta has consisted in embayment infilling behind the protection of these sand barriers, thus potentially giving rise to two distinct facies arrangements: wave-built sand bodies and back-barrier embayment facies represented by infilling fluvial deposits, including fine sands reworked from the Ogolian dunes by river meandering.

We used European Re-Analysis (ERA) hindcast wave data from 1984 to 2015 generated by the ECMWF Wave Atmospheric Model to characterise the wave climate affecting the Senegal River delta and to calculate longshore sediment transport rates along the spit. We then analysed changes in the position of the river mouth, rates of spit migration and spit width from aerial photographs and satellite images between 1954 and 2015 in order to characterise the shoreline morphodynamic context of the delta (see Materials and Methods).

3. Results

3.1. Wave Climate and Alongshore Sediment Transport

The wave climate of the Senegal delta shoreline is characterised by two components with strongly contrasting behaviour: wind waves generated locally and a dominant component of long swell waves from mid- to high latitudes (Figure 3). The region is not directly affected by major storms or cyclones but the influence of these distant high-energy events in the North Atlantic is materialised in the wave climate. Averaging over the 1984–2015 period gives annual significant swell and wind wave heights respectively of H_s = 1.52 m and 0.53, and peak swell and wind wave periods of T_p = 9.23 s and 3.06 s. The dominant swell waves originate from WNW to N and have a mean direction of 325°. The direction graph (bottom, Figure 3) shows a brief August swing dominated by swell waves from the south. Wind waves show a much wider directional window and a mean of 295°. There is a clear seasonal modulation, swell activity peaking during the northern hemisphere winter with strong storm activity at mid to high latitudes. Wind waves also show larger day-to-day and monthly variability. Contrary to swell waves, these wind waves are driven by local tropical winds and show peaks in spring and autumn that correspond to the passages of the Intertropical Convergence Zone over Senegal.

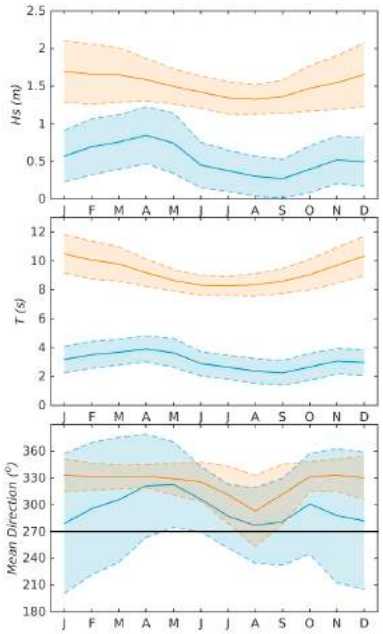

Figure 3. Mean wave characteristics (significant wave height (H_s), peak wave period (T), and incident direction (°)) along the Senegal River delta coast from 1984 to 2015 ERA hindcast data. Orange: swell waves, blue: wind waves.

As both swell and wind waves originate dominantly from W to N, this results in an oblique approach to the coastline that generates a large longshore sediment transport (LST) towards the south. Figure 4 depicts the annual LST along the Senegal delta coast for swell waves and wind waves computed using the formula of Kaczmarek et al. [23] as described in the Methods Section. The mean annual net transport induced by swell waves over the 32-year period of the ERA dataset is of the order of 669 $\times$ 10^3 m^3/year, i.e., ~89% of the total transport, the total wind-wave-induced LST amounting to only 80 $\times$ 10^3 m^3/year. LST is very largely dominated by southwards swell-induced drift which amounts to an annual mean of 611 $\times$ 10^3 m^3/year, while net wind-wave-induced transport in the same direction is only 59 $\times$ 10^3 m^3/year. Counter LST towards the north is nearly an order of magnitude less: 58 $\times$ 10^3 m^3/year for swell waves and 21 $\times$ 10^3 m^3/year for wind waves, i.e., only ~14% of the total LST. These computed sediment transport volumes are remarkably similar to those provided by

the French engineering firm [24] SOGREAH (1994) who calculated a drift volume that decreases from north to south along the spit from 700 to 600 $\times$ 10^3 m^3/year.

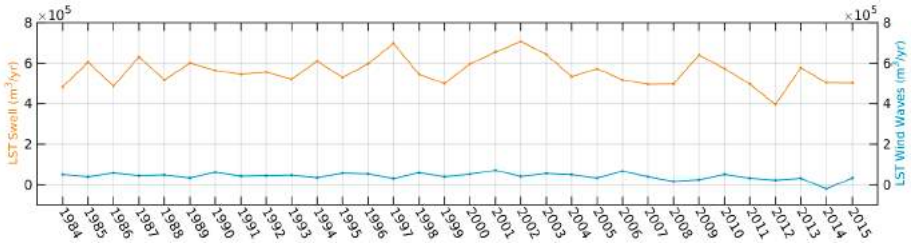

Figure 4. Gross annual longshore sediment transport (LST) along the Senegal River delta coast from 1984 to 2015. Orange: swell waves, blue: wind waves. Note the significant drop in swell-induced LST between 2009 and 2012, corresponding to a decrease of >35%, and the sharp rise the following year.

3.2. LST and Growth Dynamics of the Langue de Barbarie Spit

The Langue de Barbarie spit is a product of the strong wave action and high LST that have controlled the morphosedimentary development of the seaward fringe of the Senegal River delta (Figure 2). These observations and the satellite data also provide insight on the sand sourcing the seaward face of the Langue de Barbarie, which is derived from the coast and shoreface of Mauritania updrift of the historic mouth of the Senegal (Figure 1), in agreement with a conclusion also reached by Barusseau et al. [25]. The satellite data show that the Langue de Barbarie spit is a 100–400 m-wide feature. The spit is capped by aeolian dunes 5–10 m high. Widening of the spit and dune accretion occur through abstraction of the large alongshore sediment supply, especially in the distal section where bare, unvegetated dunes prevail, as well as through distal spit extension [26]. In contrast, the proximal sector, near St. Louis has been characterised by a much more stabilised dune system. Since 1900, a major coastal management preoccupation in the lower Senegal delta has been that of preventing natural breaches in the Langue de Barbarie in the vicinity of St. Louis, as this posed a threat for developing tourist facilities and infrastructure on the spit downdrift of every breach. Spit protection was achieved through the fixing and consolidation of the aeolian dunes via plantations of Filao (*Casuarina equisetifolia*) [27]. The alongshore transport volume would appear to undergo increasingly larger aeolian dune trapping of sand in the relatively poorly vegetated distal zone, compared to the relatively more urbanised and vegetated proximal sector of St. Louis. The former zone also represents one of active remigration following past natural breaches. The longshore gradient in sediment transport highlighted by SOGREAH [24] would appear to correspond to these morphological variations as one goes from the proximal to the distal sector of the spit.

The successive locations of the mouth of the Senegal River have been controlled by spit breaching followed by downdrift spit elongation. Spit breaching has generally been caused by increases in river water level, especially over the narrowest and lowest parts of the spit [26]. Once breaching occurs, the new breach is exploited by river discharge, tidal ingression, and waves, and forms a new river mouth. This leads to the older mouth becoming underfit and sealed by distal spit attachment to the shore. Natural breaching is attended by spit elongation through the classic formation of dune-capped beach ridges at the distal end, and this process has undoubtedly been favoured by the shallow overall depths of the mouth (2.5–3.5 m according to Bâ et al. [28]). The mouth is characterised by bars and spit recurves, remnants of which are identified in updrift locations on the spit. The mouth bars apparently serve as platforms for spit extension and eventual river-mouth diversion southwards.

3.3. Historical and Recent Changes of the Langue de Barbarie Spit Prior to the 2003 Artificial Breach

Joiré [29] and Tricart [30] situated the mouth of the river in the vicinity of St. Louis at about the mid-17th century, while a historical analysis of spit mobility and of the associated locations of

mouth openings documented even earlier mouth scars north of St. Louis [27]. The Langue de Barbarie lengthened by 11 km between 1850 and 1900 (about 220 m a year), with a distal tip located 15 km south of St. Louis at the turn of the 20th century, and the spit was affected over this 50-year period by seven breaches [27]. Between 1900 and 1973, 13 other breaches occurred across the Langue de Barbarie [27], thus suggesting a breaching timescale (see Nienhuis et al. [31]) of ~6 years. There were no breaches between 1973 and 2003.

Following the 1973 breach, the Langue de Barbarie lengthened by 12.5 km (at a mean rate of ~400 m/year) before the spit was artificially breached in 2003. Spit elongation calculated from satellite images, aerial photographs and field measurements has, however, fluctuated widely from low values of nearly nil to <170 m/year (1985–1986, 1990–1991) to >1200 m/year (1987–1989, 2000–2002) (Figure 5). Gac et al. [27] showed that the farthest downdrift position of the mouth of the river, which corresponds to the maximal distal spit extension, did not exceed 30 km over the 80-year period covered by their observations, which is close to a value of 28 km reported in an earlier study [32]. The successive locations of the mouth of the Senegal River since 1973, which also correspond to those of the distal tip of the southward-extending spit, are shown in Figure 5, alongside the migration rates. The migration between 1973 and 2003 brought the distal tip of the spit close to the maximum spit length. The data from satellite images show a relatively narrow mouth (0.25–<1 km-wide) with the exception of the years 1968–1973 and 1988–1989 when the width exceeded 1.5 km (Figure 6).

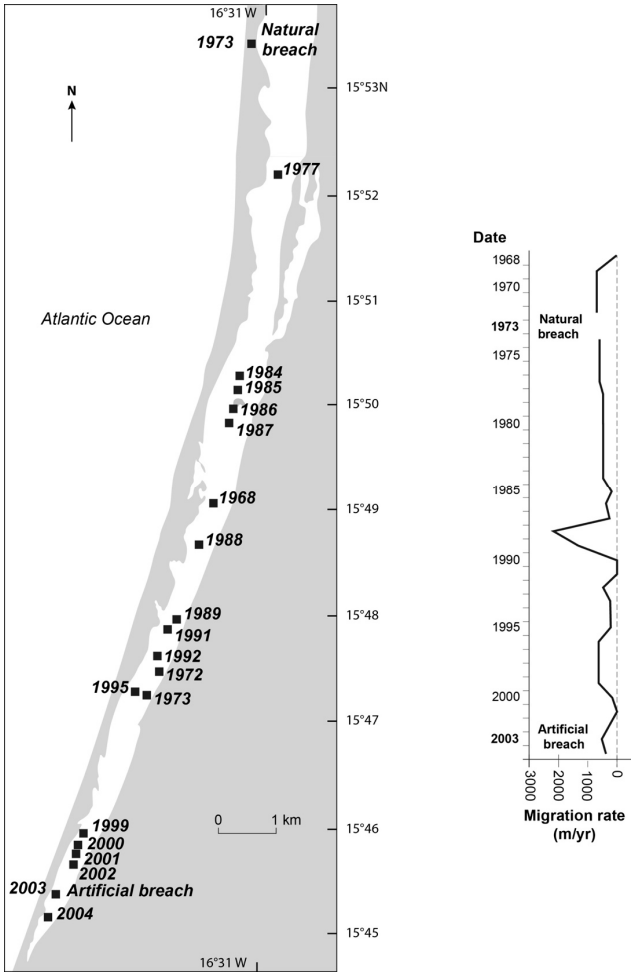

Figure 5. Successive dated locations of the mouth of the Senegal River delta materialised by the distal tip of the Langue de Barbarie spit (**left**); and spit migration rates in m/year from 1968 to 2004 (**right**).

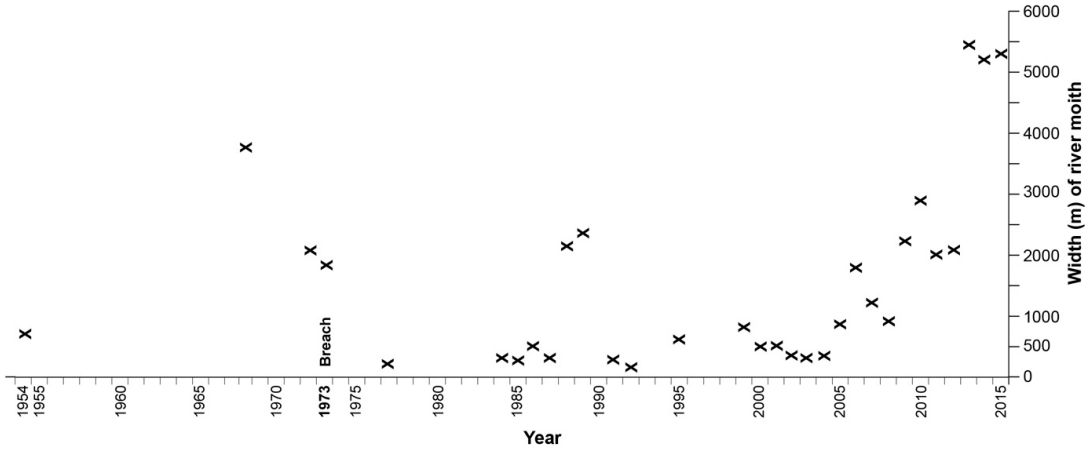

Figure 6. Width of the mouth of the Senegal River delta between 1954 and 2015. Except for the years 1968–1973 and 1987–1988, the width did not exceed 1 km, prior to the 2003 artificial breach. Following this breach, the width of the mouth fluctuated to attain ~1 km in 2008, which corresponds to the average width of the "fluvial" river mouth. A further rapid increase, not related to river-mouth hydraulics (see Discussion), occurred thereafter, peaking in 2013.

3.4. The Artificial Breach in 2003 and Post-Breach Spit and River-Mouth Evolution

An emergency water level in St. Louis prompted artificial breaching, on the night of 3 October 2003, of the Langue de Barbarie in the vicinity of the city to alleviate flooding. This high flood level had been preceded by several other episodes in the 1990s. One function of the Diama dam was to alleviate floods in the lower valley, notably in the deltaic sector. Mietton et al. [33] highlighted the rather mixed results from the flood-control function of the dam since the 1990s, and reported repeated episodes of severe flooding in St. Louis in 1994 (1.26 m above IGN datum), 1995 (1.21 m), 1997 (1.28 m), 1998 (1.43 m), 1999 (1.47 m), 2001 (1.2 m) and 2003 (1.38 m). The latter events preceding the artificial breach are depicted in Figure 7. The water level of 1.47 m above IGN datum attained at the height of the 1999 high-flow season exceeded the 1.2 m flooding threshold for 12 days, and the concern voiced by the population of St. Louis regarding this flooding progressively brought pressure to bear on the administrative authorities in their recourse to artificial breaching [34]. A 4 m-long and 1.5 m-deep trench was cut across a relatively narrow (100 m-wide) portion of the spit about 7 km south of St. Louis by engineers in the night of 3 October 2003. This induced a rapid overnight drop in water level of up to 1 m (Figure 7) that prevented further flooding [34]. Following this opening, the trench widened rapidly (Figure 8) and became the new river mouth, a case of inadvertent delta-mouth diversion generated by humans. The width of this artificial breach grew to 250 m 3–4 days after the opening. The depth of the breach increased to 6 m by 2007 [28], while the width increased to nearly 2 km in October 2006, three years after the breach (Figure 6), before decreasing once more to ~1 km in early 2008. Channelling of the Senegal River flow in the new enlarged mouth led to closure of the former natural mouth located further downdrift. An accelerated phase of widening ensued afterwards, peaking to nearly 5.5 km between October 2012 and June 2013 (Figure 6). Figure 9 summarises the dynamics of the spit and river mouth since the 2003 artificial breach. The rapid widening was related to an additional natural breach created in October 2012 by overwash 500 m south of the new mouth. Much of the remaining spit between this new opening and the mouth was eroded through several other washovers that tended to coalesce, widening the mouth and sea-intrusion pathways, as sand was transported southward by longshore drift.

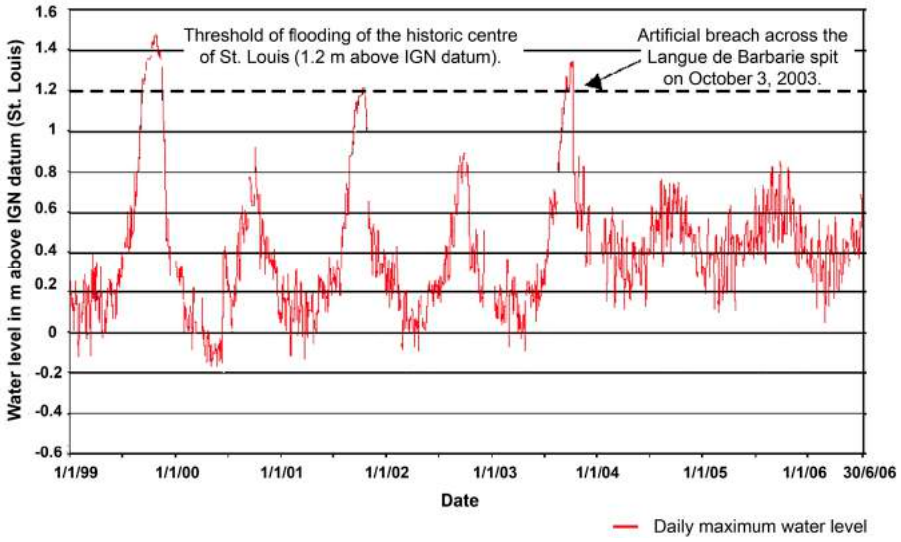

Figure 7. Maximum water levels in the Senegal River channel at St. Louis from 1999 to 2006. Adapted from [34].

Figure 8. Ground photographs showing the initial trench (4 October 2003), dug on the night of 3 October 2003, across the Langue de Barbarie to alleviate flooding of parts of St. Louis. The 5 October 2003 photograph shows the trench considerably widened by river and tidal flow (Photo credit: Service régional de l'Hydraulique, St. Louis du Sénégal).

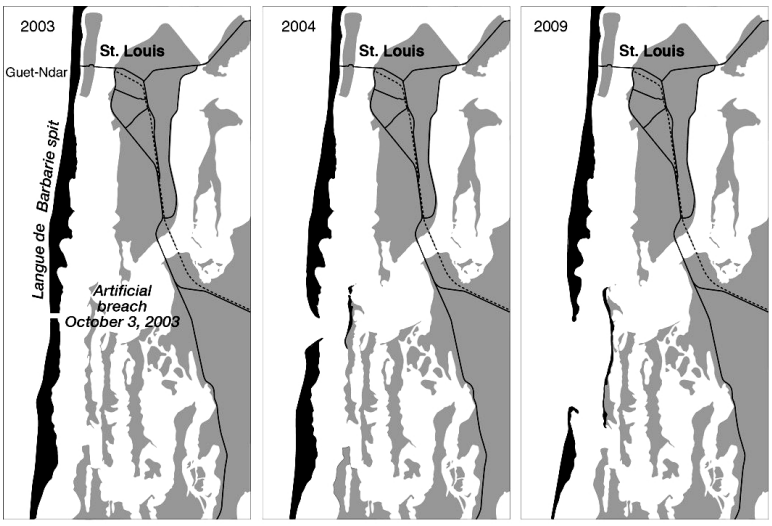

Figure 9. *Cont.*

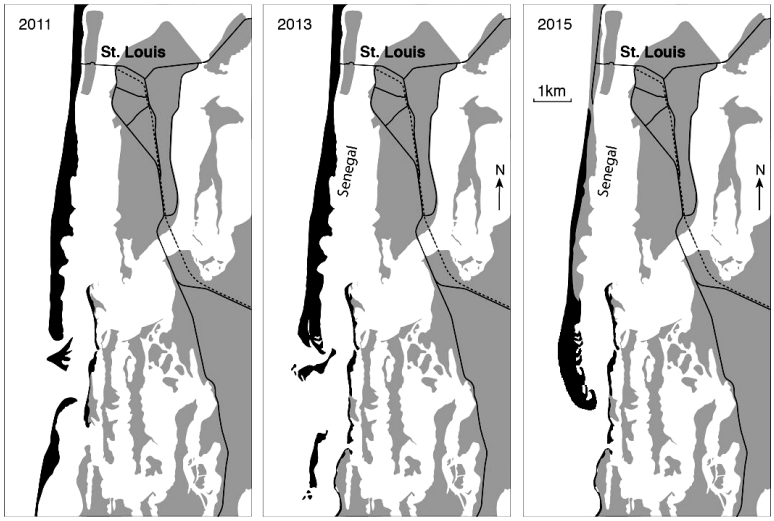

Figure 9. Assemblage from Google Earth images showing changes in the Langue de Barbarie spit and Senegal River mouth between March 2003, prior to the October 2003 artificial breach, and 2015. Black: Langue de Barbarie spit and beach sand; dark grey: subaerial lower delta plain potentially subject to river flooding (including St. Louis); light grey: delta plain seasonally flooded by the Senegal River. From 2012 to 2013, rapid wave-induced erosion of the residual spit downdrift of the mouth led to considerable mouth widening, an increase in tidal influence within the lower Senegal delta, and direct wave attack of parts of the delta plain hitherto protected by the residual spit.

4. Discussion

The shoreline of the Senegal delta offers an interesting example of strong wave influence on delta evolution. Two clear manifestations of this strong influence are the absence of a notable classic deltaic "bulge", and the presence of a persistent sand spit, the Langue de Barbarie, an extremely mobile feature that generates river-mouth diversion. This spit has been subject to repeated past breaches, and delta-mouth migration over a total distance of 28–30 km at least since the mid-17th century. The dominant natural mode of behaviour of the Senegal delta shoreline is thus one imprinted by strong longshore transport of sand generated by Atlantic waves from NW to N. The Senegal River mouth is thus a fine example of a wave-influenced delta illustrating the relationship between river-mouth migration, spit elongation and spit breaching by the river mouth [31], although a simple relationship between these processes cannot be expected because of the influence of fluctuations in river discharge and river-mouth bar dynamics [11]. Whereas high river discharge and the formation of river-mouth bars can lead to reduced sediment bypassing, which affects in turn the river-mouth migration rate and the size of the river-mouth spit [31], reduced discharge at the river mouth, tantamount to a decrease in hydraulic efficiency, can lead to bypassing of sediment around the mouth, thus reducing migration [31,35]. Natural breaches of spits barring river mouths and tidal inlets are a commonly cyclic process determined by a combination of spit lengthening, river discharge and river hydraulic efficiency, and also in many cases, storm wave action [31,36].

The absence of breaching between 1973 and 2003 associated with the lengthening of the Langue de Barbarie spit over this period constitutes a much longer timescale than past breaching timescales [27]. The reasons for this are not clear. They are unlikely to be related to the wave climate, which is devoid of storms, whereas breaching tends to be initiated by high river discharge during the flood season. The longshore transport volumes, of which the period 1984–2003 may be considered as representative, fluctuated but presumably were high enough to ensure spit elongation, without natural breaching updrift that could have been caused by a decrease in the alongshore budget. Spit morphometry (width, depth and migration range) as a criterion for determining the fraction of the LST sequestered in the spit, yields a value of 54%. This value is moderate relative to the relatively high hindcast and predicted

values of the sediment bypassing fraction, β [31] (respectively, 0.83 and 0.74, 1 representing 100% bypassing) for the Senegal River mouth. These rates are, however, quite similar to those (0.8–0.9) calculated from our data on spit morphometry and LST using the sediment bypassing fraction equation and 50% of the river mouth depth as an estimate of the "updrift sediment spit depth" (see Materials and Methods). The mouth of the Senegal has thus been characterised by moderate to high bypassing that assured a degree of growth of the Langue de Barbarie but also the stability of the barrier and coast downdrift of the 2003 artificial breach. The absence of breaching over this long phase has been attributed to a decrease in river discharge [37]. Unfortunately, there are no available data on river water discharge to enable us to tie up natural breaches with the hydraulic efficiency of the river mouth. Mietton et al. [33] noted a total absence of critical floods between 1974 and 1993 associated with the Sahelian drought. This period also incorporates the construction of the Diama dam in 1986.

While the breaching timescale since 1973 appears exceptional compared to the pre-1973 conditions, the breaching length is also an important parameter in the onset of breaching [31]. The elevation of the water surface at the upstream boundary of a river channel is directly related to the channel length, such that an increase in the latter, as the river mouth migrates, results in a constant water surface slope, with the eventuality of breaching when a critical channel length is attained [31]. Guilcher [32] and Gac et al. [27] reported that the Langue de Barbarie spit generally did not exceed a maximum length of 28–30 km, beyond which breaching tended to occur. This length probably corresponds to the breaching length defined by Nienhuis et al. [31]. There is a probability, therefore, that a natural breach could have been imminent close to the time frame of the 2003 artificial breach. A reason for advancing this hypothesis is the increase in flooding (Figure 7), which suggests increasing impoundment of flood waters over the lower delta plain and decreasing hydraulic efficiency of the mouth. Whereas natural breaching has been a characteristic of the spit, spit instability since 2003 reflects, in part, the consequences of hasty artificial breaching to solve an impending flooding problem facing St. Louis. By protecting St. Louis and numerous smaller settlements and agricultural land within the delta plain from waves and marine influence, the spit is a major feature of the dynamics and management of the Senegal delta shoreline. Paradoxically, by impounding flood waters of the Senegal River, the spit also contributes to a flood risk that has grown apace with the urban extension of St. Louis. The long phase of absence of breaching between 1973 and 2003 coincided with a period of rapid tourism development in the Senegal delta associated with the emplacement of tourist infrastructure on the rectilinear spit that provided sandy grounds well above flood level. Although much of the lower delta is characterised by a population density of only about ten inhabitants/km^2, there are zones of very high population concentrations, as in St. Louis and certain areas of the Langue de Barbarie such as Guet-Ndar (Figure 9) where the 2013 census shows densities exceeding 80,000 inhabitants/km^2 [6]. The artificial breach annihilated the risk of flooding of St. Louis in 2003 and in the following years by enabling more rapid seaward drainage of river water during the high-flow season [34].

As in the pre-2003 period, the sediment bypassing fraction, β [31], across the mouth of the Senegal River has been quite high (0.8–0.9), although balancing spit morphometry against LST over the same period suggests up to 40% of sand locked up in spit growth, a value lower, however, than that of the pre-2003 breach. There have been marked fluctuations in spit growth, however, with even spit erosion in 2005–2006, 2008–2010 and 2012–2013. Under conditions of spit growth, sand has been incorporated in new recurves that mark the current form of elongation of the residual updrift spit sector, which is also characterised by an enlarged distal tip (Figure 9). The reasons for alternations between spit growth (including widening) and spit erosion are not clear. They may be related to variations in higher-energy waves, and potentially varying LST, as shown by the drop in the number of days with high-energy waves in 2012 (Figure 10) and the correlative drop in LST (Figure 4), but they could also be an outcome of variability in river discharge and sediment bypassing.

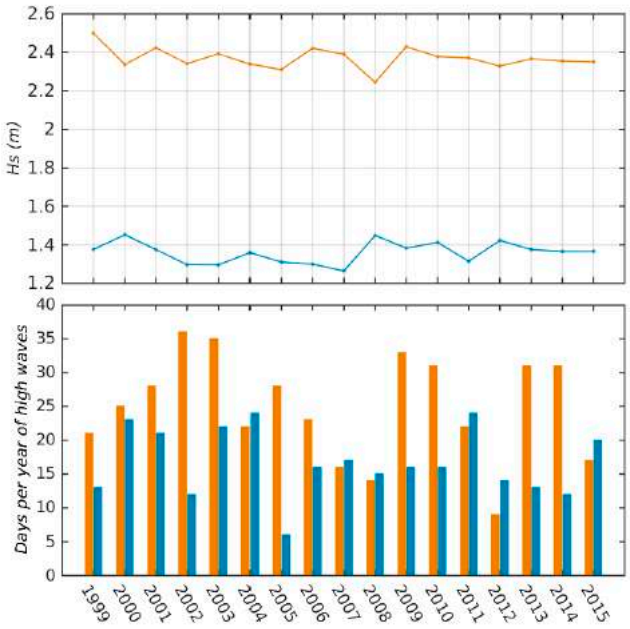

Figure 10. Significant heights (*Hs*) of high-energy waves (±1.6 standard deviations around mean *Hs*) from 1999 to 2015 (**top**); and number of days per year with high-energy waves along the Senegal River delta coast, derived from ERA hindcast data (**bottom**). Orange: swell waves ($Hs \geq 2.37$ m), blue: wind waves ($Hs \geq 1.36$ m). Note the significant drop in high-energy swell waves in 2012 (see also Figure 4).

Over this post-2003 period, fluctuations of the width of the river mouth (Figure 6) are presumably a function of the balance between the river's hydraulic efficiency, including the tidal discharge, and incident wave energy and sediment bypassing [11]. The width of the "fluvial" mouth of the river is very likely in the range of ~0.5–1 km, which is the "usual" mouth width (Figure 6) and the stabilised width attained shortly after the artificial breach. The rapid widening between October 2012 and June 2013 occurred following wave overwash and erosion of the remaining spit downdrift of the mouth. This rapid erosion would appear to result from a combination of the most significant drop in LST recorded (2010–2012) over the period 1984–2015 (Figure 4), with a lag effect in time, and possible sequestering of sand in the river mouth. Lower bypassing (due to higher river discharge?) and a sharp increase in LST from 2012 to 2013 (an increase of about ~45% relative to the 2010–2012 LST (Figure 4)) could explain the ensuing exceptionally rapid elongation of the Langue de Barbarie spit between June 2013 and May 2015 (~2 km) (Figure 9). A review of conceptual advances in wave-river-mouth interactions [11] and modelling of alongshore sediment bypassing at river mouths [31] have shown that waves refracting over the river-mouth bar create a zone of low alongshore sediment transport updrift which reduces sediment bypassing. These observations imply that the LST potential south of the new mouth is being assured by a degree of "cannibalisation" of the rest of the spit, as sand transported from the north has been increasingly trapped updrift of the wider mouth, presumably leading to lower bypassing. Except for 2007–2009, and 2010–2011, this sector has been in erosion. This demise of the spit downdrift of the new mouth has led to the destruction of villages, campsites and other tourist structures. The delta plain in this eroding sector is now directly exposed to ocean waves and erosion that are threatening numerous villages.

Much of the lower delta plain and the main river channel are now situated over 20 km upstream of the former mouth, between the new mouth and the anti-salt intrusion Diama dam that confines the tidal prism to the lower delta plain. In consequence, the much wider mouth appears to have become favourable to a larger tidal prism, manifested by an increase in the tidal range in St. Louis, and confirmed by recent studies [33,34]. Durand et al. [34] showed that the maximum semi-diurnal tidal range downstream of the Diama dam has increased three-fold, from a mean of 0.30 m in 2001–2002 to

0.93 m in 2004–2005, whereas the mean maximum spring tide range attained 1.18 m, for a predicted value of 1.29 m, along the Langue de Barbarie spit. These authors have also noted that the semi-diurnal tidal effects are now more clearly expressed even during the high river flood waters. The impacts of these changes are still to be studied, but it may be expected that they are leading to increasing soil salinization in the lower delta plain, to the extension of bare saline flats, and to modifications in biodiversity.

The extent to which accelerated subsidence, one of the two major causes of delta vulnerability (together with rapid and chronic erosion), affects the delta is not known, although it may be inferred that a decreasing sediment load and damming may be contributing to more exacerbated flooding in the delta plain. However, the problem seems to have more to do with accelerated urbanisation of St. Louis over the last few decades, bringing new populations to encroach on areas of the delta that are susceptible to flooding during exceptionally wet years. Durand et al. [34] have highlighted the potential vulnerability of the city and the surrounding low delta plain to sea-level rise. Their model simulating flood propagation in the city, and based on various sea-level scenarios, shows the susceptibility of St. Louis to flooding during the highest annual water levels in the course of the 21st century.

5. Materials and Methods

5.1. Waves and Wave-Induced Longshore Transport

In order to estimate the wave-induced alongshore transport on the Langue de Barbarie, we extracted bulk wave parameters (significant height H_s, peak period T_p and direction of both swell and wind waves) from hindcast data in the Atlantic Ocean between 1984 and 2015, generated by the ECMWF Wave Atmospheric Model (WAM) model [38]. The wave data are part of the ERA-Interim dataset, which involves a reanalysis of global meteorological variables [39,40]. Wave data were extracted from the ECMWF data server on a $0.5^\circ \times 0.5^\circ$ grid, with a 6-h temporal resolution and covering the sector 16.5° N/17° W. The ERA-40 and the following ERA-Interim reanalysis are the first in which an ocean wind–wave model is coupled to the atmosphere, and the quality of the wave data has been extensively validated against buoy and altimeter data. Sterl and Caires (2005) [40] demonstrated a very good correlation between the ERA-40 data and these sources, except for high waves ($H_s > 5$ m) and low waves ($H_s < 1$ m), which tend, respectively, to be under- and over-estimated [41]. These critical wave conditions are not typical of the relatively constant wave regime affecting the Senegal delta coast, and extreme wave condition issues reported for ERA-40 are partially resolved for higher resolution ERA-Interim. However, the Senegal coast has scarce observations, and this affects the hindcast quality. ERA-40 and -Interim results in this region should be taken with caution.

Several alongshore sediment transport formulae exist and are widely applied by coastal engineers and dynamicists. However, there is still an important research effort on the improvement of alongshore sediment transport parameters and no large consensus on the choice of a formulation, as dispersion between predictors is often substantial [42], and validation dataset at the regional scale scarce. Here, we chose the formula of Kaczmarek et al. [23] because of its straightforward implementation for remote sites such as the Langue de Barbarie where only limited observations exist and because it has been applied to similar environments [43,44]. The amount of sediment drifting alongshore was computed as follows:

$$Q = 0.023\left(H_b^2 V\right) \qquad if\left(d_b^2 V\right) < 0.15 \tag{1}$$

$$Q = 0.00225 + 0.008\left(H_b^2 V\right) \qquad if\left(d_b^2 V\right) > 0.15 \tag{2}$$

where H_b is the breaking wave height and V an estimation of the alongshore current within the surf zone derived from the commonly used formula of Longuet-Higgins [45]:

$$V = 0.25 k_v \sqrt{\gamma g d_b}\, sin2\alpha_b \tag{3}$$

where α_b is the local breaking wave angle, $\gamma = H_b/d_b = 0.78$ is the breaker parameter constant [46], g the gravitational acceleration (m/s^2), H_b the breaking wave height, d_b the local water depth and k_v an empirical constant. Here, we used $k_v = 2.9$ based on the values of Bertin et al. [43] for wave-dominated environments with similar grain-size characteristics. A separate computation for sediment transport induced, respectively, by wind waves and swell waves was conducted.

Alongshore sediment transport formulae necessitate breaking wave parameters as inputs, but global wave hindcast only provide deepwater characteristics. While a nested model (e.g., SWAN or WW3) to propagate waves from deepwater to the breakpoint would be ideal for a short-term study, the present analysis focuses on seasonal to inter-annual wave variations covering a long period of 32 years. We chose therefore to use the direct breaking wave predictor proposed by Larson et al. [47]. This formula provides breaking wave height H_b and angle α_b from deepwater wave height H_o, period T and incidence angle α_0:

$$H_b = \lambda C^2/g \tag{4}$$

$$\alpha_b = \text{asin}\left(\sin(\alpha_0)\sqrt{\lambda}\right) \tag{5}$$

with a correction factor λ computed as:

$$\lambda = \Delta\lambda_a \tag{6}$$

considering

$$\Delta = 1 + 0.1649\,\xi + 0.5948\,\xi^2 - 1.6787\xi^3 + 2.8573\,\xi^4 \tag{7}$$

$$\xi = \lambda_a sin\theta_0{}^2,\ \lambda_a = [\cos(\alpha_0)/\theta]^{2/5}, \theta = \left(\frac{C}{\sqrt{gH}}\right)^4 \left(\frac{C}{C_g}\right)\gamma^2 \tag{8}$$

where deep water phase celerity is given by $C = 1.56T$, wavelength $L = 1.56T^2$, and group celerity $C_g = C/2$.

5.2. Shoreline Change and Spit and River-Mouth Dynamics

In order to highlight recent deltaic shoreline changes, we resorted to available aerial photographs (1954), a CORONA satellite image (1968) and LANDSAT (1984–1988, 1992, 1999–2004, 2006–2011, 2013, 2015–2016) and SPOT satellite images (2005) with moderate pixel size resolution (30 to 60 m) made available by the USGS and the French IGN. The main items analysed were spit length and corresponding migration rates, spit width, and river-mouth width and the underlying dynamics. The spatial data were chosen to cover the entire "delta-influenced" shoreline for each year of analysis and with a cloud cover not exceeding 10%. We limited our choice to images taken at low tide and systematically in January of every year to minimise seasonal and tidal distortions (tides induce very little variability in the microtidal context of the Senegal River delta). The results on shoreline change were completed by a literature review on the past dynamics of the Langue de Barbarie and by field observations of this spit conducted in 2005, 2007 and 2016.

Based on data from the satellite images and aerial photographs on spit and river-mouth characteristics, the fraction of sediment bypassing the mouth, β, assuming conservation of mass, was inferred from the following relationship [31]:

$$\nu = Qs(1 - \beta)/Ab \tag{9}$$

where ν is the migration rate of the mouth (m·s^{-1}), Qs is the volumetric alongshore sediment transport rate (m^3·s^{-1}), and $Ab = Ws{\cdot}Ds$ which is the cross-sectional area of the river mouth spit (m^2) composed of blocked littoral sediment from the updrift coast, Ws the width of the spit, and Ds spit updrift sediment depth.

Acknowledgments: This work benefited from the ECMWF ERA Interim dataset (www.ECMWF.Int/research/Era), and from Landsat satellite images provided by the United States Geological Survey, and Spot satellite images provided by Centre National d'Etudes Spatiales. We acknowledge funding from the Belmont Forum Project: *BF-Deltas: Catalyzing Action Towards Sustainability of Deltaic Systems with an Integrated Modeling Framework for Risk Assessment*. Mamadou Sadio benefited from a partial PhD grant provided by the Embassy of France in Senegal. We thank the anonymous reviewers for their salient suggestions for improvement.

Author Contributions: Mamadou Sadio, Edward J. Anthony, Amadou Tahirou Diaw and Alioune Kane designed the project. Mamadou Sadio, Amadou Tahirou Diaw, Philippe Dussouillez and Jules T. Fleury analysed the satellite images. Mamadou Sadio., Edward J. Anthony, Amadou Tahirou Diaw, and Alioune Kane conducted field reconnaissance. Rafael Almar and Elodie Kestenare analysed the E.R.A. data and longshore transport products. All authors wrote the paper.

Conflicts of Interest: We declare no conflicts of interests.

References

1. Crossland, C.J.; Kremer, H.H.; Lindeboom, H.J.; Marshall Crossland, J.I.; Le Tissier, M.D.A. *Coastal Fluxes in the Anthropocene*; Springer: Berlin, Germany, 2007; p. 231.
2. Van Rijn, L.C. Coastal erosion and control. *Ocean Coast. Manag.* **2011**, *54*, 867–887. [CrossRef]
3. Davies, J.L. *Geographical Variation in Coastal Development*, 2nd ed.; Longman: London, UK, 1980; p. 212.
4. Anthony, E.J. Coastal progradation in response to variations in sediment supply, wave energy and tidal range: Examples from Sierra Leone, West Africa. *Géodynamique* **1991**, *6*, 57–70.
5. Anthony, E.J. The muddy tropical coast of West Africa from Sierra Leone to Guinea-Bissau: Geological heritage, geomorphology and sediment dynamics. *Afr. Geosci. Rev.* **2006**, *13*, 227–237.
6. Diatta, I. L'ouverture d'une Brèche à Travers la Langue de Barbarie (Saint-Louis du Sénégal). Les Autorités Publiques et les Conséquences de la Rupture. Master's Thesis, Université Gaston Berger, St Louis, Senegal, 2004.; p. 116.
7. Sy, B.A. L'ouverture de la brèche sur la Langue de Barbarie et ses conséquences. Approche géomorphologique. *Revue de Géographie de Saint-Louis* **2004**, *4*, 50–60. (In French)
8. Bhattacharya, J.P.; Giosan, L. Wave-influenced deltas: Geomorphological implications for facies reconstruction. *Sedimentology* **2003**, *50*, 187–210. [CrossRef]
9. Coleman, J.M.; Huh, O.K. *Major Deltas of the World: A Perspective from Space*; Coastal Studies Institute, Louisiana State University: Baton Rouge, LA, USA, 2004.
10. Anthony, E.J. Patterns of sand spit development and their management implications on deltaic, drift-aligned coasts: The cases of the Senegal and Volta River delta spits, West Africa. In *Sand and Gravel Spits*; Randazzo, G., Cooper, J.A.G., Eds.; Springer: Berlin, Germany, 2015; Volume 12, pp. 21–36.
11. Anthony, E.J. Wave influence in the construction, shaping and destruction of river deltas: A review. *Mar. Geol.* **2015**, *361*, 53–78. [CrossRef]
12. Nienhuis, J.H.; Ashton, A.D.; Giosan, L. What makes a delta wave-dominated? *Geology* **2015**, *43*, 511–514. [CrossRef]
13. Galloway, W.E. Process framework for describing the morphologic and stratigraphic evolution of delta depositional systems. In *Deltas: Models for Exploration*; Broussard, M.L., Ed.; Texas Geological Society: Houston, TX, USA, 1975; pp. 87–98.
14. Sall, M. Crue et Elévation du Niveau Marin à Saint-Louis du Sénégal: Impacts Potentiels et Mesures D'adaptation. Ph.D. Thesis, Université du Maine, Le Mans, France, 2006.
15. Kamara, S.; Martin, Ph.; Coly, A. Organisation traditionnelle du bas delta du Sénégal et nouvelles régulations hydrauliques. Dimension anthropospatiale d'un développement. *Revue Espaces et Sociétés en Mutation* **2015**, *2015*, 127–144. (In French).
16. Mahé, G.; Olivry, J.C. Variations des précipitations et des écoulements en Afrique de l'Ouest et central de 1951 à 1989. *Sécheresse* **1995**, *6*, 109–117. (In French).
17. Kane, A.; Niang-Fall, A. *Hydrologie du Sénégal*; Atlas Jeune Afrique: Dakar, Sénégal, 2007; p. 14. (In French)
18. Ostenfeld, C.; Jonson, N. *Etude de la Navigabilité et des Ports du Fleuve Sénégal; Études Portuaires à Saint-Louis, Kayes et Ambidebi. Vol. 1: Travaux Préliminaires; Vol. 2, Annexe 2: Rapport Sur les Enquêtes Hydrauliques*; Surveyer-Nenninger et Chevenert Inc.: Montréal, QC, Canada, 1972. (In French)

19. Gac, J.Y.; Kane, A. Le fleuve Sénégal. Bilan hydrique et flux continentaux de matières particulaires à l'embouchure. *Sci. Geol.* **1986**, *39*, 99–130 & 151–172. (In French).
20. Food and Agriculture Organization of the United Nations (FAO). *Caractérisation Des Systèmes de Production Agricole au Senegal*; Document de Synthese; FAO: Rome, Italy, 2007. (In French)
21. Michel, P. The southwestern Sahara margin: Sediments and climate change during the recent Quaternary. *Palaeoecol. Afr. Surround. Isl.* **1980**, *12*, 297–306.
22. Monteillet, J. *Environnements Sédimentaires et Paléohcologie du Delta du Sénégal au Quaternaire*; Lmprimerie des Tilleuls: Millau, France, 1986; p. 267. (In French)
23. Kaczmarek, L.M.; Ostrowski, R.; Pruszak, Z.; Rozynski, G. Selected problems of sediment transport and morphodynamics of a multi-bar nearshore zone. *Estuar. Coast. Shelf Sci.* **2005**, *62*, 415–425. [CrossRef]
24. SOGREAH. *Etudes de Faisabilité et D'avant Projet Sommaire de L'émissaire Delta*; Rapport Final: Grenoble, France, 1994; p. 70. (In French)
25. Barusseau, J.P.; Bâ, M.; Descamps, C.; Diop, E.S.; Diouf, B.; Kane, A.; Saos, J.L.; Soumaré, A. Morphological and sedimentological changes in the Senegal River estuary after the constuction of the Diama dam. *J. Afr. Earth Sci.* **1998**, *26*, 317–326. [CrossRef]
26. Sall, M.M. Dynamique et Morphogenèse Actuelles au Sénégal Occidental. Ph.D. Thesis, Université Louis Pasteur-Strasbourg I, Strasbourg, France, 1982.
27. Gac, J.Y.; Kane, A.; Monteillet, J. Migrations de l'embouchure du fleuve Sénégal depuis 1850. *Cahiers ORSTOM Série Géologie* **1982**, *12*, 73–76. (In French).
28. Bâ, K.; Wade, S.; Niang, I.; Trébossen, H.; Rudant, J.P. Cartographie radar en zone côtière à l'aide d'images multidates RSO d'Ers-2: Application au suivi environnemental de la Langue de Barbarie et de l'estuaire du fleuve Sénégal. *Télédétection* **2007**, *7*, 129–141. (In French).
29. Joiré, J. Amas de coquillages du littoral sénégalais dans la banlieu de Saint-Louis. *Bulletin de l'Institut Français de l'Afrique Noire* **1947**, *9*, 170–340. (In French).
30. Tricart, J. *Notice Explicative de la Carte Géomorphologique du Delta du Sénégal*; Mémoires, B.R.G.M., Ed.; Bureau de Recherches Geologiques et Minieres: Orléans, France, 1961; Volume 8, p. 137. (In French)
31. Nienhuis, J.H.; Ashton, A.D.; Nardin, W.; Fagherazzi, S.; Giosan, L. Alongshore sediment bypassing as a control on river mouth morphodynamics. *J. Geophys. Res. Earth Surf.* **2016**, *121*, 664–683. [CrossRef]
32. Guilcher, A.; Nicholas, J.P. Observation sur la Langue de Barbarie et les bras du Sénégal aux environs de Saint-Louis. *Bulletin d'Information du Comité Océanographique pour les Etudes Côtières* **1954**, *6*, 227–242. (In French)
33. Mietton, M.; Dumas, D.; Hamerlynck, O.; Kane, A.; Coly, A.; Duvail, S.; Baba, M.L.O.; Daddah, M. Le delta du fleuve Sénégal. Une gestion de l'eau dans l'incertitude chronique. In *Incertitudes et Environnement—Mesures, Modèles, Gestion*; d'Allard, P., Denis, F., Picon, B., Eds.; Ecologie Humaine/Edisud: Arles, France, 2006; pp. 321–336. (In French)
34. Durand, P.; Anselme, B.; Thomas, Y.F. L'impact de l'ouverture de la brèche dans la langue de Barbarie à Saint-Louis du Sénégal en 2003: Un changement de nature de l'aléa inondation? *Cybergeo* **2010**, *496*. (In French) [CrossRef]
35. Balouin, Y.; Ciavola, P.; Michel, D. Support of subtidal tracer studies to quantify the complex morphodynamics of a river outlet: The Bevano, NE Italy. *J. Coast. Res.* **2006**, *39*, 602–606.
36. Cooper, J.A.G. Ephemeral stream-mouth bars at flood-breach river mouths on a wave dominated coast: Comparison with ebb-tidal deltas at barrier inlets. *Mar. Geol.* **1990**, *95*, 57–70.
37. Niang, A.J. Les Processus Morphodynamiques, Indicateurs de L'état de la Désertification Dans le Sud-Ouest de la MAURITANIE. Approche Par Analyse Multisource. Ph.D. Thesis, Université de Liège, Liège, Belgium, 2008.
38. The Wamdi Group. The WAM model—A third generation ocean wave prediction model. *J. Phys. Oceanogr.* **1988**, *18*, 1775–1810.
39. Dee, D.P.; Uppala, S.M.; Simmons, A.J.; Berrisford, P.; Poli, P.; Kobayashi, S.; Andrae, U.; Balmaseda, M.A.; Balsamo, G.; Bauer, P.; et al. The ERA-interim reanalysis: Configuration and performance of the data assimilation system. *Q. J. R. Meteorol. Soc. Bull.* **2011**, *137*, 553–597. [CrossRef]
40. Sterl, A.; Caires, S. Climatology, variability and extrema of ocean waves—The web-based KNMI/ERA-40 Wave Atlas. *Int. J. Climatol.* **2005**, *25*, 963–977. [CrossRef]

41. Caires, S.; Swail, V.R.; Wang, X.L. Projection and analysis of extreme wave climate. *J. Clim.* **2006**, *19*, 5581–5605. [CrossRef]
42. Pinto, L.; Fortunato, A.B.; Freire, P. Sensitivity analysis of non-cohesive sediment transport formulae. *Cont. Shelf Res.* **2006**, *26*, 1826–1839. [CrossRef]
43. Bertin, X.; Castelle, B.; Chaumillon, E.; Butel, R.; Quique, R. Alongshore drift estimation and inter-annual variability at a high-energy dissipative beach: St. Trojan Beach, SW Oleron Island, France. *Cont. Shelf Res.* **2008**, *28*, 1316–1332. [CrossRef]
44. Almar, R.; Kestenare, E.; Reyns, J.; Jouanno, J.; Anthony, E.J.; Laibi, R.; Hemer, M.; Du Penhoat, Y.; Ranasinghe, R. Part 1. Wave climate variability and trends in the Gulf of Guinea, West Africa, and consequences for longshore sediment transport. *Cont. Shelf Res.* **2015**, *110*, 48–59. [CrossRef]
45. Longuet-Higgins, M.S. Alongshore currents generated by obliquely incident sea waves. *J. Geophys. Res.* **1970**, *75*, 6788–6801.
46. Battjes, J.A.; Janssen, J.P.F.M. Energy loss and setup due to breaking of random waves. In Proceedings of the ASCE International Conference on Coastal Engineering, Hamburg, Germany, 27 August–3 September 1978; pp. 569–587.
47. Larson, M.; Hoan, L.X.; Hanson, H. A direct formula to compute wave properties at incipient breaking. *J. Waterw. Port Coast. Ocean Eng.* **2010**, *136*, 119–122. [CrossRef]

water

MDPI

Article

Dynamics of Suspended Sediments during a Dry Season and Their Consequences on Metal Transportation in a Coral Reef Lagoon Impacted by Mining Activities, New Caledonia

Jean-Michel Fernandez [1,*], Jean-Dominique Meunier [2], Sylvain Ouillon [3], Benjamin Moreton [1], Pascal Douillet [4] and Olivier Grauby [5]

1 Analytical and Environmetal Laboratory (AEL), Institut de Recherche pour le Développement (IRD)-Nouméa, BP A5, 98800 Nouméa, Nouvelle-Calédonie; bmoreton@ael-environnement.nc
2 Aix Marseille University, Centre National de la Recherche Scientifique (CNRS), IRD, Unité Mixte de Recherche CEREGE, 13545 Aix en Provence CEDEX 05, France; meunier@cerege.fr
3 Unité Mixte de Recherche LEGOS, Université de Toulouse, IRD, Centre National d'Etudes Spatiales (CNES), CNRS, Université Paul Sabatier (UPS), 14 avenue Edouard Belin, 31400 Toulouse, France; sylvain.ouillon@legos.obs-mip.fr
4 Mediterranean Institute of Oceanography (MIO), Unité Mixte de Recherche 110, IRD, CNRS/Institut National des Sciences de l'Univers (INSU), Aix Marseille Université, Université de Toulon, 13284 Marseille, France; pascal.douillet@ird.fr
5 CINaM-CNRS-Aix-Marseille Université, Campus de Luminy Case 913, 13288 Marseille CEDEX 9, France; grauby@cinam.univ-mrs.fr
* Correspondence: jmfernandez@ael-environnement.nc; Tel.: +687-76-84-30

Academic Editor: Roger A. Falconer
Received: 30 March 2017; Accepted: 8 May 2017; Published: 10 May 2017

Abstract: Coral reef lagoons of New Caledonia form the second longest barrier reef in the world. The island of New Caledonia is also one of the main producers of nickel (Ni) worldwide. Therefore, understanding the fate of metals in its lagoon waters generated from mining production is essential to improving the management of the mining activities and to preserve the ecosystems. In this paper, the vertical fluxes of suspended particulate matter (SPM) and metals were quantified in three bays during a dry season. The vertical particulate flux (on average 37.70 ± 14.60 $g \cdot m^2 \cdot d^{-1}$) showed fractions rich in fine particles. In Boulari Bay (moderately impacted by the mining activities), fluxes were mostly influenced by winds and SPM loads. In the highly impacted bay of St Vincent and in the weakly impacted bay of Dumbéa, tide cycles clearly constrained the SPM and metal dynamics. Metals were associated with clay and iron minerals transported by rivers and lagoonal minerals, such as carbonates, and possibly neoformed clay as suggested by an unusually Ni-rich serpentine. Particle aggregation phenomena led to a reduction in the metal concentrations in the SPM, as identified by the decline in the metal distribution constants (K_d).

Keywords: suspended sediment; sediment transport; lagoon; geochemistry; Ni mining; sediment trap; hydrodynamics; New Caledonia; dry season

1. Introduction

The mining industry in New Caledonia is one of the most important environmental concerns for the tropical island lagoonal ecosystem [1–9].

With about 85% endemism among terrestrial plants, 24 different species of mangroves among the 70 listed throughout the world, about 2800 species of molluscs and the second longest barrier reef in

the world [10–15], New Caledonia's ecosystems and biodiversity are highly sensitive to anthropogenic activities (e.g., [16–23] for its lagoons). Since the beginning of mining in New Caledonia, more than 160 $\times$ 10^6 tonnes of ore have been extracted. This has led to the mobilization and transport of approximately 300 million m^3 of soil material (laterites). Opencast Ni mines have enhanced soil erosion and transportation of sediments and metals into the lagoon [19,24–27] with several consequences on the lagoonal ecosystems, including increased sedimentation rates; decreased light penetration and dissolved oxygen levels; and an increased metal contamination in the food web which may affect humans [23,28,29]. The Ni mining industry has flourished for over 25 years, and New Caledonia will remain one of the major worldwide Ni producers for the foreseeable future, with global Ni reserves estimated at around 20–25% [30]. As a consequence, environmental studies are required in order to mitigate the effects of 400–500 km^2 of deforestation specifically related to the mining industry in New Caledonia.

Numerous studies of the south-western lagoon of New Caledonia have been conducted investigating hydrodynamics, sediment transport, sedimentation dynamics, metal fluxes, accumulation zones, and particle sources [23,27,31–37]. In complement to these works, this paper aims at characterizing the suspended sediment mineralogy and geochemistry (including metals) in three bays; analysing the relationships between their composition and the mining activities; determining how hydrodynamics forced by wind regimes affect the transportation of particulate metals bounded to the lateritic Suspended Particulate Matter (SPM) into the lagoon. Three contrasting bays in the south west lagoon, where hydrodynamics modelling has been carried out [38–40] were selected: Boulari Bay, Dumbéa Bay and Saint Vincent Bay. Samples were collected during a dry season in order to limit the influence of riverine inputs which could affect the understanding of hydrodynamic regimes, during distinct wind regimes (trade wind and west-breezes) and two neap/spring tide cycles.

2. Study Area

New Caledonia is located at the southern end of the Melanesian Arc, near the Tropic of Capricorn. In New Caledonia, mining activities are almost exclusively conducted on the main island (16,642 km^2, [41]). In its south-western part, host rocks are composed of peridotites and harzburgites incorporating metals like Ni, Co, Cr, Fe and Mn [42,43] in Mg and Fe-minerals. Elements like Pb and Zn are only present in significant quantities in rocks from the northernmost part of the island [44–49]. The weathering of peridotites results in the accumulation of transition metals in the saprolite (also called "garnierite") and the yellow lateritic layers which are subjected to mining extraction. On the top of the series, the red lateritic layer corresponds to a more advanced weathering state of the peridotites where the structure of the bedrock is no longer visible [50]. Mg and Si are very low and the main constituents are ferric hydroxides more or less widely crystallized in goethite. In the upper part of the profile, the ultimate term of the weathering process is represented by a ferricrete composed mostly of goethite and, in lower proportions, hematite.

The climate of New-Caledonia is dry-tropical [51] with alternating dry and wet seasons. South-East trade winds blow from October to May with a mean speed of 8 $m{\cdot}s^{-1}$ and from April to September a variable northern wind blows. The temperatures vary moderately between dry and wet seasons.

In the south-west lagoon of New Caledonia, the tide is mixed and mainly semi diurnal [38]. Due to the interaction between the different components, spring tide and neap tide periods alternate during a lunar month. The maximum tidal amplitude is 1.5 m during a spring tide.

Similar to most of the New Caledonian Rivers, the Coulée, Dumbéa and Tontouta Rivers have steep upper courses and much flatter lower courses where deposits of weathered bedrock products accumulate (Figure 1). Due to the tropical climate conditions in New Caledonia, the hydrological regime is of torrential type. During the dry season, sediment loads carried by the rivers are low because of the low energy for erosion and the weak transport capacity [52,53]. Rain events reaching 700 mm and more over a 24-h period lead to intense weathering of the slopes and flushing of large quantities

of suspended matter to the lagoon. Baltzer and Trescases [52] reported that during cyclone Brenda in 1968, over 20,000 t of particles were discharged in a single day through the Dumbéa River estuary. The present study focuses on the three above-mentioned estuaries located on the south-west coast of New Caledonia influenced by their respective watersheds (Figure 1).

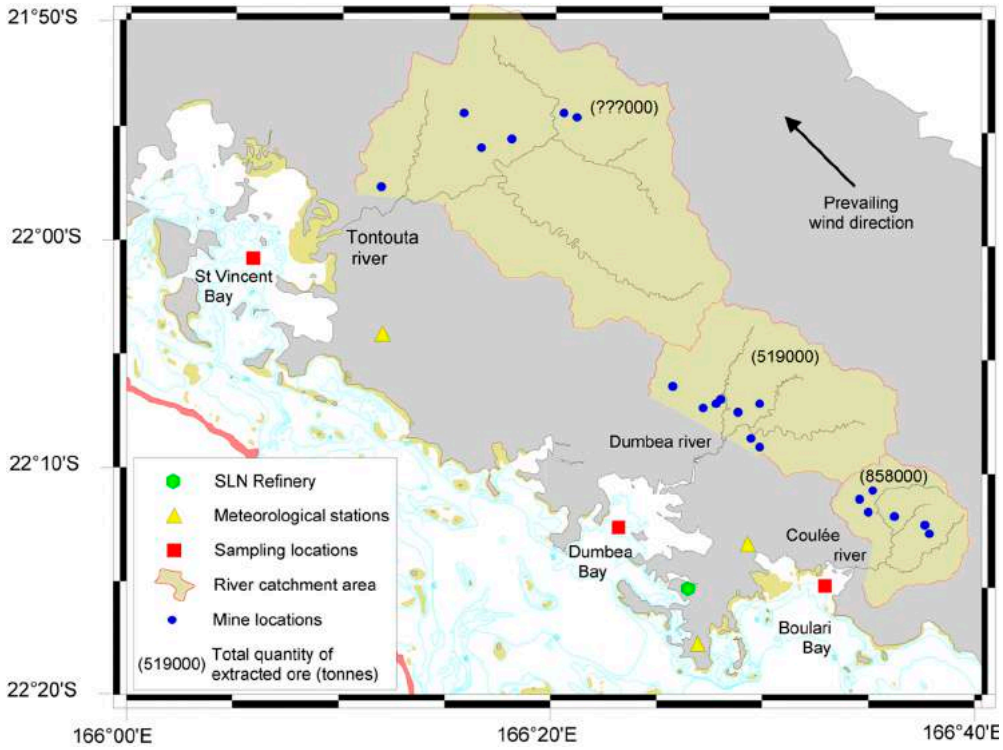

Figure 1. Map location of the study area in the west coast of New-Caledonia: Boulari Bay, influenced by a medium-scale mine activities until 1981; Dumbéa Bay, halted mining activity in order to maintain the water supply of Nouméa (the peninsula between Dumbéa Bay and Boulari Bay); St Vincent Bay, affected by intense opencast mining activities.

2.1. Boulari Bay

The Coulée River catchment (92 km^2) is located almost entirely in the ultrabasic Grand Massif of the South New-Caledonia. An intermediate-scale mining operation was active in the area until 1981, but erosion from the initial prospecting and extraction sites has continued. The present terrigenous inputs delivered to Boulari Bay by the Coulée River result from combined natural and anthropogenic influences [19,25]. The river is extending its delta into the southern part of Boulari Bay where tidal mudflats are being formed.

2.2. Dumbéa Bay

The catchment area of Dumbéa River covers about 233 km^2 and only a few small-scale localized garnierite extractions have occurred in the headwater regions. Similar to other drainage basins near the main city, Nouméa, any mining activities in the area have been forbidden since 1927 to maintain a quality water supply for the city. The sediment load yielded at the river mouth—where a mangrove extends—and delivered to Dumbéa Bay consists of clay, silts and sand, and the effects of mining activities have been limited [25,26].

2.3. St Vincent Bay

The Tontouta River and its tributaries form the largest of the three river catchments (476 km^2) and drain a peridotic hinterland where opencast mining is still intense today. These activities extend to the mountain crests, and on hillslopes, only a few kilometres from the coast. The Tontouta River carries substantial amounts of fine terrigenous material that has resulted in a shallowing of the Saint Vincent Bay, particularly nearshore. The impact of mining activities appears to be stronger than in the Coulée catchment because of the lack of conservation work along the river and tributaries between 1960s and 1980s. This has led to a drastic increase in the sediment load at the river mouth.

3. Materials and Methods

During the dry season between 21 November and 14 December, 2005, SPM was sampled in the three bays every two days, and currents were measured continuously (Figure 1, Table 1). Rainfall rates, and wind direction and velocity were obtained from Météo-France's meteorological stations at Magenta airport, Mont Coffin and Tontouta airport close to Boulari Bay, Dumbéa Bay and Saint Vincent Bay, respectively.

Table 1. Sampling sites, depth and localisation.

Site	Longitude	Latitude	Depth (m)
Boulari Bay	E 166°32.126	S 22°15.355	13.2
Dumbéa Bay	E 166°23.243	S 22°12.291	13.0
St Vincent Bay	E 166°06.635	S 22°00.561	12.8

3.1. SPM Sampling

Three sequential sediment traps (model PPS 4/3; section of 0.05 m^2, Technicap, La Turbie, France) were used for suspended particulate matter (SPM) sampling. They were moored at sites of ~13 m depth downstream of the mouth of the Coulée, Dumbéa and Tontouta Rivers (Figure 1, Table 1). Samples were collected at a frequency of 48 h, 3 m above the seabed. The sediment traps were equipped with twelve 250 mL polypropylene vials filled with 5% formaldehyde-filtered seawater solution before mooring in order to preserve the particles from microbiological activity [54]. After sampling, the samples were placed in a refrigerator at 2–4 °C before analysis. Particles fluxes were calculated using the formula:

$$\text{Flux } (g \cdot m^{-2} \cdot d^{-1}) = \text{sample load (g)} / (\text{Section area } (m^2) * \text{Collecting time (d) per flask}) \quad (1)$$

3.2. Current Measurement

Currents were measured using an Acoustic Doppler Current Profilers (RDI Workhorse Monitor ADCP, Teledyne RD Instruments, Poway, USA 300 kHz, 12 cells, 1-m resolution) placed on the seabed in Dumbéa and St Vincent Bays (Figure 1). In Boulari Bay, local currents were measured using an Acoustic Doppler Velocimeter (Sontek) located 3 m above the seabed. Moored in the vicinity of the 3 sediment traps, the three current meters simultaneously recorded measurements during the SPM sampling period (one month). Unfortunately, due to technical problems, measurements are not available for Dumbéa Bay during the last ten days of the field campaign.

3.3. In Situ Laser Grain Size and CTD Profiling

Turbidity was measured regularly at each station by the use of a Seapoint Optical Backscattering Sensor (Seapoint Sensors, Inc., Brentwood, NH, USA) (λ = 880 nm) connected to a Seabird SBE19 CTD profiler. The Seapoint sensor was factory-adjusted for a consistent response to Formazin Turbidity Standard measured in Formazin Turbidity Units (FTU). A former calibration showed that, in the

south-west lagoon of New Caledonia, turbidity is related to the mass concentration (C) of SPM following [55]:

$$\text{Turbidity (FTU)} = 1.85\ \text{C (mg·L}^{-1}) \quad (2)$$

An in situ Laser Scattering and Transmissometry device (LISST-100X; Sequoia Scientific Inc., Bellevue, WA, USA) was used in situ to quantify the SPM and the Particle Size Distribution (PSD). The LISST-100X provides the distribution of particle volume concentrations in 32 size classes logarithmically spaced within the range 1.25–250 µm (e.g., [56]). Jouon et al. [55] gave an extended presentation of its first application in the lagoon of New Caledonia.

Synthetic parameters were defined to characterize the particle distribution: (1) the median diameter (D_{50}) as the diameter of a particle for which the cumulative volumetric distribution reaches 50% of the SPM volume concentration; (2) the Junge parameter (*s*) characterizing the slope of the particle size distribution (PSD) (e.g., [57,58]): high values correspond to SPM dominated by fine particles or aggregates, while low values correspond to macro-flocs; (3) the percentage of particles with diameter > 60 µm that was shown to be an indicator of the state of aggregation [55].

3.4. Geochemistry

All apparatus was acid soaked (10% nitric acid) for a minimum of five days and rinsed with ultrapure water (Milli-Q), and then stored in acid cleaned plastic bags until needed. While analytical acid grades were used for all cleaning steps, high purity reagents were used for all parts of the analytical procedure.

Seawater samples: Seawater was collected from the three bays using 5L teflon lined Go-Flo™ water samplers (General Oceanics Inc., Miami, FL, USA). The Go-Flo™ water samplers were primed to be open at the site and lowered into the water, rinsed thoroughly and closed using a teflon-coated messenger. Once at the surface, samples were transferred in situ into acid cleaned HDPE bottles and sealed in clean plastic bags. After an on-line filtration at 0.45 µm (Millipore acetate filters, Merck Millipore, Billerica, MA, USA), samples were then preconcentrated and analysed using ICP-OES following the procedure described by Moreton et al. [35]. Only the results for Fe, Mn and Ni, which represent the main elements used to trace watershed lixiviation, are presented in this article.

The accuracy and precision of the analytical results was controlled by assaying a SLEW-3 certified water sample (National Research Council, Canada), to check the preconcentration method. The stability of the ICP-OES was controlled inserting independent standards in the sample series: in our case, one at the beginning and one at the end. The quantification limits (LQ) of the method for the 3 metals, obtained after deduction of blanks, are given in Table 2.

Table 2. Results of the analysis of the reference material SLEW-3 and LQ of the method.

Metal	Reference Material SLEW-3 (µg·L^{-1})		LQ (µg·L^{-1})
	Analysed (*n* = 1)	Certified	
Fe	0.32	0.57 ± 0.06	0.068
Mn	1.92	1.61 ± 0.22	0.028
Ni	1.17	1.23 ± 0.07	0.022

Particulate samples: Swimmers were removed from SPM collected at each site with sediment traps by sieving at 40 µm. The formaldehyde solution and salt were removed by rinsing several times and centrifuging. Organic matter and faecal pellets were destroyed using a solution of 30% hydrogen peroxide. The purified sediments were then oven dried at 60 °C for a period of 72 h.

Particulate metals were then dissolved by an alkaline fusion digestion performed using 0.5 g of lithium tetraborate mixed with 100 mg of SPM and heated in a muffle furnace (1100 °C) for 15 min. The resulting amalgam was dissolved into 0.5M HCl, and the metals analysed.

Analysis of 9 elements (Al, Ca, Co, Cr, Fe, Mg, Mn, Ni and Si) in SPM was performed using an inductively coupled plasma optical emission spectrometer (Vista, Varian, Inc., Palo Alto, CA, USA).

The validity of the analysis was verified by assaying a MESS-3 certified sediment sample (National Research Council, Canada). The quantification limits (LQ) of the method for the 9 metals, obtained after deduction of blanks, are given in Table 3.

Table 3. Results of the analysis of the reference material MESS-3. The Quantification Limits of the method were not estimated because of the high levels of concentrations measured in SPM.

Reference Material MESS-3 ($mg \cdot kg^{-1} \cdot dw$)		
Metal	**Analyzed**	**Certified**
Al	90,053	85,900 ± 2300
Ca	13,746	14,700 ± 600
Co	15.2	14.4 ± 2.0
Cr	97	105 ± 4
Fe	37,815	32,400 ± 1200
Mg	16,905	16
Mn	308	324 ± 12
Ni	40.6	46.9 ± 2.2
Si	232,765	270,000 *

Note: * Information value only.

3.5. Kd Calculation

Trace metal mobility in the lagoon water column was quantified through its distribution coefficient (K_d, in $mL \cdot g^{-1}$), given by the following general formula:

$$K_d = \frac{C_p}{C_w} \quad (3)$$

with C_p = metal concentration in SPM, C_w = dissolved metal concentration in sea water.

3.6. Mineralogy

The mineralogical composition of the suspended sediments was determined using X-ray diffractometry (XRD), and Transmission Electron Microscopy (TEM). XRD analyses were done on slightly ground samples using Philips (PW1050/81) equipment (Philips, Eindhoven, The Netherlands) with a Cu anticathode. TEM observations were carried out on a JEOL-2000 FX microscope (JEOL USA, Inc., Peabody, MA, USA), operating with a beam intensity of 126 mA and an accelerating voltage of 200 kV. Microanalyses were acquired with a Si(Li) detector filled with a UTW and a Brucker Esprit EDS System. Quantitative data were obtained by the method developed by Cliff and Lorimer [59] after calibration of the $k_{x,Si}$ factors (x = Al, Mg ...) against natural and synthetic layer silicates of known and homogeneous composition.

4. Results

4.1. Rainfall

During the study period (21 November to 14 December 2005), rainfall was low, scarce and irregular over all 3 sites. Only one day of significant rainfall (12 December) was recorded at the meteorological stations at Magenta airport (18 mm) and Mont Coffin (10 mm). At the Tontouta airport station, the maximum rainfall was 6 mm on 9 December. Besides this, only 2 mm were recorded at the 3 stations on the 20 and 21 November and on 26 November. Generally, rainfall at the Tontouta station was systematically lower than at the two other stations.

4.2. Wind

The meteorological stations at Magenta airport (near Boulari Bay) and Mont Coffin (between Dumbéa Bay and Boulari Bay, but representative of Dumbéa Bay conditions) recorded mainly two distinct regimes (Figure 2):

- A typical dominant trade wind regime during the study period, with the direction changing from NE during the night to SE in the day, increasing in strength until the beginning of the afternoon and reaching a maximum of 10 $m \cdot s^{-1}$ (periods B, D);
- A regime characterized by variable and weaker winds (below 5 $m \cdot s^{-1}$) (periods A, C and E).

The meteorological station at Tontouta airport (St Vincent Bay) recorded winds that were systematically weaker than those recorded at Magenta airport (Boulari Bay) and Mont Coffin (Dumbéa Bay). In the Saint Vincent Bay, wind speeds were lower than 6 $m \cdot s^{-1}$ and wind direction was irregular. In this area, trade winds are weakened by relief and coastal thermal breezes.

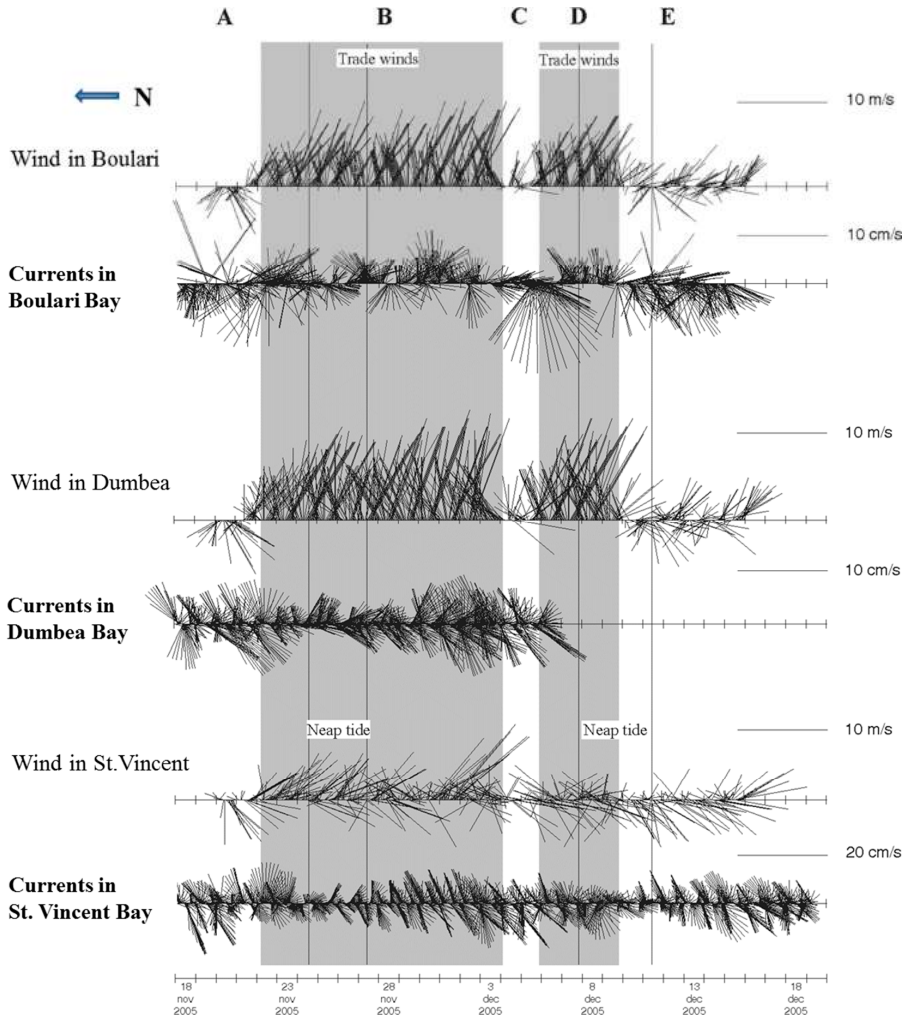

Figure 2. Wind and current speeds and directions for Boulari, Dumbéa and St Vincent bays during the study period (21 November to 14 December 2005).

4.3. Hydrodynamics

During the study period, the amplitudes of the semi-diurnal tides changed from 0.6 to 1.2 m. Neap tide periods are identified in Figures 2 and 3.

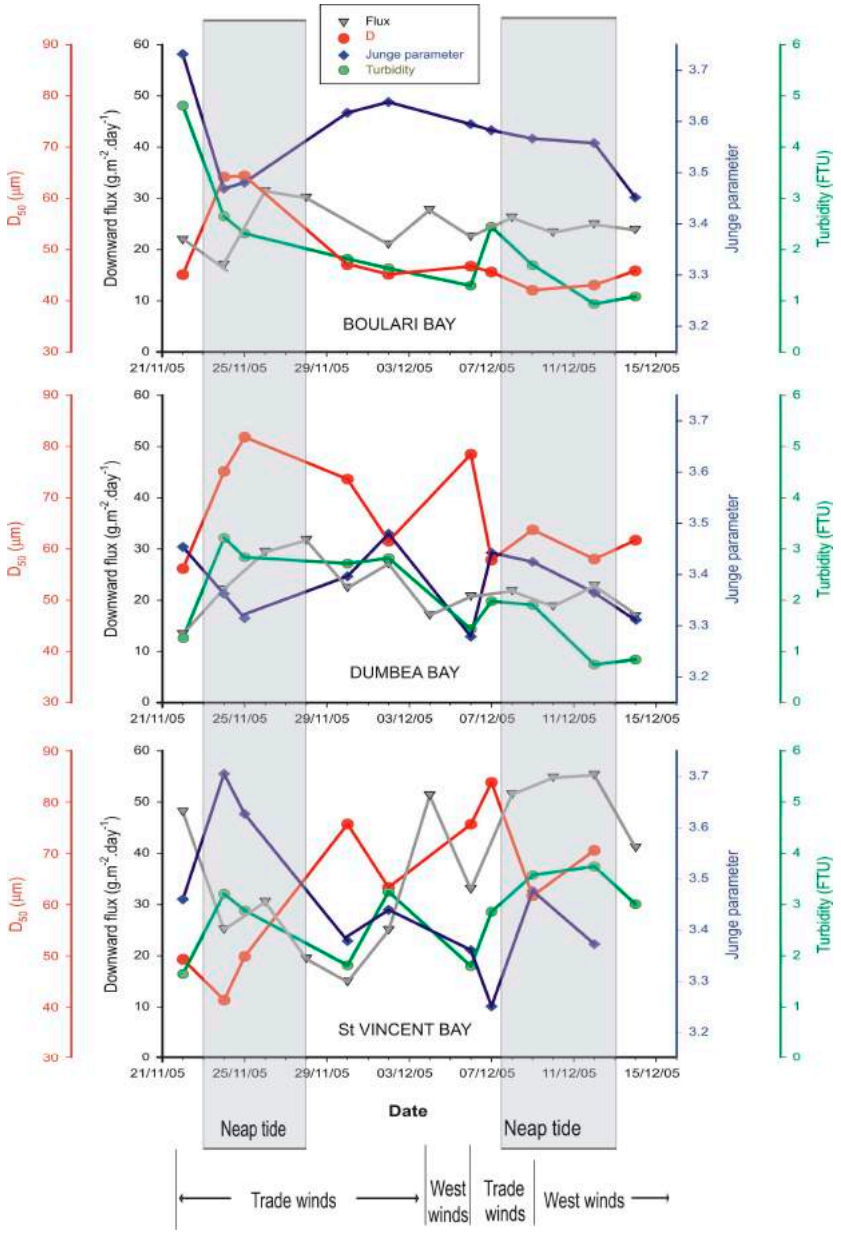

Figure 3. Median diameter (D50), Junge parameter (*s*), flux and turbidity for Boulari, Dumbéa and St Vincent bays over the study period (21 November to 14 December 2005), 3 m above the seabed.

In Boulari Bay, the neap/spring tide cycles had a non-significant influence on the currents measured 3 m above the seabed (Figure 2). In the absence of trade winds (periods C and E), a strong westward flow was observed during several days and may indicate the development of a cyclonic gyre circulation along the isobaths from Mont-Dore (SW of Boulari Bay) towards Nouméa (as described by Fernandez et al. [27]). This gyre results from the conjunction of the propagation of the tide along the coastline of the bay. During trade winds (periods B and D), which blew from an E-NE direction in the Coulée River valley in the morning and from the SE in the afternoon, an anticyclonic gyre generated flows toward the East (as described by Douillet et al. [39]). However, during short periods (28 and 30 November and 2 December), flows in the opposite direction were observed. The present data suggest the strong impact of winds on currents in Boulari Bay, and the formation of a drive out phenomena of waters which were accumulated at the bottom of the bay only when trade winds blow.

In Dumbéa Bay, the strong tidal influence and the weak effects of the wind on the direction and the strength of the currents 3 m above seabed were noticed: flows were the highest during spring tides and lowest during neap tides (Figure 2). Furthermore, currents were similar at the same periods of the tide but with different wind forcings, for example, during a neap tide, with low wind (20 and 21 November) and with a trade wind (3 and 4 December). This suggests that the wind has little influence on the water circulation in an area that is partly protected from the trade winds by the topography.

In St Vincent Bay, the strength of the currents 3 m above the seabed strongly depended on tide cycles (Figure 2); currents rotated 180 degrees during a neap-spring tide cycle, the currents being stronger during spring tides and lower during neap tides. The weakest flows were measured between 24 to 27 November and 24 to 27 December during neap tides. The strongest currents were recorded during spring tides around 3 December. Tides are thus the major factor influencing hydrodynamics in St Vincent Bay. A residual drift of the current to the S-W was observed; however, its value was low.

4.4. SPM Collection

In Boulari Bay, the SPM load collected over 48-h periods ranged between 1.72 and 3.16 g, corresponding to downward fluxes in the range 17.23 to 31.63 $g \cdot m^{-2} \cdot d^{-1}$ (Table 4), with an average value of 24.14 $g \cdot m^{-2} \cdot d^{-1}$ (σ = 4.50 $g \cdot m^{-2} \cdot d^{-1}$). The maximum fluxes were recorded over the period of 4 days from 25 to 28 November ($F > 30$ $g \cdot m^{-2} \cdot d^{-1}$) and the minimum on 23 to 24 November and 29 to 30 November ($F \approx 17$ $g\ m^{-2} \cdot d^{-1}$).

Table 4. Mass (g) of suspended particulate matter collected over 48 h in sediment traps in the three sampling bays during the study period (21 November to 14 December 2005).

Date	Boulari Bay	Dumbéa Bay	St Vincent Bay
21–22 November	2.21	1.29	4.83
23–24 November	1.72	2.16	2.53
25–26 November	3.16	2.84	3.07
27–28 November	3.03	3.19	1.96
29–30 November	1.74	2.26	1.51
1–2 December	2.12	2.78	2.52
3–4 December	2.79	1.95	5.15
5–6 December	2.27	2.09	3.32
7–8 December	2.64	2.20	5.17
9–10 December	2.35	1.90	5.50
11–12 December	2.51	2.30	5.55
13–14 December	2.40	1.71	4.12

In Dumbéa Bay, the SPM load was similar to that of Boulari Bay with fluxes between 12.92 and 31.93 $g \cdot m^{-2} \cdot d^{-1}$, and a mean value of 22.24 $g \cdot m^{-2} \cdot d^{-1}$ (σ = 5.20 $g \cdot m^{-2} \cdot d^{-1}$). The maximum fluxes were recorded over the period of 4 days from 25 to 28 November ($F \approx 32$ $g \cdot m^{-2} \cdot d^{-1}$) and the minimum on 22 November ($F \approx 13$ $g \cdot m^{-2} \cdot d^{-1}$).

The values in St Vincent Bay were clearly different with a higher average value of 37.70 $g \cdot m^{-2} \cdot d^{-1}$ (σ = 14.60 $g \cdot m^{-2} \cdot d^{-1}$). Variations around the average value were large with frequent loads higher than 50 $g \cdot m^{-2} \cdot d^{-1}$. Except on 21 and 22 November, the first half of the sampling period was characterised by low fluxes ($15 < F < 31$ $g \cdot m^{-2} \cdot d^{-1}$) and from 4 December onwards, the values were much higher ($33 < F < 56$ $g \cdot m^{-2} \cdot d^{-1}$).

For each bay, variations in the fluxes, turbidity, D_{50} (mean diameter of SPM from measurements in the range 1.25–250 µm) and Junge parameter (s) during the study period are presented in Figure 3.

4.5. Turbidity, Water Column Structure, and Particle Dynamics

Turbidity was systematically higher in the bay of St Vincent with an average value of 2.8 FTU, compared with average values around 2.0 FTU in the other two bays (Table 5).

In Boulari Bay between 21 and 24 November, the median diameter (D_{50}) increased from 45 to 64 µm while the Junge parameter (*s*) decreased from 3.75 to 3.48 (Figure 3). While fine particles dominated initially, coarser and medium sizes suddenly increased (24 and 25 November) two days after the beginning of the trade-winds. After 25 November, the decrease of D_{50} was fairly constant up to the end of the study period, when the value reached 42 µm. Conversely, the Junge parameter increased until December 2 (s = 3.63), then decreased gradually up to 12 December and then increased sharply until December 14. The downward flux of particles increased just after the peak of coarser particles (26 November) and slightly decreased afterwards (Figure 3). Although generally ranging between 1 and 3 FTU, turbidity showed values around 7.5 FTU in the bottom first four metres above seabed, at the beginning of the study period. Another nepheloid layer, of weaker intensity (4.5 FTU), was also observed around 7 December. The particle grain size distribution was fairly homogeneous throughout the water column during the study period except on the 12 and 14 December when the concentration of fine particles (<7.75 µm) increasing towards the seabed was observed.

Table 5. Main characteristics (mean temperature, salinity and turbidity) recorded in the three sites during the study period (21 November to 14 December, 2005).

Site	Statistics	Temperature (°C)	Salinity (‰)	Turbidity (FTU)
Boulari Bay	Mean ± Std Dev.	26.0 ± 0.6	35.9 ± 0.3	2.1 ± 1.1
	Min.–Max.	25.3–27.5	35.4–36.9	0.5–7.6
Dumbéa Bay	Mean ± Std Dev.	26.5 ± 0.5	36.1 ± 0.1	2.0 ± 0.9
	Min.–Max.	24.8–27.6	35.3–36.6	0.5–5.5
St Vincent Bay	Mean ± Std Dev.	26.9 ± 1.0	36.1 ± 0.1	2.8 ± 0.8
	Min.–Max.	25.3–28.8	35.2–36.5	1.4–7.8

In Dumbéa Bay, the evolution of the median diameter and the Junge parameter were almost inversely related (Figure 3): for example, the two maximum values of D_{50} measured on 25 November (82 µm) and 6 December (79 µm) corresponded with the minimal values of *s* (3.32 and 3.28), respectively. Turbidity stayed fairly homogeneous throughout the water column, but decreased with time from 3.2 FTU to 0.8 FTU. Only two profiles (11 November and 12 December) showed a clear increase in turbidity towards the bottom. A general decrease in the volumetric concentration, detected between 24 November (10 $\mu L \cdot L^{-1}$) and 14 December (5 $\mu L \cdot L^{-1}$), combined with a decrease in turbidity, was caused by a reduction in the largest particle-size ranges ($\varnothing$ > 40.6 µm). After 9 December, the reduction in the volumetric concentration was due to a decrease in both the smallest ($\varnothing$ < 7.75 µm) and largest particle-size ($\varnothing$ > 40.6 µm) populations. At the very end of the measurement period, an increase in the amount of fine particles ($\varnothing$ < 7.75 µm) was observed at depth, with large particles ($\varnothing$ > 40.6 µm) towards the surface.

In St Vincent Bay, the minimum median diameter (42 µm) was measured at the beginning of the study period (24 November) (Figure 3). D_{50} increased gradually until 7 December (85 µm) with an intermediate maximum value observed on 30 November (76 µm). From the 9 to the 12 December, the median diameter increased from 62 to 70 µm. The Junge parameter followed an exact opposite evolution. The maximum value was 3.70 on 24 November and the minimal value was 3.25 on 7 December. From the 9 to the 12 December, the parameter *s* decreased from 3.46 to 3.38. Turbidity ranged between 1.5 and 3.0 FTU in the first few metres below the surface. From 2 December until the end of the study period, turbidity systematically increased towards the seabed with a consistently higher total volumetric concentration. A significant population of particles above 40 µm and high downward fluxes of particles were observed throughout the study period (Figure 3). High downward fluxes varied similar to turbidity after a short delay.

The values of the median diameter and the Junge parameter strongly differed from one bay to another (Figure 3). D_{50} values ranged between 42 and 65 µm in Boulari Bay (median D_{50} = 48.9 µm), between 55 and 82 in Dumbéa Bay (median D_{50} = 66.8 µm) and between 42 and 84 µm in St Vincent

Bay (median D_{50} = 63.4 µm). The Junge parameter *s* values ranged between 3.45 and 3.73 in Boulari Bay (median *s* = 3.58), 3.28 and 3.48 in Dumbéa Bay (median *s* = 3.38) and 3.25 and 3.70 in St Vincent Bay (median *s* = 3.45). The *s* parameter variation was minimal in Dumbéa Bay and maximal in St Vincent Bay, the variation of D_{50} was minimal in Boulari Bay and maximal in St Vincent Bay.

4.6. Geochemistry

The chemical composition of the seawaters in the 3 bays (Table 6) differed in their dissolved Fe, Mn and Ni concentration. The respective highest and the lowest concentrations were measured in St Vincent Bay and in Boulari Bay. Fe and especially Mn were found at much lower concentration than Ni.

These values are high but reflect the influence of the geology of New Caledonia on the concentrations in dissolved metals. The values show a typical "coast-to-offshore" gradient, with maximum concentrations in bays influenced by rivers and minimum near the coral reef-barrier (Table 7). This evolution is similar to that of the lateritic metals analysed in the sedimentary cover [27].

During the study, Mn concentrations were similar for the 3 bays, with limited variation between 0.33 to 1.24 $\mu g \cdot L^{-1}$. The respective Fe and Ni ranges were larger, i.e., 0.23–2.65 $\mu g \cdot L^{-1}$ and 0.95 to 7.10 $\mu g \cdot L^{-1}$ in the 3 bays. Indeed, in Boulari Bay, the maximum Fe values were measured on 24 and 30 November, and were slightly higher on 8 December, and seemed to coincide with those of Ni. For the other two bays, the concentrations of theses metals changed differently over time. For example, for Ni, maximum concentrations were measured on 24 November, 2 December and 22 November, for Boulari, Dumbéa and St Vincent bays, respectively.

Table 6. Concentration of the dissolved Fe, Mn and Ni in seawater during the study period from 22 November to 14 December 2005 in the 3 bays.

Sampling Date	Boulari Bay			Dumbea Bay			StVincent Bay		
	Fe ($\mu g \cdot L^{-1}$)	Mn ($\mu g \cdot L^{-1}$)	Ni ($\mu g \cdot L^{-1}$)	Fe ($\mu g \cdot L^{-1}$)	Mn ($\mu g \cdot L^{-1}$)	Ni ($\mu g \cdot L^{-1}$)	Fe ($\mu g \cdot L^{-1}$)	Mn ($\mu g \cdot L^{-1}$)	Ni ($\mu g \cdot L^{-1}$)
22 November 2005	0.58	0.66	2.00	0.73	0.56	2.87	1.09	0.73	7.10
24 November 2005	1.19	0.40	3.92	0.74	0.59	1.30	1.33	0.80	5.49
26 November 2005	0.70	0.48	2.11	1.41	0.46	2.87	1.43	1.07	4.86
28 November 2005	0.24	0.45	1.17	0.64	0.49	3.84	1.59	1.24	5.11
30 November 2005	1.38	0.35	1.60	1.07	0.57	4.52	2.51	0.96	1.95
2 December 2005	0.69	0.33	1.06	1.07	0.55	4.04	1.87	0.96	2.45
6 December 2005	0.32	0.45	1.31	0.77	0.55	3.65	1.43	0.67	3.23
8 December 2005	0.55	0.60	1.70	1.30	0.58	3.35	2.65	1.06	4.92
10 December 2005	0.40	0.53	1.18	0.91	0.57	2.77	1.99	0.88	4.71
12 December 2005	0.30	0.46	0.95	0.23	0.73	1.99	0.71	0.40	6.50
14 December 2005	0.28	0.69	1.24	0.30	0.57	1.78	0.95	0.61	4.87
Min	0.24	0.33	0.95	0.23	0.46	1.30	0.71	0.40	1.95
Max	1.38	0.69	3.92	1.41	0.73	4.52	2.65	1.24	7.10

The analytical results showed that the SPM collected in St Vincent Bay had a distinctly different chemical composition to that of the other two bays (Table 8 and Figure 4). Indeed, in St Vincent Bay's SPM, 7 of the 9 analysed metals (Co, Cr, Fe, Mg, Mn, Ni, Si) were highly enriched, up to one order of magnitude (e.g., Co, Ni or Mn) compared with the two others sites. Only the behaviour of Ca differed, being slightly more concentrated in the SPM collected in Dumbéa Bay, particularly during the second half of the sampling period (Figure 4).

In terms of intra–site variability, the metal and Ca concentrations remained relatively constant in St Vincent Bay's SPM, while they evolved in Dumbéa Bay and particularly in Boulari Bay (Figure 4). This time-variation started with high metal concentrations at the beginning of the study period (21 and 22 November) followed by a strong decrease over a 4-day period (23 to 27 November) before increasing to the highest values at the end of the sampling period. This increasing trend was irregular in Dumbéa Bay, where the highest concentrations were observed from 4 December, while in Boulari

Bay, the increase was slight but continuous to reach the maximum values for all the metals and Ca on 14 December. The mean concentrations increased about 2, 3 and 5 times, in St Vincent, Dumbéa and Boulari bays, respectively.

Table 7. Concentrations of dissolved Fe, Mn and Ni in bays and coral reef barrier (n = 965). Analysis carried out between November 2013 and August 2016 in the frame of marine environmental monitoring along the west coast of New Caledonia (unpublished environmental monitoring data of the surrounding area of the KNS plant). Observed especially in the shallow bays, the extreme Std Deviations demonstrate the high variability of the metal concentration levels generated by the lixiviation of the exploited basins.

Location	Fe ($\mu g \cdot L^{-1}$)	Mn ($\mu g \cdot L^{-1}$)	Ni ($\mu g \cdot L^{-1}$)
Bays (n = 288)	0.241 ± 0.444	4.565 ± 9.802	2.904 ± 4.700
Intermediate (n = 315)	0.123 ± 0.095	0.422 ± 0.659	0.322 ± 0.423
Reef (n = 362)	0.058 ± 0.061	0.103 ± 0.095	0.115 ± 0.100

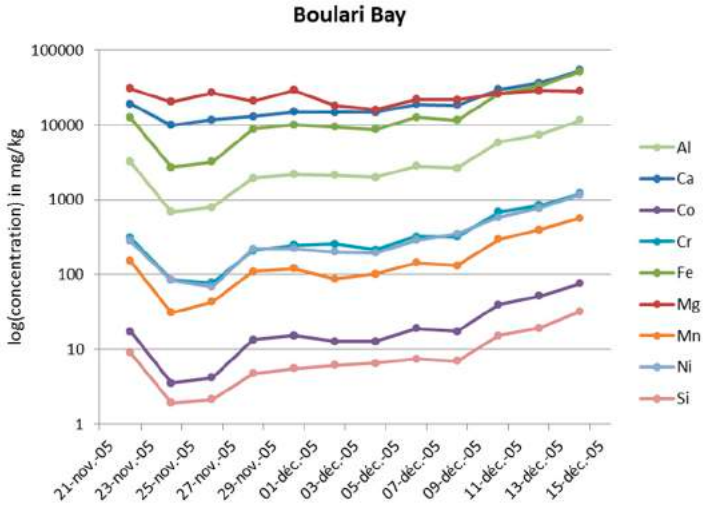

(**a**)

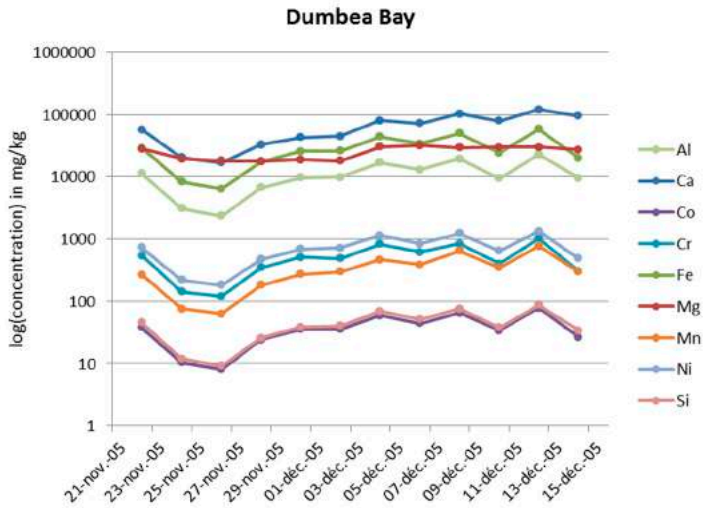

(**b**)

Figure 4. *Cont.*

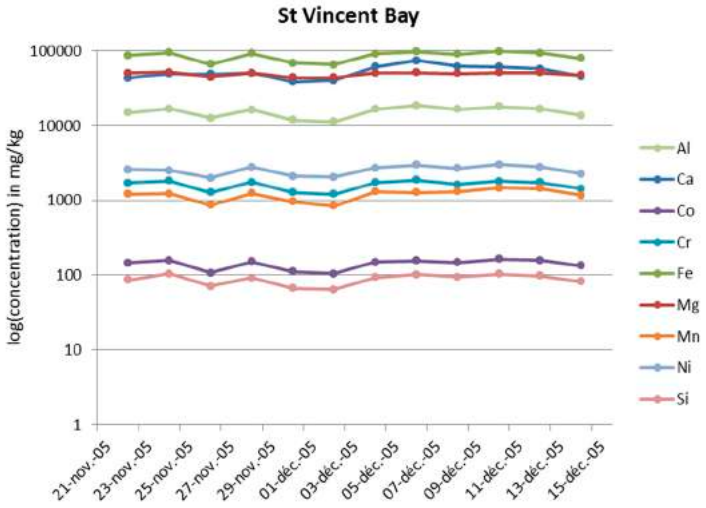

(**c**)

Figure 4. Time variation of the Ca and the 8 metals analysed in SPM trapped during study period from 21 November to 14 December, 2005 in each sampling site: (**a**) Boulari Bay; (**b**) Dumbéa Bay and (**c**) St Vincent Bay.

Table 8. Minimum and maximum concentrations for the analysed elements in SPM trapped during study period from 21 November to 14 December 2005 in each sampling site.

Concentration (mg kg^{-1})		Al	Ca	Co	Cr	Fe	Mg	Mn	Ni	Si
Boulari bay	Min	1930	12,990	13	208	690	15,874	87	195	4750
	Max	11,520	53,710	76	1209	51,820	29,169	568	1157	31,850
Dumbéa bay	Min	6740	33,060	24	306	17,420	17,672	183	473	25,830
	Max	22,740	119,600	78	1025	58,190	32,064	765	1332	86,590
StVincent bay	Min	11,220	38,360	105	1204	64,670	43,684	844	2033	63,780
	Max	18,440	73,950	164	1856	97,900	51,051	1459	3012	102,940

For each bay, variations in elements concentrations were remarkably correlated ($R^2 > 0.850$) except for (Table 9): (i) Mg, where concentrations showed poor correlations with other SPM metals in Dumbéa Bay (mean $R^2 \approx 0.480$) and no correlation in Boulari Bay (mean $R^2 \approx 0.223$); (ii) Ca and all the other metals in St Vincent Bay (mean $R^2 \approx 0.534$), and, to a lesser extent, in Dumbéa Bay (mean $R^2 \approx 0.710$), and with Mg in Boulari Bay ($R^2 = 0.236$).

Table 9. Correlation coefficients (R^2) for Ca, Mg, Fe, Co, Cr, Mn, Ni, Al and Si concentrations in the suspended matter trapped from 21 November to 14 December in each sampling site: (a) Boulari Bay, (b) Dumbéa Bay and (c) St Vincent Bay.

Boulari Bay									
	Ca	**Mg**	**Fe**	**Co**	**Cr**	**Mn**	**Ni**	**Al**	**Si**
Ca	1	0.236	**0.994**	**0.989**	**0.987**	**0.988**	**0.988**	**0.995**	**0.993**
Mg		1	0.221	0.223	0.217	0.248	0.209	0.233	0.212
Fe			1	**0.998**	**0.994**	**0.995**	**0.993**	**0.999**	**0.993**
Co				1	**0.996**	**0.998**	**0.994**	**0.995**	**0.986**
Cr					1	**0.992**	**0.992**	**0.993**	**0.983**
Mn						1	**0.991**	**0.994**	**0.984**
Ni							1	**0.991**	**0.982**
Al								1	**0.996**
Si									1

(**a**)

Table 9. *Cont.*

Dumbéa Bay									
	Ca	**Mg**	**Fe**	**Co**	**Cr**	**Mn**	**Ni**	**Al**	**Si**
Ca	1	0.688	0.702	0.701	0.604	**0.826**	0.655	0.772	0.734
Mg		1	0.484	0.468	0.419	0.497	0.461	0.514	0.516
Fe			1	**0.998**	**0.985**	**0.946**	**0.988**	**0.992**	**0.997**
Co				1	**0.986**	**0.948**	**0.990**	**0.989**	**0.994**
Cr					1	**0.888**	**0.986**	**0.962**	**0.977**
Mn						1	**0.912**	**0.962**	**0.945**
Ni							1	**0.971**	**0.988**
Al								1	**0.995**
Si									1

(**b**)

St Vincent Bay									
	Ca	**Mg**	**Fe**	**Co**	**Cr**	**Mn**	**Ni**	**Al**	**Si**
Ca	1	0.438	0.542	0.448	0.483	0.450	0.634	0.725	0.552
Mg		1	**0.953**	**0.958**	**0.961**	**0.808**	**0.813**	**0.878**	**0.920**
Fe			1	**0.986**	**0.963**	**0.869**	**0.905**	**0.954**	**0.963**
Co				1	**0.941**	**0.903**	**0.866**	**0.904**	**0.949**
Cr					1	**0.754**	**0.853**	**0.922**	**0.932**
Mn						1	**0.833**	**0.796**	**0.806**
Ni							1	**0.908**	**0.803**
Al								1	**0.948**
Si									1

(**c**)

The geochemical compositions of SPM (Figure 4, Table 8, which differed substantially between the 3 bays, contrast strongly with the average composition of red laterites (Table 10). Comparatively, red laterite showed much lower levels of Ca, Mg and Si (Table 10), being composed principally of Fe with a high proportion of Cr. The concentrations of the other elements in the red laterites were the same order of magnitude as those observed in the SPMs collected in the bays.

Table 10. Mean concentrations (n = 22) of the main elements analysed in the red laterite of the south and west coastal ore sites of New Caledonia.

Concentration (mg·kg^{-1})	**Al**	**Ca**	**Co**	**Cr**	**Fe**	**Mg**	**Mn**	**Ni**	**Si**
Mean	26,566	117	437	19,677	586,760	2560	3887	5760	6920
StDev	3170	69	21	1309	46,928	381	221	939	1803

4.7. Mineralogy

The minerals detected in both fractions ∅ < 40 µm and ∅ > 40 µm were not significantly different between each sampled site; the main difference being that clay minerals were enhanced in the finer fraction. The main minerals detected in the suspended sediments of the 3 bays analysed were: carbonates (calcite, Mg-calcite and aragonite), goethite, talc, serpentine and quartz (Figure 5). Smectite was detected in St Vincent and Boulari Bays, but was not significant in Dumbéa Bay. The peaks of talc and serpentine were less intense in Dumbéa Bay than in the two other bays. In the 3 sites, other detected, but less abundant, minerals were: kaolinite, feldspar, pyroxene, and olivine.

TEM observations were mainly focused on the Ni-bearing minerals found in the bays. Carbonates, quartz, feldspar, biogenic silica (diatom tests) detected by TEM did not contain Ni, according to EDS spectra. Ni was detected in goethite and clay minerals (Figure 6 and Table 11).

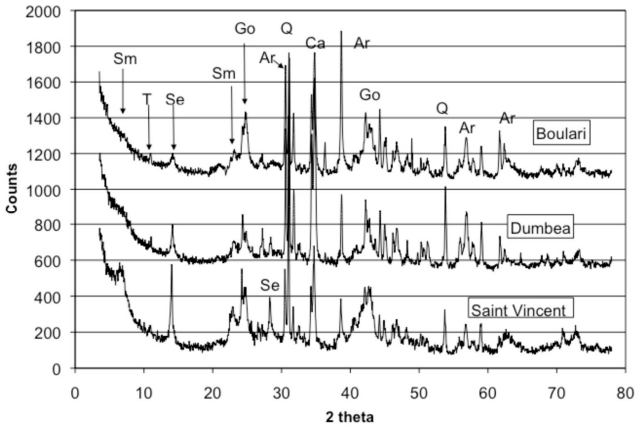

Figure 5. X-ray diffractograms of suspended particulate matter showing the main minerals found in the three study sites (Sm = smectite; T = talc; Se = serpentine; Go = goethite; Ar = aragonite; Q = quartz; Ca = Calcite).

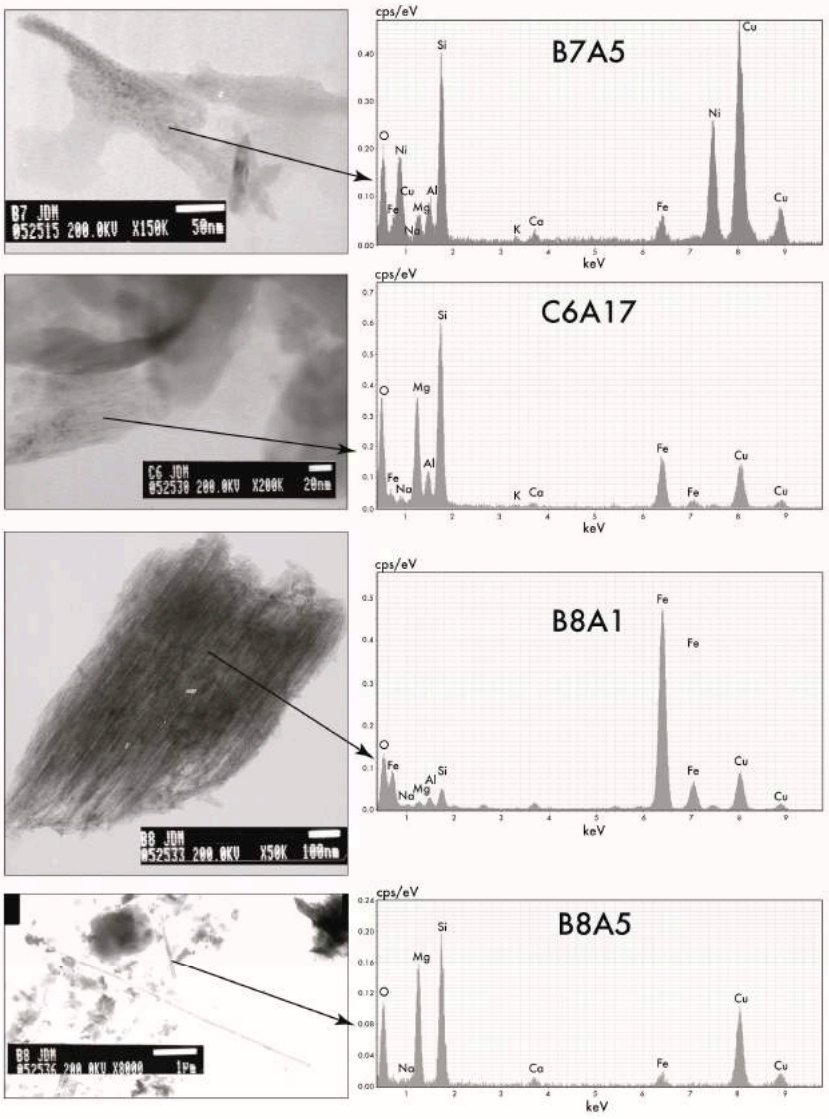

Figure 6. Images and composition determined by transmitted electron microscopy of some particles collected during the study. The chemical formulae are given in Table 11.

Table 11. Chemical formulas of particles (from Figure 6) collected with sequential sediment traps compared to minerals reported in the literature: B7(*A5*) from St Vincent Bay collected on 12 December 2005; B8(*A1*) and B8(*A5*) collected from St Vincent Bay on 6 December, 2005 and C6(*A17*) collected from Dumbéa Bay on 2 December 2005.

Sample	SiO_2 (%)	Al_2O_3	Fe_2O_3	MgO	Cr_2O_3	TiO_2	CaO	Na_2O	K_2O	NiO
B7(*A5*)	42.22	7.11	6.93	4.82	0.21	0.00	1.77	0.17	0.44	36.33
B8(*A1*)	5.77	1.95	86.84	0.58	0.98	0.00	1.75	0.00	0.00	2.14
B8(A5)	51.58	0.12	4.95	39.31	0.29	0.00	2.33	0.42	0.25	0.7
C6(*A17*)	48.57	7.4	16.11	25.49	0.49	0.00	0.84	0.13	0.26	0.72
Goethite *	4.86	3.62	88.53	1.69	0.47	0.00	0.00	0.00	0.00	0.83
Lizardite **	42.20	0.15	2.57	35.00	0.00	0.00	0.00	0.00	0.00	4.50
Antigorite *	49.84	0.26	2.04	46.65	0.64	0.00	0.13	0.00	0.00	0.45
Talc *	66.39	0.00	0.00	32.98	0.00	0.00	0.63	0.00	0.00	0.00
CryptoNont *	51.58	8.42	24.21	12.63	0.00	0.00	0.00	0.00	0.00	3.16
CryptoSapo *	50.53	10.53	13.68	25.26	0.00	0.00	0.00	0.00	0.00	0.00
Nontronite *	55.67	4.26	33.02	3.65	0.23	0.00	0.26	0.00	0.00	2.91
Smectite *	55.59	3.87	33.96	6.58	0.00	0.00	0.00	0.00	0.00	0.00

Notes: * Trescases [50]; ** Manceau et Calas [60]; 0.00 = below detection limit or undetermined.

5. Discussion

5.1. Impact of Mining Activities on the Suspended Sediment Composition

The high proportions in Mg and Si content measured in SPM correspond to the geochemical signature of the exploited saprolitic layers, with Mg and Si concentrations being strongly correlated (R^2 = 0.920). These enrichments result from weathering phenomena occuring in the upper layers, which lead to the formation of laterites [49,50]. Moreover, the Mg concentrations measured in SPM cannot have a predominantly marine origin (aragonite) since the correlation coefficients between Ca and Mg are not significant, except for Dumbéa Bay where biological activity seems more important than in the other two bays. Studies of sedimentary records [19,26] demonstrate the effects of the weathering mechanisms on the marine environment in terms of SPM composition.

The highest Mg and Si concentrations were measured in St Vincent Bay, which is supplied with SPM from the active mining of the La Tontouta basin. There are few differences between Dumbéa and Boulari bays.

5.1.1. Boulari Bay

The strong correlation obtained between all the major and metal elements (R^2 > 0.982), except for Mg, is probably the consequence of the erosion of former mining sites, which have been abandoned for more than 30 years. Indeed, all the correlated elements are present in both the metals-bearing garnierite and the exploitable laterites as the result of the weathering of the ultra-mafic rocks. As for Mg (with Si and Ca), this element is subject to a preferential leaching [50,61], and consequently, the concentration of Mg decreases in the upper lateritic non exploitable layers that are washed away by surface runoff into the lagoon.

Concerning Mg, XRD analysis showed that Mg-bearing minerals may be carbonates or clay minerals. The lack of Ca/Mg correlation and the relatively similar concentrations of these two minerals suggested that Mg is mainly bound to an Mg clay mineral devoid of metals such as talc (Table 9). The good correlation between Ca and metal may be surprising because these elements are not the main metal-bearing minerals transported from the soils (Table 6). Two reasons may explain this correlation: (i) co-precipitation of dissolved metals with coral reef $CaCO_3$ [26,62], suggesting these could have been formed from inputs of SPM from former mines from the beginning of the 20th century until the late 1970s; (ii) Ca is also present in the metal-bearing iron hydroxides and clay minerals (Table 11 and Figure 6).

The high content of metals in SPM collected at the beginning of the sampling period (21 to 22 November) can be correlated with the presence of a large amount of fine particles as suggested by both the Junge parameter (s = 3.7) and the high turbidity (4.7 FTU) (Figure 3). In the days that followed, the increase in the mean diameter (D_{50}) and the decrease in the Junge parameter s demonstrated that a fast physical and chemical aggregation occurred from 24 to 26 November. This aggregation, probably with organic matter, was accompanied by a significant solid dilution in the terrigenous metal concentrations in the SPM (Figure 4). This reduction in the metal concentration was highlighted by the sharp decrease in the distribution coefficients (K_d) of the lateritic metal nickel (Figure 7). Later, aggregates became finer (Figure 3) with a higher specific surface area, and relatively stable concentrations in metals (28 November to 7 December, Figure 7). From 8 December onwards, the flux of trapped SPM was fairly constant; however, a drastic increase in metal concentrations was observed. These results suggest that sedimentation resulted mostly from settling of small particles (∅ < 10 µm).

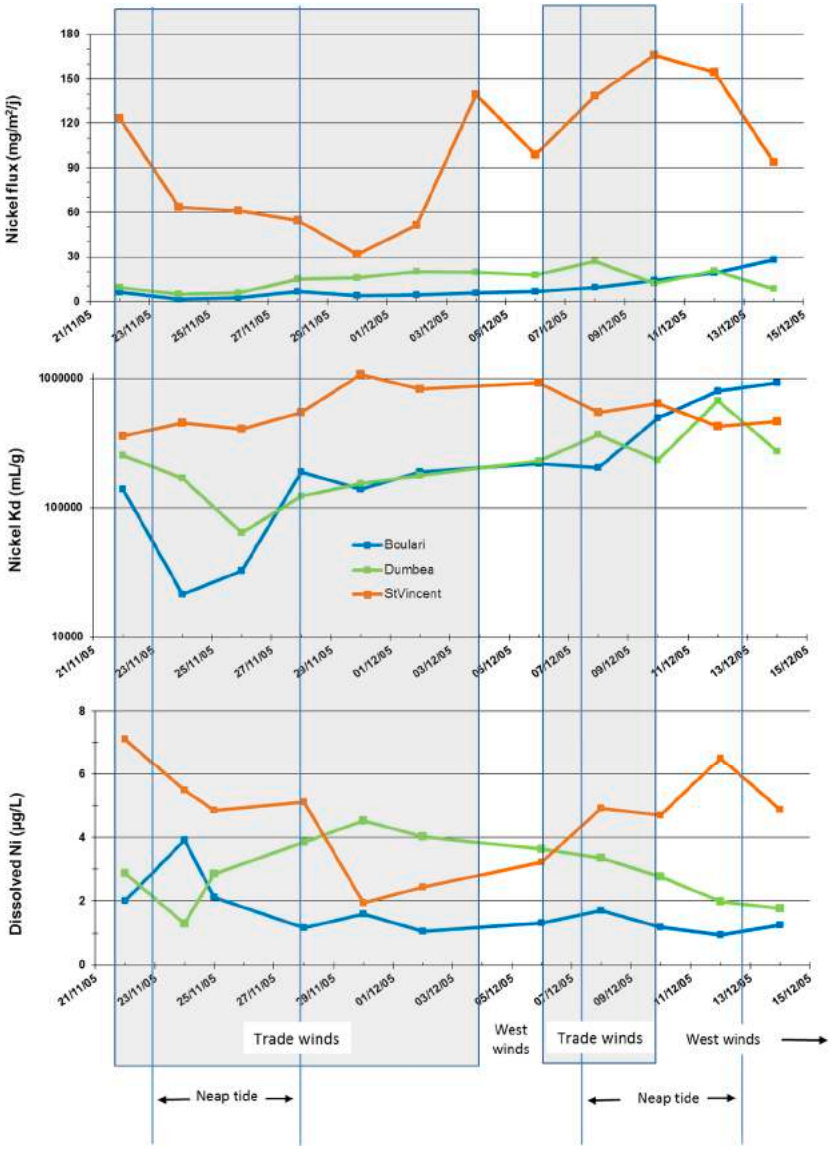

Figure 7. Particulate Ni flux, distribution constant (K_d) of Ni and dissolved concentration of Ni for Boulari, Dumbéa and St Vincent bays over the study period (21 November to 14 December 2005), 3 m above the seabed.

5.1.2. Dumbéa Bay

A strong correlation was observed between the metals and the major elements Si and Fe. For Mg, no correlation was found with the other analysed elements (Table 9). Mg concentrations were similar to those measured in Boulari Bay's SPM but two times lower than the ones observed in St Vincent Bay. This can be interpreted as a low contribution of smectite as shown by the XRD determinations (Figure 5). Regarding Ca, its concentrations in Dumbéa Bay were much higher than in Boulari Bay and is likely to be generated by strong resuspension of carbonated debris from numerous coral reef colonies, by trade winds upstream of the sampling area (Table 8). Indeed, Dumbéa Bay shelters fringing reefs and corals both, alive and dead, on its sea bottom which constitute an important source of carbonates compared to the Coulée River mouth [36]. The metals were only slightly correlated to Ca and this probably reflects the low residence time of seawaters in this bay [63].

The concentrations of metals determined in the SPM were averaged at the beginning of the study period (22 November), and correlated well with the presence of fine particles (s = 3.45); in spite of this, the turbidity remained low (1.3 FTU) (Figures 3 and 4). From the 24 of November onwards, the strong increase in median diameter (D_{50} > 75 µm) and reduction in the Junge parameter (s < 3.36) preceded a strong sedimentation (Figure 3); this increase in particle size led to a reduction in the metal concentrations in the SPM, a phenomenon identified by the decline in the metal distribution constants (K_d), for example Nickel (Figure 7).

The concentrations of particulate metals progressively increased with the reduction in turbidity and median diameter of SPM until the end of the study period. This phenomenon was probably due to the increase in the specific surface area of the particles. The turbidity and especially the SPM flux was correlated with the strength and direction of the wind while the bottom currents were quite low. Hence, the increase in the mass of SPM probably corresponded to the resuspension of carbonate particles originating from the fringing coral patches of shallow depth found south-east of the bay and subjected to trade winds, as shown by the significant increase in Ca concentrations observed (Figure 4). Until 11 December, the trade winds may have been the cause of occasional deposition of aeolian nickel dust generating the high metal concentration increase observed in the SPM; this dust is generated by the nickel processing SLN plant (Figure 1) located on the south-east coast of Dumbéa Bay. After that date, the westerly winds that blew until the end of the study period were probably responsible for the decrease in the concentration of metals (Figures 2 and 4).

5.1.3. St Vincent Bay

Except for Ca, a strong correlation was also observed between the metals and the major elements (Si, Fe and Mg) but the values of R^2 were slightly lower than in Boulari Bay (Table 9). The correlation is well explained by the present-day mining extraction of less weathered lateritic layers enriched with metals. The main difference with Boulari Bay is that a high correlation was observed between Mg and the metals and a lower correlation between Ca and the metals. XRD from St Vincent Bay samples showed the presence of smectite (Figure 5) not observed in Boulari Bay's SPM, which might explain the difference. SPM in St Vincent Bay was also enriched in Fe and Si (and Al, not presented in this paper) compared to the other bays, which might be explained by the higher proportion of clays. The high concentrations of Ca suggested a sizeable contribution of resuspended carbonates as a result of the regular effect of the winds in this shallow bay. Besides this, a significant proportion of former resuspended coral reef debris could explain the lower correlation of Ca with the metals in St Vincent Bay.

Over the study period, some variations were observed in the metal concentrations present in the SPM with no major trends evident and of smaller amplitude than in the 2 other bays. However, a clear correlation between K_d values and the tide was detected, with smaller K_d at neap tides than at spring tides (Figure 7). During spring tides, the resuspension of fine particles and subsequent adsorption of metals (K_d values) increased. Nevertheless, resuspension was not only caused by tides, but also by the wind regimes. Indeed, on the 24 November, an increase in turbidity and in the Junge parameter

and a decrease in D_{50} highlighted a resuspension event at the end of a spring tide period, due to the re-establishment of trade winds (Figures 2, 3 and 7). Aggregation of suspended particles and subsequent deposition followed, but was interrupted by a short resuspension event on the 2 December, likely due to the combined effect of spring tides and waves generated by the wind. This resuspension likely induced the high amount of SPM collected on 4 December. Immediately after a short period of trade winds, aggregation and deposition were observed from 8 December during weak westerly and variable winds, hence promoting the deposition of aggregates.

5.2. Origin of the Minerals

All of the detrital minerals detected were previously described [50] from the weathering profiles of the plateaus. The predominance of clay minerals in St Vincent Bay and Boulari Bay may be attributed to the presence of, respectively, actual and former open cast mines in their watershed which erode the deeper lateritic horizons where clay minerals are for the most part located.

In all the lagoon sediments, carbonates minerals (calcite, aragonite, Mg carbonate), absent in the riverine sediments, provide evidence of sediment resuspension [26]. Other authors [64] also showed that in the different typical bottoms of the lagoon, more than 80% of total sedimentation was linked to deposition of resuspended benthic material. Suspended sediments present in St Vincent Bay contain the same main terrestrial minerals as those detected in the Tontouta River: quartz, goethite, talc, serpentine and smectite. However, smectite and serpentinite may also result from neoformation in the delta area or in the bay itself [26,50,65]; the presence of smectite was higher in St Vincent Bay than in the connected Tontouta River. In tBoulari Bay under trade wind conditions, SPM contained the same minerals as those found in St Vincent Bay except that goethite was more present than clays. During a west wind regime, no clay minerals were detected, and goethite and quartz were the only terrestrial minerals found. During the same period, SPM collected in Dumbéa Bay were characterized by the same minerals as in St Vincent Bay, but clays and goethite contents were lower and samples were dominated by lagoonal material (calcites and aragonite). These results therefore show that the mineralogical composition of suspended sediments in the 3 bays was not strictly related to the composition of sediments transported by their connected rivers. These findings may be due to the presence of authigenic minerals in the bay [26,36] besides detrital particles.

A chemical analysis of a goethite particle referenced as B8A1 (Table 11 and Figure 6) yields similar results to the one given by [50]. Chrysotile (a mineral from the serpentine family) particles forming long acicular tubes were also detected (referenced as C6A17 in Table 11 and Figure 6. This mineral is formed in fractures of the ultrabasites and results from an episode of serpentinisation which concentrates Ni [50]. Compared to other serpentinites analysed previously [50,60], the analysed chrysotile particle had a comparable chemical composition (Table 11). A particle with a different composition (less Al and Mg and more Fe) was also detected (referenced as B8A5 in Table 6 and Figure 6. The composition of this particle is comparable to a poorly crystallized smectite named crypto nontronite [50], which is found in sediments of the deltaic plain and probably originates from diagenesis.

The composition of the particle referenced B7A5 (Table 11 and Figure 6) is more intriguing because of its high Ni content. It could be comparable to a clay mineral like that of a serpentine phase with a high degree of Ni substitution, but such a composition has not yet been reported in New Caledonia. Neoformed serpentine has been identified [26] in the lagoonal sediments of Dumbéa Bay but was not quantified. In addition, the serpentinite was of the Fe (III) type and comparable to the authigenic green phyllosilicates described by Odin et al. [66] in the lagoonal sediments of New Caledonia. Authigenic clay minerals in the Amazon delta have also been described by Michalopoulos and Aller [67], who demonstrated that clay minerals may form rapidly in the sediment pores after liberation of Si from the diatoms and Al and Fe from the oxy-hydroxides derived from the drainage basin. The amount of diatoms or other biogenic silica sources is not known in New Caledonia but their presence has been detected here by TEM. Besides this, goethite is abundant. We therefore support the idea that the high amount of Ni in the clay particle B7A5 resulted from Ni incorporation in the

structure of the clay during diagenesis. This statement implies that part of the dissolved Ni in the lagoon may be fixed by minerals, which limit its dissemination.

6. Conclusions

Our approach combining mineralogy, geochemistry and hydrodynamics allowed us to determine how driving factors are affecting the dynamics of particulate matter in lagoonal ecosystems influenced by the mining industry (Table 12). During the dry season, the concentrations of metal present in the water of the 3 bays were principally governed by the alternating south-easterly (trade winds) and westerly winds. The spring and neap tides do not appear to play a major role in the conditions observed during the study period, except in St Vincent Bay. The driving forces behind the resuspension of particles were similar in Boulari and Dumbéa bays, but clearly differed in St Vincent Bay. This difference can be attributed to the shallow depths present in the bay, the intense mixing and the resulting aggregation mechanisms. This resuspension phenomenon was responsible for the distribution of dissolved and particulate metals in the water column (K_d).

In St Vincent Bay, during periods of intense resuspension, the adsorption of Ni onto many particles was promoted and reversely, the concentration of dissolved nickel increased during the sedimentation phase as a result of calm meteorological conditions. In Boulari Bay, the sedimentation stages and constant Ni concentrations coincided with west weak wind periods allowing the coastal waters blocked along the coast-line by the long trade winds periods to flow off-shore. This phenomenon was reversed in Dumbéa Bay where the redissolution of Ni seemed to be higher during the period of resuspension of the particles richer in carbonates. Table 12 summarizes the effects of the different wind regimes in these 3 bays during the dry season.

Table 12. Effects of wind regimes on the dynamics of the particulate matter in lagoonal ecosystems influenced by the mining industry in New-Caledonia.

Bay	Trade Wind Regime (5–10 Knots)	Light West Wind Regime (<5 Knots)	Coastal Breeze Regime (<5 Knots)
Boulari Bay	Off-shore water inputs, resuspension of SPM transported eastwards and blocked, settling in-shore	Drainage of blocked coastal waters toward off-shore (westward), SPM aggregation and sedimentation	Settling of a benthic turbid layer and westwards transport of SPM: increase in metal fluxes (dissolved and particulate)
Dumbéa Bay	Resuspension of SPM rich in carbonates debris, followed by sedimentation	Off-shore water inputs low both in SPM and metal content	Sedimentation of SPM and reduction in metal fluxes (dissolved and particulate)
St Vincent Bay	Intense resuspension of SPM by the tide and winds over shallow water, then settling and high particulate metal flux	Sedimentation of a small fraction of SPM, reduction in metal fluxes	Important persistence of resuspension of SPM: high metal fluxes (dissolved and particulate)

In terms of environmental impact, the amounts of lateritic particles that have accumulated over time can modify the geochemical equilibriums in the water column, particularly in shallow and sheltered bays. Reducing the concentration of SPM injected into the lagoon seems essential to limit the effects of the bio-accumulation in exposed marine organisms, for example, dissolved Ni, up to 7 $\mu g \cdot L^{-1}$ in St Vincent Bay (vs. 2 $\mu g \cdot L^{-1}$ in Boulari Bay) correspond to the higher particulate Ni fluxes of 170 $mg \cdot m^{-2} \cdot d^{-1}$ observed in the bay.

Acknowledgments: This work was supported by the Institut de Recherche pour le Développement. The authors are grateful to the diving IRD team (J.L. Menou, E. Folcher and C. Jeoffroy), the R/V Captains (M. Clarque, S. Tereua and N. Colombani), Alain Belhandouz and Jean Pierre Lamoureux for their assistance in the field trips and sample collections.

Author Contributions: Jean Michel Fernandez, Jean Dominique Meunier and Sylvain Ouillon conceived and designed the experiments; Jean Michel Fernandez, Benjamin Moreton performed the experiments;

Jean Michel Fernandez, Benjamin Moreton, Pascal Douillet, Olivier Grauby, Jean Dominique Meunier and Sylvain Ouillon analysed the data; Jean Michel Fernandez, Jean Dominique Meunier and Sylvain Ouillon wrote the paper.

Conflicts of Interest: The authors declare no conflict of interest.

References

1. Labrosse, P.; Fichez, R.; Farman, R.; Adams, T. New Caledonia. In *Seas at the Millenium, an Environmental Evaluation*; Sheppard, C., Ed.; Elsevier: Amsterdam, The Netherlands, 2000; Volume 2, pp. 723–736.
2. Pandolfi, J.M.; Bradbury, R.H.; Sala, E.; Hughes, T.P.; Bjorndal, K.A.; Cooke, R.G.; McArdle, D.; McClenachan, L.; Newman, M.J.H.; Paredes, G.; et al. Global trajectories of the long-term decline of coral reef ecosystems. *Science* **2003**, *301*, 955–958. [CrossRef] [PubMed]
3. Doney, S.C. The growing human footprint on coastal and open-ocean biogeochemistry. *Science* **2010**, *328*, 1512–1516. [CrossRef] [PubMed]
4. Burke, L.; Reytar, K.; Spalding, M.; Perry, A. *Reefs at Risk Revisited*; World Resources Institute: Washington, DC, USA, 2011; Available online: http://pdf.wri.org/reefs_at_risk_revisited.pdf (accessed on 3 January 2017).
5. Maina, J.; McClanahan, T.R.; Venus, V.; Ateweberhan, M.; Madin, J. Global gradients of coral exposure to environmental stresses and implications for local management. *PLoS ONE* **2011**, *6*, e23064. [CrossRef] [PubMed]
6. Brodie, J.E.; Kroon, F.J.; Schaffelke, B.; Wolanski, E.C.; Lewis, S.E.; Devlin, M.J.; Bohnet, I.C.; Bainbridge, Z.T.; Waterhouse, J.; Davis, A.M. Terrestrial pollutant runoff to the Great Barrier Reef: An update of issues, priorities and management responses. *Mar. Poll. Bull.* **2012**, *65*, 81–100. [CrossRef] [PubMed]
7. De'ath, G.; Fabricius, K.E.; Sweatman, H.; Puotinen, M. The 27-year decline of coral cover on the Great Barrier Reef and its causes. *PNAS* **2012**, *109*, 17995–17999. [CrossRef] [PubMed]
8. Erftemeijer, P.L.A.; Riegl, B.; Hoeksema, B.W.; Todd, P.A. Environmental impacts of dredging and other sediment disturbances on corals: A review. *Mar Poll. Bull.* **2012**, *64*, 1737–1765. [CrossRef] [PubMed]
9. Morrison, R.J.; Denton, G.R.W.; Bale Tamata, U.; Grignon, J. Anthropogenic biogeochemical impacts on coral reefs in the Pacific Islands-An overview. *Deep-Sea Res. II* **2013**, *96*, 5–12. [CrossRef]
10. Myers, N.; Mittermeier, R.A.; Mittermeier, C.G.; da Fonseca, G.A.B.; Kent, J. Biodiversity hotspots for conservation priorities. *Nature* **2000**, *403*, 853–858. [CrossRef] [PubMed]
11. Alongi, D.M. Present state and future of the world's mangrove forests. *Environ. Conserv.* **2002**, *29*, 331–349. [CrossRef]
12. Bouchet, P.; Lozouet, P.; Maestrati, P.; Heros, V. Assessing the magnitude of species richness in tropical marine environments: Exceptionally high numbers of molluscs at a New Caledonia site. *Biol. J. Linn. Soc.* **2002**, *75*, 421–436. [CrossRef]
13. Nagelkerken, I.; Blaber, S.J.M.; Bouillon, S.; Green, P.; Haywood, M.; Kirton, L.G.; Meynecke, J.O.; Pawlik, J.; Penrose, H.M.; Sasekumar, A.; et al. The habitat function of mangroves for terrestrial and marine fauna: A review. *Aquat. Bot.* **2008**, *89*, 155–185. [CrossRef]
14. Adjeroud, M.; Fernandez, J.M.; Caroll, A.G.; Harrison, P.L.; Penin, L. Spatial patterns and recruitment processes of coral assemblages among contrasting environmental conditions in the southwestern lagoon of New Caledonia. *Mar. Poll. Bull.* **2010**, *61*, 375–386. [CrossRef] [PubMed]
15. Losfeld, G.; L'Huillier, L.; Fogliani, B.; Jaffré, T.; Grison, C. Mining in New Caledonia: Environmental stakes and restoration opportunities. *Environ. Sci. Pollut. Res.* **2015**, *22*, 5592–5607. [CrossRef] [PubMed]
16. Hédouin, L.; Bustamante, P.; Fichez, R.; Warnau, M. The tropical brown alga Lobophora variegate as a bioindicator of mining contamination in the New Caledonia lagoon: A field transplantation study. *Mar. Environ. Res.* **2008**, *66*, 438–444. [CrossRef] [PubMed]
17. Metian, M.; Bustamante, P.; Hédouin, L.; Warnau, M. Accumulation of nine metals and one metalloid in the tropical scallop Comptopallium radula from coral reefs in New Caledonia. *Environ. Pollut. (Oxford, UK)* **2008**, *152*, 543–552. [CrossRef] [PubMed]
18. Hédouin, L.; Bustamante, P.; Churlaud, C.; Pringault, O.; Fichez, R.; Warnau, M. Trends in concentrations of selected metalloid and metals in two bivalves from the SW lagoon of New Caledonia. *Ecotoxicol. Environ. Saf.* **2009**, *72*, 372–381. [CrossRef] [PubMed]

19. Debenay, J.P.; Fernandez, J.M. Benthic foraminifera records of complex anthropogenic environmental changes combined with geochemical data in a tropical bay of New Caledonia. *Mar. Poll. Bull.* **2009**, *59*, 311–322. [CrossRef] [PubMed]
20. Bonnet, X.; Briand, M.; Brischoux, F.; Letourneur, Y.; Fauvel, T.; Bustamante, P. Anguilliform fish reveal large scale contamination by mine trace elements in the coral reefs of New Caledonia. *Sci. Total Environ.* **2014**, *470–471*, 876–882. [CrossRef] [PubMed]
21. Cuif, M.; Kaplan, D.M.; Lefèvre, J.; Faure, V.M.; Caillaud, M.; Verley, P.; Vigliola, L.; Lett, C. Wind-induced variability in larval retention in a coral reef system: A biophysical modelling study in the South-West Lagoon of New Caledonia. *Prog. Oceanogr.* **2014**, *122*, 105–115. [CrossRef]
22. Gilbert, A.; Heintz, T.; Hoeksema, B.W.; Benzoni, F.; Fernandez, J.M.; Fauvelot, C.; Andrefouet, S. Endangered New Caledonian endemic mushroom coral Cantharellus noumeae in turbid, metal-rich, natural and artificial environments. *Mar. Poll. Bull.* **2015**, *100*, 359–369. [CrossRef] [PubMed]
23. Heintz, T.; Haapkylä, J.; Gilbert, A. Coral health on reefs near mining sites in New Caledonia. *Dis. Aquat. Org.* **2015**, *115*, 165–173. [CrossRef] [PubMed]
24. Dugas, F. La sedimentation en baie de St Vincent (Côte ouest de la Nouvelle-Caledonie). In *Cah. ORSTOM, ser. Géol.*; Office de la recherche scientifique et technique outre-mer (ORSTOM): Paris, France, 1974; Volume VI, pp. 41–62.
25. Bird, E.C.F.; Dubois, J.P.; Iltis, J.A. *The Impact of Opencast Mining on the Rivers and Coasts of New Caledonia*; The United Nation University: Shibuya, Japan, 1984; Available online: http://archive.unu.edu/unupress/unupbooks/80505e/80505E00.htm (accessed on 9 May 2017).
26. Ambatsian, P.; Fernex, F.; Bernant, M.; Parron, C.; Lecolle, J. High metal inputs to close seas: The New-Caledonia Lagoon. *J. Geochem. Explor.* **1997**, *59*, 59–74. [CrossRef]
27. Fernandez, J.-M.; Ouillon, S.; Chevillon, C.; Douillet, P.; Fichez, R.; Le Gendre, R. A combined modelling and geochemical study of the fate of terrigenous inputs from mixed natural and mining sources in a coral reef lagoon (New Caledonia). *Mar. Poll. Bull.* **2006**, *52*, 320–331. [CrossRef] [PubMed]
28. Fichez, R.; Adjeroud, M.; Bozec, Y.M.; Breau, L.; Chancerelle, Y.; Chevillon, C.; Douillet, P.; Fernandez, J.M.; Frouin, P.; Kulbicki, M.; et al. A review of selected indicators of particle, nutrient and metal input in coral reef lagoon systems. *Aquat. Living Res.* **2005**, *18*, 125–147. [CrossRef]
29. Grenz, C.; Le Borgne, R.; Fichez, R.; Torreton, J.P. Tropical lagoon multidisciplinary investigations: An overview of the PNEC New Caledonia pilot site. *Mar. Poll. Bull.* **2010**, *61*, 267–268. [CrossRef] [PubMed]
30. A collective of 75 authors. *Atlas de la Nouvelle Calédonie*, IRD ed.; Institut de Recherche pour le Développement (IRD): Marseille, France, 2013; ISBN: 978-2-7099-1740-7.
31. Breau, L. Extractions Séquentielles et Analyses de Métaux dans une Carotte de Sédiments Lagonaires Datée: Mise en Evidence de L'évolution des Apports Terrigènes Liée aux Activités Humaines au Cours des 150 Dernières Années. Master's Thesis, University Aix-Marseille II, Marseille, France, 1998.
32. Magand, O. Contribution à la Modélisation du Transport de la Matière Particulaire dans le Lagon Sud-Ouest de Nouvelle-Calédonie: Etude des flux, Détermination des Signatures Minéralogiques et Evolution Spatiale. Master's Thesis, University Perpignan, Perpignan, France, 1998.
33. Magand, O. Recherche et Définition des Signatures Géochimiques (Métaux Lourds et Lanthanides) des Sources Terrigènes du Lagon Sud-Ouest de Nouvelle-Calédonie. Master's Thesis, University Aix-Marseille II, Marseille, France, 1999.
34. Fernandez, J.-M.; Moreton, B.; Fichez, R.; Breau, L.; Magand, O.; Badie, C. Advantages of combining ^{210}Pb and geochemical signature determinations in sediment record studies, application to coral reef lagoon environments. In *Environmental Changes and Radioactive Tracers*, IRD ed.; Fernandez, J.-M., Fichez, R., Eds.; Institut de Recherche pour le Développement (IRD): Paris, France, 2002; pp. 187–200.
35. Moreton, B.M.; Fernandez, J.-M.; Dolbecq, M.B.D. Development of a field preconcentration/elution unit for routine determination of dissolved metal concentrations by ICP-OES in marine waters: Application for monitoring of the New Caledonia lagoon. *Geostand. Geoanal. Res.* **2009**, *33*, 205–218. [CrossRef]
36. Ouillon, S.; Douillet, P.; Lefebvre, J.P.; Le Gendre, R.; Jouon, A.; Bonneton, P.; Fernandez, J.M.; Chevillon, C.; Magand, O.; Lefèvre, J.; et al. Circulation and suspended sediment transport in a coral reef lagoon: The southwest lagoon of New Caledonia. *Mar. Poll. Bull.* **2010**, *61*, 269–296. [CrossRef] [PubMed]

37. Fichez, R.; Chifflet, S.; Douillet, P.; Gérard, P.; Gutierrez, F.; Jouon, A.; Ouillon, S.; Grenz, C. Biogeochemical typology and temporal variability of lagoon waters in a coral reef ecosystem subject to terrigeneous and anthropogenic inputs (New Caledonia). *Mar. Poll. Bull.* **2010**, *61*, 309–322. [CrossRef] [PubMed]
38. Douillet, P. Tidal dynamics of the south-west lagoon of New Caledonia: Observations and 2D numerical modelling. *Oceanol. Acta* **1998**, *21*, 69–79. [CrossRef]
39. Douillet, P.; Ouillon, S.; Cordier, E. A numerical model for fine suspended sediment transport in the south-west lagoon of New-Caledonia. *Coral Reefs* **2001**, *20*, 361–372. [CrossRef]
40. Jouon, A.; Lefebvre, J.P.; Douillet, P.; Ouillon, S.; Schmied, L. Wind wave measurements and modelling in a fetch-limited semi-enclosed lagoon. *Coast. Eng.* **2009**, *56*, 599–608. [CrossRef]
41. Andréfouët, S.; Cabioch, G.; Flamand, B.; Pelletier, B. A reappraisal of the diversity of geomorphological and genetic processes of New Caledonian coral reefs: A synthesis from optical remote sensing, coring and acoustic multibeam observations. *Coral Reefs* **2009**, *28*, 691–707. [CrossRef]
42. Lillie, A.R.; Brothers, R.N. The geology of New-Caledonia. *N. Zeal. J. Geol. Geophys.* **1970**, *13*, 159–167. [CrossRef]
43. Paris, J.P. *Les Ressources Minérales de Nouvelle-Calédonie*; Mémoire 113, Bureau de Recherches Géologiques et Minières (BRGM): Orléans, France, 1981.
44. Antheaume, B. Chronique de l'Atlas de la Nouvelle-Calédonie, un bilan méthodologique et critique. Cahiers ORSTOM. *Série Schum* **1981**, *18*, 389–398.
45. Paris, J.P. Gîtes minéraux et substances utiles. In *Atlas de Nouvelle-Calédonie*; Sautter, G., Ed.; ORSTOM: Paris, France, 1981.
46. Perrier, N.; Ambrosi, J.P.; Colin, F.; Gilkes, R.J. Biogeochemistry of a regolith: The new Caledonian Koniambo ultramafic massif. *J. Geochem. Explor.* **2006**, *88*, 54–58. [CrossRef]
47. Dublet, G.; Fandeur, D.; Juillot, F.; Morin, G.; Ambrosi, J.P.; Fritsch, E.; Brown, G.E., Jr. Ni speciation in a New Caledonian lateritic regolith: A quantitative X-ray absorption spectroscopy investigation. *Geochim. Cosmochim. Acta* **2012**, *95*, 119–133. [CrossRef]
48. Dublet, G.; Juillot, F.; Morin, G.; Fritsch, E.; Noel, V.; Brest, J.; Brown, G.E., Jr. XAS evidence for Ni sequestration by siderite in a latéritic Ni-deposit from New Caledonia. *Am. Miner.* **2014**, *99*, 225–234. [CrossRef]
49. Dublet, G.; Juillot, F.; Morin, G.; Fritsch, E.; Fandeur, D.; Brown, G.E., Jr. Goethite aging explains Ni depletion in upper units of ultramafic lateritic ores. *Geoch. Cosmoch. Acta* **2015**, *160*, 1–15. [CrossRef]
50. Trescases, J.J. L'évolution Geochimique Supergène des Roches Ultrabasiques en Zone Tropicale. Formation des Gisements Nickélifères de Nouvelle-Calédonie. Ph.D. Thesis, University Louis Pasteur, Strasbourg, France, 1973.
51. Pesin, E.; Blaize, S.; Lacoste, D. *Atlas Climatique de la Nouvelle Calédonie*; Météo France: Nouméa, New Caledonia, 1995.
52. Baltzer, F.; Trescases, J.J. Erosion, transport et sédimentation liés aux cyclones tropicaux dans les massifs d'ultrabasites de Nouvelle-Calédonie. *Cahiers ORSTOM Série Géologie III* **1973**, *2*, 221–244.
53. Dugas, F.; Debenay, J.P. *Carte Sédimentologique et carte Annexe du Lagon de Nouvelle Calédonie au 1/50000—Mont Dore, Tontouta, Prony, Nouméa*; Notices explicatives n° 76, 86, 91 and 95; ORSTOM: Paris, France, 1982.
54. Heussner, S.; Ratti, C.; Carbonne, J. The PPS3 times series sediment trap and the trap sample processing techniques used during the ECOMARGE experiment. *Cont. Shelf Res.* **1990**, *10*, 943–958. [CrossRef]
55. Jouon, A.; Ouillon, S.; Douillet, P.; Lefebvre, J.P.; Fernandez, J.-M.; Mari, X.; Froidefond, J.M. Spatio-temporal variability in suspended particulate matter concentration and the role of aggregation on size distribution in a coral reef lagoon. *Mar. Geol.* **2008**, *256*, 36–48. [CrossRef]
56. Lefebvre, J.-P.; Ouillon, S.; Vinh, V.D.; Arfi, R.; Panche, J.-Y.; Mari, X.; Thuoc, C.V.; Torreton, J.P. Seasonal variability of cohesive sediment aggregation in the Bach Dang-Cam Estuary, Haiphong (Vietnam). *Geo-Mar. Lett.* **2012**, *32*, 103–121. [CrossRef]
57. Mobley, C.D. *Light and Water Radiative Transfer in Natural Water*; Academic Press: San Diego, CA, USA, 1994.
58. Pinet, S.; Martinez, J.-M.; Ouillon, S.; Lartiges, B.; Villar, R.E. Variability of apparent and inherent optical properties of sediment-laden waters in large river basins—Lessons from in situ measurements and bio-optical modeling. *Opt. Express* **2017**, *25*, A283–A310. [CrossRef] [PubMed]
59. Cliff, G.; Lorimer, G.W. The quantitative analysis of thin specimens. *J. Microsc.* **1975**, *103*, 203–207. [CrossRef]

60. Manceau, A.; Calas, G. heterogneous distribution of nickel in hydrous silicates from New Caledonia ore deposits. *Am. Miner.* **1985**, *70*, 549–558.
61. Pelletier, B. Serpentines in Nickel Silicate Ore from New-Caledonia. In Proceedings of the Publications-Australasian Institute of Mining and Metallurgy, Kalgoolie, Australia, 27–29 November 1996; Volume 27–29, pp. 197–206.
62. Wartel, M.; Skirer, M.; Auger, T.; Boughriet, A. Interaction of manganese II with carbonates in sea water: Assessment of the solubility product of $MnCO_3$ and Mn distribution coefficient between the liquid phase and $CaCO_3$ particles. *Mar. Chem.* **1990**, *29*, 99–117. [CrossRef]
63. Jouon, A.; Douillet, P.; Ouillon, S.; Fraunié, P. Calculations of hydrodynamic time parameters in a semi-opened coastal zone using a 3D hydrodynamic model. *Cont. Shelf Res.* **2006**, *26*, 1395–1415. [CrossRef]
64. Clavier, J.; Chardy, P.; Chevillon, C. Sedimentation of particulate matter in the South-west lagoon of New Caledonia: Spatial and Temporal Patterns. *Est. Coast. Shelf Sci.* **1995**, *40*, 281–294. [CrossRef]
65. Baltzer, F. *Géodynamique de la Sédimentation et Diagénèse Précoce en Domaine Ultrabasique, Nouvelle-Calédonie*; ORSTOM: Paris, France, 1982.
66. Odin, G.S. *Green Marine Clays*; Elsevier: Amsterdam, The Netherlands, 1988.
67. Michalopoulos, P.; Aller, R.C. Rapid clay mineral formation in Amazon delta sediments: Reverse weathering and oceanic elemental cycles. *Science* **1995**, *270*, 614–617. [CrossRef]

water

MDPI

Article

Modelling Hydrology and Sediment Transport in a Semi-Arid and Anthropized Catchment Using the SWAT Model: The Case of the Tafna River (Northwest Algeria)

Amin Zettam [1,2,*], Amina Taleb [1], Sabine Sauvage [2], Laurie Boithias [3], Nouria Belaidi [1] and José Miguel Sánchez-Pérez [2]

1 Laboratoire d'Écologie et Gestion des Ecosystmes Naturels (LECGEN), University of Tlemcen, 13000 Tlemcen, Algeria; taleb_14@hotmail.com (A.T.); belaidi_nr@yahoo.fr (N.B.)
2 Laboratoire Ecologie Fonctionnelle et Environnement (EcoLab), Université de Toulouse, CNRS, INPT, UPS, 31400 Toulouse, France; sabine.sauvage@univ-tlse3.fr (S.S.); jose-miguel.sanchez-perez@univ-tlse3.fr (J.M.S.-P.)
3 Géosciences Environnement Toulouse, Université de Toulouse, CNES, CNRS, IRD, UPS, 31400 Toulouse, France; laurie.boithias@ird.fr
* Correspondence: zettam.amine@gmail.com; Tel.: +213-551-71-5309

Academic Editor: Sylvain Ouillon
Received: 15 December 2016; Accepted: 7 March 2017; Published: 14 March 2017

Abstract: Sediment deposits in North African catchments contribute to around 2%–5% of the yearly loss in the water storage capacity of dams. Despite its semi-arid climate, the Tafna River plays an important role in Algeria's water self-sufficiency. There is continuous pressure on the Tafna's dams to respond to the demand for water. The Soil and Water Assessment Tool (SWAT) was used to evaluate the contribution of different compartments in the basin to surface water and the dams' impact on water and sediment storage and its flux to the sea in order to develop reservoir management. The hydrological modelling fitted well with the observed data (Nash varying between 0.42 and 0.75 and R^2 varying between 0.25 and 0.84). A large proportion of the surface water came from surface runoff (59%) and lateral flow (40%), while the contribution of groundwater was insignificant (1%). SWAT was used to predict sediments in all the gauging stations. Tafna River carries an average annual quantity of 2942 t·yr^{-1} to the Mediterranean Sea. A large amount of water was stored in reservoirs (49%), which affected the irrigated agricultural zone downstream of the basin. As the dams contain a large amount of sediment, in excess of 27,000 t·yr^{-1} (90% of the sediment transported by Tafna), storage of sediment reduces the lifetime of reservoirs.

Keywords: soil erosion; SWAT; water scarcity; sediment transport modelling; Tafna catchment; North Africa

1. Introduction

As in most semi-arid and arid regions, which cover over 40% of the world's land surface, water resource management in the Middle East and North Africa is more complex than it is in humid zones due to the lack of perennial rivers and other readily available water sources [1]. The population of the Middle East and North Africa was 432 million in 2007, and is projected to reach nearly 700 million by 2050 [2]. This alone would lead to a 40% drop in per capita water availability in the region by 2050 [3]. In Maghreb (Northwest Africa), which has only scarce water resources, most damage is associated with the loss of alluvial sediments from the catchment and subsequent dam siltation [4]. The study of semi-arid North African environments is problematic for several reasons. These include data gaps and considerable anthropic pressures coupled with increasingly intense dry seasons [5].

As in all North African countries, water in Algeria is one of its most valuable resources because it is one of the poorest countries in the region in terms of water potential [6]. Algeria's rivers transport a large quantity of sediments [7,8]. The sediment deposited in Algerian dams is estimated to be 20×10^6 $m^3 \cdot yr^{-1}$ [9]. Competition for water between agriculture, industry, and drinking water supply—accentuated by a drought in Algeria—has shown the need for greater attention to be paid to water [10] and for it to be managed at the large basin scale [11]. Surface water resources in Algeria are evaluated to be approximately 8376 billion m^3 for an average year [12]. These water resources in Algeria are characterized by wide variability—the resources for the last nine years have been significantly below this average [13]. In this context, several dams were built in Algeria to ensure water resources for the supply of drinking water to all its cities and allowed approximately 12,350 km^2 of irrigated land to be developed [12–14]. However, dam reservoirs lose about 20×10^6 to 30×10^6 m^3 of water storage every year [15,16].

Despite its semi-arid climate, the Tafna catchment plays an important role in water self-sufficiency in northwest Algeria [17]. There is always huge pressure on Tafna dams, which have a capacity of 398×10^6 m^3, in order to meet the demand expressed specifically and continuously by the largest cities of northwest Algeria (Oran, which is Algeria's second largest city with 10,000 $m^3 \cdot day^{-1}$; Sidi Bel Abbes, 20,000 $m^3 \cdot day^{-1}$; Ain Temouchent, 15,000 $m^3 \cdot day^{-1}$; and Tlemcen, 37,000 $m^3 \cdot day^{-1}$) [12,17].

The deposits of sediment in Maghreb contribute about 2%–5% of the yearly loss in the dams' water storage capacity. In Algeria, the intercepted runoff in dams and weirs hold about 5.2 billion m^3, which makes up 42% of total runoff [18]. The construction of dams has raised questions about their hydrological impacts on water resources at basin scale, especially where there are conflicts between upstream and downstream water users [19,20].

Hydrological models serve many purposes [21]. The accuracy and skill of flow prediction models can have a direct impact on decisions with regard to water resources management. Various statistical and conceptual streamflow prediction models have been developed to help urban planners, administrators, and policy makers make better and more informed decisions [22]. Hydrological models including distributed physically-based model—such as SHE [23], TOPMODEL [24], HEC [25], VIC [26], IHDM [27], and WATFLOOD [28]—are capable of simulating temporal-spatial variations in hydrological processes and assist in the understanding of mechanisms of influence behind land use impacts [29].

Out of the distributed physically-based models, the Soil and Water Assessment Tool (SWAT) [30] has been used widely to assess agricultural management practices [31], help identify pollution sources and contaminant fate [32,33], evaluate the impacts of climate change [34], and assess the hydrology and sediment transfer in various catchments [35,36]. Many authors have applied SWAT in semi-arid areas, such as southeast Africa [37], southern Australia [38], in the Mediterranean coastal basin in Spain [39], and in North Africa [40,41]. Some authors have focused on the impact of dams on water balance using SWAT because of its reservoir module [42,43], as shown in China [44] and Pakistan [45].

By applying the SWAT model, which is not widely used in Algeria, to a semi-arid anthropized catchment, the objectives of this study were: (1) to evaluate the contribution of the different compartments of the basin to surface water; (2) to evaluate the impact of the construction of dams in semi-arid catchments on water and sediment storage and (3) on suspended sediment flux to the sea, in order to facilitate, plan, and assess the management of these important reservoirs, which are a crucial part of water self-sufficiency in semi-arid regions.

2. Materials and Methods

To achieve these objectives, the study was divided into two parts. First a model with dams was considered in which hydrology and sediment flux were calibrated on all the gauging stations. Then a model without dams was considered, retaining the same calibration parameters as the first model, which revealed the impact of the installation of this infrastructure on hydrology and sediment flux

in this basin. To verify this method, the flows of the two projects were verified on the basis of the literature published by the Algerian National Agency of Hydrologic Resources [46–48].

2.1. Study Site

The Tafna watershed covers much of western Algeria (Figure 1). The Tafna Wadi is the main stream with a drainage area of 7245 km^2 and elevation varying from sea level to 1100 m.a.s.l. After a 170-km course, the river reaches the Mediterranean Sea near the town of Beni-Saf. It is located between 34°11′ N, 35°19′ N latitude and 0°50′ W, 2°20′ W longitude. The catchment area of the Tafna is divided into two zones that are of a different geological nature: the upstream sector where the river runs in a canyon through Jurassic rocks rich in limestone and dolomite, and the downstream sector where it runs in a tertiary basin characterized by marls covered by recent alluvium [49].

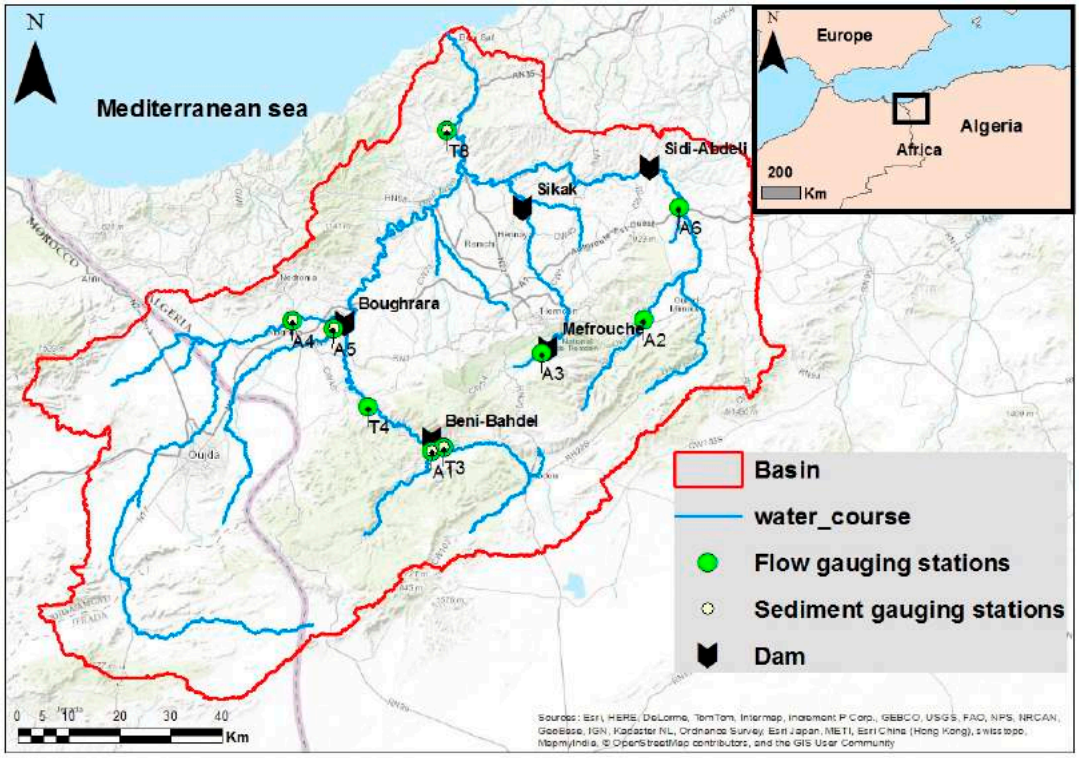

Figure 1. Location of the Tafna River catchment and its dams and gauging stations (A: located in tributaries; T: located in the main watercourse).

The climate is Mediterranean with two main seasons: a long, dry, hot summer-autumn and a winter-spring with abrupt and frequent heavy rainfall. During the summer, most of the streams, especially in their downstream parts, become mostly dry between June and October. The annual average water temperature varies from 11° in winter to 28° in summer [5]. Annual rainfall is between 240 and 688 mm·yr^{-1} [50]. The flow at the watershed outlet ranges from 0 to 108 m^3·s^{-1} [51]. The Tafna River has several tributaries. The most important tributary is the Mouillah Wadi, situated in Maghnia region, which is an industrial area. This tributary is polluted by domestic sewage and industrial effluent from the Moroccan cities of Oujda and El Abbes and the Ouerdeffou Wadi. Another important tributary is the Isser Wadi, but its water supply to the Tafna has decreased significantly since the construction of the Al Izdahar dam, which retains most of the water during the rainy season for irrigation purposes [52]. Five dams have been constructed in the catchment of the Tafna: Beni Bahdel, Meffrouch, Hammam Boughrara, Al Izdahar (Sidi-Abdeli), and Sikkak. Their capacities vary between 15 and 177 million m^3 (Table 1).

According to the Algerian Ministry of Agriculture, agriculture occupies an important place in the catchment of the Tafna, with cereal covering 1699 km^2 (23.6% of the total area), horticulture 342 km^2 (4.75% of the total area) and arboriculture 263 km^2 (3.65% of the total area). The basin has about 1,450,000 inhabitants [53]. The more densely populated areas are the cities of Oujda (Morocco) with 548,280 inhabitants, followed by the city of Tlemcen (Algeria), which has 140,158 inhabitants.

Table 1. Characteristics of the dams built in the Tafna catchment.

Dams	Capacity (Mm^3)	Construction Date	Used for
Beni Bahdel	65.5	1952	Drinking water/irrigation
Hammame Boughrara	177	1998	Drinking water/irrigation
Mefrouche	15	1963	Drinking water
Sikkak	30	2005	Drinking water/irrigation
Al Izdahar (Sidi Abdeli)	110	1988	Drinking water/irrigation

2.2. Discharge and Sediment Monitoring

Tafna's daily discharge and monthly sediment measurement has been monitored since 2003 by the National Agency of Hydrologic Resources (ANRH) at nine hydrometric stations (Figure 1). River discharge was obtained from the water level, which is continuously measured by a limnimetric ladder and float water level recorder using a rating curve. Suspended sediments are defined as the portion of total solids retained by a fiberglass membrane (Whatman GF/F) of 0.6 µm porosity. The sediment collected was weighed after being dried at 105 °C for 24 h. The difference in the weight of the filter before and after filtration allowed the calculation of the suspended sediment concentration based on the volume of water filtered (C, in g·L^{-1}).

2.3. Modelling Approach

2.3.1. The SWAT Model

SWAT was developed at the USDA Agricultural Research Service [30]. It was designed for application in catchments ranging from a few hundred to several thousand square kilometres. The model is semi-distributed: the catchment is first divided into sub-catchments and then into hydrologic response units (HRUs), which represent homogeneous combinations of soil type, land use type, and slope. Any identical combination of these three features is assumed to produce a similar agro-hydrologic response [54].

The Hydrological Component in SWAT

SWAT uses a modified SCS curve number method (USDA Soil Conservation Service, 1972) to compute the surface runoff volume for each HRU. The peak runoff rate is estimated using a modification of the rational method [55]. Daily climatic data are required for calculations. Flow is routed through the channel using a variable storage coefficient method [56].

The hydrologic cycle as simulated by SWAT is based on the water balance equation:

$$SW_t = SW_0 + \sum_{i=1}^{i} \left(R_{day} - Q_{surf} - E_a - W_{seep} - Q_{gw} \right)$$

where SW_t is the final soil water content on day i (mm), SW_0 is the initial soil water content on day i (mm), t is the time (days), R is the amount of precipitation on day i (mm), Q_{surf} is the amount of surface runoff on day i (mm), E_a is the amount of evapotranspiration on day i (mm), W_{seep} is the amount of water entering the vadose zone from the soil profile on day i (mm), and Q_{gw} is the amount of return flow to the stream on day i (mm) [57].

The water balance of dams is given by the following equation:

$$V = V_{stored} + V_{flowin} - V_{flowout} + V_{pcp} - V_{evap} - V_{seep}$$

where V is the volume of water in the impoundment at the end of the day (m^3 H_2O), V_{stored} is the volume of water stored in the water body at the beginning of the day (m^3 H_2O), V_{flowin} is the volume of water entering the water body during the day (m^3 H_2O), $V_{flowout}$ is the volume of water flowing out the water body during the day (m^3 H_2O), V_{pcp} is the volume of the precipitation falling on the water body during the day (m^3 H_2O), V_{evap} is the volume of water removed from the water body by evaporation during the day (m^3 H_2O), and V_{seep} is the volume of water lost from the water body by seepage during the day (m^3 H_2O) [57].

Flow is routed through the channel using a variable storage coefficient method [56] or the Muskingum routing method [57].

Suspended Sediment Modelling Component in SWAT

The sediment from sheet erosion for each HRU is calculated using the modified universal soil loss equation (MUSLE) [58]. Details of the MUSLE equation factors can be found in theoretical documentation of SWAT [59]. Sediment was routed through stream channels using a modification of Bagnold's sediment transport equation [60]. The deposition or erosion of sediment within the channel depends on the transport capacity of the flow in the channel.

2.4. SWAT Data Inputs

The following spatialized data were used in this study: (i) a digital elevation model with a 30 m × 30 m resolution from the US Geological Survey (Figure 2a); (ii) a soil map [61] (Figure 2b); (iii) a land-use map [62] (Figure 2c); (iv) daily climate data between 2000 and 2013 from eight meteorological stations (Figure 2) provided by the Algerian National Office of Meteorology that were used to simulate the reference evapotranspiration in the model using the Hargreaves method because it is the best in semi-arid regions [63]; and (v) daily discharge outflow data for the five Tafna dams provided by the Algerian National Agency for Dams and Transfers (ANBT). Version 2012 of ArcSWAT (Texas Agrilife Research, Usda Agricultural Research Service, Temple, TX, USA) was used to set up the model. The catchment was discretized into 107 sub-basins with a minimum area of 7020 km^2 (Figure 2d) and 1067 HRUs. To measure the impact of the dams, two SWAT projects were undertaken with and without dams, retaining the same parameter values.

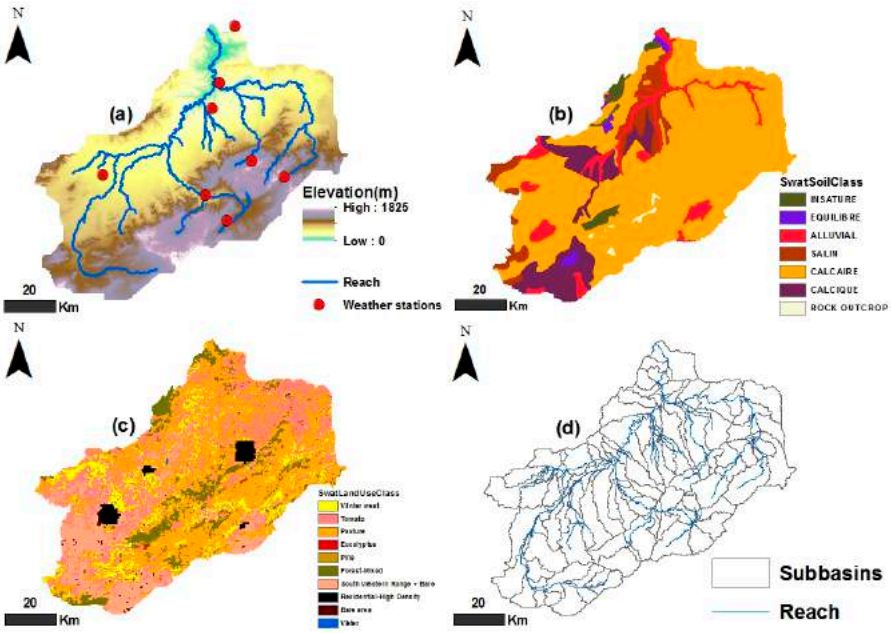

Figure 2. (**a**) 30 m digital elevation model; (**b**) main soils; (**c**) main land uses; and (**d**) SWAT DEM delineated sub-basins of the Tafna catchment

2.5. Model Calibration

In this study, the SUFI-2 (sequential uncertainty fitting, ver. 2) algorithm [64] was used for calibration and sensitivity analysis for flow and sediment output. This program is currently linked to SWAT in the calibration package SWAT-CUP (SWAT calibration uncertainty procedures) (EAWAG, Zurich, Switzerland.). The whole simulation was performed daily from January 2000 to December 2013 (excluding a three-year warm-up from 2000 to 2003). Stream flow was calibrated at a monthly time-step because of the lack of good observed daily data from January 2003 to August 2011, while sediments were calibrated at a daily time-step from January 2003 to December 2006 except for station A5, which was from January 2003 to December 2005. 150 simulations were performed for each gauging station by SWAT-CUP.

2.6. Model Evaluation

The monthly discharge performance of the model was evaluated using the Nash-Sutcliffe efficiency (NSE) index [65] and the coefficient of determination (R^2):

$$\mathrm{NSE} = 1 - \frac{\sum_{i=1}^{n}(O_i - S_i)^2}{\sum_{i=1}^{n}(O_i - \overline{O})^2}$$

$$R^2 = \left\{ \frac{\sum_{i=1}^{n}(O_i - \overline{O})(S_i - \overline{S})}{[\sum_{i=1}^{n}(O_i - \overline{O})^2]^{0.5}[\sum_{i=1}^{n}(S_i - \overline{S})^2]^{0.5}} \right\}$$

where O_i and S_i are the observed and simulated values, n is the total number of paired values, $\overline{O}$ is the mean observed value, and $\overline{S}$ is the mean simulated value.

In this study, monthly NSE was deemed satisfactory at >0.5 [66] and daily and monthly R^2 satisfactory at >0.5 [66].

3. Results

3.1. Discharge and Sediment Calibration

For discharge and sediment calibration, the following parameters, presented in (Table 2), were calibrated.

Table 2. Calibrated parameter values with a ranking of the most sensitive parameters (Rank 1 = most sensitive).

Parameter		Definition	Units	Initial Range	Calibrated Range	Rank
Parameters related to flow	CN2.mgt	SCS runoff curve number for moisture condition II		[35; 98]	[38.5; 94]	3
	SOL_Z.sol	Depth from soil surface to bottom of layer	(mm)	[0; 4500]	[1500; 3500]	16
	SOL_AWC.sol	Soil available water storage capacity	(mm H_2O/mm soil)	[0; 1]	[0.116; 0.169]	7
	SOL_K.sol	Soil conductivity	(mm·h^{-1})	[0; 2000]	[4.71; 180]	14
	ALPHA_BF.gw	Base flow alpha factor characterizes the groundwater recession curve	(days)	[0; 1]	[0.055; 0.975]	4
	GW_DELAY.gw	Groundwater delay: time required for water leaving the bottom of the root zone to reach the shallow aquifer	(days)	[0; 500]	[89.223; 176.363]	13
	GW_REVAP.gw	Groundwater "revap" coefficient: controls the amount of water which evaporates from the shallow aquifer		[0.02; 0.2]	[0.069; 0.191]	9
	REVAPMN.gw	Threshold depth of water in the shallow aquifer for "revap" to occur	(mm)	[0; 1000]	[185; 892.294]	12
	RCHRG_DP.gw	Deep aquifer percolation fraction		[0; 1]	[0.176; 0.673]	2

Table 2. *Cont.*

Parameter		Definition	Units	Initial Range	Calibrated Range	Rank
Parameters related to flow	ESCO.hru	Soil evaporation compensation coefficient		[0; 1]	[0.50; 0.86]	5
	OV_N.hru	Manning's "n" value for overland flow		[0.01; 30]	[0.177; 0.823]	11
	CH_N2.rte	Manning's "n" value for the main channel		[−0.01; 0.3]	[0.01; 0.2]	10
	CH_K2.rte	Effective hydraulic conductivity of main channel	($mm \cdot h^{-1}$)	[−0.01; 500]	[58; 406]	8
	EVRCH.bsn	Reach evaporation adjustment factor		[0.5; 1]	0.669	6
	TRNSRCH.bsn	Fraction of transmission losses from main channel that enter deep aquifer		[0; 1]	0.211	1
	SURLAG.bsn	Surface runoff lag coefficient		[0; 1]	2.15	15
Parameters related to sediment	USLE-K.sol	USLE soil erodibility factor	0.013 ($t \cdot m^2 \cdot hr$)/($m^3 \cdot t \cdot cm$))	[0; 0.65]	0.005	1
	USLE-P.mgt	USLE equation support practice factor		[0; 1]	[0.003; 0.8]	2
	PRF.bsn	Peak rate adjustment factor for sediment routing in the main channel		[0; 1]	0.18	3

For the calibrated parameter set, the average annual rainfall of the total simulation period over the area of the catchment is 364 $mm \cdot yr^{-1}$. The model predicted the potential evapotranspiration to be 1301.4 $mm \cdot yr^{-1}$, and runoff as 26.16 $mm \cdot yr^{-1}$.

In this study, only the monthly calibration of flow without validation was performed because there were several difficulties with calibration due to the poor measurement of daily water flow in the gauging stations (renovations of the limnimetric scales and maintenance of the stations need to be undertaken). The flow was calibrated at nine gauging stations. Monthly simulated discharges were satisfactorily correlated to observations for the calibration periods, except for the A4 station (Figure 3, Table 3). It should be noted that the values of the performance of the model evaluation parameters were more satisfactory in the upstream portion, with NSE varying between 0.5 and 0.75 and R^2 between 0.49 and 0.84, while in the downstream part NSE between 0.42 and 0.59 and R^2 between 0.25 and 0.62 were found.

The hygrogram of the Tafna River modelled by SWAT (Figure 4) showed that a large proportion of surface water came from surface runoff (59%) and lateral flow (40%), while the contribution of groundwater was insignificant (1%).

Table 3. Model performance for the simulation of runoff.

Stations	NSE	R^2
A1	0.67	0.7
A2	0.67	0.7
A3	0.53	0.58
A4	0.42	0.25
A5	0.59	0.62
A6	0.5	0.49
T3	0.75	0.84
T4	0.66	0.73
T8	0.51	0.53

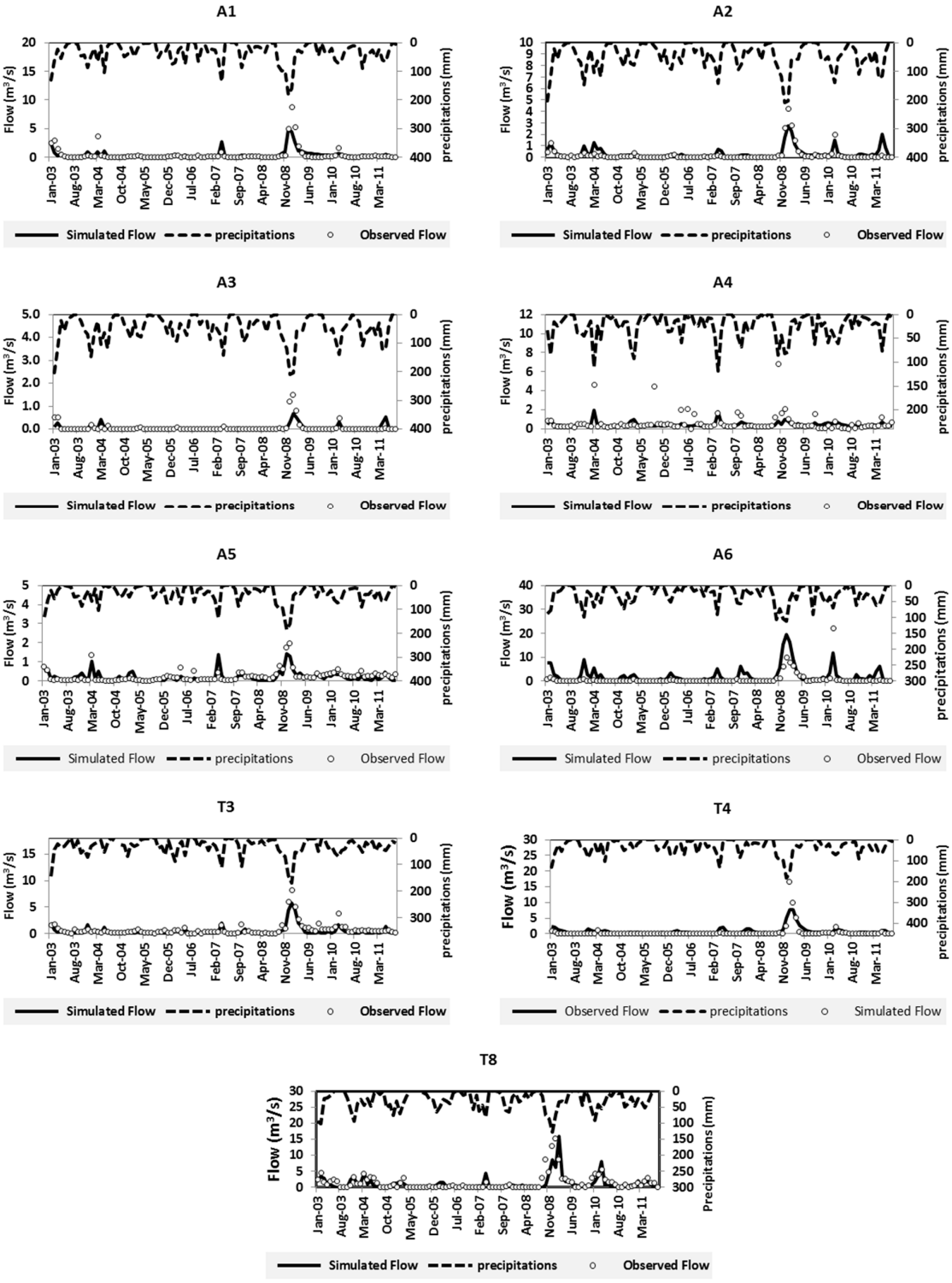

Figure 3. Monthly simulated and observed discharge ($m^3 \cdot s^{-1}$) at the gauging stations (calibration period: January 2003–August 2011).

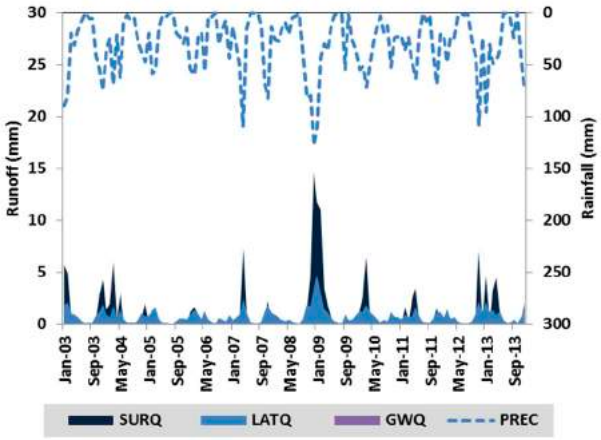

Figure 4. Hygrogram of the Tafna at the outlet modelled by SWAT (SURQ: surface runoff/LATQ: lateral flow/GWQ: groundwater flow/PREC: rainfall).

The results of sediment calibration are shown in Figure 5.

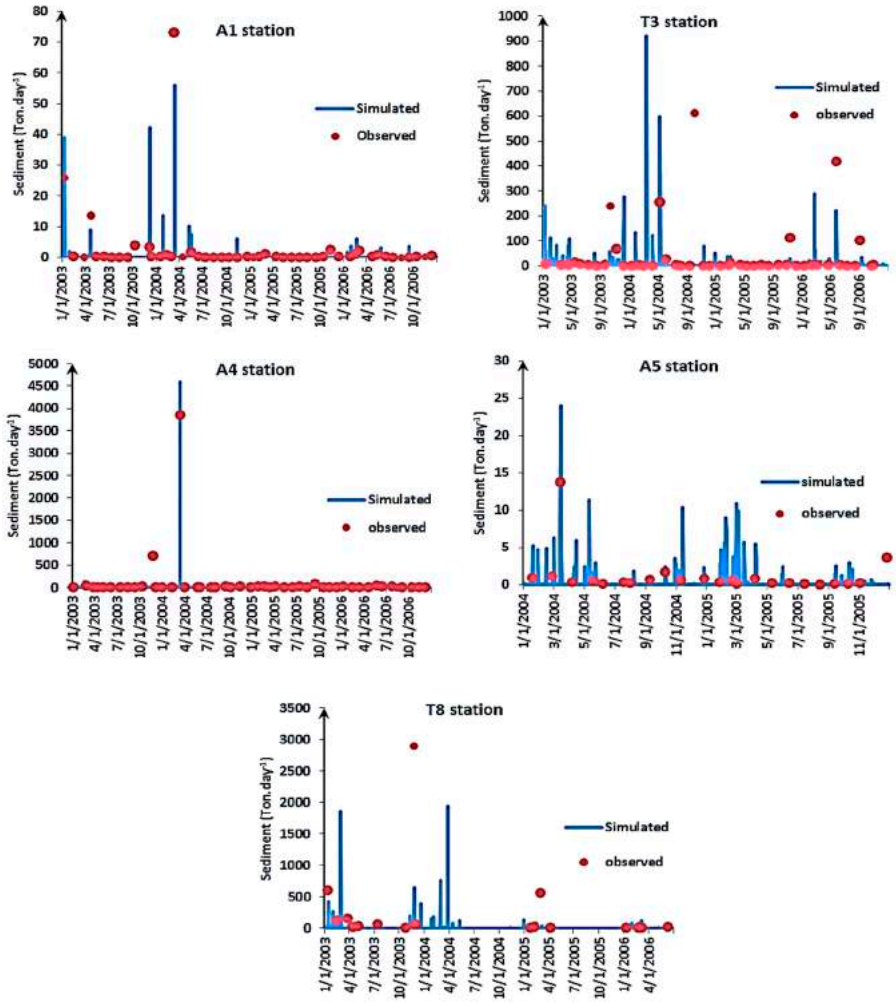

Figure 5. Daily simulated and observed sediment ($t \cdot day^{-1}$) at the gauging sediment stations. (There is no observed data after 2006).

Figure 5 compares graphically measured and simulated daily sediment yield values for the calibration. Although the observed data were limited, sediment estimation by the model showed that simulated and measured sediment yields were in a similar range for the calibration period.

The annual simulations for each sub-catchment (Figure 6) show that rainfall (Figure 6A) varied between 270 and 550 mm·yr^{-1}, and the largest quantity (450–550 mm·yr^{-1}) was in the Tlemcen Mountains sub-basins. The potential evapotranspiration (Figure 6B) was between 993 and 1300 mm in the downstream portion, while it was between 1300 and 1500 mm in the entire basin. Surface runoff (Figure 6C) varied between 0 and 120 mm·yr^{-1} (semi-arid catchment). The highest values were located in the upstream sub-basin (between 10 and 30 mm), while the lowest were downstream (between 0 and 10 mm). The rate of soil erosion ranged from 0 to 0.2 t·ha^{-1}·yr^{-1} (Figure 6D), and the eastern upstream basins were identified as areas with high soil erosion in the Tafna.

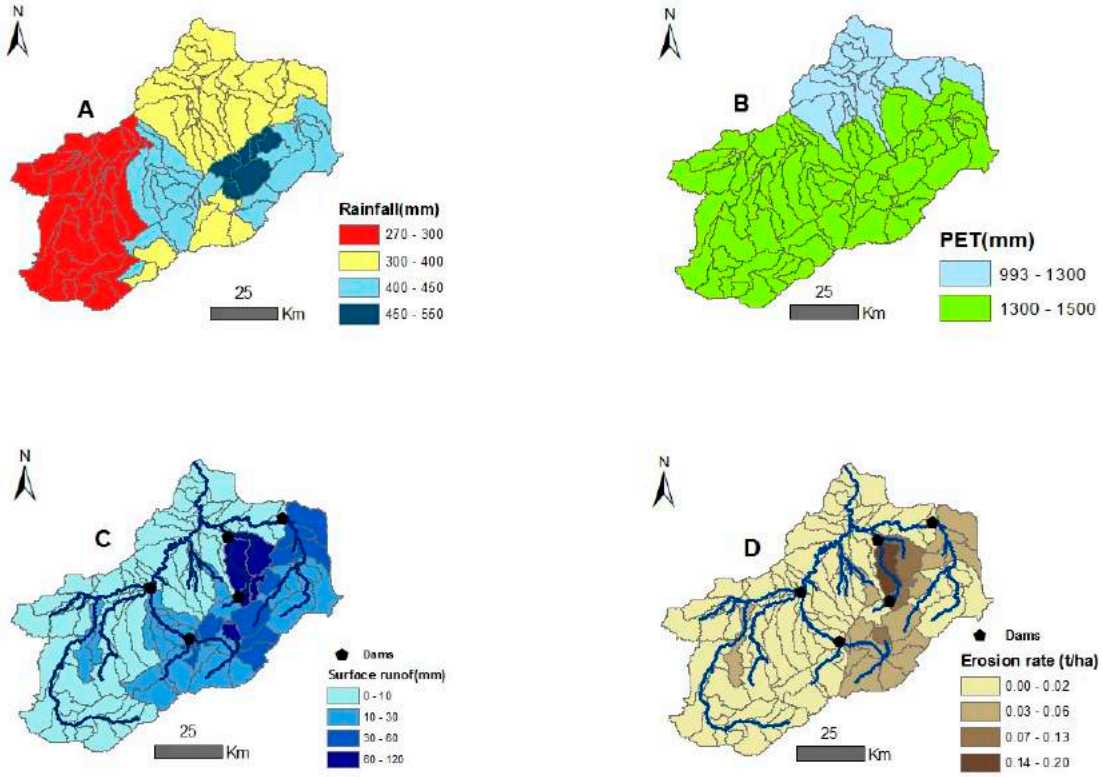

Figure 6. Inter-annual averages for each sub-catchment between 2000 and 2013. (**A**) rainfall (mm·yr^{-1}); (**B**) Hargreaves potential evapotranspiration (mm·yr^{-1}); (**C**) simulated surface runoff loads (mm·yr^{-1}); (**D**) simulated sediment yield (t·ha^{-1}·yr^{-1}).

3.2. Impact of Dams on Water Balance and Sediment Loading

To assess the impact of dam construction on water balance and sediments, the SWAT model was run both with and without dams.

3.2.1. Impact of Dams on Water Balance

Figure 7 shows the average annual basin value for water balance, calculated as a relative percentage of average annual rainfall.

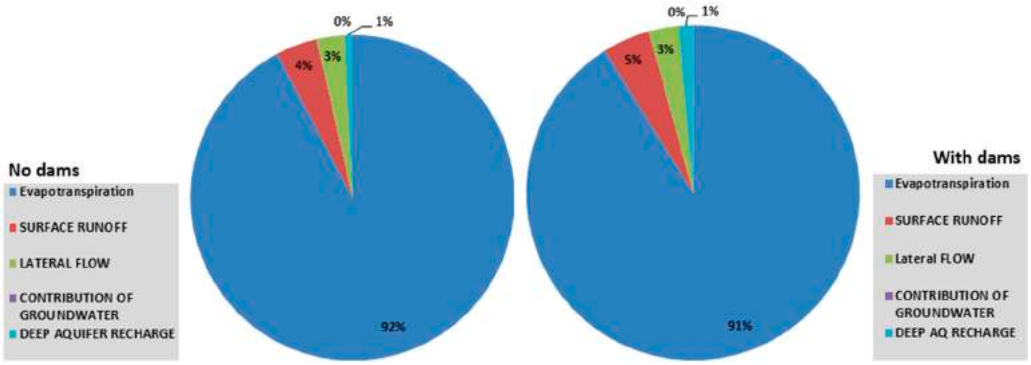

Figure 7. Impact of dams on average annual water balance as a relative percentage to precipitation.

The results of the simulation between 2000 and 2013 (Figure 7) show that the construction of the dams did not disturb the Tafna water balance.

The simulation results (Figure 8) reveal that dams greatly reduced the quantity of water arriving at the outlet of the Tafna between 2003 and 2013. A large amount of water was stored in five reservoirs (49%). This difference is significant according to ANOVA (p = 0.006 <0.05).

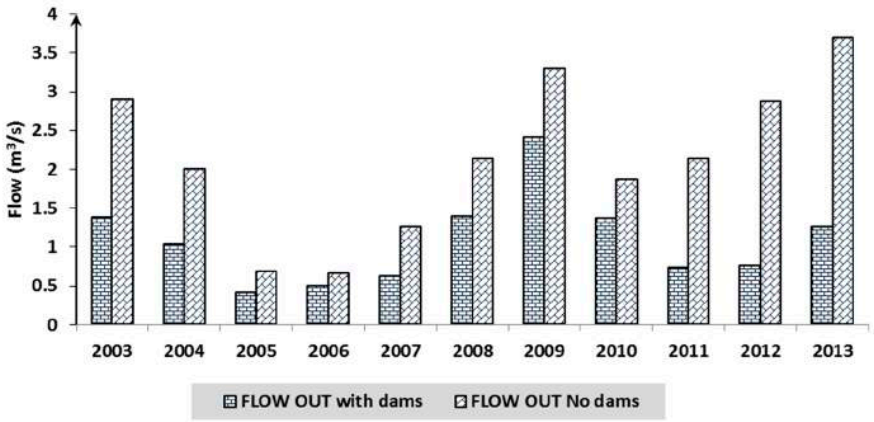

Figure 8. Impact of dams on flow at the outlet of the basin.

3.2.2. Impact of Dams on Sediment

The cumulative annual sediment load was also compared at the outlet of the basin (Figure 9) to quantify the amount of sediment stored in Tafna's dams.

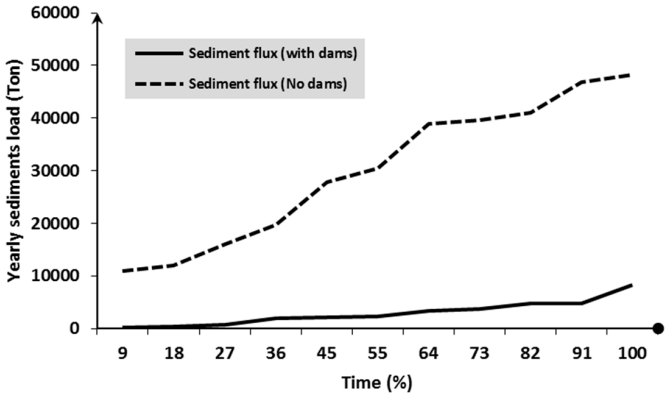

Figure 9. Cumulative annual sediment load at the outlet of the basin between 2003 and 2013.

The SWAT simulation showed that the reservoirs in these basins stocked a large amount of sediment, in excess of 27,000 t·yr^{-1} (90%). Large quantities were retained mainly during flood events, representing 87%–95% of the annual sediment export.

4. Discussion

Simulation results between 2003 and 2011 showed that the model adequately predicted the watershed hydrology of the Tafna River. These values remained consistent with the values published by ANRH , which were based on a series of observations between September 1965 and August 2002 [46,47,50] concerning runoff (SWAT value = 26.16 mm·yr^{-1}; ANRH (10–100 mm·yr^{-1})), potential evapotranspiration (SWAT value = 1301.4 mm·yr^{-1}; ANRH (900–1400 mm·yr^{-1})), rainfall (SWAT value = 364 mm·yr^{-1}; ANRH (250–550 mm·yr^{-1})) and limited groundwater resources [48]. The Tafna was characterized by very irregular flow with frequent dry summers, indicating very limited permanent reserves [67]. This study confirmed those results, affirming the good performance of SWAT in Mediterranean Karstic semi-arid watersheds [68].

The fraction of transmission losses from the main channel that enter the deep aquifer, the deep aquifer percolation fraction, and the curve number were the most sensitive parameters for stream flow. The value of the first parameter was 0.211, and the second parameter varied between 0.176 and 0.673. The Tafna sub-basins are essentially formed by semi-permeable and permeable formations that cover the whole surface of the basin, thus increasing the infiltration of surface water [69]. It was also evident that the curve number was the third most sensitive factor, varying relatively between −0.5 and 0.09. In a study of the Hathab river in Tunisia, the curve number ranged relatively between −0.5 and +0.5 [70]. In another study in Hamadan–Bahar watershed in Iran, this parameter ranged relatively between −0.32 and 1.02 [71]. These results confirmed the effect of land use spatial heterogeneity on runoff spatial heterogeneity in semi-arid catchments [72].

The results were analyzed by computing the coefficients of efficiency and determination on a monthly basis for nine water flow gauges. Multi-gauge calibration is an important step in developing a reliable watershed model in semi-arid watersheds, because the single outlet calibration of the watershed in arid and semi-arid regions can be misleading and thus requires spatial calibration to capture the spatial heterogeneity and discontinuities in the watershed [73]. Goodness-of-fit indices were satisfactory for discharge for the monthly calibration period. The Nash-Sutcliffe efficiencies at the nine flow gauges ranged from 0.42 to 0.75 and the coefficient R^2 was varying from 0.25 to 0.84 for the calibrated monthly flow for sub-basins for the period from January 2003 to August 2011. It should be noted that the upstream basin stations (A1, T3, A2, A6, A3) that had a less anthropic influence had higher index efficiencies (Nash varying between 0.50 and 0.75 and R^2 varying between 0.49 and 0.84) than the downstream stations (A4, A5, T8), which had a lower index efficiency (Nash varying between 0.42 and 0.59 and R^2 varying between 0.25 and 0.62). These are influenced by domestic and industrial waste from the major cities of Tlemcen and Maghnia in Algeria and Oujda in Morocco. In a study of the Medjerda River basin in Tunisia, the authors found a range of Nash-Sutcliffe efficiencies between 0.31 and 0.65, and range of coefficient R^2 between 0.62 and 0.8 [40]. In another study on the semi-arid river of the Hamadan-Bahar watershed in Iran, the authors found a Nash-Sutcliffe efficiency range of between 0.33 and 0.77, and a range of coefficient R^2 of between 0.38 and 0.83 [68]. The calibrated SWAT model can be used successfully to predict the volume inflow to the dams and facilitate the storage and release of water [44].

Gaps between observed and simulated flow values were partly explained by errors in observed and simulated values [31]. Uncertainty in the observed discharge values came from the precision of the sensor and the use of a rating curve. Errors in simulated values could be attributed to actual local rainfall storms that were not well represented by the SWAT rainfall data interpolation [31]. The model could not capture the small peaks. Aside from the uncertainty attributed to the precipitation input, the SCS curve number method, which works on daily rainfall depths, does not consider the duration

and intensity of precipitation. Representing this precipitation characteristic is necessary for semi-arid watersheds, where high-intensity short-duration precipitation occurs [74].

There were few observed suspended sediment data because, ANRH measures sediment once a month (sometimes there are no measurements) and sampling during flood periods is problematic. It is very difficult to assess the quality of the model performance as suspended matter sampling was not systematically performed for all storms, while the major losses of suspended matter occur during a small number of intensive rain events [39]. However, it was noticed that the simulated values were in the same range as the observed values. A similar observation was made in a study in Tunisia where the predicted concentrations of suspended matter were in the order of magnitude of the measured concentrations [39]. However, the low sampling frequency and lack of detailed land use and land management data did not allow an in-depth evaluation of the SWAT performance. It is recommended that future studies collect data at a greater frequency and spread along the river stretch [39]. Despite these shortcomings, the results from this study were still useful for representing the measured data [75]. The USLE soil erodibility factor, USLE equation support practice factor and peak rate adjustment factor for sediment routing in the main channel were the three sensitive parameters for sediment calibration. The value of the first parameter was 0.005, the second varied between 0.003 and 0.8, and the value of the third was 0.18.

A quantification of changes in water balance is necessary, especially after the construction of dams, for integrated watershed management in order to identify their effects on the basin [18]. The simulation results showed a considerable reduction in the quantity of water arriving at the outlet of the Tafna between 2003 and 2013, with a large amount of water stored in five reservoirs (49%). This decrease in flow downstream, which represents 18% of the basin surface, can affect the irrigated agricultural zone, especially as most of this land depends on Tafna water.

The comparison between the cumulative annual sediment load at the outlet with and without dams shows that reservoirs stock a large quantity of sediment, in excess of 27,000 $t \cdot yr^{-1}$ (90%). Large quantities are retained mainly during flood events, representing 87%–95% of the annual sediment export. In the Koiliaris river in Greece, flood events account for 63%–70% of the annual sediment export in a wet or dry year [68]. Between 37% and 98% of sediment settles in North African reservoirs [76]. These deposits contribute around 2%–5% of the yearly loss of water storage capacity [77]. The mean annual suspended sediment flux in North African rivers was estimated to be 254 million tons [78]. This storage reduces the lifetime of dams. The results of this study showed the need to implement a water resources management strategy to reduce reservoir sediment deposition, as in Tunisia where there are contour ridges for water harvesting in semi-arid catchments. The result was checked using the SWAT model in the Merguellil catchment (central Tunisia) and the contour ridges for water harvesting retained a large proportion of the entrained sediment (26%) [18].

5. Conclusions

In the present study, the hydrological SWAT model was applied to the Tafna River, which is a semi-arid basin. The model reproduced water flow and sediment in all gauging stations. The model's weakness at simulating runoff for some months was probably due to errors in the observed values and to the poor representation of small peaks. The weakness of the model at simulating sediment was due to the improper runoff simulation and the nature and accuracy of the measured sediment data.

Prediction of runoff and soil loss is important for assessing soil erosion hazards and determining suitable land uses and soil conservation measures for a catchment [75]. In turn, this can help to derive the optimum benefit from the use of the land while minimizing the negative impacts of land degradation and other environmental problems. As there are limited data available from the study region, the model developed here could help assess different land management options [75].

The application of the model enabled an evaluation of the contribution of the different compartments of the basin to surface water. SWAT has shown that a large proportion of surface water comes from surface runoff and lateral flow, while the contribution of groundwater was insignificant.

It was also noted that the application of the model gave a general idea of the impact of dam building on water balance and sediment in the Tafna semi-arid watershed. It highlighted that a large amount of water (49%) was stored in five reservoirs, decreasing the water flow in the downstream part of the basin, and could affect the irrigated agricultural zone, especially as most of this land depends on Tafna water. The dams of the Tafna have been built for the supply of drinking water and for irrigation. However, according to statistics of the National Agency of Basin and Transfer (ANBT) from January 2003 to July 2011, the largest dam basin (Hammame Boughrara) is devoted exclusively to drinking water.

These hydraulic structures were observed to stock a large quantity of sediment—in excess of 27,000 $t \cdot yr^{-1}$ (90%). Large quantities were retained mainly during flood events, representing 87%–95% of the annual sediment export. The results of this study showed the need for the implementation of a better water resources management strategy such as reforestation, and contour ridges for water harvesting upstream of the reservoirs to reduce the amount of sediment transported by the river. This is particularly important with dams in semi-arid and arid regions where water resources are limited and vary greatly with more intense low flow episodes and where rivers transport a high quantity of sediments, in order to reduce the siltation of dams and increase their lifetime. In fact, hydrological models such as SWAT demonstrate that it is a useful tool for understanding hydrological processes, even when the amount of measured data available is poor. It can be useful for identifying the most appropriate location for reservoirs and optimizing them to reduce their impact on water resources [18].

However, a general problem in watershed modelling that still needs to be addressed is the limited availability of data, especially in terms of measured water quality for calibrating and validating these models. The lack of a long time series of sediment with a daily time step and high spatial resolution limited this study's ability to evaluate the simulations [18].

Finally, the results obtained were very encouraging. SWAT allows the dynamics of water and sediment on the Tafna to be correctly represented. This model can be useful for understanding the impact of sediment transport on the water storage capacity of dams in a semi-arid region.

Acknowledgments: The authors thank the National Agency of Hydrologic Resources (ANRH) Oran, the Algerian agency in charge of stream gauging, which provided all water flow and nitrate concentration data, especially Sidi Mohammed Boudaliya and Belkacem Sardi. The National Agency for Dams and Transfers (ANBT) Ain youcef-Tlemcen, which provided all the data on dam management, especially Bensmaine. Ayoub Bouazzaoui, a PhD student at the University of Tlemcen-Algeria, in the SVTU faculty, agroforestry department, for his help during the realization of soil map.

Author Contributions: Amin Zettam, Amina Taleb, Sabine Sauvage, Nouria Belaidi and José Miguel Sánchez-Pérez conceived and designed the experiments; Amin Zettam performed the experiments; Amin Zettam, Sabine Sauvage and José Miguel Sánchez-Pérez analyzed the data; Laurie Boithias contributed analysis tools; Amin Zettam, Amina Taleb, Sabine Sauvage, Laurie Boithias and José Miguel Sánchez-Pérez wrote the paper.

Conflicts of Interest: The authors declare no conflict of interest.

References

1. Souza, J.O.P.; Correa, A.C.B.; Brierley, G.J. An approach to assess the impact of landscape connectivity and effective catchment area upon bedload sediment flux in Saco CreekWatershed, Semiarid Brazil. *Catena* **2016**, *138*, 13–29. [CrossRef]
2. Roudi-Fahimi, F.; Kent, M. Challenges and opportunities—The population of the Middle East and North Africa. *Popul. Bull.* **2007**, *62*, 1–20.
3. Terink, W.; Immerzeel, W.; Droogers, P. Climate change projections of precipitation and reference evapotranspiration for the Middle East and Northern Africa until 2050. *Int. J. Climatol.* **2013**, *33*, 3055–3072. [CrossRef]
4. Megnounif, A.; Terfous, A.; Ouillon, S. A graphical method to study suspended sediment dynamics during flood events in the Wadi Sebdou, NW Algeria (1973–2004). *J. Hydrol.* **2013**, *497*, 24–36. [CrossRef]

5. Taleb, A.; Belaidi, N.; Sanchez-Perez, J.M.; Vervier, P.; Sauvage, S.; Gagneur, J. The role of the hyporheic zone of a semi-arid gravel bed stream located downstream of a heavily polluted reservoir (Tafnawadi, Algeria). *River Res. Appl.* **2008**, *24*, 183–196. [CrossRef]
6. Touati, B. Les Barrages et la Politique Hydraulique en Algérie:état, Diagnostic et Perspectives d'un Aménagement Durable. Ph.D. Thèse, Université de Constantine, Constantine, Algérie, 2010.
7. Bourouba, M. Contribution a l'etude de l'erosion et des transports solides de l'Oued Medjerda superieur (Algerie orientale). *Bull. Reseau Erosion* **1998**, *18*, 76–97. (In French)
8. Colombani, J.; Olivry, J.C.; Kallel, R. Phénomènes exceptionnels d'érosion et de transport solide en Afrique aride et semi-aride. In *Challenges in African Hydrology and Water, Ressources*; IAHS Publication: Oxfordshire, UK, 1984; Volume 144, pp. 295–300. (In French)
9. Kettab, A. Les ressources en eau en Algérie: Stratégies, enjeux et vision. *Desalination* **2001**, *136*, 25–33. (In French) [CrossRef]
10. Remini, B. *La Problématique de l'eau en Algérie*; Office des publications Universitaires: Alger, Algérie, 2005; p. 162. (In French)
11. Boithias, L.; Acuña, V.; Vergoñós, L.; Ziv, G.; Marcé, R.; Sabater, S. Assessment of the water supply:demand ratios in a Mediterranean basin under different global change scenarios and mitigation alternatives. *Sci. Total Environ.* **2014**, *470–471*, 567–577. [CrossRef] [PubMed]
12. Surface Water Resources Mobilization; Document of Algerian Ministry of Water Resources. Available online: http://www.mree.gov.dz (accessed on 13 March 2017).
13. Hamiche, A.; Boudghene Stambouli, A.; Flazi, S. A review on the water and energy sectors in Algeria: Current forecasts, scenario and sustainability issues. *Renew. Sustain. Energy Rev.* **2015**, *41*, 261–276. [CrossRef]
14. Bouzid-Lagha, S.; Djelita, B. Study of eutrophication in the Hamman Boughrara Reservoir (Wilaya de Tlemcen, Algeria). *Hydrol. Sci. J.* **2012**, *57*, 186–201. [CrossRef]
15. Bessenasse, M.; Kettab, A.; Paquier, A.; Galeas, G.; et Ramez, P. Simulation numérique de la sédimentation dans les retenues de barrages : Cas de la retenue de Zardezas, Algérie. *J. Water Sci.* **2003**, *16*, 103–122. (In French) [CrossRef]
16. Remini, B.; Avenard, J.-M.; Kettab, A. Évolution dans le temps de l'envasement dans une retenue de barrage dans laquelle est pratiquée la technique du soutirage. *La Houille Blanche* **1997**, *6*, 4–8. (In French)
17. Benyahia, M.; Bechlaghem, N.; Habi, M.; Kerfouf, A. Importance des ressources hydriques de la wilaya de Tlemcen dans le cadre de l'Oranie (Algérie Nord Occidentale) et Perspectives de développement durables. In Proceedings of the Vème Colloque International-Energie, Changement Climatiques et Développement Durable, Hammamet, Tunisia, 15–17 Juin 2009. (In French)
18. Ounissi, M.; Bouchareb, N. Nutrient distribution and fluxes from three Mediterranean coastal rivers (NE Algeria) under large damming. *C. R. Geosci.* **2013**, *345*, 81–92. [CrossRef]
19. Abouabdillah, A.; White, M.; Arnold, J.G.; De Girolamo, A.M.; Oueslati, O.; Maataoui, A.; Lo porto, A. Evaluation of soil and water conservation measures in a semi-arid river basin in Tunisia using SWAT. *Soil Use Manag.* **2014**, *30*, 539–549. [CrossRef]
20. Le Goulven, P.; Leduc, C.; Bachta, M.S.; Poissin, J.C. Sharing scarce resources in a Mediterranean river basin: Wadi Merguellil in Central Tunisia. In *River Basin Trajectories: Societies, Environments and Development*; Molle, F., Wester, P., Eds.; MPG Books Group: Bodmin, UK, 2009; pp. 147–170, ISBN-13: 978-1-84593-538-2.
21. Todini, E. Hydrological catchment modelling: Past, present and future. *Hydrol. Earth Syst. Sci.* **2007**, *11*, 468–482. [CrossRef]
22. Noori, N.; Kalin, L. Coupling SWAT and ANN models for enhanced daily stream flow Prediction. *J. Hydrol.* **2016**, *533*, 141–151. [CrossRef]
23. Abbott, M.B.; Bathurst, J.C.; Cunge, J.A.; O'Connell, P.E.; Rasmussen, J. An introduction to the European Hydrological System—Système Hydrologique Européen, "SHE", 1: History and Philosophy of a physically-based, distributed modelling system. *J. Hydrol.* **1986**, *87*, 45–59. [CrossRef]
24. Wendling, J. Théorie de TOPMODEL. Extrait de thèse de Doctorat, Université de Grenoble, Grenoble, France, 1992. (In French)
25. Feldman, A.D. *Hydrologic Modeling System HEC-HMS*; Technical Reference Manual; U.S. Army Corps of Engineers, Hydrologic Engineering Center (HEC): Davis, CA, USA, 2000.
26. Liang, X.; Lettenmaier, D.P.; Wood, E.F.; Burges, J. A simple hydrologically based model of land surface water and energy fluxes for general circulation models. *J. Geophys. Res.* **1994**, *99*, 14415–14428. [CrossRef]

27. Beven, K.; Calver, A.; Morris, E.M. *Institute of Hydrology Distributed Model, Report No. 8*; Institute of Hydrology: Wallingford, UK, 1987.
28. Kouwen, N.; Soulis, E.D.; Pietroniro, A.; Donald, J.; Harrington, R.A. Grouping Response Units for Distributed Hydrologic Modelling. *ASCE J. Water Resour. Plan. Manag.* **1993**, *119*, 289–305. [CrossRef]
29. Lin, B.; Chen, X.; Yao, H.; Chen, Y.; Liu, M.; Gao, L.; James, A. Analyses of land use change impacts on catchment runoff using different time indicators based on SWAT model. *Ecol. Indic.* **2015**, *58*, 55–63. [CrossRef]
30. Arnold, J.G.; Srinivasan, R.; Muttiah, R.S.; Williams, J.R. Large-area hydrologic modeling and assessment: Part, I. Model development. *J. Am. Water Res. Assoc.* **1998**, *34*, 73–89. [CrossRef]
31. Moriasi, D.N.; Steiner, J.L.; Arnold, J.G. Sediment measurement and transport modeling: Impact of riparian and filter strip buffers. *J. Environ. Qual.* **2011**, *40*, 807–814. [CrossRef] [PubMed]
32. Boithias, L.; Sauvage, S.; Taghavi, L.; Merlina, G.; Probst, J.L.; Sanchez Perez, J.M. Occurrence of metolachlor and trifluralin losses in the Save river agricultural catchment during floods. *J. Hazard. Mater.* **2011**, *196*, 210–219. [CrossRef] [PubMed]
33. Oeurng, C.; Sauvage, S.; Sánchez-Pérez, J.M. Temporal variability of nitrate transport through hydrological response during flood events within a large agricultural catchment in south-west France. *Sci. Total Environ.* **2010**, *409*, 140–149. [CrossRef] [PubMed]
34. Singh, A.; Gosain, A.K. Climate-change impact assessment using GIS based hydrological modelling. *Water Int.* **2011**, *36*, 386–397. [CrossRef]
35. Arnold, J.G.; Moriasi, D.N.; Gassman, P.W.; Abbaspour, K.C.; White, M.J.; Srinivasan, R.; Santhi, C.; Harmel, R.D.; Van Griensven, A.; Van Liew, M.W.; et al. SWAT: Model use, calibration, and validation. *Trans. ASABE* **2012**, *55*, 1491–1508. [CrossRef]
36. Gassman, P.W.; Sadeghi, A.M.; Srinivasan, R. Applications of the SWAT Model Special Section: Overview and Insights. *J. Environ. Qual.* **2014**, *43*, 1–8. [CrossRef] [PubMed]
37. Baker, T.J.; Miller, S.N. Using the Soil and Water Assessment Tool (SWAT) to assess land use impact on water resources in an East African watershed. *J. Hydrol.* **2013**, *486*, 100–111. [CrossRef]
38. Shrestha, M.K.; Recknagela, F.; Frizenschafb, J.; Meyer, W. Assessing SWAT models based on single and multi-site calibration for the simulation of flow and nutrient loads in the semi-arid Onkaparinga catchment in South Australia. *Agric. Water Manag.* **2017**, in press. [CrossRef]
39. Molina-Navarro, E.; Trolle, D.; Martínez-Pérez, S.; Sastre-Merlín, A.; Jeppesen, E. Hydrological and water quality impact assessment of a Mediterranean limno-reservoir under climate change and land use management scenarios. *J. Hydrol.* **2014**, *509*, 354–366. [CrossRef]
40. Bouraoui, F.; Benabdallah, S.; Jrad, A.; Bidoglio, G. Application of the SWAT model on the Medjerda river basin (Tunisia). *Phys. Chem. Earth* **2005**, *30*, 497–507. [CrossRef]
41. Sellami, H.; Benabdallah, S.; La Jeunesse, I.; Vanclooster, M. Quantifying hydrological responses of small Mediterranean catchments under climate change projections. *Sci. Total Environ.* **2016**, *543*, 924–936. [CrossRef] [PubMed]
42. Neitsch, S.L.; Arnold, J.G.; Kiniry, J.R.; Srinivasan, R.; Williams, J.R. *Soil and Water Assessment Tool User's Manual, Version 2000*; Texas Water Resources Institute: College Station, TX, USA, 2002; p. 412.
43. Neitsch, S.L.; Arnold, J.G.; Kiniry, J.R.; Williams, J.R.; King, K.W. *Soil and Water Assessment Tool Theoretical Documentation, Version 2000*; Texas Water Resources Institute: College Station, TX, USA, 2002; p. 458.
44. Wang, G.; Xia, J. Improvement of SWAT 2000 modelling to assess the impact of dams and sluices on streamflow in the Huai River basin of China. *Hydrol. Process.* **2010**, *24*, 1455–1471. [CrossRef]
45. Ghoraba, S.M. Hydrological modeling of the Simly Dam watershed (Pakistan) using GIS and SWAT model. *Alex. Eng. J.* **2015**, *54*, 583–594. [CrossRef]
46. National Agency of Hydrologic Resources (ANRH). *Map of Potential Evapotranspiration in the North of Algeria*; ANRH: Alger, Algeria, 2003.
47. National Agency of Hydrologic Resources (ANRH). *Map of Average Annual Runoff in the North of Algeria*; ANRH: Alger, Algeria, 2003.
48. National Agency of Hydrologic Resources (ANRH). *Map of Groundwater Resources in the North of Algeria*; ANRH: Alger, Algeria, 2003.

49. Guardia, P. Géodynamique de la Marge Alpine du Continent Africain. D'après l'Etude de l'Oranie Nord Occidentale. Relations Structurales et Paléogéographiques Entre le tell Extrème et L'avant Pays Atlassique+ Carte au 1/100 000. Thèse 3 ème cycle, Université de Nice, Nice, France, 1975; p. 285. (In French)
50. National Agency of Hydrologic Resources (ANRH). *Map of Annual Rainfall in the North of Algeria*; ANRH: Alger, Algeria, 2003.
51. National Agency of Hydrologic Resources (ANRH). *Daily Data Flow in the Outlet of Tafna Catchment from 2000 to 2011*; ANRH: Alger, Algeria, 2012.
52. Taleb, A.; Belaidi, N.; Gagneur, J. Water Quality before and after AAM building on a heavily polluted river in semi-arid Algeria. *River Res. Appl.* **2004**, *20*, 943–956. [CrossRef]
53. Ministère Algérien de l'agriculture. *Type et Superficie de l'Agriculture de la Wilaya de Tlemcen et Ain Temouchent*; Ministère Algérien de l'agriculture: Alger, Algérie, 2011. (In French)
54. Laurent, F.; Ruelland, D. Assessing impacts of alternative land use and agricultural practices on nitrate pollution at the catchment scale. *J. Hydrol.* **2011**, *409*, 440–450. [CrossRef]
55. Chow, V.; Maidment, D.; Mays, L. *Applied Hydrology*; Chow, V., Maidment, D., Eds.; McGraw Hill: New York, NY, USA, 1988.
56. Williams, J.R. Flood routing with variable travel time or variable storage coefficients. *Trans. ASAE* **1969**, *12*, 100–103. [CrossRef]
57. Cunge, J.A. On the subject of a flood propagation method (Muskingum method). *J. Hydraul. Res.* **1969**, *7*, 205–230. [CrossRef]
58. Williams, J.R. Sediment routing for agricultural watersheds. *J. Am. Water Resour. Assoc.* **1975**, *11*, 965–974. [CrossRef]
59. Neitsch, S.L.; Arnold, J.G.; Kiniry, J.R.; Williams, J.R.; King, K.W. *Soil and Water Assessment Tools: Theoretical Documentation Version*; Grassland, Soil and Water Reasearch Laboratory, ARS: Temple, TX, USA, 2005; p. 494.
60. Bagnold, R.A. Bed load transport by natural rivers. *Water Resour. Res.* **1977**, *13*, 303–312. [CrossRef]
61. Barbut, M.M.; Durand, M.J.-H. *Carte des Sols d'Algérie. Oran. Feuille N.I. 30-N.E*; Service Géographique de l'Armée: Alger, France, 1952.
62. Land-Use Map, the European Space Agency. Available online: http://due.esrin.esa.int/page_globcover.php (accessed on 13 March 2017).
63. Aouissi, J.; Benabdallah, S.; Chabaâne, Z.; Cudennec, C. Evaluation of potential evapotranspiration assessment methods for hydrological modelling with SWAT—Application in data-scarce rural Tunisia. *Agr. Water Manag.* **2016**, *174*, 39–51. [CrossRef]
64. Abbaspour, K.C. *User Manual for SWAT-CUP SWAT Calibration and Uncertainty Analysis Programs*; Swiss Federal Institute of Aquatic Science and Technology: Dübendorf, Switzerland, 2007.
65. Nash, J.E.; Sutcliffe, V. River flow forecasting through conceptual models: Part I. A discussion of principles. *J. Hydrol.* **1970**, *10*, 282–290. [CrossRef]
66. Moriasi, D.N.; Arnold, J.G.; Van Liew, M.W.; Bingner, R.L.; Harmel, R.D.; Veith, T.L. Model evaluation guidelines for systematic quantification of accuracy in watershed simulation. *Am. Soc. Agric. Biol. Eng.* **2007**, *50*, 885–900.
67. Khaldi, A. Impacts de la Sécheresse sur le Régime des Ecoulements Souterrains Dans les Massifs Calcaires de l'Ouest Algérien "Monts de Tlemcen-Saida". Thèse de doctorat d'état, Université d'Oran, Oran, Algérie, 2005; p. 239. (In French)
68. Nerantzaki, S.D.; Giannakis, G.V.; Efstathiou, D.; Nikolaidis, N.P.; Sibetheros, I.A.; Karatzas, G.P.; Zacharia, I. Modeling suspended sediment transport and assessing the impacts of climate change in a karstic Mediterranean watershed. *Sci. Total Environ.* **2015**, *538*, 288–297. [CrossRef] [PubMed]
69. Bouanani, A. Hydrologie, Transport Solide et Modélisation étude de Quelques Sous Bassins de la Tafna (NW–Algérie). Ph.D. Thèse, Université Tlemcen, Tlemcen, Algérie, 2000; p. 250. (In French)
70. Chaâbane Ben Salah, N.; Abida, H. Modélisation des écoulements et de Transport Solide du Bassin d'Oued Hathab en Tunisie Centrale: Couplage d'un SIG avec le Modèle Agro Hydrologique SWAT. In Proceedings of the Actes du Séminaire sur les Systèmes d'Information Géographique pour l'Etude de l'Environnement, Djerba, Tunisia, 21–23 Mai 2012; Revue des Régions Arides—Numéro Spécial—n° 33. Institue des Régions Arides: Médenine, Tunisia, 2014; pp. 87–92. (In French)

71. Akhavan, S.; Abedi-Koupaia, J.; Mousavia, S.; Afyunib, M.; Eslamiana, S.; Abbaspour, K. Application of SWAT model to investigate nitrate leaching in Hamadan–Bahar Watershed, Iran. *Agric. Ecosyst. Environ.* **2010**, *139*, 675–688. [CrossRef]
72. Lin, K.; Lv, F.; Chen, L.; Singh, V.P.; Zhang, Q.; Chen, X. Xinanjiang model combined with Curve Number to simulate the effect of land use change on environmental flow. *J. Hydrol.* **2014**, *519*, 3142–3152. [CrossRef]
73. Niraula, R.; Norman, L.M.; Meixner, T. and Callegary, J.B. Multi-gauge Calibration for modeling the Semi-Arid Santa Cruz Watershed in Arizona-Mexico Border Area Using SWAT. *Air Soil Water Res.* **2012**, *5*, 41–57. [CrossRef]
74. Nie, W.; Yuan, Y.; Kepner, W.; Nash, M.; Jackson, M.; Erickson, C. Assessing impacts of land use and land cover changes on hydrology for the upper San Pedro watershed. *J. Hydrol.* **2011**, *407*, 105–114. [CrossRef]
75. Rostamian, R.; Jaleh, A.; Afyuni, M.; Farhad, M.; Heidarpour, M.; Jalalian, A.; Abbaspour, K.C. Application of a SWAT model for estimating runoff and sediment in two mountainous basins in central Iran. *Hydrol. Sci. J.* **2008**, *53*, 977–988. [CrossRef]
76. Ghorbal, A.; Claude, J. *Mesure de l'Envasement Dans les Retenues de Sept Barrages en Tunisie: Estimation des Transports Solides*; IAHS Publication: Wallingford, UK, 1977; Volume 122, pp. 219–232. (In French)
77. Kassoul, M.; Abdelgader, A.; Belorgey, M. Caractérisation de la sédimentation des barrages en Algérie. *Rev. Sci. Eau* **1997**, *3*, 339–358. [CrossRef]
78. Probst, J.L.; Amiotte-Suchet, P. Fluvial suspended sediment transport and mechanical erosion in the Maghreb (North Africa). *Hydrol. Sci. J.* **1992**, *37*, 621–637. [CrossRef]

water

MDPI

Article

The June 2016 Australian East Coast Low: Importance of Wave Direction for Coastal Erosion Assessment

Thomas R. Mortlock [1,*], Ian D. Goodwin [2], John K. McAneney [1] and Kevin Roche [1]

[1] Risk Frontiers, Macquarie University, North Ryde, NSW 2109, Australia; john.mcaneney@mq.edu.au (J.K.M.); kevin.roche@mq.edu.au (K.R.)

[2] Marine Climate Risk Group, Department of Environmental Sciences, Macquarie University, North Ryde, NSW 2109, Australia; ian.goodwin@mq.edu.au

* Correspondence: thomas.mortlock@mq.edu.au

Academic Editor: Sylvain Ouillon

Received: 5 December 2016; Accepted: 6 February 2017; Published: 14 February 2017

Abstract: In June 2016, an unusual East Coast Low storm affected some 2000 km of the eastern seaboard of Australia bringing heavy rain, strong winds and powerful wave conditions. While wave heights offshore of Sydney were not exceptional, nearshore wave conditions were such that beaches experienced some of the worst erosion in 40 years. Hydrodynamic modelling of wave and current behaviour as well as contemporaneous sand transport shows the east to north-east storm wave direction to be the major determinant of erosion magnitude. This arises because of reduced energy attenuation across the continental shelf and the focussing of wave energy on coastal sections not equilibrated with such wave exposure under the prevailing south-easterly wave climate. Narrabeen–Collaroy, a well-known erosion hot spot on Sydney's Northern Beaches, is shown to be particularly vulnerable to storms from this direction because the destructive erosion potential is amplified by the influence of the local embayment geometry. We demonstrate the magnified erosion response that occurs when there is bi-directionality between an extreme wave event and preceding modal conditions and the importance of considering wave direction in extreme value analyses.

Keywords: East Coast Low; nearshore processes; coastal erosion; coastal management; climate change; numerical modelling; Southeast Australia

1. Introduction

East Coast Low (ECL) storms bring heavy rain, strong winds and powerful coastal wave conditions to the Southeast Australian coast. They are often responsible for significant beach erosion and lowland inundation and pose a threat to coastal infrastructure and public safety. The 'Pasha Bulker' storm in June 2007, for example, was responsible for normalised insurance losses of AUD$1.97 billion [1,2]; economic losses arising from that event are likely to have been at least double this figure.

ECLs are a common feature across the Southern Hemisphere extra-tropics [3,4]. In Australia, they typically form in the late Austral autumn to early winter and are a regular feature of the winter climate [5]. They typically bring storm wave conditions over a 3-day period before decaying eastwards into the Tasman Sea [6]. Their steep build up to peak storm wave conditions makes them one of the more dangerous weather systems affecting the New South Wales coast (NSW) and poses difficulties for forecasting.

The weather pattern of the June 2016 event was unusual in the context of the last few decades and is referred to as a "Black Nor'easter" because the black skies and north-easterly winds recorded by mariners in the late 1800s. The heavy rainfall and unusual wave direction coincided with some of the highest tides of the year further amplifying impacts at the coast. During most ECLs, the rotation of the low-pressure cell (clockwise flow in the Southern Hemisphere) and extra-tropical origin usually

produce a south to south-easterly wave direction. The June 2016 event, however, produced east to north-east storm waves along the entire east coast (~2000 km of shoreline length) (Figure 1). Wave heights increased from north to south and the Eden buoy (far south coast of NSW) recorded a maximum individual wave height of 17.7 m—the largest wave ever recorded along the NSW coast [7]. Peak storm significant wave heights offshore of Sydney were considerably smaller (1-hourly H_s 6.4 m) yet still led to significant erosion at the coast.

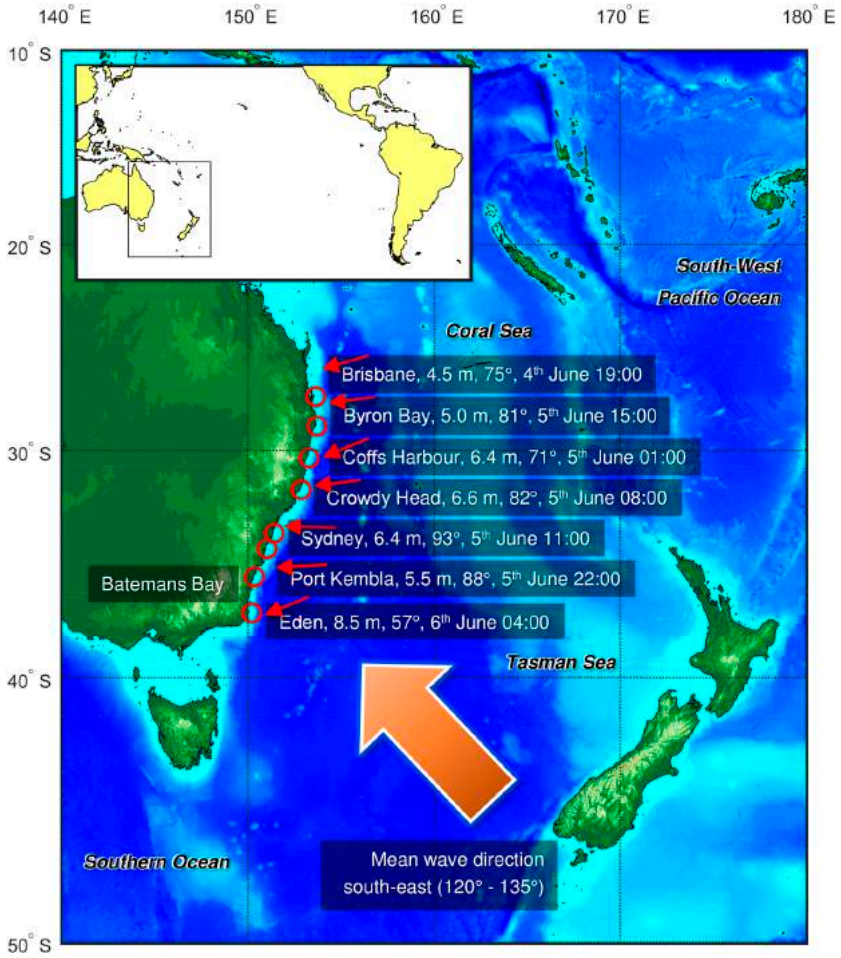

Figure 1. Map of the Tasman and Coral Seas region with locations of waverider buoys in Southeast Australia (red circles). The Tasman Sea borders the east coast of Australia, and extends west to New Zealand. It extends north to where it meets the Coral Sea at approximately 30° S [8]. The peak storm hourly significant wave height, mean wave direction, and time of peak storm wave conditions during the June 2016 event, are given for each buoy location. The Batemans Bay buoy data transmission failed during the event [7]. Red arrows illustrate peak storm wave direction. Mean wave direction (range of averages for all buoys over portions of records having directional observations) is also shown. Inset shows the study region in relation to the Pacific Basin.

The north-easterly wave direction was the result of a hybrid Anticyclonic Intensification (AI)/Easterly Trough Low (ETL) synoptic weather pattern as described in [5]. The low-pressure cell developed over the Coral Sea and northern Tasman Sea and was directed down the east coast by a strong blocking anticyclone which intensified over the South Island of New Zealand (Figure 2). The long fetch of approximately 1500 km produced sustained long wave periods (in excess of 14 s) that are unusual for the Tasman Sea from this direction and further contributed to powerful wave conditions at the coast.

Storm wave events from the north-east are uncommon, having occurred on average twice per decade at Sydney over the past 40 years [9]. The long-term mean annual wave direction is 135° (south-easterly), and waves approaching clockwise of east constitute almost 70% of observations. The south-easterly wave climate is moderately oblique to the shoreline and leads to increasing south-to-north alongshore wave energy and littoral transport [10]. The beach morphology is equilibrated to this wave energy gradient [11] and provides a natural buffer to erosion when the storm wave direction is similar to the modal (non-storm) wave direction. A more extreme erosion response occurs when the storm and modal wave directions are different, as occurred in June 2016. Even a relatively subtle change in wave obliquity can make a big difference to the magnitude and direction of littoral transport, as demonstrated empirically [12], and can drive a significant shoreline response on wave-dominated sandy coasts [13].

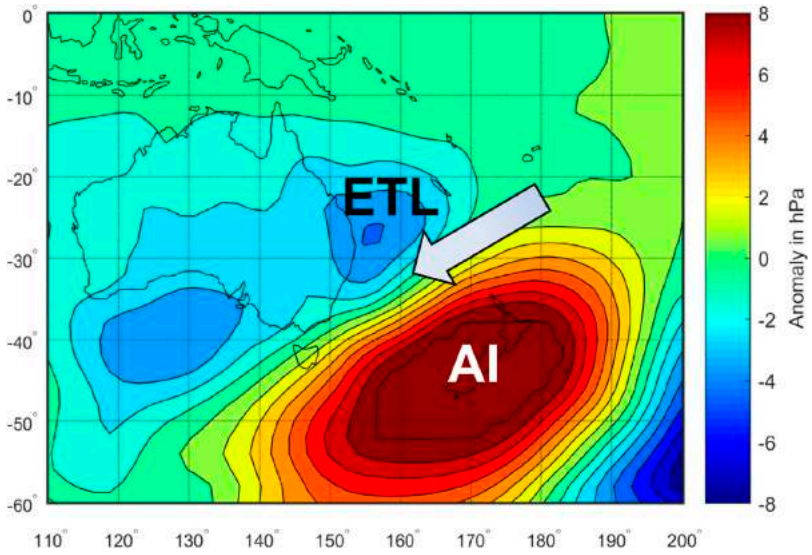

Figure 2. Composite sea level pressure (SLP) anomaly (in hectopascals, hPa) for all east-northeast Anticyclonic Intensification (AI)/Easterly Trough Low (ETL) storm wave events since 1974, using events identified from buoy records in Shand et al. [9], and the European Centre for Medium-Range Weather Forecasts (ECMWF) ERA 20th Century reanalysis (ERA-20C) [14]. The composite anomaly was calculated relative to the ERA-20C long-term mean (1900–2010).

One of the worst affected areas was Collaroy, a suburb situated at the south end of the Narrabeen–Collaroy embayment on Sydney's Northern Beaches (Figure 3). Beach erosion and accretion trends have been monitored here since 1976 [15] and have been shown to be synchronous with other beach compartments along the NSW coast [16,17]. Despite being well recognised as an erosion hot spot, the shorefront of Collaroy is characterised by a legacy of inappropriate development into the active beach zone [18]. How to best to manage this legacy poses a significant challenge and fraught policy area for governments [19]. Management decisions are purportedly based on cost-benefit analyses, which are chiefly controlled by the value of the land and property at risk. As population density and demand for coastal property continues to increase, the cost of not providing ongoing protection also rises. Contemporaneously, the hazard threatening coastal communities is also likely to increase with climate change.

The primary focus of our study is to demonstrate the importance of storm wave direction for coastal erosion impacts, using Narrabeen–Collaroy as an example of regional significance. The hydrodynamics controlling the erosion risk are examined, by comparing impacts from the June 2016 event with another ECL event that impacted Sydney in April 2015 but with a different offshore wave direction. A re-assessment of extreme wave conditions at Sydney, combined with nearshore

buoy observations, also demonstrates the importance of wave direction considerations when assessing erosion potential in a changing climate.

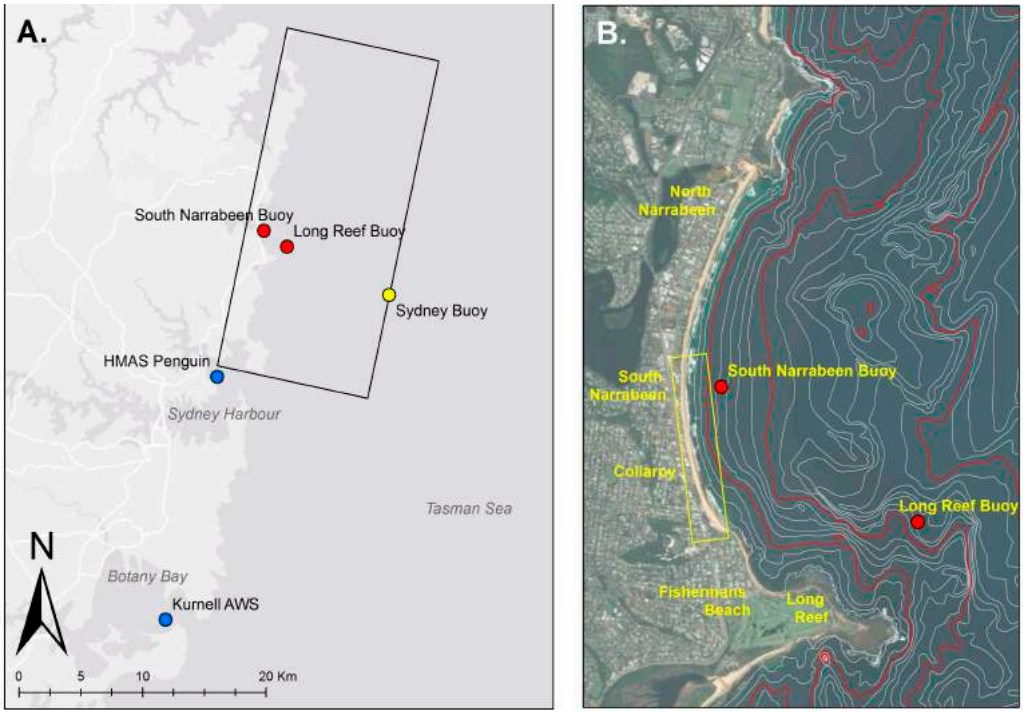

Figure 3. (**A**) Regional map showing approximate extents of numerical model domain (black box); locations of nearshore wave buoys (red); location of Sydney wave buoy (yellow); and locations of tide and wind stations used in this study (blue); and (**B**) local map of Narrabeen–Collaroy beach with bathymetry (5, 15 and 30 m isobaths in red); locations of nearshore wave buoys shown in (**A**); and approximate area of erosion damage at Collaroy during the June 2016 storm (yellow box).

2. Observational Data

2.1. Wave Conditions

Hourly parametric wave data were sourced over the period 3 to 10 June 2016 from observations at the Sydney waverider buoy located approximately 9 km off the Narrabeen–Collaroy embayment in 90 m water depth (Figure 3). The significant wave height, H_s (m), maximum wave height, H_{max} (m), peak wave period at the first and second spectral peak, Tp_1 and Tp_2 (s) and mean wave direction at the first and second spectral peak, MWD_{Tp1} and MWD_{Tp2} (degrees true north coming from) were the wave parameters used. The long-term parametric wave record from the Sydney buoy (non-directional since 1987, directional since 1992) was also used in this study. Observations from two other wave buoys deployed inside the Narrabeen embayment (Figure 3) between August and November 2011 were also used. These buoys were deployed at South Narrabeen (~12 m depth) and at Long Reef (~20 m depth). The South Narrabeen buoy was directional, while the Long Reef buoy was not.

2.2. Tide Conditions

Tide levels over the duration of the storm were taken at 15-min intervals from the gauge at the naval base of Her Majesty's Australian Ship (HMAS) Penguin, Middle Head, Sydney Harbour (Figure 3). This station is considered representative of the open coast tide. Tides are semi diurnal and micro tidal (mean range of 1.3 m) along the NSW coast and approach almost perpendicular to the shelf, so that geographical differences in the timing of high and low tides across the state are negligible. Both forecast and observed tidal data were used to measure the surge component of the water level.

2.3. Wind Conditions

Half-hourly wind observations of velocity (m/s) and direction (degrees true north coming from) were obtained from the Kurnell weather station, 10 m above sea level, in Botany Bay (Figure 3). In the absence of over-sea wind measurements, Wood et al. [20] found the wind climate at Kurnell to best represent coastal ocean winds for the Sydney region.

2.4. Coastal Erosion

Pre- and post-storm beach surveys (above the water line) were undertaken at Narrabeen–Collaroy by University of New South Wales as part of a long-term beach monitoring program [15]. Shore-normal transects were surveyed at five locations along the beach using GPS, each extending from the dune behind the beach down to the water line. Pre- and post-storm hydrographic surveys (below the water line) were also undertaken at Narrabeen–Collaroy by NSW Office of Environment and Heritage [21]. Both surveys used a jet ski bottom-mounted single-beam echo sounder, narrow-beam transducer and GPS system and covered the shoreface from approximately 2 m to 15 m water depth with 50 m-spaced shore-normal survey lines.

3. Numerical Modelling

Wave, water level and wind observations over the duration of the storm were input to a coupled wave, flow and morphological model of the Sydney region to investigate coastal processes associated with the June 2016 event. A MIKE 21/3 Coupled Model developed by the Danish Hydraulic Institute (DHI) was used [22]. In this instance, the modelling system coupled a spectral wave model with a hydrodynamic flow model and a sediment transport model to simulate waves, currents, water levels and bed elevation change during the storm.

The wave model (MIKE 21 Spectral Wave, SW) simulates the growth, decay and transformation of wind-generated waves and swell in coastal locations. Directionally-decoupled and quasi-stationary formulations were used. Wave- and wind-driven currents and water level variations drive the hydrostatic flow model (MIKE 21 Flow Model), which is based on the two-dimensional Reynolds-averaged Navier–Stokes equations. Hydrodynamic conditions from the flow model and wave radiation stress terms from the wave model were used as input to the sand transport model (STPQ3D) to simulate morphological changes during the storm. The effect of bed ripples, bed slope, cross-current transport, rips and undertow were all included in the calculations. All model components were dynamically coupled, in other words a full feedback between the morphology, waves and currents took place at each time step. For a more detailed description of coupled model physics, the reader is referred to [22].

3.1. Model Bathymetry

The model domain covered the Sydney Northern Beaches area from North Head, Sydney Harbour in the south to Palm Beach in the north (Figure 3) and extended offshore to the 90-m isobath where the Sydney wave buoy is located. A mosaic of best-available bathymetries was used to generate a seabed topography in the model, including the pre-storm hydrographic survey undertaken at Narrabeen–Collaroy [21]. Bathymetric data also included a series of Single-Beam Echosounder (SBES) surveys of the upper shoreface of the Sydney Northern Beaches area undertaken by the Office of Environment and Heritage (OEH) between 2011 and 2016 (average 50 m line spacing); a Multi-Beam Echosounder (MBES) survey of the lower shoreface area offshore of the Northern Beaches undertaken by OEH in 2014 (5 m point density); and a series of SBES survey lines of the inner shelf offshore of the Northern Beaches area undertaken by the Royal Australian Navy (RAN) in the 1970s (average 200 m line spacing). The bathymetric data was mapped onto a flexible computational mesh, composed of a series of irregular Delaney triangles (elements), using a natural neighbor interpolation method. The interpolated bathymetric mesh was then refined based on a depth/gradient ratio to improve the computational resolution for shallow water and areas of complex subaqueous reef. This led to

a computational mesh with an average element length of 200 m offshore (in approximately 90 m water depth), grading to 20 m at the shoreline. An approximate 20 m resolution at the shoreline was considered sufficient to resolve cross- and along-shore transport processes and ensured all available bathymetry soundings were used.

The coastal planform and elevation of the subaerial beach was idealized using the pre-storm cross-shore profile data from the Narrabeen beach monitoring program [15], and recent aerial photography. The dry beach was included in the model to provide a sediment source for storm cut and for flooding and drying at the shoreline.

3.2. Model Boundary Conditions

Boundary wind, wave and tide data were derived from point-source measurements close to or within the model domain, as described in Section 2. These time-series data (hourly waves, half-hourly winds, and 15-min tides) were applied at all three open boundaries of the model (south, east and north), apart from the waves which were only applied on the east (ocean) boundary. A depth-integrated approximation based on linear wave theory [22] was used for wave forcing on both lateral boundaries (north and south) to estimate waves entering the two sides of the model domain. Sensitivity testing ensured that the model domain was sufficiently wide to avoid potential errors propagating from the lateral boundaries into the area of interest. A computational time step of 15 min was used to resolve all boundary conditions, and a 12-h model spin up period was imposed.

An inherent assumption of the model was that the measured waves, tides and winds were representative of, and constant along, the length of the model boundaries on which they were applied. The east (ocean) boundary ran through the moored location of the Sydney waverider buoy and followed the same isobath (90 m). Wind data was sourced from the most representative source and was chosen over other wind hindcasts as the latter can under-estimate near-coast wind fields in this area [20,23]. Because an atmospheric model was not used, the wind field was spatially constant throughout the model domain for each time step, so localized variations were not captured. Tide measurements were applied as variations in the surface water elevation at each boundary. This included a barometric surge element as measured on top of the astronomical tide. Local wind and wave set-up were generated by the model.

Parametric wave data from the Sydney buoy (H_s, Tp_1, MWD_{Tp1}) were used assuming a JONSWAP spectrum as full spectral conditions from the buoy during the storm were unavailable at the time of writing. Thus, any bi-modality during the storm was not replicated in the model and is likely to have contributed to residual errors after calibration (Section 3.5). Directional spreading of the parametric wave data was estimated for each time step based on wave-age curves generated using the method of [24]. The entire Sydney buoy record (1987–2016) was used to approximate wave steepness limits of wind-sea, intermediate sea-swell, and swell, based on H_s and Tp_1 (Figure A2). All wave events classed as wind-sea were assigned a spreading of ~25°, intermediate sea-swell ~20°, and swell ~15°, after [22]. From Figure A2, it is interesting to note that most wave conditions during this event were theoretically swell waves because of the unusually long wave periods.

3.3. Model Bed Characteristics

Bed resistance, bottom friction and bed layer thickness varied spatially within the model domain in accord with a comprehensive set of observations of subaqueous reef areas and sediment samples collated in [25]. In this way, the influence of the roughness and non-erodibility of rock reefs was accounted for in the model. An estimate of the physical roughness height of rock reef was derived from Light Detection And Ranging (LiDAR) imagery of low-tide exposed rock platforms around Long Reef headland. Transects were taken through the reef sections, following the method of [26]. Results ranged from 0.08 m to 0.33 m with a mean of 0.16 m. These values are similar to those reported for coral reef platforms (e.g., 0.16 m [27]) with the upper values reflecting the greater rugosity of bare rock reef than that of coral. The mean value of 0.16 m was used to calculate bed resistance effects for all

areas of rock reef within the model domain. A value of 0.05 m was used elsewhere to account for the effect of small sand ripples on flow resistance [22,28].

To describe the bottom frictional effects of reef, the physical roughness height, k_w, was converted to a hydraulic (Nikuradse) roughness value, k_n, using the approximation $k_n \approx 2.k_w$ [29], giving a k_n of 0.32 m. Using similar logic, Huang et al. [30] arrived at a comparable value for k_n of 0.27 m for coral reef. For non-reef areas, a k_n of 0.04 m was used to approximate the effect of small sand ripples on the frictional dissipation of wave energy [31].

Where reef areas existed, the bed thickness was set to zero to ensure that no erosion could take place. Elsewhere, an infinite thickness was used. At the land boundary, areas of reef headland were assigned a reflection coefficient of 0.8 (1.0 being fully reflective) to describe the intensity of a reflected wave heights relative to incident wave heights against a headland [22]. Full wave reflection effects (such as standing waves) were not accounted for. Beach sections were fully absorptive.

A cross-shore gradation in the median grain diameter, d_{50}, was used based on observations in [25]. d_{50} varied from 0.33 mm on the sub-aerial beach, to 0.22 mm in the surf zone, coarsening thereafter to 0.48 mm on the lower shoreface. Observations were not of sufficient density to derive any along-shore variation in grain size. Sediment samples from various sources collated in [25] suggest the grain size distribution around d_{50} did not vary significantly in a cross-shore direction, thus, a single grading coefficient of 1.34 was used. A porosity of 0.4 was used consistent with that of quartz sand. Carbonate material present in beach sediments along the Northern Beaches is likely to vary the porosity (and specific density) of sand in a cross-shore direction, but is not included here.

3.4. Model Calibration

The sensitivity of the model to varying mesh resolution, seabed substrate type, wave breaking, directional resolution and wave theory were examined. A Brier Skill Score (BSS) was used to assess the model's morphological performance, and by inference the nearshore flow field, using observed bathymetric change from pre- and post-storm hydrographic surveys undertaken at Narrabeen–Collaroy [21]. A skill score was calculated for each mesh element within the survey area so the spatial variance in model error could be assessed. The scoring method and classification system described in Sutherland et al. [32] was used.

The most significant improvement in model skill was obtained by increasing the resolution of the computational mesh from the 30-m isobath to the shoreline. Changes to the mesh resolution seaward of this had negligible effects on model performance. A coarse resolution mesh grading from an approximate element length of 250 m along the 30-m isobath to 50 m at the shoreline, returned a median BSS across the survey area of -5 ('Bad'). A more highly-resolved mesh covering the whole of the Narrabeen–Collaroy embayment (from 30-m isobath to shoreline) at a 20-m resolution, dramatically improved the median BSS to 0.22 ('Good').

The cost of not including areas of rock reef in the model, and their effect on flow resistance, bottom friction and erodible layer thickness, was a reduction in model skill from 0.22 ('Good') to 0.12 ('Fair'). A wave breaking parameter, γ, of 0.9, best replicated the observed volume in the surf zone bar, as has been also found by [33] in a similar setting. Increasing the directional resolution of the wave forcing (from 10° to 5°) made no significant improvement, perhaps because the coarser binning in part compensated for deficiencies in the directionality of boundary wave forcing (Section 3.2).

The model sensitivity to two wave theories was tested; the first using a combination of Stokes and Cnoidal fifth-order classic wave theories, and another combining the semi-empirical wave theories of Doering and Bowen [34] and Isobe and Horikawa [35]. The Stokes/Cnoidal theories led to a wider area of small-scale bed lowering seaward of the surf zone bar but did not replicate the accretion volume in the bar as well as the Doering and Bowen/Isobe and Horikawa formulation. Thus, the latter was used here.

3.5. Model Verification

The wave component of the model was verified against the four months of directional, hourly wave buoy observations collected from the South Narrabeen and Long Reef nearshore wave buoys (described in Section 2.1, locations shown in Figure 3). The model showed good predictive skill for significant wave height (R^2 = 0.9, slope = 0.9, at both buoy locations) and mean wave direction (R^2 = 0.8, slope = 0.9) but exhibited a small positive bias in the mean wave period (1–2 s) at both buoy locations.

After calibration, the morphological model attained a median skill score across the surveyed area of 0.35, a figure considered 'Good' [32]. In describing the location and geometry of the surf zone storm bar, in most places the skill score exceeded 0.7, a rating considered 'Excellent' (Figure 4). However, morphological change at the southern end of the embayment was not well replicated. This may have been because data transmission issues at the buoy during the storm [7] meant the wave direction and period around the storm peak are interpolated values. Moreover, there was no spectral wave data available at the time of writing thus wave bi-modality was not accounted for in the model. These factors collectively may have led to an under-representation of north-easterly wave energy responsible for bar build-up at the south end of the embayment.

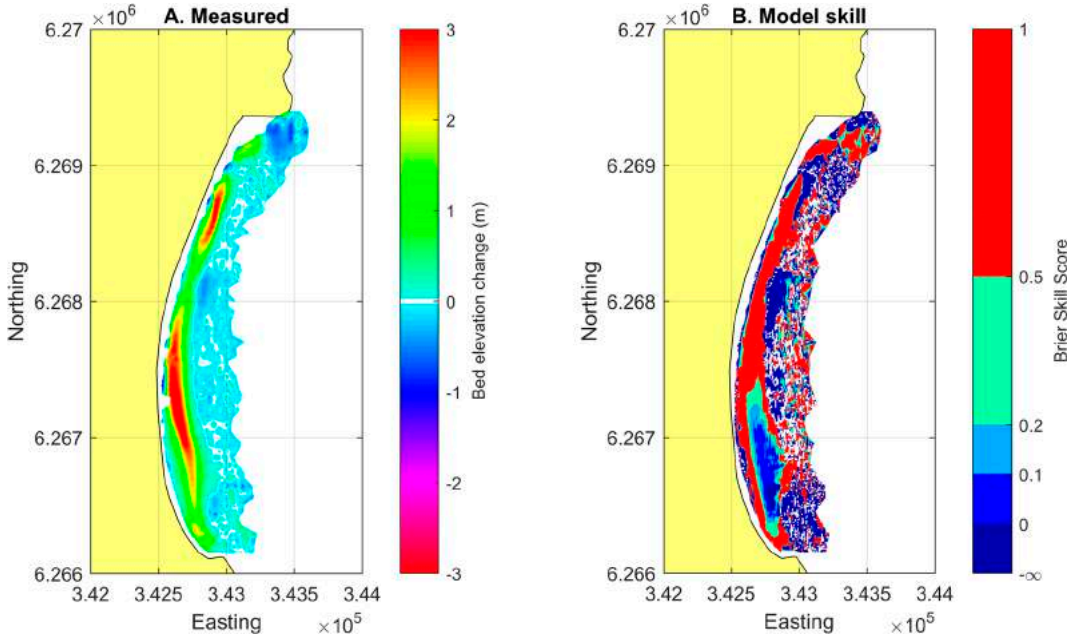

Figure 4. Measured morphological change (in metres) during the June 2016 storm event (**A**) and model skill in replicating observed change (**B**). The pre- and post-storm surveys in (**A**) extend from ~2 m to ~15 m water depth. The colour scheme in (**B**) reflects the Brier skill assessment of [32]. Morphological change within the vertical error of the surveyed data (±0.03, [21]) was omitted from both plots.

4. Coastal Conditions at Sydney

4.1. Peak Storm Conditions

Storm peak wave conditions coincided with the winter solstice spring tide, a period of strong onshore winds and heavy rainfall. Figure 5 shows the wave heights and water levels observed at Sydney during the storm. Wave period and direction and wind speed and direction observations are given in the Appendix A (Figure A1).

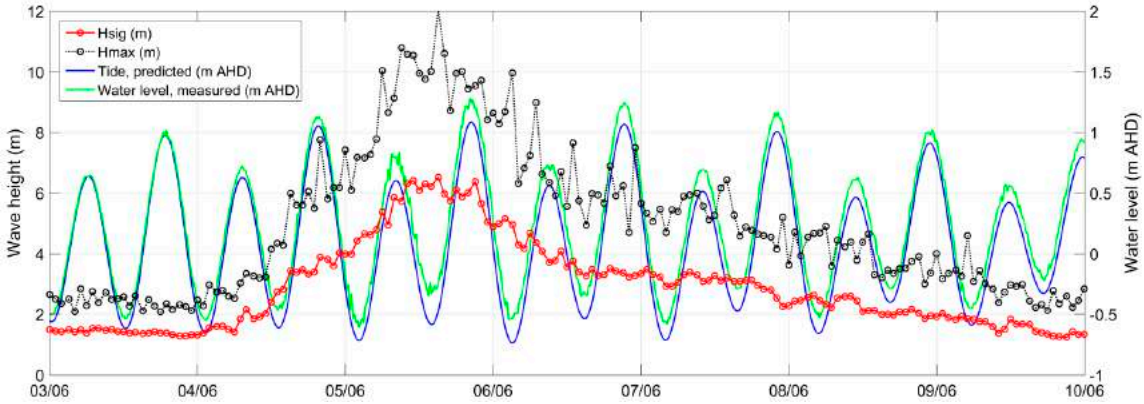

Figure 5. Observations of significant and maximum hourly wave heights and 15-min water levels observed and predicted at the Sydney wave buoy and the tide gauge at Her Majesty's Australian Ship (HMAS) Penguin, Sydney Harbour, from 3 to 10 June 2016. Water levels are given relative to Australian Height Datum (AHD) which approximates to the mean sea level.

A maximum water level of 1.29 m Australian Height Datum (AHD) was recorded at the tide gauge at HMAS Penguin around 20:00 on 5 June, which represents an Average Recurrence Interval (ARI) of approximately 2.5 years [7]. This included a positive tidal residual of up to 0.34 m (storm surge). Water levels on the open coast would have variably been higher than this because of wave and wind set up. Modelling here suggests that maximum water levels may have exceeded 1.7 m AHD around 21:00 at Long Reef headland and North Narrabeen (comprising a ~0.6 m surge). This does not include wave run up which can easily be an order of magnitude greater than the surge component [36]. Onshore winds observed at the Kurnell weather station averaging 15 $m \cdot s^{-1}$ (~30 knots) were sustained for almost 20 h leading up to and during the storm peak, with gusts of up to 24 $m \cdot s^{-1}$ (~60 knots).

Storm wave conditions at Sydney (defined as the hourly H_s exceeding 2 m for a period of 72 h or more, after [9]) began around midday on Friday 4 June and lasted until late evening on Wednesday 8 June (106 h). A peak storm wave height (H_s) of 6.4 m was recorded at 11:00 on Sunday 5 June. H_s then remained around 6 m for the next 10 h (until 21:00), after which it began to gradually decline. Maximum wave heights (H_{max}) exceeded 8 m between 06:00 on the Sunday to 03:00 the following morning peaking at 12 m at 15:00 on Sunday afternoon.

Some wave period and direction information was missing due to transmission problems at the buoy over the peak of the storm [7], but interpolated values suggest a storm peak direction (MWD_{Tp1}) of around 93°, and period (Tp_1) of around 11.5 s. While the exact variation of MWD_{Tp1} and Tp_1 over the period of missing data is unknown, the interpolated values are in broad agreement with the peak direction and period of other mid-shelf wave buoys along the coast (Figure 1). As the storm intensified, the wave period at Sydney lengthened to around 14 s and the wave direction simultaneously rotated clockwise from north-east to east. Over this period, the synoptic weather pattern suggests that the deep-water wind and wave field was still north-east (Figure 6C,D).

The more easterly direction recorded at the buoy may be a result of the longer-period waves having already refracted around towards shore-normal by the time they reached the buoy location. Wave base—the depth at which surface waves begin to be influenced by the sea bed—was around 150 m, suggesting that waves had already refracted on the edge of the continental shelf far seawards of the buoy location (on the 90-m isobath).

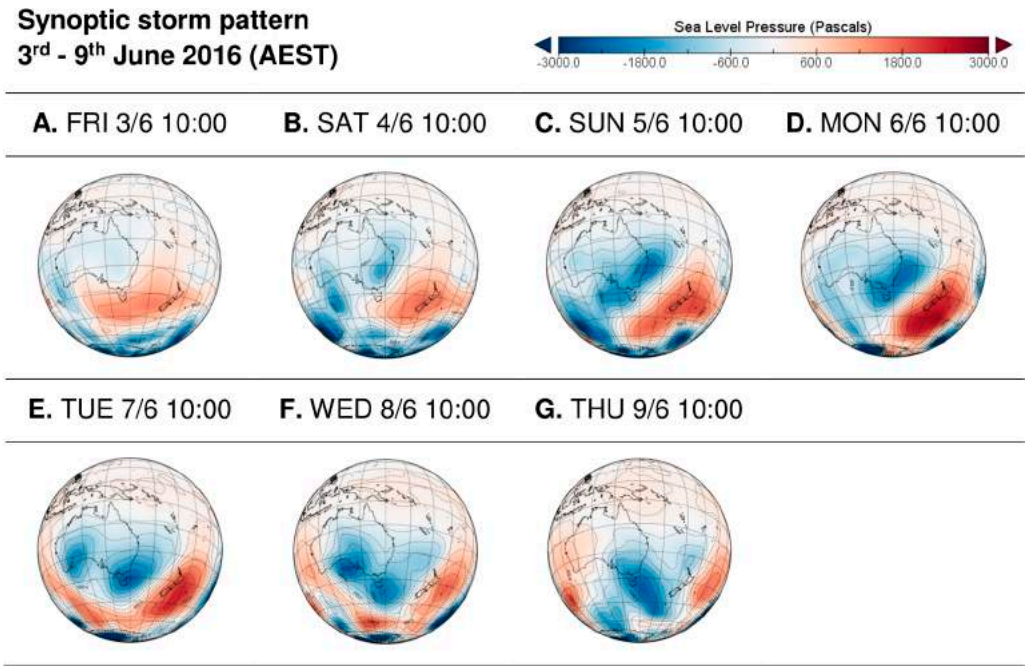

Figure 6. Sea level pressure patterns over the Tasman Sea every 24 h from 3 to 9 June 2016 from the NCEP/NCAR reanalysis at a 2.5° resolution [37]. High pressure (red) is associated with anti-cyclonic winds and low pressure (blue) is associated with cyclonic winds. The low-pressure trough that formed in (**A**,**B**) was directed down the length of the New South Wales coast in (**C**,**D**) and into Tasmania in (**E**) by the anticyclone that intensified over New Zealand. Only when the anticyclone migrated eastwards into the South-West Pacific in (**F**) could the low-pressure cell move off the coast into the South Tasman Sea (**G**).

4.2. Post Storm Conditions

As the low-pressure trough tracked south down the coast, the mean wave direction at Sydney rotated clockwise from around 70° (East–North–East) at the start of the storm to around 110° (East–South–East) by the early morning of Monday 6 June. Up until this point, buoy observations showed that wave conditions were largely uni-modal, meaning most wave energy was travelling at the same speed from the same direction. This suggests that wave conditions during the peak of the storm were generated from a single source (the low-pressure system). This can be seen in Figure A1 where wave periods and directions at the first and second spectral peaks have similar values. As the storm moved away from Sydney during Monday, the parametric wave data suggests that conditions became bi-modal as the amount of wave energy generated by the low-pressure system was replaced by longer period (Tp_1–14 s) swell from the east. Figure 6D suggests that this long-period easterly swell was generated off the northern limb of the anticyclone situated over New Zealand. Long wave periods between 12 and 14 s were sustained for the following 96 h as wave heights decreased. At the same time, very oblique (southerly) waves were still being produced by the low-pressure system as it tracked south down the east coast (MWD_{Tp2}, Figure A1A).

5. The Importance of Wave Direction for Coastal Risk

5.1. Wave Direction Control on Nearshore Wave Heights

Traditional assessments of coastal risk relate the offshore wave height to beach erosion and inundation with secondary, or no, consideration of wave direction. The June 2016 event highlighted the importance of storm wave direction for coastal impacts at Sydney. The peak storm offshore wave height (6.4 m) was unremarkable yet wave energy conditions at the coast were extra-ordinary (Figure 7).

Figure 7. Nearshore wave conditions at South Narrabeen on Monday 6 June 2016. Authors' and photographer's visual estimates of breaking wave heights from these images are between 4 and 5 m (~13 to 16 ft.). Reproduced with permission from Mark Onorati [38]. The images in (**A**,**C**) are of the beach section behind Narrabeen Fire Station (red brick building in foreground in (**C**)) approximately half the way along the Narrabeen-Collaroy embayment; the image in (**B**) is 100 m north of (**A**,**C**) adjacent to Robertson Street.

The high-energy coastal wave conditions were a result of the unusual offshore wave direction rather than large offshore wave heights. Concurrent wave data previously recorded at the Sydney (mid-shelf) buoy and the nearshore buoy at South Narrabeen (over the period August to November 2011—not during the June 2016 storm), suggest that waves from the north-east to east undergo less energy dissipation (reduction in wave height) and refraction (change in wave direction) when travelling across the continental shelf towards the coast than do waves approaching from the south-east to south (Figure 8). The dissipation coefficients in Figure 8A were calculated as the nearshore H_s divided by the offshore H_s. Likewise, the refraction coefficients in Figure 8B were calculated as nearshore MWD_{Tp1} divided by the offshore MWD_{Tp1}. These values were then normalized between 0 and 1 to make rates of dissipation and refraction comparable across wave directions.

Nearshore wave heights (seaward of shoaling in shallow water) are usually smaller than offshore wave heights because wave energy is dissipated across the shelf and shoreface, principally because of friction with the seabed. The South Narrabeen buoy was moored in ~12 m water depth, meaning most waves recorded at this location were only weakly shoaled and unbroken. Thus, most nearshore wave heights recorded over the observation period were lower than the offshore (mid-shelf) wave height because of energy dissipation across the shelf.

However, the rate of dissipation is often a function of wave direction. Figure 8A indicates that energy dissipation is lowest for waves from the north-east to east, and increases as the wave direction rotates towards the south. Likewise, Figure 8B shows that waves from the south-east to south undergo most refraction to reach the Sydney coast.

The dissipation and refraction coefficients (red lines Figure 8A) were applied to the entire directional wave record at the mid-shelf buoy (1992–2016) to obtain the likely long-term wave height distribution (Figure 8C) and probability of occurrence of wave directions (Figure 8D) at Narrabeen, compared to the offshore wave data. Figure 8C shows that the highest waves recorded offshore come from 160° to 190°, while the highest waves at Narrabeen (centre of embayment, ~12 m water depth) are from 70° to 90°. Similarly, Figure 8D shows that the most frequent waves offshore are from 160° to 180° while the most frequent waves at Narrabeen are from 90° to 110°.

This highlights two important points: first, that the offshore wave observations are not a good representation of the nearshore wave climate at Sydney. Second, that there is a strong directional control on coastal wave conditions at Sydney, which explains how extreme surf zone waves, as shown in Figure 7, can occur for modest offshore storm wave heights when approaching from the north-east to east.

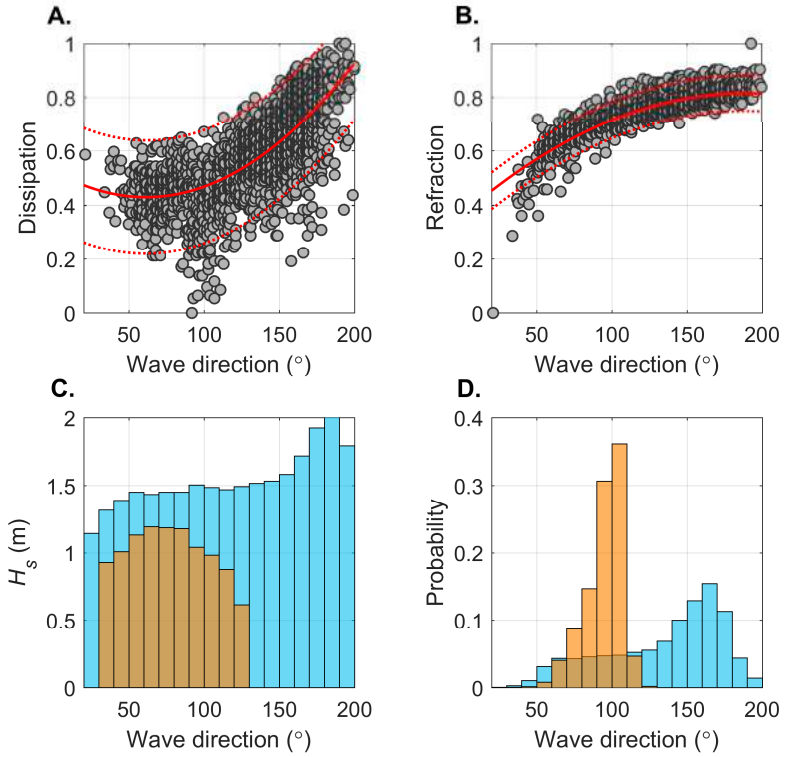

Figure 8. Rates of energy dissipation (**A**) and refraction (**B**) for waves approaching Narrabeen between August and November 2011. Wave direction on the *x*-axis relates to the offshore (mid-shelf) wave direction as measured at the Sydney buoy. Polynomial functions (solid red lines) describe the dissipation/refraction curves with 95% confidence intervals (dashed red lines). The long-term wave height distribution (**C**) and occurrence probability of wave directions (**D**) are shown for the Sydney offshore (blue, observed) and Narrabeen nearshore (orange, modelled) for the period 1992–2016. The Narrabeen nearshore data was obtained by applying the dissipation and refraction coefficients in (**A**,**B**) to the offshore data.

5.2. Wave Direction Control on Nearshore Hydrodynamics

As shown above, the Sydney coast is most exposed to north-east to easterly wave energy, despite south-east to southerly waves being more powerful and frequent offshore. Modelling here shows that the geometry and aspect of the Narrabeen–Collaroy compartment further increases the vulnerability of the Collaroy beachfront to north-east to easterly storm waves because of the effect of wave direction on the nearshore hydrodynamics.

To demonstrate this, the model was run for the June 2016 storm and for another ECL event that impacted Sydney between 19 and 23 April 2015. The April 2015 event had a significantly larger peak storm wave height (H_s 8.0 m) and some of the strongest-ever winds recorded at the Kurnell weather station with gusts exceeding 130 km·h^{-1}. It also produced a more 'regular' south-easterly storm wave direction (145° at the storm peak) than in June 2016. The wave refraction pattern, nearshore current field and sediment transport patterns at Narrabeen–Collaroy at the peak of the storm in April 2015 and June 2016 are shown in Figures 9A–C and 10A–C, respectively. The modelled bathymetric change after each storm event is shown in Figures 9D and 10D.

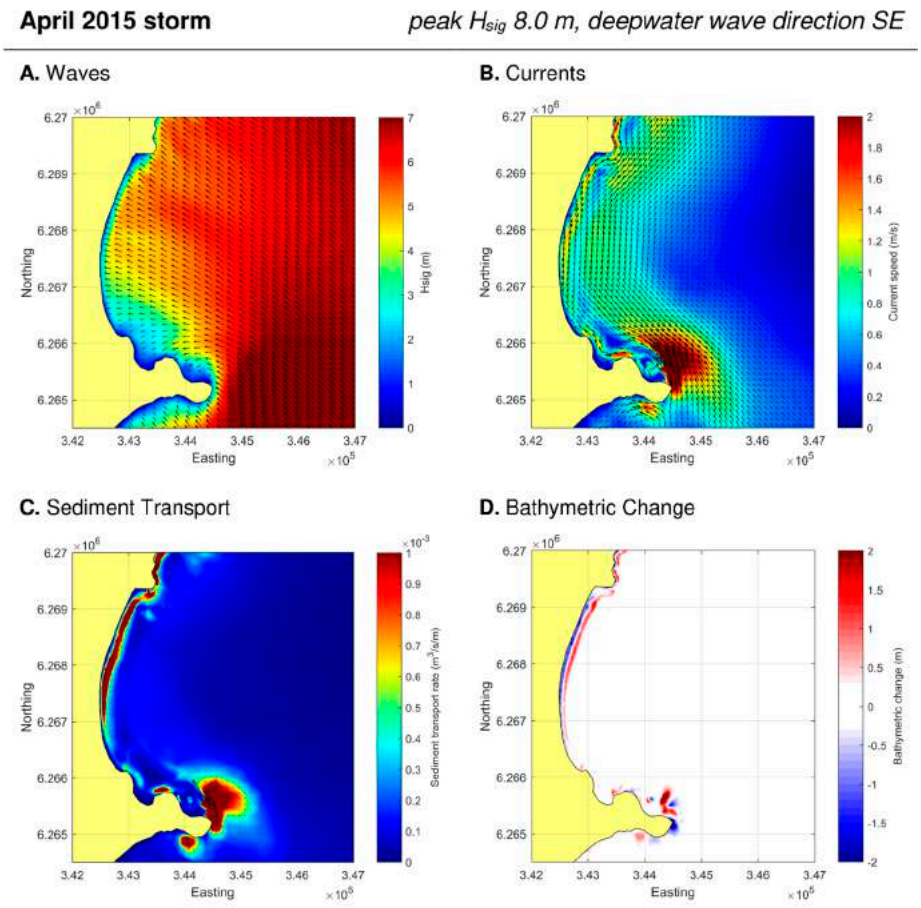

Figure 9. Modelling results for (**A**) significant wave height and mean wave direction; (**B**) current velocity and direction (**C**) sediment transport rate and direction; and (**D**) bathymetric change at Narrabeen–Collaroy during the April 2015 storm event. Results shown in (**A**–**C**) are at the storm peak; while (**D**) is the cumulative change post-event. Bathymetric change in (**D**) less than ±0.03 m was omitted, consistent with limits of model calibration (Section 3).

The modelled flow and transport pattern in June 2016 was very different. The easterly nearshore wave direction produced a southward, rather than northward, alongshore current for almost all beaches on Sydney's Northern Beaches. The only exception to this regional pattern was the Long Reef to Collaroy coastal section where a strong northward littoral current exceeding 2 ms^{-1} at the peak of the storm occurred (Figure 10B). This current met a powerful southward current around Collaroy/South Narrabeen, which the model suggests produced an offshore-directed mega-rip extending out to ~20 m water depth offshore of Collaroy. This current then deflected south and re-entered the surf zone at Long Reef forming a large rip cell.

The positioning of rip currents is well known to correspond to 'erosion hot spots', as the offshore-directed flow scours a trough, lowering the beach level and leaving adjacent dunes (and property) more exposed to storm wave erosion. Figure 11 illustrates how the positioning of the modelled mega-rip current during the peak of the June storm aligns with locations of observed erosion damage. The northward-directed flow between Long Reef and Collaroy was unique within the Northern Beaches region because of the eastward extension of Long Reef headland, which bifurcated the wave-driven current south towards the neighbouring embayment, DeeWhy, and north towards Collaroy.

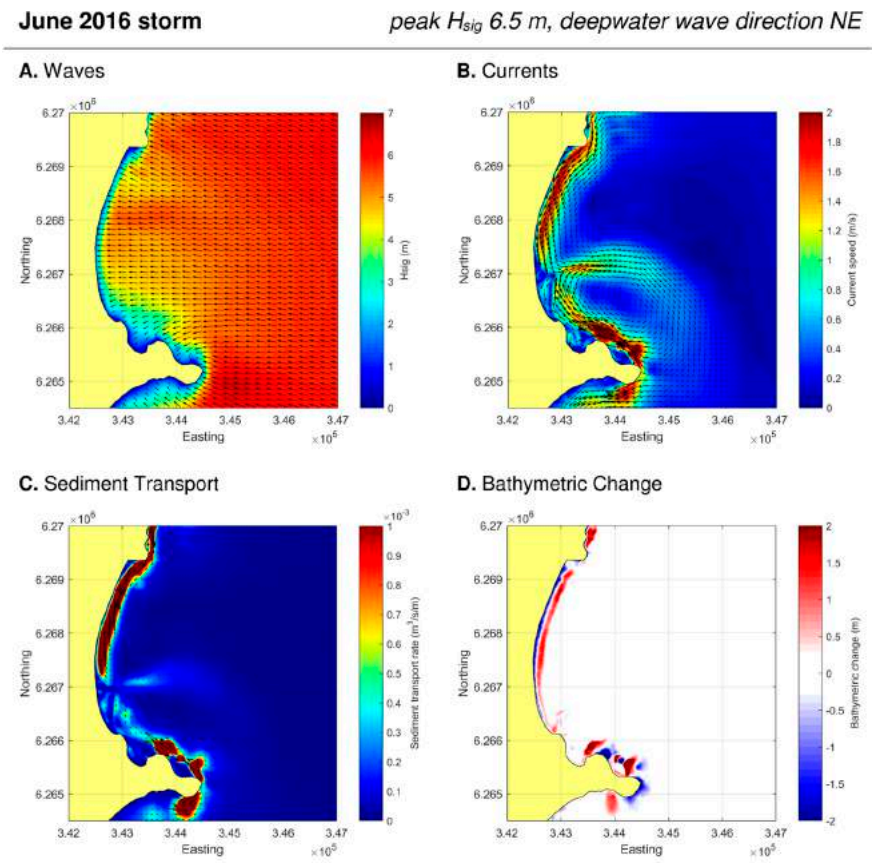

Figure 10. As for Figure 9 but for the June 2016 storm event.

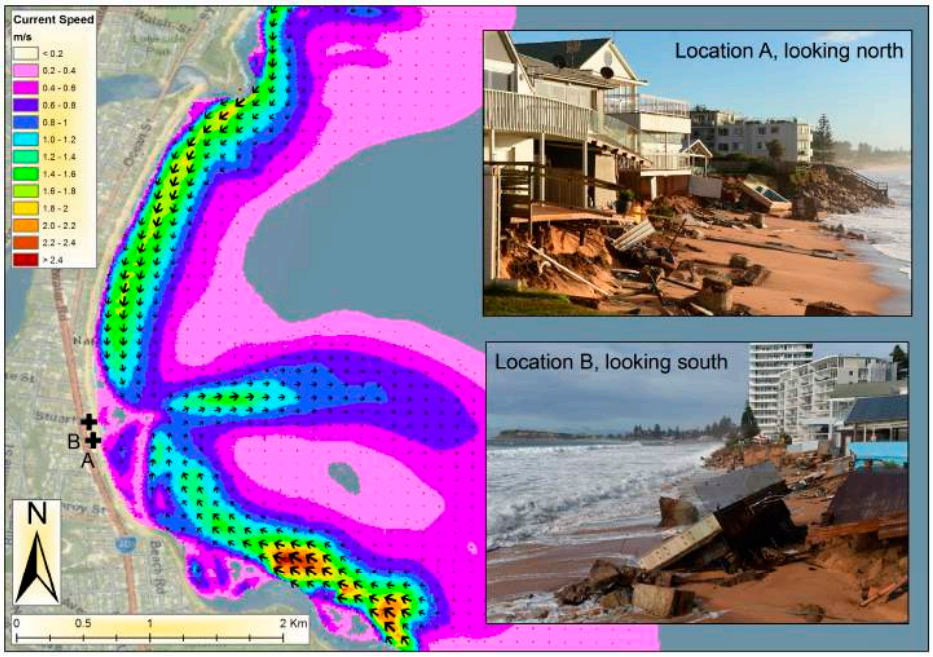

Figure 11. Modelled nearshore current pattern (m/s) at Narrabeen–Collaroy during the peak of the June 2016 storm (as shown in Figure 10B), and locations of observed severe erosion damage at Collaroy. Area of most extreme erosion corresponds to the location of the modelled storm rip current. Source of images Australian Associated Press (rights for reproduction purchased) [39].

The modelled littoral flow velocities, sediment transport rates and volumes of offshore sand movement at Narrabeen–Collaroy were all greater in June 2016 than April 2015, despite significantly lower offshore wave heights in 2016. Long-term beach monitoring [15] also shows that the 2016 storm led to the largest eroded subaerial beach volume at Narrabeen–Collaroy since recording began in 1976. Erosion of the subaerial beach was not explicitly modelled here because of insufficient information on the pre-storm beach condition. On the other hand, the amount of sand moved below the water line within the surf zone is a robust indicator of erosion to the subaerial beach, since the surf zone and beach morphologies at Narrabeen are closely coupled [40]. The same starting bathymetry was used for both storm events, meaning any differences in post-storm surf zone bathymetry are primarily a result of nearshore wave conditions during the two storms.

Our modelling suggests that in April 2015 the surf-zone bar accreted by approximately 90,500 m^3 (an average of ~25 m^3 per m of alongshore length) compared to an accretion of approximately 205,000 m^3 (~60 m^3 per m of alongshore length) in June 2016. The 'bar' was defined as any positive post-storm cumulative bed elevation change over 0.3 m on the upper shoreface. These volumes may not reflect the actual change because of several factors not included in the model as discussed in Section 3. Moreover, not all sand that forms the storm bar comes from the beach. Some sand is also moved from depths seaward of the surf zone because of wave asymmetry leading to a net shoreward transport in depths where there are no breaking waves or undertow [41–43]. The ratio between the offshore/onshore sources depends on the dominance of alongshore or cross-shore transport, which in turn depends on the storm wave direction. Our modelling indicates that during April 2015 over 95% of sand that formed the storm bar originated from the beach, whereas in June 2016 around 85% came from the beach and the remainder from onshore transport outside the surf zone.

The beach monitoring program at Narrabeen shows a slightly lower but comparable ~40% difference between the amount of subaerial beach erosion in June 2016 and April 2015. This is based on the Subaerial Beach Volume Index (SVI), a ratio of the dry beach volume relative to the long-term mean [15]. Prior to the April 2015 event, the beach was close to the mean state (SVI + 2.6), but after the storm it had been reduced to −24.9 (a net change of 27.5). Prior to the June 2016 event, the early winter was characterised by a period of quiescent, southerly waves that had acted to considerably build up the beach (+13.6). After the storm, the beach was down to its lowest SVI value recorded (−34.0)—a net change of 47.6 (thus, a ~40% difference between the April 2015 and June 2016 storms). While this is not directly comparable to the ~50% difference derived from modelling in this study (the monitoring is of the subaerial beach while the modelling is of the subaqueous shoreface), it serves to highlight the magnitude differences in the erosion impacts between the events and is broadly in agreement with the modelled shoreface change.

Bathymetric surveys at Narrabeen (Section 3) and well as the modelling here indicate that sand removed from the subaerial beach during storms does not leave the embayment. Narrabeen and other embayments along the central and south coast of NSW are known to be essentially 'closed' each with a finite sediment budget [44]. Most sand during a storm is transferred down the upper shoreface to around 4–5 m water depth, after which it is progressively reworked shoreward during subsequent non-storm wave conditions. This loss/recovery cycle can be seen in the long-term beach monitoring record at Narrabeen, which shows no significant net change in the subaerial beach volume over the past 40 years [15]. Indeed, previous analyses of the Narrabeen record highlight the importance of time intervals between successive storms in allowing the post-storm recovery of the beach [45,46]. While the beach may recover after a storm, erosion to the foredune and damage sustained to property is lasting.

5.3. Wave Direction Control on Recurrence Estimates

Estimates of the return period, or Average Recurrence Interval (ARI), of storm wave conditions are usually derived from an extreme value analysis of storm peak wave heights from a long-term set of observations. Since wave height is the most important design parameter for coastal engineering, ARI estimates are traditionally non-directional; i.e., one extreme value curve is used for storm wave

conditions from all directions. Per this approach, the ARI estimate for the June 2016 event is only ~2 years (Figure 12A). However, this estimate is misleading because the powerful inshore wave conditions generated by this event were far greater than that seen on average every two years.

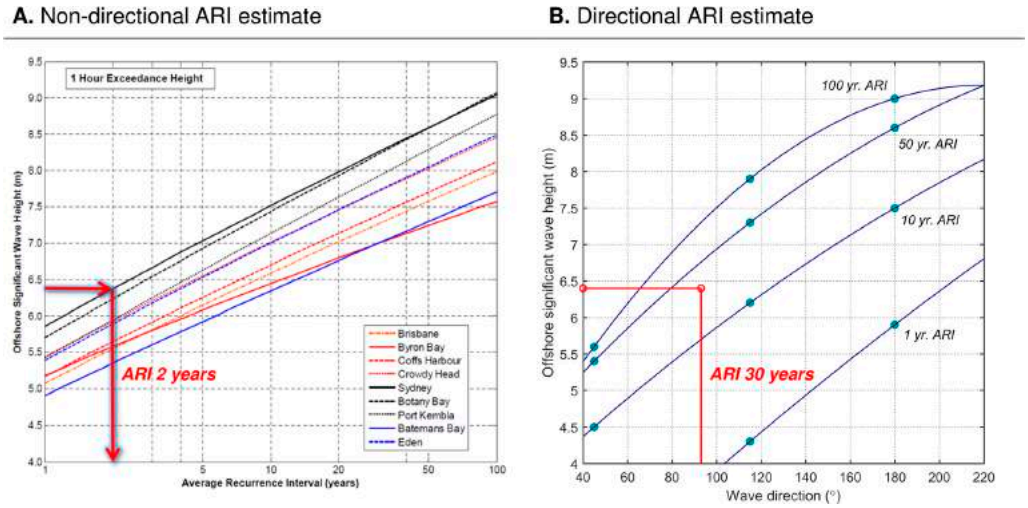

Figure 12. (**A**) Average Recurrence Interval (ARI) estimates for storm wave heights not accounting for wave direction. The peak storm wave height and ARI estimate for the June 2016 event are highlighted (red) for the Sydney buoy (black solid line). Original figure reproduced from [47]; (**B**) ARI estimates for storm wave heights at Sydney accounting for wave direction. Original data from [47].

A more relevant ARI of the June 2016 storm needs to consider wave direction. Shand et al. [47] re-examined ARI estimates at Sydney (up to 2009) for storm waves coming from three directional quadrants; <90° (north-east to east), 90°–135° (south-east), and >135° (south-east to south). We interpolated these results across directional bins (using a second-order polynomial) to obtain an indication of the ARI of peak storm wave heights across all wave directions (Figure 12B). Indicative results here suggest that the June 2016 peak storm conditions (6.4 m H_s from 93°) have an ARI of approximately 30 years when wave direction is considered. It is important to note that this estimate is derived from only 17 years of directional wave data (1992–2009, yet to be updated), which is not considered sufficient for reliable extreme value analysis on the NSW coast [7]. Nonetheless, it serves to demonstrate the importance of accounting for wave direction when estimating the likelihood of recurrence of storm wave conditions. Incorporating wave directional effects into extreme value analyses can significantly affect the design of coastal structures [48,49], especially when projecting future extreme conditions where there may be shifts in the directional wind and wave climate [50,51].

6. Implications for Coastal Management in a Changing Climate

The June 2016 East Coast Low was an unusual storm, both in terms of the synoptic configuration and wave conditions. However, storm wave events from this direction are projected to become more common in Southeast Australia in the future with tropical expansion [6]. One of the most robust signatures of present and near-future climate warming is a widening of the tropics, with a continued poleward expansion of ~1° to 2° projected for later this century [52]. This tropical expansion may lead to an increased frequency of easterly and north-easterly waves along the Southeast Australian coast [51] and, as a result, the regional wave climate is predicted to rotate anticlockwise [50].

It is unclear, however, whether this will be manifest in both the modal and storm wave climate, or whether tropical expansion will lead to an increase in bi-directionality between extreme wave events and the mean state. Currently, there is a ~10° difference between the long-term (past 40 years) modal and storm wave directions along the NSW coast, meaning beach systems are largely equilibrated with the distribution of wave energy during and between storms. However, when extreme wave events

come from different directions to modal conditions, the erosion response is magnified. The June 2016 storm exemplified this, as the east to north-east wave conditions followed several months of quiescent southerly swell.

At present, the minimum criteria for estimating current and future rates of shoreline recession in coastal zone management plans in NSW include recession due to sediment budget deficits and projected sea level rise [53]. The requirements for beach erosion revolve around a storm bite magnitude arising from an event with an ARI of ~100 years [53]. The requirements for both shoreline recession and beach erosion ignore potential changes in wave direction. An allowance for beach rotation (resulting from inter-annual changes in wave direction associated with El Niño Southern Oscillation) is usually included, but this does not address the control that long-term changes in storm wave direction may have on the propagation of wave energy into the nearshore and, as demonstrated here and in previous studies [54,55], on coastal erosion response. Neither does it address the significant influence that wave direction has on the return period estimates of storm events and their resultant erosion potential.

7. Conclusions

The June 2016 East Coast Low storm demonstrates the importance of wave direction for coastal impacts in Southeast Australia. Our modelling shows that the direction of wave propagation across the shelf was the primary control on the amount of energy in the nearshore, rather than the magnitude of storm wave conditions offshore. Dissipation and refraction coefficients derived from simultaneous offshore and nearshore buoy observations also illustrate the importance of wave direction on the nearshore distribution of wave heights and indicate that the offshore wave record alone is a misleading proxy for erosion risk. Hydrodynamic modelling suggests that the Collaroy to South Narrabeen coastal section is particularly vulnerable to erosion impacts during storms from the east to north-east because of the local embayment geometry. A re-assessment of extreme wave heights at Sydney also demonstrates the importance of considering wave direction when deriving storm recurrence parameters for coastal engineering.

Both observational and climate model based studies suggest an anti-clockwise rotation in the mean wave direction for the South-West Pacific region over the coming decades in association with a poleward expansion of the tropics. It is unclear, however, whether these changes will lead to an increase in bi-directionality between the extreme and mean wave climate. As demonstrated in June 2016, the coastal erosion response is magnified when the modal and storm wave directions are different. Assessments of erosion risk in Southeast Australia do not yet consider impacts of future changes to the directional wave climate. This is symptomatic of the global emphasis on sea level rise over wave climate change, and should be identified as an important knowledge gap for coastal management. Our findings are also of relevance for other Southern Hemisphere east coasts in the sub-tropics, such as the Southern Brazil and Natal to Mozambique regions, where tropical expansion may lead to similar changes in the directional wave climate.

Acknowledgments: This research was part funded by a NSW Office for Environment and Heritage (OEH) grant to CI Goodwin as part of the OEH/Sydney Institute of Marine Science (SIMS), Coastal Processes and Response Research Node (Grant Project 1A Quantification of Sand Supply from the NSW Shoreface). Nearshore wave data from buoys deployed at South Narrabeen and Long Reef were collected as part of an Australian Research Council Linkage Project (grant number LP100200348). Wave data from these deployments are available on request from the authors. Wave data from waverider buoys in New South Wales (NSW) and tidal data from the HMAS Penguin tide gauge are collected as part of the NSW Coastal Data Network Program managed by the Office of Environment and Heritage (OEH) and was sourced from Manly Hydraulic Laboratory. Wave data from the Brisbane waverider buoy is funded by State of Queensland, Department of Science, Information Technology, Innovation and the Arts and is available from https://data.qld.gov.au/dataset/coastal-data-system-waves-brisbane. Wind data from the Kurnell automatic weather station was sourced from the Bureau of Meteorology. Beach profile information from the long-term monitoring program at Narrabeen–Collaroy beach was sourced from http://narrabeen.wrl.unsw.edu.au. Pre- and post-storm hydrographic surveys of Narrabeen–Collaroy beach were undertaken by OEH for the OEH/SIMS Coastal Processes and Response Research Node of the NSW Climate Change Adaptation Hub. All other bathymetric data used for modelling was obtained on request from OEH. A Macquarie University academic licence for MIKE by DHI software was used for modelling. Permission for reproduction of images of

wave conditions in Figure 7 was kindly given by the photographer Mark Onorati for use in this publication only. Rights of reproduction of images of coastal damage in Figure 11 was purchased by Risk Frontiers from Australian Associated Press under a Multimedia Commercial Use agreement. The authors also thank the anonymous reviewers of this paper whose comments significantly improved the quality of the manuscript.

Author Contributions: All authors jointly conceived the idea for the paper; Thomas R. Mortlock performed all data analysis and modelling; Thomas R. Mortlock wrote the bulk of the paper; Ian D. Goodwin and Thomas R. Mortlock made observations of the storm meteorology, nearshore wave conditions and coastal impacts; Ian D. Goodwin, Kevin Roche and John K. McAneney made substantial edits to the final draft of the paper.

Conflicts of Interest: The authors declare no conflict of interest.

Appendix A

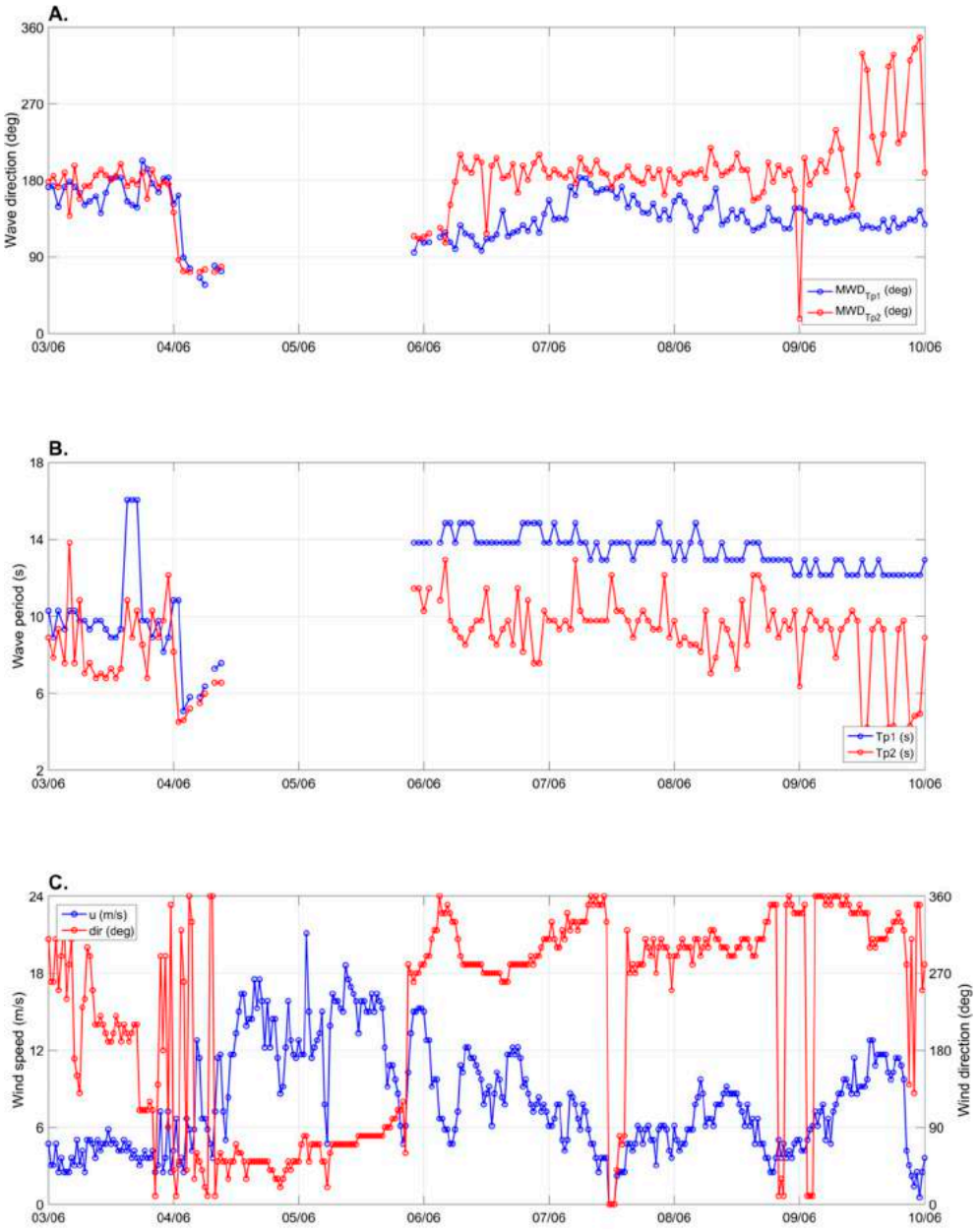

Figure A1. Observations of (**A**) mean wave direction at the first and second spectral peaks (MWD_{Tp1} and MWD_{Tp2}); (**B**) wave period at the first and second spectral peaks (Tp_1 and Tp_2); and (**C**) wind speed (u) and direction (dir) from 3 to 10 June 2016. Wave data was recorded at the Sydney waverider buoy and wind data was recorded at the Kurnell Automatic Weather Station (locations Figure 3).

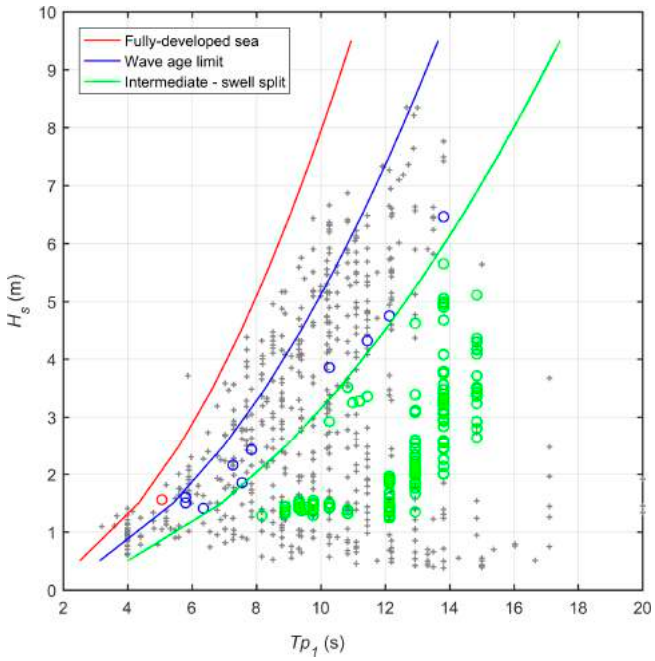

Figure A2. Wave age curves derived from all H_s and T_{p1} values recorded at the Sydney waverider buoy (1987–2016). Grey crosses represent unique wave steepness occurrences at the buoy and circles represent wave conditions as measured during the June 2016 storm. The red line represents the Pierson–Moskowitz limit for fully-developed seas [56]; the green line represents the wave age limit between wind-sea and swell [57]; and the blue line is a line of constant steepness that divides the sea and swell components into two equal parts [24]. All wave events falling between the red and blue lines are 'wind-sea'; between the blue and green lines are 'intermediate sea-swell'; and beyond the green line are 'swell'. In this way, the long-term wave climate defines the divisions between wave types. Values for directional spreading of parametric wave data can then be defined (Section 3.2).

References

1. Crompton, R.P.; McAneney, K.J. Normalised Australian insured losses from meteorological hazards: 1967–2006. *Environ. Sci. Policy* **2008**, *1*, 371–378. [CrossRef]
2. McAneney, J.; McAneney, D.; Musulin, R.; Walker, G.; Crompton, R. Government-sponsored natural disaster insurance pools: A view from down-under. *Int. J. Disaster Risk Reduct.* **2006**, *15*, 1–9. [CrossRef]
3. Taljaard, J.J. *Atmospheric Circulation Systems, Synoptic Climatology and Weather Phenomena of South Africa. Part 2: Atmospheric Circulation Systems in the South African Region*; Department of Environmental Affairs and Tourism, South Africa, Report No. 27-32; South African Weather Bureau: Pretoria, South Africa, 1995.
4. Cuchiara, D.C.; Fernandes, E.H.; Strauch, J.C.; Winterwerp, J.C.; Calliari, L.J. Determination of the wave climate for the southern Brazilian shelf. *Cont. Shelf Res.* **2009**, *29*, 545–555. [CrossRef]
5. Browning, S.; Goodwin, I.D. Large-Scale Influences on the Evolution of Winter Subtropical Maritime Cyclones Affecting Australia's East Coast. *Mon. Weather Rev.* **2013**, *141*, 2416–2431. [CrossRef]
6. Goodwin, I.D.; Mortlock, T.R.; Browning, S. Tropical and Extratropical-Origin Storm Wave Types and Their Contrasting Directional Power Distribution on the Inner Shelf. *J. Geophys. Res. Oceans* **2016**, *121*, 4833–4853. [CrossRef]
7. Louis, S.; Couriel, E.; Lewis, G.; Glatz, M.; Kulmar, M.; Golding, J.; Hanslow, D. NSW East Coast Low Event—3 to 7 June 2016 Weather, Wave and Water Level Matters. In Proceedings of the NSW Coastal Conference, Coffs Harbour, Australia, 9–11 November 2016.
8. International Hydrographic Organization (IHO). *Limits of Oceans and Seas*; International Hydrographic Organization: Bremerhaven, Germany, 1953.

9. Shand, T.D.; Goodwin, I.D.; Mole, M.A.; Carley, J.T.; Browning, S.; Coghlan, I.; Harley, M.D.; Pierson, W.J. *NSW Coastal Inundation Hazards Study: Coastal Storms and Extreme Waves*; Water Research Laboratory (WRL) & Climate Futures at Macquarie University, WRL Technical Report 2010/16; University of New South Wales: Sydney, Australia, 2011.
10. Short, A.D. Role of geological inheritance in Australian beach morphodynamics. *Coast. Eng.* **2010**, *57*, 92–97. [CrossRef]
11. Wright, L.D.; Short, A.D. Morphodynamic Variability of Surf Zones and Beaches: A Synthesis. *Mar. Geol.* **1984**, *56*, 93–118. [CrossRef]
12. Rosati, J.D.; Walton, T.L.; Bodge, K. Chapter III-2 Longshore Sediment Transport. In *Coastal Engineering Manual, Part III*; Vincent, L., Demirbilek, Z., Eds.; U.S. Army Corp of Engineers: Washington, DC, USA, 2002; pp. III-2-1–III-2-109.
13. Splinter, K.D.; Turner, I.L.; Reinhardt, M.; Ruessink, G. Rapid adjustment of shoreline behavior to changing seasonality of storms: Observations and modelling at an open-coast beach. *Earth Surf. Process. Landf.* **2017**. [CrossRef]
14. Poli, P.; Hersbach, H.; Dee, D.P.; Berrisford, P.; Simmons, A.J.; Vitart, F.; Laloyaux, P.; Tan, D.G.H.; Peubey, C.; Thépaut, N.; et al. ERA-20C: An Atmospheric Reanalysis of the Twentieth Century. *J. Clim.* **2016**, *29*, 4083–4097. [CrossRef]
15. Turner, I.L.; Harley, M.D.; Short, A.D.; Simmons, J.A.; Bracs, M.A.; Phillips, M.S.; Splinter, K.D. A multi-decade dataset of monthly beach profile surveys and inshore wave forcing at Narrabeen, Australia. *Sci. Data* **2016**, *3*, 160024. [CrossRef] [PubMed]
16. Short, A.D.; Bracs, M.A.; Turner, I.L. Beach oscillation and rotation: Local and regional response on three beaches in southeast Australia. *J. Coast. Res.* **2014**, *66*, 712–717. [CrossRef]
17. Bracs, M.; Turner, I.L.; Splinter, K.D.; Short, A.D.; Mortlock, T.R. Synchronised patterns of erosion and deposition observed at two beaches. *Mar. Geol.* **2016**, *380*, 196–204. [CrossRef]
18. Nielsen Lord Associates. *Narrabeen-Collaroy Fishermans Beach Coastal Management Strategy, Phase One: Hazard Definition*; Nielsen Lord Associates Report No. 87020.01.003; Prepared for Warringah Shire Council; Wavelength Press: Sydney, Australia, 1988; p. 17.
19. Roche, K.; Goodwin, I.D.; McAneney, J. Management of the coastal zone in Bryon Bay: The neglect of medium-term considerations. *Agenda* **2013**, *20*, 21–39.
20. Wood, J.E.; Roughan, M.; Tate, P.M. Finding a proxy for wind stress over the coastal ocean. *Mar. Freshw. Res.* **2012**, *63*, 528–544. [CrossRef]
21. Holtznagel, S.; Ingleton, T. Field Survey QAQC for Sydney Northern Beaches—Narrabeen Beach Hydro June 2016. In *Single-Beam QAQC Metadata Sheet*; NSW Office of Environment and Heritage: Sydney, Australia, 2016.
22. Danish Hydraulics Institute (DHI). *MIKE21/3 Coupled Model FM User Guide*; MIKE by DHI; Danish Hydraulics Institute: Hørsholm, Denmark, 2016.
23. Cardno. *NSW Coastal Waves: Numerical Modelling Final Report*; Cardno Report No. LJ2949/R2745; Prepared for Office of Environment and Heritage (NSW); Cardno: St Leonards, Australia, 2012; p. 281.
24. Le Cozannet, G.; Lecacheux, S.; Delvallee, E.; Desramaut, N.; Oliveros, C.; Pedreros, R. Teleconnection Pattern Influence on Sea-Wave Climate in the Bay of Biscay. *J. Clim.* **2011**, *24*, 641–652. [CrossRef]
25. Goodwin, I.D.; Mortlock, T.R.; Ribó, M.; O'Brien, P. *Wave Climate and the Distribution of Inner to Middle Shelf Sand Bodies on the South-Eastern Australian Shelf*; Prepared for NSW Office of Environment and Heritage; Marine Climate Risk Group, Macquarie University: Sydney, Australia, 2017.
26. McCormick, M.I. Comparison of field methods for measuring surface topography and their associations with a tropical reef fish assemblage. *Mar. Ecol. Prog. Ser.* **1994**, *112*, 87–94. [CrossRef]
27. Lowe, R.J.; Falter, J.L.; Bandet, M.D.; Pawlak, G.; Atkinson, M.J.; Monismith, S.G.; Koseff, J. Spectral wave dissipation over a barrier reef. *J. Geophys. Res.* **2005**, *110*, C04001. [CrossRef]
28. Thornton, E.B.; Guza, R.T. Transformation of wave height distribution. *J. Geophys. Res.* **1983**, *88*, 5925–5938. [CrossRef]
29. Nielsen, P. *Coastal Bottom Boundary Layers and Sediment Transport*; World Scientific: Singapore, 1992; Volume 4.
30. Huang, Z.-C.; Lenain, L.; Kendall Melville, W.; Middleton, J.H.; Reineman, B.; Statom, N.; McCabe, R.M. Dissipation of wave energy and turbulence in a shallow coral reef lagoon. *J. Geophys. Res.* **2012**, *117*, C03015. [CrossRef]

31. Weber, N. Bottom Friction for Wind Sea and Swell in Extreme Depth-Limited Situations. *J. Phys. Oceanogr.* **1991**, *21*, 149–172. [CrossRef]
32. Sutherland, J.; Peet, A.H.; Soulsby, R.L. Evaluating the performance of morphological models. *Coast. Eng.* **2004**, *51*, 917–939. [CrossRef]
33. Sedigh, M.; Tomlinson, R.; Cartwright, N.; Etemad-Shahidi, A. Numerical modelling of the Gold Coast Seaway area hydrodynamics and littoral drift. *Ocean Eng.* **2016**, *121*, 47–61. [CrossRef]
34. Doering, J.C.; Bowen, A.J. Parameterization of orbital velocity asymmetries of shoaling and breaking waves using bispectral analysis. *Coast. Eng.* **1995**, *26*, 15–33. [CrossRef]
35. Isobe, M.; Horikawa, K. Study on water particle velocities of shoaling and breaking waves. *Coast. Eng. Jpn.* **1982**, *25*, 109–123.
36. Morris, B.; Foulsham, E.; Laine, R.; Wiecek, D.; Hanslow, D. Evaluation of Runup Characteristics on the NSW Coast. *J. Coast. Res.* **2016**, *75*, 1187–1191. [CrossRef]
37. Kalnay, E.; Kanamitsu, M.; Kistler, R.; Collins, W.; Deaven, D.; Gandin, L.; Iredell, M.; Saha, S.; White, G.; Woollen, J.; et al. The NCEP/NCAR 40-year reanalysis project. *Bull. Am. Meteorol. Soc.* **1996**, *77*, 437–471. [CrossRef]
38. Onorati, M. Images of Coastal Wave Conditions at South Narrabeen during the June 2016 Storm. Images taken 06/06/16 Reproduced with Permission from M. Onorati for This Publication Only. Available online: https://www.instagram.com/markonorati/ (accessed on 5 November 2016).
39. Australian Associated Press (AAP). *Images of Coastal Erosion Damage at South Narrabeen During the June 2016 Storm*; Images Taken 07/06/16; Image ID 20160607001262647757 and 20160607001262620563, Purchased under Commercial Agreement by Risk Frontiers 02/12/16; Australian Associated Press: Sydney, Australia, 2016.
40. Harley, M.D.; Turner, I.L.; Short, A.D. New insights into embayed beach rotation: The importance of wave exposure and cross-shore processes. *J. Geophys. Res. Earth Surf.* **2015**, *120*, 1470–1484. [CrossRef]
41. Patterson, D.C.; Nielsen, P. Depth, bed slope and wave climate dependence of long term average sand transport across the lower shoreface. *Coast. Eng.* **2016**, *117*, 113–125. [CrossRef]
42. O'Donoghue, T.; Wright, S. Flow tunnel measurements of velocities and sand flux in oscillatory sheet flow for well-sorted and graded sands. *Coast. Eng.* **2004**, *51*, 1163–1184. [CrossRef]
43. Ruessink, B.G.; Michallet, H.; Abreu, T.; Sancho, F.; Van der A, D.A.; Van der Werf, J.J.; Silva, P.A. Observations of velocities, sand concentrations, and fluxes under velocity-asymmetric oscillatory flows. *J. Geophys. Res. Oceans* **2011**, *116*, 2156–2202. [CrossRef]
44. Short, A.D. *Beaches of the New South Wales Coast: A Guide to Their Nature, Characteristics, Surf and Safety*, 2nd ed.; Sydney University Press: Sydney, Australia, 2007.
45. Callaghan, D.P.; Nielsen, P.; Short, A.; Ranasinghe, R. Statistical simulation of wave climate and extreme beach erosion. *Coast. Eng.* **2008**, *55*, 375–390. [CrossRef]
46. Karunarathna, H.; Pender, D.; Ranasinghe, R.; Short, A.D.; Reeve, D.E. The effects of storm clustering on beach profile variability. *Mar. Geol.* **2014**, *348*, 103–112. [CrossRef]
47. Shand, T.; Mole, M.A.; Carley, J.T.; Peirson, W.L.; Cox, R.J. *Coastal Storm Data Analysis: Provision of Extreme Wave Data for Adaptation Planning*; Water Research Laboratory (WRL) Technical Report 2011/242; University of New South Wales: Sydney, Australia, 2011.
48. Jonathon, P.; Ewans, K. The effect of directionality on extreme wave design criteria. *Ocean Eng.* **2007**, *34*, 1977–1994. [CrossRef]
49. Thompson, P.; Cai, Y.; Reeve, D.; Stander, J. Automated threshold selection methods for extreme wave analysis. *Coast. Eng.* **2009**, *10*, 1013–1021. [CrossRef]
50. Hemer, M.A.; Fan, Y.; Mori, N.; Semedo, A.; Wang, X.L. Projected changes in wave climate from a multi-model ensemble. *Nat. Clim. Chang.* **2013**, *3*, 471–476. [CrossRef]
51. Mortlock, T.R.; Goodwin, I.D. Directional wave climate and power variability along the Southeast Australian shelf. *Cont. Shelf Res.* **2015**, *98*, 36–53. [CrossRef]
52. Lucas, C.; Timbal, B.; Nguyen, H. The expanding tropics: A critical assessment of the observational and modeling studies. *WIREs Clim. Chang.* **2014**, *5*, 89–112. [CrossRef]
53. Office of Environment and Heritage (OEH). *Guidelines for Preparing Coastal Zone Management Plans*; Report No. OEH 2013/0224; Office of Environment and Heritage: Sydney, Australia, 2013; p. 26.

54. Splinter, K.D.; Davidson, M.A.; Golshani, A.; Tomlinson, R. Climate controls on longshore sediment transport. *Cont. Shelf Res.* **2012**, *48*, 146–156. [CrossRef]
55. Zacharioudaki, A.; Reeve, D.E. Shoreline evolution under climate change wave scenarios. *Clim. Chang.* **2011**, *108*, 73–105. [CrossRef]
56. Pierson, W.J.; Moskowitz, L. A proposed spectral form for fully developed wind seas based on the similarity theory of A.A. Kitaigorodskii. *J. Geophys. Res.* **1964**, *69*, 5181–5190. [CrossRef]
57. Carter, D.J.T. Prediction of wave height and period for a constant wind velocity using the JONSWAP results. *Ocean. Eng.* **1982**, *9*, 17–33. [CrossRef]

water

MDPI

Article

Statistical Analysis of the Spatial Distribution of Multi-Elements in an Island Arc Region: Complicating Factors and Transfer by Water Currents

Atsuyuki Ohta *, Noboru Imai, Yoshiko Tachibana and Ken Ikehara

National Institute of Advanced Industrial Science and Technology, Geological Survey of Japan, Central 7, 1-1-1 Higashi, Tsukuba, Ibaraki 305-8567, Japan; noboru.imai@aist.go.jp (N.I.); y.tachibana@aist.go.jp (Y.T.); k-ikehara@aist.go.jp (K.I.)

* Correspondence: a.ohta@aist.go.jp; Tel.: +81-29-861-3848; Fax: +81-29-861-3566

Academic Editor: Sylvain Ouillon

Received: 13 October 2016; Accepted: 5 January 2017; Published: 10 January 2017

Abstract: The compositions and transfer processes affecting coastal sea sediments from the Seto Inland Sea and the Pacific Ocean are examined through the construction of comprehensive terrestrial and marine geochemical maps for western Japan. Two-way analysis of variance (ANOVA) suggests that the elemental concentrations of marine sediments vary with particle size, and that this has a greater effect than the regional provenance of the terrestrial material. Cluster analysis is employed to reveal similarities and differences in the geochemistry of coastal sea and stream sediments. This analysis suggests that the geochemical features of fine sands and silts in the marine environment reflect those of stream sediments in the adjacent terrestrial areas. However, gravels and coarse sands do not show this direct relationship, which is likely a result of mineral segregation by strong tidal currents and the denudation of old basement rocks. Finally, the transport processes for the fine-grained sediments are discussed, using the spatial distribution patterns of outliers for those elements enriched in silt and clay. Silty and clayey sediments are found to be transported and dispersed widely by a periodic current in the inner sea, and are selectively deposited at the boundary of different water masses in the outer sea.

Keywords: geochemical map; particle transfer process; tidal current; analysis of variance (ANOVA); Cluster analysis; Mahalanobis' generalized distances; Seto Inland Sea

1. Introduction

The Geological Survey of Japan, part of the National Institute of Advanced Industrial Science and Technology (AIST), provides nationwide geochemical maps of elements within stream and marine sediments [1]. These geochemical maps have been utilized to explore mineral occurrences and determine the natural abundance of elements, and nationwide and cross-boundary geochemical maps have been developed for such purposes in many countries (e.g., [2–6]). In addition, Japanese geochemical maps have also been created specifically for the purposes of environmental assessment. Ohta and Imai [7] demonstrate an additional use of land and marine geochemical maps, examining particle transfer processes from the land to the sea, or within the marine environment. However, determining provenances with geochemical maps is typically challenging, due to the mixing and homogenization of marine sediments, especially fine sediments such as silt, during transport (e.g., [8]).

In this study, we sought to use geochemical maps of the provenance and transfer analyses of coastal sea sediments in the Chugoku and Shikoku regions, including the Seto Inland Sea and nearby Pacific Ocean as inner and outer seas, respectively (Figure 1a). This region is appropriate for clarifying the influence of terrestrial source materials on the adjacent marine environment, because most rock

types found in Japan are distributed in the study area. The Seto Inland Sea is subject to significant tidal variation, while the Pacific Ocean off the Shikoku region is influenced by the Kuroshio Current and the Kuroshio Counter-Current. A number of previous studies of the Seto Inland Sea have analyzed the seafloor topography [9], periodic currents [10], marine organization [11], surface sediments [12], particle transport by marine currents [13,14], and contamination processes [15]. Therefore, this region is well-understood and is considered suitable for investigations into water-current transport processes, especially those between an inner and outer sea. The present study is intended to objectively reveal the complex factors affecting the spatial distributions of elements in coastal sea sediments using various statistical analyses.

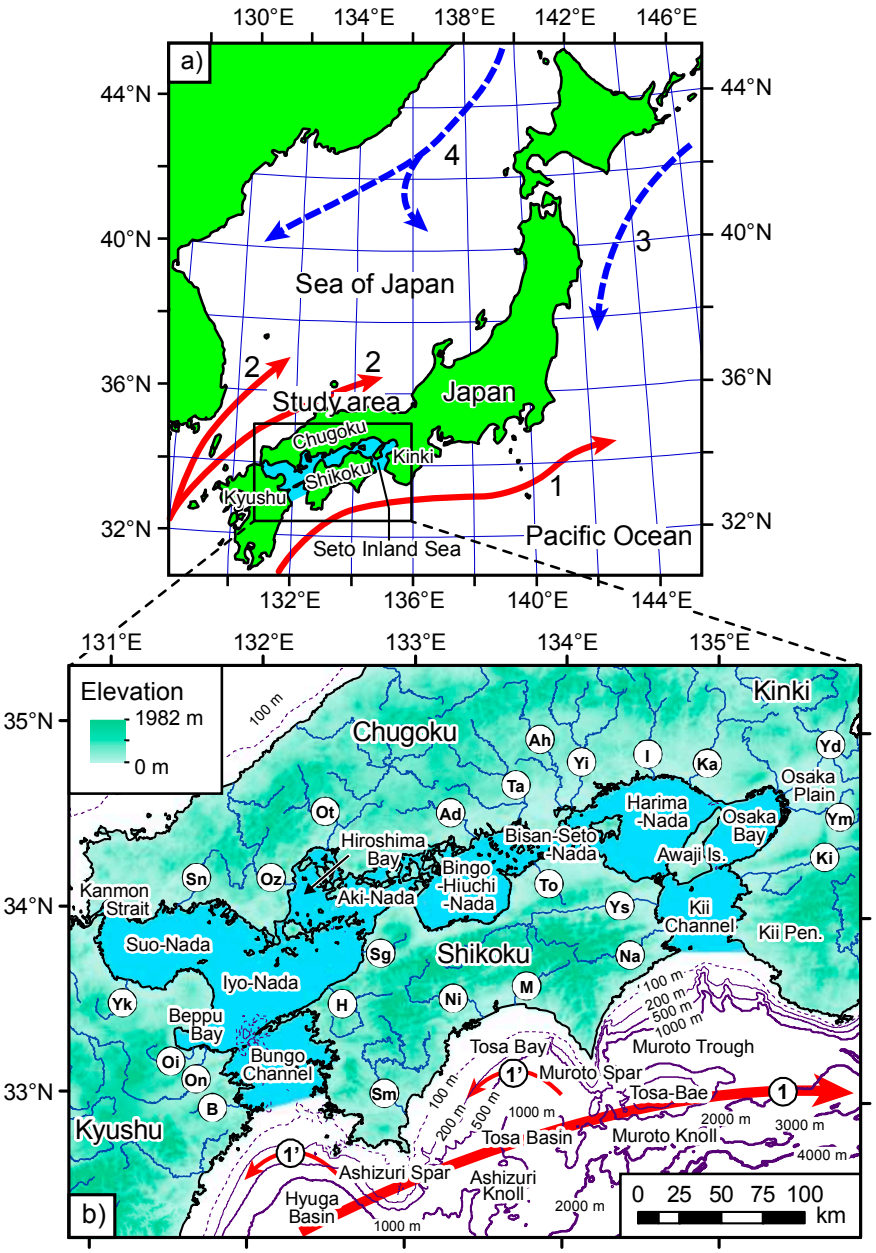

Figure 1. (**a**) Generalized location map of the study area; (**b**) Geographic map of the study area. Solid blue lines in terrestrial areas show major rivers. The abbreviations indicate the river names, as listed in Table A1. The blue colored area is the Seto Inland Sea. 1: Kuroshio Current; 1': Kuroshio Counter-Current; 2: Tsushima-Current; 3: Oyashio-Current; 4: Liman-Current. Bathymetric depth contours are delineated using a dataset provided by the Japan Oceanographic Data Center.

2. Geological and Marine Settings

2.1. Riverine System

Figure 1b presents a generalized location map of the study area showing the 24 major rivers. The region is mainly mountainous with small tracts of flat land. The bed slope of the streams on Shikoku Island and the Kii Peninsula is very steep, so rainwater is immediately discharged through the rivers to the sea. Table 1 presents the potential sediment yield from each terrestrial region, which is calculated using the data of Akimoto et al. [16] (Appendix A). Several rivers in the Chugoku and Kyushu regions that flow directly into the Sea of Japan, and from which marine sediments were collected, are not discussed in this study. In this regard, the sediment yield data of these rivers are excluded from Table 1. The Yodo, Yoshino, and Shimanto Rivers are the three largest rivers, each with a high sediment yield (Yd, Ys, and Sm, respectively, in Figure 1b), and the Chugoku, Kinki, Shikoku, and Kyushu regions supply 15%, 5%, 5%, and 1% of the total sediment yield to the Seto Inland Sea, respectively. Therefore, it can be seen that most sediments in the Seto Inland Sea originate from the Chugoku region. The Yodo River flows through several large cities, including Kyoto and Osaka, and discharges into Osaka Bay. Together, the Yodo and Yamato Rivers supply 19% of the total sediment yield to Osaka Bay. Rivers on Shikoku Island are the primary source of sediments to the Pacific Ocean side with 22% of the total sediment yield supplied to Tosa Bay. The Kii Channel also receives a high sediment discharge of 23% from Shikoku Island and the Kii Peninsula. In contrast, little sediment is discharged from rivers into the Bungo Channel.

Table 1. Sediment yield of each region and discharge to adjacent marine environment.

Region	Discharged Area			
	Pacific Ocean	Kii or Bungo Channel	Seto Inland Sea	Inner Bay
Chugoku region	0%	0%	15%	4% to Hiroshima Bay
Kinki region	0%	5% to Kii Channel	5%	19% to Osaka Bay
Shikoku region	22%	18% to Kii Channel	5%	0%
Kyushu region	0%	1% to Bungo Channel	1%	5% to Beppu Bay

2.2. Geology and Terrestrial Metalliferous Deposits

Figure 2 presents a geological map of the study area, simplified from the Geological Map of Japan 1:1,000,000 [17]. The geology varies considerably between the Chugoku, Kinki, Shikoku, and Kyusyu regions. Rhyolitic-dacitic volcanic rocks and granitic rocks of Cretaceous and Paleogene age are widely distributed in the Chugoku region. In addition, Permian accretionary complexes associated with large limestone blocks, and Triassic high-pressure Sangun metamorphic rocks outcrop in western and central Chugoku. On Shikoku Island, the zonal arrangement of rock units from north to south is as follows: (1) Cretaceous granite-granodiorite; (2) Cretaceous sedimentary rocks; (3) Jurassic–Cretaceous high-pressure Sambagawa metamorphic rocks, comprising quartz schist and greenschist, associated with Mikabu greenstones consisting of basaltic, pyroclastic and ultramafic rocks; and (4) sedimentary rocks of accretionary complexes dated mainly to the Cretaceous-Paleogene. These rock types also outcrop on southern Kyushu Island and on the Kii Peninsula, while andesitic volcanic rocks and debris-pyroclastic rocks of Neogene-Quaternary age extensively outcrop in the northeast of Kyushu Island. Sedimentary rocks of accretionary complexes dating mostly to the Jurassic-Cretaceous outcrop in the northern Kinki region. Unconsolidated Quaternary sediments are restricted in distribution, occurring mainly in the Kinki region. The Osaka Plain is formed of these Quaternary sediments and is the widest plain in the entire study area, with a population of approximately 10 million people.

Figure 2 also shows the locations of some major economic metalliferous deposits. The Besshi mine is the largest Copper (Cu) mine in Japan, and the Kaneuchi and Ohtani mines are large-scale Tungsten-Tin (W-Sn) mines. The Ikuno and Akenobe mines are the largest polymetallic mineralization mines, and the Ichinokawa mine has the highest levels of Antimony (Sb) in Japan.

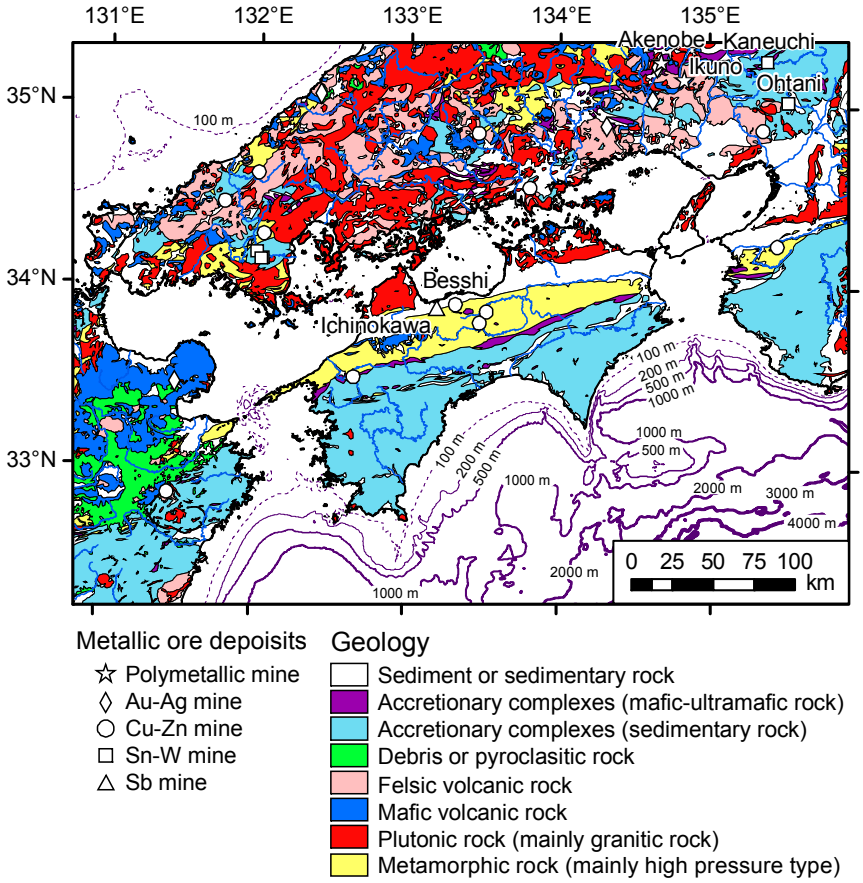

Figure 2. Geological map of the study area simplified from the Geological Map of Japan 1:1,000,000 [17].

2.3. Marine Topography, Hydrographic Condition, and Geology

The Seto Inland Sea is mostly less than 60 m deep, and passes through to the Pacific Ocean through the Bungo and Kii Channels, and to the Sea of Japan through the Kan-mon Strait. The Seto Inland Sea is divided into several regions, termed "Nada", for example, Suo-Nada, Iyo-Nada, Aki-Nada, Bingo-Nada, Hiuchi-Nada, Bisan-Seto-Nada, and Harima-Nada (Figure 1b). Periodic currents flow from the Pacific Ocean through the Bungo and Kii Channels, meeting at Hiuchi-Nada and concentrating fine sediments in the water mass there [10,18]. The marine geology of the Seto Inland Sea comprises mainly glacial to Holocene sediments [12].

The Pacific side of Shikoku Island is characterized by a narrow continental shelf. Topographic highs include Ashizuri Spar, Muroto Spar, Tosa-Bae, Ashizuri Sea Knoll, and Muroto Sea Knoll, and consist of Miocene-Pliocene siltstones, which include benthic foraminifer fossils that are distributed in the deep sub-bottom of the basin [19] In contrast, Tosa Basin, Hyuga Basin, and Muroto Trough are deep-sea basins in which the water depth exceeds 1000 m. Tosa Basin is covered thickly by Quaternary turbidite deposits. The continental shelf and slope of Tosa Bay, the Kii Channel, and the Bungo Channel comprise delta deposits formed during Quaternary regression and transgression cycles [19]. Within the water mass, the Kuroshio Current flows off the coast of Shikoku Island from the southwest to the northeast, while the Kuroshio Counter-Current flows anticlockwise in Tosa Bay and Hyuga Basin [20,21] (Figure 1b).

3. Materials and Methods

3.1. Samples, Sampling Methods, and Processing

Terrestrial and marine sampling locations are presented in Figure 3. A total of 554 stream samples were collected from the study area for a regional geochemical mapping project during 1999–2004 [22]. In addition, for the current study, 22 stream sediments were collected in 2008 from small islands, including Awaji Island in the Seto Inland Sea. Sediment sample were air-dried and sieved using a 180 μm (83-mesh) screen. Magnetic minerals were removed from the sieved samples using a magnet, to minimize the effect of magnetic mineral accumulation [22,23].

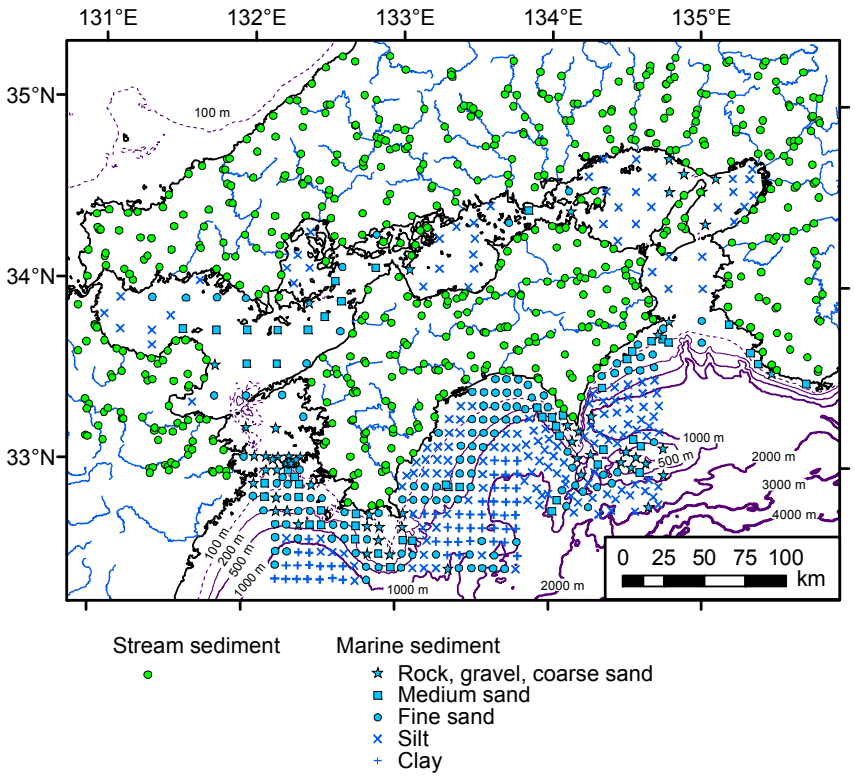

Figure 3. Sample locations for stream and coastal sea sediments.

A total of 366 marine samples were collected from the Pacific Ocean during cruises GH82-1 and GH83-2, in 1982 and 1983, respectively [24–26]. In addition, 97 samples were collected from the Seto Inland Sea and around the Kii Peninsula in 2005. The total 463 samples were collected using a K-grab sampler, and the uppermost 3 cm of each sediment sample was separated, air-dried, ground with an agate mortar and pestle, and retained for chemical analysis. Some samples were composed mainly of rock fragments and gravels, in which case, the sandy infilling materials were collected. The particle sizes of 223 marine sediments were determined, based on the median particle diameter of the surface sediments, and were classified as: coarse sediments, comprising lithic fragments, gravels, and coarse sand; medium sand; fine sand; silt; and clay (Figure 3). The median particle diameter was not measured for the remaining 240 samples, so their classification is based solely on a visual inspection of texture.

Figure 3 shows that silty sediments occur in Suo-Nada, Hiuchi-Nada, Bingo-Nada, and Harima-Nada, as well as basins affected by small periodic current flows or eddies [10]. These localities are also associated with high turbidity [12,27]. Coarse sands were collected from Aki-Nada and Bisan-Seto-Nada, and in northeastern Iyo-Nada. Rocks, gravels, and coarse sands occur in the Bungo Channel. In contrast, the Kii Channel is dominated by silty sediments, despite the presence of high velocity periodic currents similar to those in the Bungo Channel. This is likely due to the greater

terrestrial sediment supply to the Kii Channel (18%) compared with the Bungo Channel (1%) (Table 1). On the Pacific side, silty sediments are widely distributed obliquely across the depth contour in the western part of Tosa Bay. Fine sands are found: (1) near to river mouths; (2) at water depths of 100–500 m on the shelf and slope off Tosa Bay; and (3) around Ashizuri Knoll and Muroto Knoll where the water depth is 500–1600 m. Silty and clayey sediments are found in Tosa Basin, Hyuga Basin, and Muroto Trough, where the water depth exceeds 1000 m, and rock, gravels, and coarse sands were sampled from the topographic highs of Ashizuri Spar, Muroto Spar, and Tosa-Bae.

3.2. Geochemical and Spatial Analyses

The geochemical analytical method is detailed by Imai [28]. Each 0.2 g sample was digested using HF, HNO_3, and $HClO_4$ solutions at 120 °C for 2 h. The degraded solution was evaporated to dryness at 200 °C, before the residue was dissolved in 100 mL of 0.35 M HNO_3 solution. Concentrations of Na_2O, MgO, Al_2O_3, P_2O_5, K_2O, CaO, MnO, total (T-) Fe_2O_3, V, Sr, and Ba were determined using ICP atomic emission spectrometry, while contents of Li, Be, Sc, Cr, Co, Ni, Cu, Zn, Ga, Rb, Nb, Y, Mo, Cd, Sn, Sb, Cs, lanthanides (Ln: La–Lu), Ta, Tl, Pb, Bi, Th, and U were measured using ICP mass spectrometry. Analyses of As in all samples and Hg in stream sediment samples were subcontracted to ALS Chemex in Vancouver, B.C. Levels of Hg in marine sediments were determined using an atomic absorption spectrometer that measured the quantity of Hg vapor generated by direct thermal decomposition. Table 2 presents a summary of the analytical results obtained from the marine and stream sediments. The Na_2O component of marine sediments should be used only as a guide, since these marine sediments were not desalinated.

Table 2. Summary for the geochemistry of marine sediments (n = 463) and stream sediments (n = 576).

Element	Marine Sediment				Stream Sediment			
	Min	Mean	Median	Max	Min	Mean	Median	Max
wt %								
Na_2O	0.91	2.97	2.82	6.35	0.46	2.10	2.04	4.42
MgO	0.49	2.77	2.68	6.71	0.19	2.10	1.65	9.79
Al_2O_3	2.01	9.49	9.60	16.62	3.91	11.39	11.52	17.94
P_2O_5	0.025	0.113	0.108	2.56	0.021	0.125	0.109	1.22
K_2O	0.53	2.03	2.06	3.12	0.66	2.18	2.24	3.79
CaO	0.33	6.51	5.22	34.1	0.12	1.83	1.41	8.40
TiO_2	0.087	0.501	0.492	2.15	0.14	0.71	0.60	3.28
MnO	0.012	0.082	0.066	0.451	0.014	0.128	0.116	1.10
T-Fe_2O_3	0.73	4.91	4.38	23.7	1.41	5.24	4.67	15.8
mg/kg								
Li	7.58	51.9	50.0	136	9.33	38.5	38.3	107
Be	0.32	1.41	1.44	2.25	0.71	1.77	1.67	4.75
Sc	1.77	9.82	9.69	35.1	2.31	11.6	9.57	46.8
V	11.7	84.8	80.1	680	10.9	103	83.4	420
Cr	6.50	58.0	59.0	172	4.47	84.9	52.8	884
Co	1.76	10.9	9.90	41.2	1.79	13.8	11.5	60.7
Ni	1.35	28.2	28.8	138	1.38	34.3	21.7	349
Cu	2.42	20.5	18.4	86.6	5.66	49.7	31.5	2599
Zn	16.1	88.1	80.9	347	17.1	165	118	11,444
Ga	2.77	13.5	14.2	19.0	6.97	17.4	17.2	31.7
As	0.2	6.3	5.0	68	1.0	18.2	8.1	1578
Rb	17.7	73.2	74.9	114	12.3	105	103	265
Sr	70.2	326	259	2525	23.4	133	111	1321
Y	4.95	12.9	12.6	28.8	2.24	19.6	18.7	63.6
Nb	1.59	6.79	6.80	13.9	2.88	9.75	8.86	33.3
Mo	0.14	0.76	0.63	14.8	0.25	1.34	0.99	27.4
Cd	0.018	0.101	0.081	0.480	0.019	0.29	0.16	28.7
Sn	0.37	2.15	1.98	18.9	0.87	5.05	3.47	170
Sb	0.092	0.59	0.55	1.89	0.099	0.98	0.74	17.2
Cs	0.60	4.06	4.25	7.65	0.41	5.63	5.03	33.6
As	0.2	6.3	5.0	68	1.0	18.2	8.1	1578
Ba	67.4	340	340	1649	136	429	431	855
La	5.31	16.0	16.5	24.7	4.73	21.2	19.9	69.2
Ce	12.8	33.8	34.6	58.7	7.20	39.2	36.9	170

Table 2. *Cont.*

Element	Marine Sediment				Stream Sediment			
	Min	Mean	Median	Max	Min	Mean	Median	Max
Pr	1.28	3.78	3.87	5.75	1.06	4.90	4.63	20.8
Nd	5.22	15.0	15.3	22.2	4.08	19.2	18.2	79.9
Sm	1.02	3.02	3.09	4.59	0.78	3.94	3.71	17.4
Eu	0.29	0.68	0.68	1.15	0.18	0.81	0.78	1.72
Gd	0.92	2.72	2.74	4.44	0.61	3.63	3.39	12.9
Tb	0.16	0.45	0.45	0.78	0.10	0.63	0.59	2.02
Dy	0.80	2.23	2.20	4.07	0.51	3.21	3.03	10.3
Ho	0.16	0.42	0.42	0.80	0.091	0.62	0.59	2.01
Er	0.47	1.23	1.19	2.34	0.26	1.83	1.76	6.29
Tm	0.069	0.19	0.19	0.36	0.036	0.29	0.28	1.05
Yb	0.41	1.18	1.15	2.20	0.21	1.82	1.74	6.88
Lu	0.051	0.17	0.16	0.31	0.032	0.26	0.25	1.03
Ta	0.13	0.61	0.60	1.23	0.28	0.85	0.75	5.23
Hg	0.0005	0.139	0.138	5.19	0.010	0.117	0.060	4.60
Tl	0.068	0.48	0.49	1.00	0.075	0.64	0.61	2.52
Pb	5.00	20.8	18.6	126	7.19	43.8	27.3	4177
Bi	0.036	0.32	0.28	1.43	0.033	0.52	0.30	32.1
Th	1.50	5.81	6.04	26.6	1.52	9.53	7.30	259
U	0.28	1.35	1.26	4.51	0.53	2.13	1.70	31.9

The spatial distributions of elemental concentrations in both the terrestrial and marine environments were plotted using geographic information system software (ArcGIS 10.3; Environmental Systems Research Institute (ESRI) Japan Corporation, Tokyo, Japan) after Ohta et al. [29]. Different classes of elemental concentrations are applied to the terrestrial and marine environments, because the chemical and mineralogical compositions of sediments differ according to particle size see the details in [7,8]. This simply improves geovisualization of the geochemical maps. If the same classification is applied to the geochemical maps of both terrestrial and marine environments, the regional geochemical differences (as depicted by color variation) of most of the elements in the land or the sea will be obscured [7,8]. For example, for CaO and Sr, which show higher concentrations in the marine sediments (Table 2), their geochemical differences in the terrestrial areas would be obscured in resulting maps using the same classification, as shown in the Legend. Percentile ranges are used for the selection of elemental concentration intervals in the geochemical maps: $0 \leq x \leq 5$, $5 < x \leq 10$, $10 < x \leq 25$, $25 < x \leq 50$, $50 < x \leq 75$, $75 < x \leq 90$, $90 < x \leq 95$, and $95 < x \leq 100$%, where x represents the elemental concentration [30]. This class selection is advantageous in that the same range of percentiles (e.g., 90%–95%) implies the same statistical weight, even at different numerical scales [7,8,30]. Subsequent statistical analysis of geochemical data is performed using EXCEL TOUKEI 7.0 (ESUMI Co. Ltd., Tokyo, Japan).

4. Results

4.1. Spatial Distribution of Terrestrial Elemental Concentrations

Figure 4 shows the terrestrial and marine geochemical maps for 12 elements. Mikoshiba et al. [23] and Ohta et al. [31,32] have examined the factors controlling spatial distribution patterns of terrestrial elemental concentrations. Be, Na_2O, K_2O, Rb, Y, Nb, Ba, Ln, Ta, Th, and U are abundant in the Chugoku region and in the northern part of Shikoku Island where predominantly granitic and felsic volcanic rocks outcrop. Stream sediments derived from granitic rocks are enriched in Li, Be, Na_2O, K_2O, Rb, Y, Nb, Ln, Ta, Th, and U. Felsic volcanic rocks also elevate the K_2O, Rb, and Ba contents of stream sediments. Li and Cs are abundant in muddy sedimentary rocks and the mélange matrix of accretionary complexes in northern Kinki. In contrast, the sandstone-dominated sedimentary rocks of accretionary complexes in the southern part of Shikoku Island and the Kii Peninsula contain fewer elements. Mafic volcanic rocks associated with debris flows and pyroclastic rocks around Aso volcano, and metamorphic rocks, dominantly greenschist, on Shikoku Island and the Kii Peninsula, elevate MgO, Al_2O_3, P_2O_5, CaO, Sc, V, TiO_2, MnO, T-Fe_2O_3, Cr, Co, Ni, and Cu concentrations in the stream sediments. Additionally, extreme enrichments of MgO, Cr, Co, and Ni are caused by the presence

of mafic-ultramafic rocks associated with accretionary complexes. Finally, elevated concentrations of P_2O_5, Cu, Zn, Mo, Cd, Sn, Sb, Hg, Pb and Bi are found in Osaka Plain, which is polluted by anthropogenic activity [32].

Therefore, lithology is considered to be the main factor affecting the concentrations of elements in stream sediments. For reference, the median elemental concentrations of stream sediments according to their representative rock type, which outcrops over more than half of the drainage basin, are summarized in Appendix B. It should be noted that Cu, Zn, As, Mo, Cd, Sn, Sb, Hg, Pb, and Bi are extremely enriched near to known metalliferous deposits, however, the effects of these mineral deposits on the geochemical maps are restricted to limited areas.

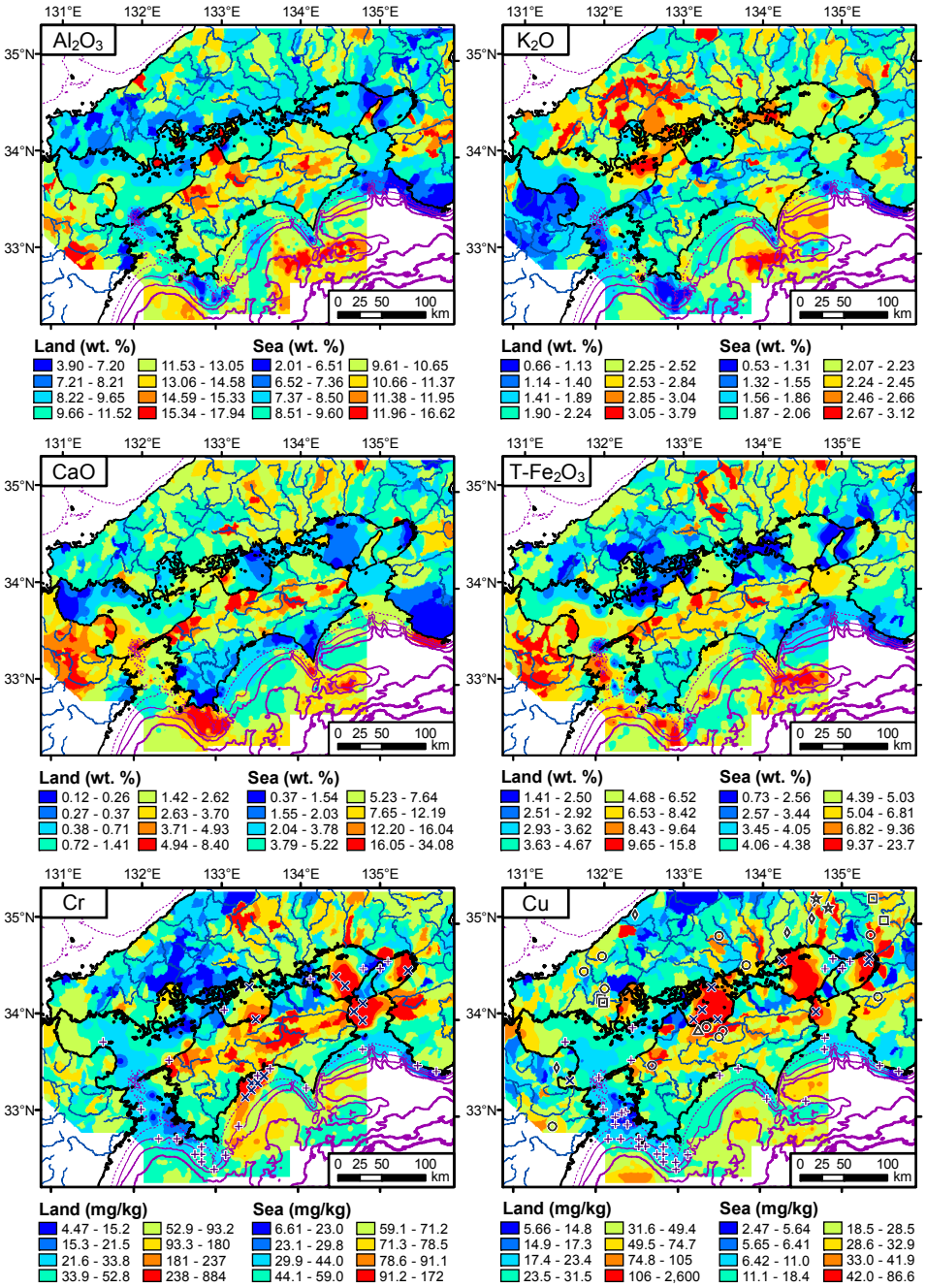

Figure 4. *Cont.*

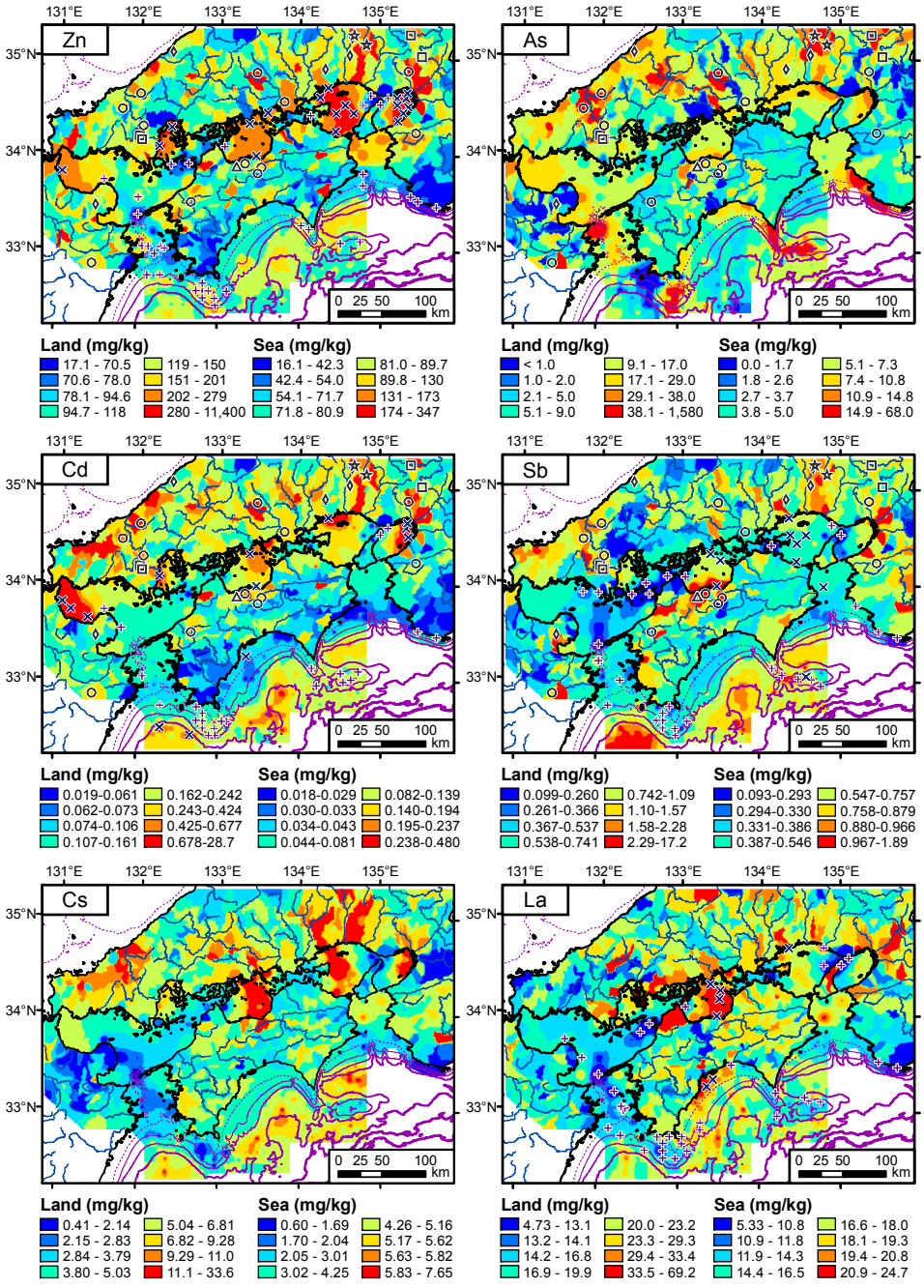

Figure 4. Spatial distributions of elemental concentrations in terrestrial and marine areas. The data are presented in wt % oxide (Al_2O_3, CaO, K_2O, and T-Fe_2O_3) and mg/kg element (Cr, Cu, Zn, As, Cd, Sb, Cs and La). Stars, circles, diamonds, squares and triangular symbols indicate major metalliferous deposits (as in Figure 1b). Cross and plus symbols indicate outliers obtained using Mahalanobis' generalized distances (details in text in Section 5.5.1).

4.2. Spatial Distribution of Elemental Concentrations in Coastal Sea Sediments

Within the Seto Inland Sea, high levels of K_2O, Rb, Ba, and Tl are found in the coarse sands of Aki-Nada and Bisan-Seto-Nada, and in northeastern Iyo-Nada (Figure 4). Coarse sediments with rock fragments, gravels, and coarse sands in western Iyo-Nada and the Bungo Channel are enriched in MgO, P_2O_5, CaO, TiO_2, MnO, Fe_2O_3, Sc, V, Co, Zn, and Sr. In contrast, the sandy sediments in eastern Iyo-Nada and the Bungo Channel are depleted in almost all of the measured elements, except CaO

and Sr. Silt and clay in Hiuchi-Nada, Harima-Nada, and the Kii Channel are abundant in Li, Be, MgO, P_2O_5, 3d transition metals, Ga, Y, Nb, Sn, Cs, Ln, Ta, Hg, Pb, Bi, and Th. Suo-Nada is enriched in Li, Zn, Ga, Sn, Mo, Cd, Ta, Pb, Bi, and U. Concentrations of P_2O_5, Cr, Ni, Cu, Zn, Mo, Cd, Sn, Hg, Pb, and Bi are especially elevated in the silt of Osaka Bay. Finally, MnO and Tl are abundant in all sediments within the Seto Inland Sea, irrespective of particle size.

On the Pacific Ocean side, coarse sediments with rock fragments, gravels, and coarse sands distributed around the topographic highs of Ashizuri Spar, Muroto Spar, Tosa-Bae, and the Muroto Sea Knoll are abundant in MgO, CaO, Al_2O_3, P_2O_5, TiO_2, MnO, T-Fe_2O_3, Sc, V, Co, As, Sr, Mo, Sb, and U. Sediments abundant in TiO_2, Cr, Co, Ni, Nb, light REEs (lanthanides from La to Sm), and Ta, occur in Tosa Bay. The silty and clayey sediments of Tosa Basin, Hyuga Basin, and the Muroto trough are enriched in Li, Cu, Nb, Cd, Sb, Cs, Hg, and U. Fine sands collected from the Ashizuri and Muroto Sea Knolls are richer in P_2O_5, CaO, Sc, TiO_2, V, MnO, Fe_2O_3, Co, Cu, As, Sr, Mo, Cd, Sb, Cs, heavy REEs (Y and lanthanides from Gd to Lu), and Bi than the fine sands distributed across the continental shelf.

5. Discussion

5.1. Analysis of Variance (ANOVA) to Reveal the Effects of Particle Size and Regional Difference

Coastal sea sediments typically originate from their adjacent terrestrial materials. Therefore, the geochemical features of terrestrial lithology are fundamentally reflected in those of nearby marine sediments. This phenomenon is referred to herein as "regional difference". Additionally, elemental concentrations in marine sediments are known to vary with particle size, in a phenomenon referred to herein as the "particle size effect". This variation is caused simply by the dilution effects of quartz and biogenic calcareous materials, which are abundant in coarse grains but less abundant in fine grains. Thus, we apply a two-way analysis of variance (ANOVA) to determine the factor that most significantly controls the chemical compositions of marine sediments: regional differences or the particle size effect [8]. The procedure is detailed by [8] (Appendix C).

The marine samples are grouped into those from the Seto Inland Sea region, including the Kii and Bungo Channels, and those from the Pacific Ocean region. They are further classified into: coarse sediments, including rock fragments, gravels, coarse sands, and medium sands; fine sands; and silt-clay. We assume that the coarse sediments, fine sands, and silt-clay are moved by water power over short, middle, and long distances, respectively. Median elemental concentrations of marine sediments are calculated for each region and particle size (Table 3). Table 3 also presents the median concentrations of stream sediments from two regions, for reference. In this regard, 96 stream sediment samples were collected from rivers that flow directly into the Sea of Japan, and so these samples are excluded from Table 3.

Table 3. Median elemental concentrations of marine sediments and stream sediments.

Element	Seto Inland Sea				Pacific Ocean			
	Stream Sed.	Marine Sed.			Stream Sed.	Marine Sed.		
		Coarse Sed.	Fine Sand	Silt and Clay		Coarse Sed.	Fine Sand	Silt and Clay
	n = 321	*n* = 26	*n* = 15	*n* = 47	*n* = 159	*n* = 75	*n* = 107	*n* = 193
wt %								
MgO	1.72	1.45	2.76	3.31	1.80	3.12	2.39	2.68
Al_2O_3	11.43	7.34	8.47	8.48	12.17	9.29	9.23	10.50
P_2O_5	0.115	0.059	0.114	0.129	0.105	0.105	0.095	0.111
K_2O	2.25	2.26	2.02	2.03	2.20	1.80	1.95	2.18
CaO	1.67	4.83	5.21	2.01	0.77	7.41	6.93	5.23
TiO_2	0.64	0.25	0.43	0.54	0.54	0.49	0.42	0.51
MnO	0.119	0.086	0.079	0.109	0.096	0.100	0.060	0.056
T-Fe_2O_3	4.88	2.39	3.54	4.59	4.45	5.13	4.50	4.29

Table 3. *Cont.*

Element	Seto Inland Sea				Pacific Ocean			
	Stream Sed.	Marine Sed.			Stream Sed.	Marine Sed.		
		Coarse Sed.	Fine Sand	Silt and Clay		Coarse Sed.	Fine Sand	Silt and Clay
	n = 321	n = 26	n = 15	n = 47	n = 159	n = 75	n = 107	n = 193
mg/kg								
Li	35	24	55	102	42	29	42	53
Be	1.7	1.2	1.4	1.7	1.6	1.2	1.4	1.5
Sc	10	4.9	8.4	9.3	9.8	10	8.3	10
V	78	37	57	75	94	82	69	90
Cr	51	25	40	74	60	39	47	68
Co	12	6.7	9.3	13	12	12	10	9.5
Ni	19	11	17	32	27	16	22	36
Cu	31	7.9	13	41	36	7.2	13	28
Zn	126	45	83	166	96	71	73	85
Ga	17	11	14	16	17	12	13	15
As	8.0	4.9	5.9	7.0	7.1	8.3	4.3	4.2
Rb	107	83	74	60	95	62	76	80
Sr	113	300	231	121	112	439	319	242
Y	21	9.6	15	15	14	12	11	13
Nb	9.1	4.0	6.3	9.4	8.5	4.4	5.7	7.9
Mo	0.98	0.47	0.74	1.1	0.96	0.46	0.47	0.68
Cd	0.18	0.041	0.079	0.19	0.10	0.054	0.050	0.13
mg/kg								
Sn	3.9	1.3	2.4	4.3	2.7	1.2	1.6	2.2
Sb	0.74	0.30	0.39	0.55	0.71	0.43	0.44	0.76
Cs	5.1	2.0	3.8	5.4	4.6	2.2	3.5	5.1
Ba	433	344	274	247	438	300	323	386
La	20	12	14	17	20	13	16	18
Ce	37	25	32	33	39	27	34	37
Pr	4.8	2.7	3.7	4.2	4.6	3.2	3.7	4.1
Nd	19	11	15	16	18	13	15	16
Sm	3.9	2.1	3.2	3.5	3.6	2.7	2.9	3.2
Eu	0.83	0.60	0.71	0.67	0.77	0.73	0.64	0.70
Gd	3.6	1.9	2.9	3.3	3.2	2.5	2.5	2.8
Tb	0.63	0.31	0.51	0.56	0.51	0.40	0.40	0.45
Dy	3.3	1.6	2.6	2.9	2.6	2.0	1.9	2.2
Ho	0.64	0.31	0.49	0.54	0.48	0.38	0.35	0.42
Er	1.9	0.9	1.4	1.6	1.3	1.1	1.0	1.2
Tm	0.31	0.15	0.22	0.26	0.21	0.17	0.16	0.19
Yb	1.9	0.9	1.4	1.5	1.3	1.0	1.0	1.2
Lu	0.28	0.14	0.20	0.22	0.18	0.15	0.14	0.16
Ta	0.75	0.40	0.60	0.92	0.76	0.38	0.51	0.73
Hg	0.050	0.030	0.079	0.167	0.110	0.026	0.100	0.179
Tl	0.62	0.56	0.60	0.68	0.55	0.34	0.41	0.51
Pb	28	20	24	39	23	17	17	19
Bi	0.31	0.18	0.32	0.77	0.26	0.18	0.19	0.34
Th	7.9	3.7	5.9	7.0	6.6	3.7	5.4	6.6
U	1.9	0.8	1.5	1.8	1.4	0.9	1.1	1.4

Table 4 presents the results of a two-way ANOVA: the variance ratios (F), probabilities (p), and effect size (η^2) due to regional difference (factor A), particle size (factor B), and the interaction effect (factor A × B). When the estimated probability is lower than 0.01, we conclude that the factor makes a significant difference to the chemical compositions, and in fact, each factor was statistically significant ($p < 0.01$) in most cases (Table 4). This is because a statistical test with a large amount of input data, such as n = 463 in this study, is highly sensitive to very small differences. Therefore, we calculate η^2 to form a plausible estimation of p value irrespective of sample number [33,34]. The η^2 is an easy-to-understand metric that is calculated as the ratio of the sum of squares (SS) for each factor and the total SS. Magnitudes of $\eta^2 < 0.01$, $0.01 \leq \eta^2 < 0.06$, $0.06 \leq \eta^2 < 0.14$, and $\eta^2 \geq 0.14$ can be considered to represent no effect, a small effect, an intermediate effect, and a large effect, respectively [33,34]. In this study, we conclude that each factor with $\eta^2 \geq 0.06$ has a significant effect on the elemental concentrations of the sediments. Furthermore, this indicator can be used to decide the most dominant factor, on the basis of the highest η^2 score [33].

Table 4. Variance ratio (F), probability (p), and size effect (η^2) of two-way ANOVA type II.

Element	Two-Way ANOVA									MF
	F (A)	F (B)	F (A × B)	p (A)	p (B)	p (A × B)	η^2 (A)	η^2 (B)	η^2 (A × B)	
MgO	2	13	67	0.20	<0.01	<0.01	<0.01	0.04	**0.22**	A × B
Al_2O_3	74	34	2	<0.01	<0.01	0.13	**0.12**	**0.11**	<0.01	Both
P_2O_5	10	19	28	<0.01	<0.01	<0.01	0.02	**0.07**	**0.10**	A × B
K_2O	1	46	31	0.36	<0.01	<0.01	<0.01	**0.15**	**0.10**	B
CaO	110	34	6	<0.01	<0.01	<0.01	**0.17**	**0.11**	0.02	A
TiO_2	14	26	19	<0.01	<0.01	<0.01	0.02	**0.09**	**0.07**	B
MnO	53	26	17	<0.01	<0.01	<0.01	**0.09**	**0.09**	**0.06**	Both
T-Fe_2O_3	37	1	38	<0.01	0.60	<0.01	**0.06**	<0.01	**0.13**	A × B
Li	98	366	59	<0.01	<0.01	<0.01	**0.07**	**0.53**	**0.09**	B
Be	44	95	13	<0.01	<0.01	<0.01	**0.06**	**0.27**	**0.04**	B
Sc	33	13	26	<0.01	<0.01	<0.01	**0.06**	0.05	**0.09**	A × B
V	77	18	23	<0.01	<0.01	<0.01	**0.13**	**0.06**	**0.08**	A
Cr	2	149	21	0.16	<0.01	<0.01	<0.01	**0.37**	0.05	B
Co	0	0	50	0.89	0.83	<0.01	<0.01	<0.01	**0.18**	A × B
Ni	29	280	15	<0.01	<0.01	<0.01	0.03	**0.52**	0.03	B
Cu	30	595	17	<0.01	<0.01	<0.01	0.02	**0.70**	0.02	B
Zn	78	104	115	<0.01	<0.01	<0.01	**0.08**	**0.22**	**0.24**	A × B
Ga	21	191	12	<0.01	<0.01	<0.01	0.02	**0.43**	0.03	B
As	11	28	16	<0.01	<0.01	<0.01	0.02	**0.10**	**0.06**	B
Rb	5	22	26	0.02	<0.01	<0.01	<0.01	**0.08**	**0.09**	A × B
Sr	120	113	5	<0.01	<0.01	<0.01	**0.15**	**0.28**	0.01	B
Y	19	25	20	<0.01	<0.01	<0.01	0.03	**0.09**	**0.07**	B
Nb	22	152	12	<0.01	<0.01	<0.01	0.03	**0.38**	0.03	B
Mo	20	16	8	<0.01	<0.01	<0.01	0.04	**0.06**	0.03	B
Cd	20	124	16	<0.01	<0.01	<0.01	0.03	**0.33**	0.04	B
Sn	180	239	42	<0.01	<0.01	<0.01	**0.15**	**0.41**	**0.07**	B
Sb	44	106	3	<0.01	<0.01	0.03	**0.06**	**0.29**	<0.01	B
Cs	2	467	5	0.14	<0.01	<0.01	<0.01	**0.67**	<0.01	B
Ba	29	34	58	<0.01	<0.01	<0.01	0.04	**0.10**	**0.17**	A × B
La	3	116	5	0.07	<0.01	<0.01	<0.01	**0.33**	0.01	B
Ce	24	89	0	<0.01	<0.01	0.86	0.04	**0.27**	<0.01	B
Pr	2	128	9	0.19	<0.01	<0.01	<0.01	**0.35**	0.02	B
Nd	1	105	12	0.26	<0.01	<0.01	<0.01	**0.30**	0.03	B
Sm	2	80	21	0.13	<0.01	<0.01	<0.01	**0.24**	**0.06**	B
Eu	4	8	6	0.07	<0.01	<0.01	<0.01	0.03	0.03	None
Gd	13	50	27	<0.01	<0.01	<0.01	0.02	**0.16**	**0.09**	B
Tb	38	43	32	<0.01	<0.01	<0.01	**0.06**	**0.13**	**0.10**	B
Dy	25	44	30	<0.01	<0.01	<0.01	0.04	**0.14**	**0.09**	B
Ho	30	39	25	<0.01	<0.01	<0.01	0.05	**0.13**	**0.08**	B
Er	38	36	20	<0.01	<0.01	<0.01	**0.06**	**0.12**	**0.07**	B
Tm	44	37	18	<0.01	<0.01	<0.01	**0.07**	**0.12**	**0.06**	B
Yb	42	36	16	<0.01	<0.01	<0.01	**0.07**	**0.12**	0.05	B
Lu	58	26	18	<0.01	<0.01	<0.01	**0.10**	**0.09**	**0.06**	A
Ta	68	163	19	<0.01	<0.01	<0.01	**0.08**	**0.37**	0.04	B
Hg	0	270	2	0.85	<0.01	0.14	<0.01	**0.54**	<0.01	B
Tl	241	107	1	<0.01	<0.01	0.59	**0.27**	**0.24**	<0.01	Both
Pb	359	58	36	<0.01	<0.01	<0.01	**0.36**	**0.11**	**0.07**	A
Bi	165	214	57	<0.01	<0.01	<0.01	**0.14**	**0.37**	**0.10**	B
Th	5	206	2	0.03	<0.01	0.14	<0.01	**0.47**	<0.01	B
U	9	114	11	<0.01	<0.01	<0.01	0.01	**0.32**	0.03	B

Notes: The factor A, B, and A × B indicate the regional difference effect, particle size effect and interaction effect, respectively. MF means major factor. The boldface in η^2 scores indicates that each factor with $\eta^2 \geq 0.06$ has a significant effect on the elemental concentrations of the sediments.

Results of the ANOVA suggest that particle size is the dominant influencing factor for many elements in the sediments (Table 4). The regional difference effect is more significant than the particle size effect only for Al_2O_3, CaO, MnO, Sc, V, Mo, and Pb. This suggests that consideration of the particle size effect must be made in order to fully understand the influence of terrestrial materials on coastal sea sediments. However, it should be noted that the interaction effect is more influential than either of the two main factors alone for MgO, P_2O_5, Fe_2O_3, Sc, Co, Rb, Ba, and Eu, and is significant for 14 elements, including K_2O and TiO_2. This interaction effect refers to the effect of one factor on the other factor, such that the two main factors synergistically affect the data e.g., [35]. To visualize the interaction effect, variations in the median values of Al_2O_3, MgO, K_2O, Co, Cs, and Ba are presented in Figure 5. When the interaction effect is insignificant, the median values vary approximately in parallel between the Seto Inland Sea and the Pacific Ocean, irrespective of particle size (Al_2O_3 and Cs in Figure 5). In the cases of large η^2 values for the interaction effect, such as for MgO and Co, the elemental concentrations in the Pacific Ocean sediments decrease with decreasing particle size, but increase in the sediments of

the Seto Inland Sea with decreasing particle size. Variations in the K_2O and Ba concentrations with particle size are exactly opposite to those of MgO and Co, and still indicate a significant contribution of the interaction effect. These results suggest that regional difference and particle size effects are not independent for many elements. Therefore, we need to evaluate the geochemical similarities and differences among groups subdivided by region and particle size.

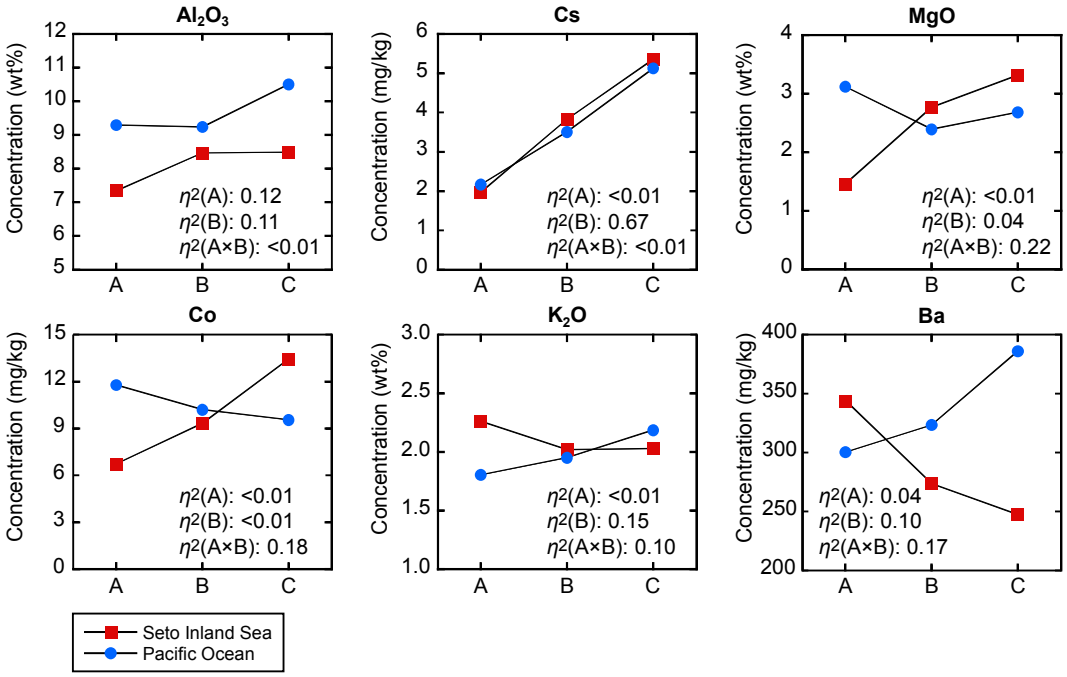

Figure 5. Median concentrations of elements and oxides in sediments from the Seto Inland Sea and the Pacific Ocean. A, B, and C represent coarse sediment, fine sand, and silty-clayey sediments, respectively. η^2 (A), η^2 (B), and η^2 (A × B) are the size effects of regional differences, particle sizes, and the interaction effect, respectively, obtained from the two-way ANOVA (Table 4).

5.2. Comparison of Elemental Abundances in Coastal Sea and Stream Sediments between the Seto Inland Sea and the Pacific Ocean

The chemical and mineralogical compositions of marine sediments differ from those of stream sediments [7,8]. Furthermore, the range in concentration completely differs for each element: major and minor elements in wt % oxide amounts, and trace elements in mg/kg or μg/kg amounts. Therefore, to eliminate the effect of scale and units, the data have to be normalized to elucidate differences amongst the elements or the samples. Thus, in this study, enrichment factors (EF) of the marine and stream sediments compared with the upper continental crust (UCC) [36] are employed to allow direct comparison (Figure 6). The EF is calculated as follows:

$$EF = ([C]_{sample}/[Al_2O_3]_{sample})/([C]_{UCC}/[Al_2O_3]_{UCC}), \quad (1)$$

where [C] and $[Al_2O_3]$ are the concentrations of a given element and Al_2O_3, respectively. Al_2O_3 is a major element group, and a dominant constituent of many minerals such as plagioclase. Therefore by using it to normalize the EFs, we can effectively remove the effects of quartz, calcareous materials, and organic matter [8]. The systematically high EFs of Li, As, Sb, Hg, and Bi, and low EFs of Nb, Sn, and Ta for all samples, as well as CaO and Sr in stream sediments, are fundamental geochemical signatures of upper crust materials in an island arc setting [37] (Figure 6a,b). The high abundance ratios of CaO and Sr in marine sediments indicate the presence of biogenic calcareous materials, such as shell fragments and foraminifera tests. In the Seto Inland Sea, the UCC normalized patterns of

fine sands are similar to those of stream sediments (Figure 6a). Abundance ratios of most elements in marine sediments decrease with increasing grain size. CaO, K_2O, Rb, Sr, and Ba are especially dominant in coarse sediments, whereas silt and clay have higher abundance ratios for Li, Cr, Co, Ni, Zn, Mo, Cd, Cs, Hg, Pb, and Bi. In the Pacific Ocean, the UCC normalized patterns of fine sands and silt-clay samples are most similar to those of stream sediments (Figure 6b). The variations in EF of most elements with particle size of the marine sediments in the Pacific Ocean are likely smaller than those for samples in the Seto Inland Sea, except for MnO, As, Ce, Eu, and Tl. Coarse sediments have relatively high abundance ratios for MnO, Fe_2O_3, Co, and As, and low abundance ratios for Li, Cu, Nb, Sn, Cs, light REEs, Ta, Hg, Tl, Th, and U. The silty and clayey sediments are particularly enriched in Cr, Ni, Cu, Cd, Sb, Hg, and Bi.

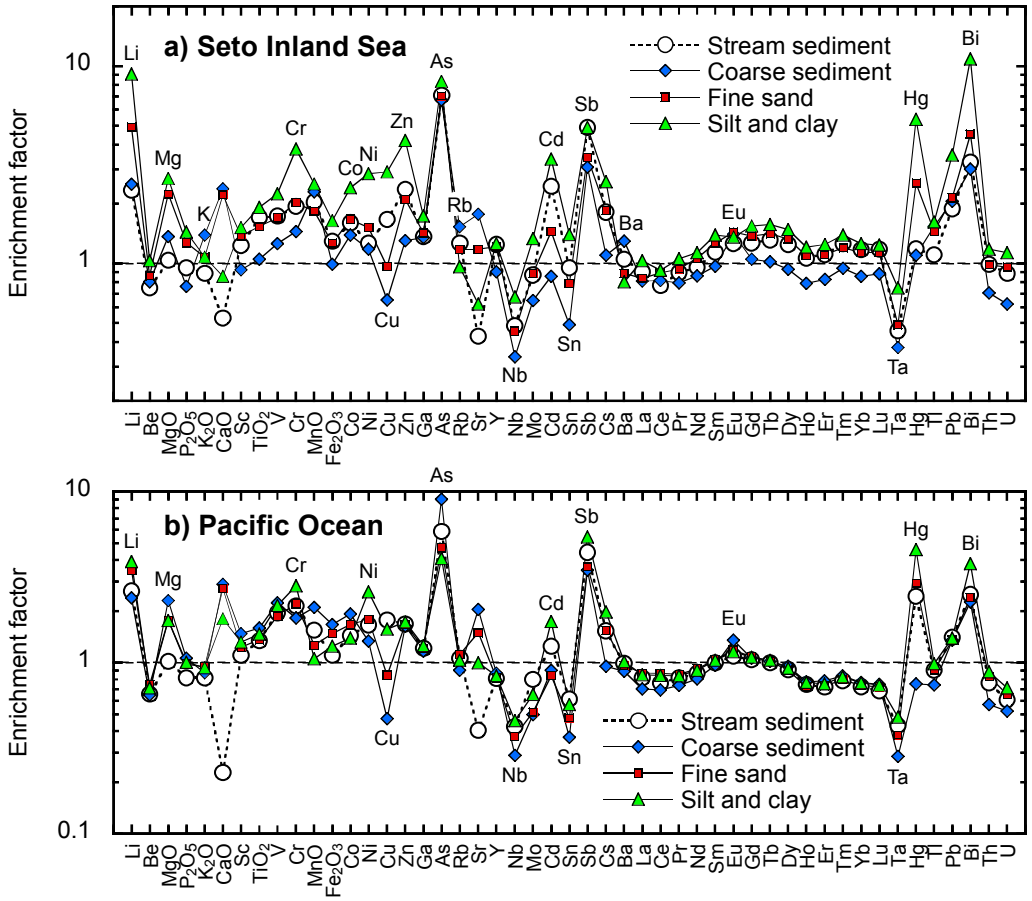

Figure 6. Enrichment factors of 49 elements and oxides in stream and marine sediments of (**a**) Seto Inland Sea and (**b**) Pacific Ocean, compared to the upper continental crust [36] (details in the text).

5.3. Discrimination of Coastal Sea Sediments Using Cluster Analysis

Coarse sediments have UCC normalized patterns that notably differ from those of terrestrial materials (Figure 6a,b), which implies that they have different origins to the modern terrestrial materials or are supplied by a particular lithology. Thus, we refine the identification of probable source materials for marine sediments using cluster analysis. The classification of marine sediment samples is as presented in Table 3. Stream sediments grouped according to the seven rock types summarized in Table B1 are used for comparison. The distance between data points was calculated as a Euclidian distance, requiring the geochemical data from marine and stream sediments to be standardized or transformed appropriately. This is because the compositional data constitute "closed" data that sum to a constant [38,39]. To mitigate biased analysis arising from data closure, there is a requirement for

data transformation to yield data with normal distributions suitable for parametric statistical analysis. Additive log-ratio, the centered log-ratio, and the isometric log-ratio transformation of compositional data have been proposed [38,39]. We used a log transformation of the EF data to generate logarithmic EFs for each sample, which were used as the input data for cluster analysis. The logarithmic EF corresponds to the additive log-ratio transformation of the compositional data [38,39]:

$$\log \mathrm{EF} = \mathrm{alr(C)}_{\mathrm{sample}} - \mathrm{alr(C)}_{\mathrm{UCC}}, \quad (2)$$

where alr(C) stands for additive log-ratio transformation (log {[C]/[Al_2O_3]}). We have confirmed that the EF is effective in eliminating the effect of scale and units, and in removing the dilution effect, although Al_2O_3 concentration is empirically used for denominator in Equation (1). The logarithmic EF also incorporates data normality and is thus amenable to multivariate parametric tests such as cluster analysis.

Figure 7 presents dendrograms that show the distances between two points. The distances between clusters were obtained by Ward's method [40]. We calculated two kinds of dendrograms using different combinations of elements. Figure 7a uses a dataset that excludes sea salt (Na_2O), biogenic carbonate materials (CaO and Sr), and heavy metals related to mining and anthropogenic activities (As, Mo, Cd, Sn, Sb, Hg, Pb, and Bi), which do not reflect the geochemistry of the parent lithology. Figure 7b uses the EFs of immobile elements (Sc, TiO_2, Cr, Nb, Ta, Y, Ln, and Th), which are not strongly influenced by weathering processes. The obtained dendrograms are mutually similar (Figure 7a,b). Coarse sediments from the Pacific Ocean plot in the same group as stream sediments derived from mafic volcanic and metamorphic rocks in Figure 7a. However, Figure 7b shows that all marine sediments in the Pacific Ocean cluster together with coarse sediments from Seto Inland Sea and accretionary complexes. Fine sand and silt-clay in the Pacific Ocean and coarse sands in the Seto Inland Sea are always grouped together with stream sediments derived from sedimentary rocks of accretionary complexes. These results for fine sands and silt-clay are reasonable, because such sedimentary rocks outcrop extensively across the southern part of Shikoku Island (Figure 2), which supplies the highest sediment yield to the Pacific Ocean (Table 1). In contrast, the fine sands and silt-clay in the Seto Inland Sea plot with those stream sediments derived from granitic and felsic volcanic rocks. This result is also expected, due to the extensive outcropping of these rock types across the Chugoku region, which supplies the highest sediment yield to the Seto Inland Sea (Table 1).

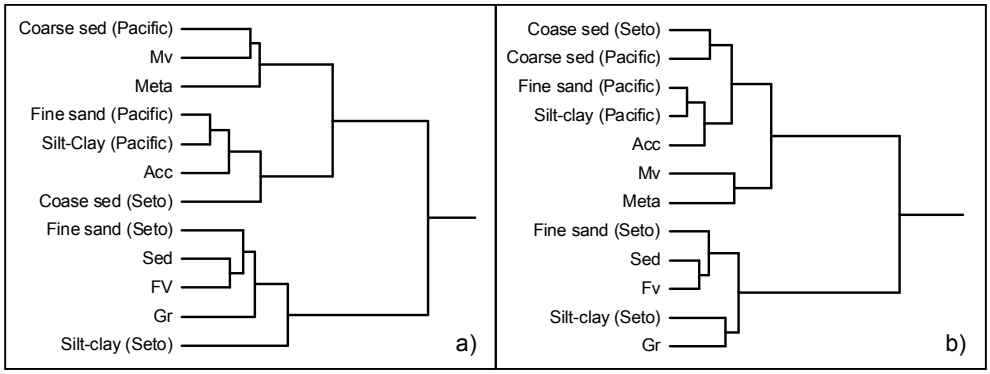

Figure 7. (**a**) Cluster dendrogram obtained using a dataset of 39 elements (excepting CaO, Sr, and heavy metals); (**b**) Cluster dendrogram obtained using a dataset of 21 elements (immobile elements). Sed: sediments and sedimentary rocks; Acc: sedimentary rocks of accretionary complexes; Mv: mafic volcanic rocks; Fv: felsic volcanic rocks; Gr: granitic rocks; Meta: metamorphic rocks.

5.4. Discrepancies in the Geochemistry of Coarse Marine Sediments and Stream Sediments

5.4.1. Fractionation of Mineralogical Compositions in Coarse Sediments by a Strong Tidal Current

Cluster analysis suggests that the coarse sediments in the Seto Inland Sea are related to stream sediments sourced from sedimentary rocks of accretionary complexes. However, granitic and felsic volcanic rocks are geographically more suitable sources for the coarse sediments, in analogy with the fine sands. To reveal their geochemical features in more detail, Figure 8a shows the abundance patterns of elements in coarse sediments collected from the narrow sea channels (Aki-Nada, Bisan-Seto-Nada and around Awaji Island), Iyo-Nada, and Bungo Channel, normalized to the stream sediments in the Seto Inland Sea region.

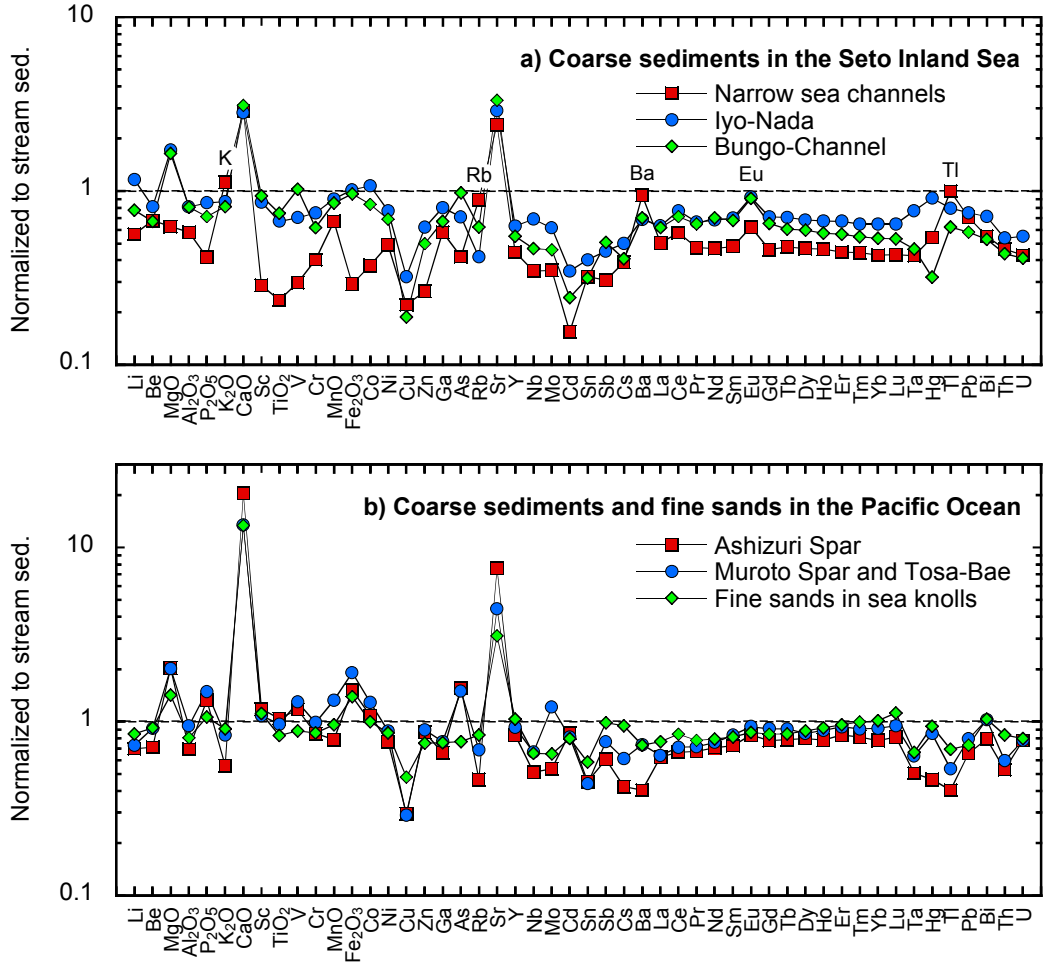

Figure 8. (**a**) Profiles of chemical compositions of coarse sediments in the narrow sea channels (around Aki-Nada, Bisan-Seto-Nada, and Awaji Island), Iyo-Nada, and the Bungo Channel, normalized to stream sediments in the Seto Inland Sea region; (**b**) Profiles of chemical compositions of coarse sediments in Ashizuri Spar, Muroto Spar and Tosa Bae, and fine sands in sea knolls normalized to stream sediments in the Pacific Ocean region.

Coarse sands in the narrow sea channels are particularly rich in K_2O, CaO, Rb, Sr, Ba, and Tl, and have a distinctive positive Eu anomaly, but are extremely depleted in many elements, such as Sc and TiO_2 (Figure 8a). These features are indicative of the selective accumulation of biogenic calcareous materials, quartz, and alkali-feldspars. Quartz and alkali-feldspar are abundant in granitic and felsic volcanic rocks, and are highly resistant to weathering processes, so are preserved as coarse particles e.g., [41]. In contrast, the coarse sediments in Iyo-Nada and the Bungo Channel are relatively

abundant in MgO, P_2O_5, CaO, Sc, TiO_2, V, Fe_2O_3, Co, and Zn in addition to the elements mentioned above (Figure 8a). These additional elements are found abundantly in mafic minerals such as biotite, hornblende, and pyroxene, as well as accessary minerals such as magnetite and ilmenite. We therefore assume that the fine particles of mafic and accessary minerals are swept away from the narrow sea channels by a strong tidal current, but this does not occur in Iyo-Nada and the Bungo Channel. In contrast, the coarse grains in all areas are rarely moved over any long distances by water power.

5.4.2. Denudation of the Basement Rocks of the Topographic Highs

Cluster analysis provides different results for coarse sediments from the Pacific Ocean (compare Figure 7a,b). This is because only three elements (Sc, TiO_2, and Cr) abundant in sediments derived from mafic volcanic rocks and metamorphic rocks (dominantly greenschist) are used in the cluster analysis of the immobile element dataset (Figure 7b). Thus, cluster analysis using immobile elements may be poorly sensitive to such rock types. Consequently, we conclude that Figure 7a would provide a more plausible result: mafic volcanic and metamorphic rocks are the probable sources of coarse sediments in the Pacific Ocean. However, these rock types are located relatively distantly from the coarse sediment deposition sites (Figure 2). The high EFs of MnO, Fe_2O_3, Co, and As in coarse sediments from the Pacific Ocean (Figure 6b) can be explained by Fe hydroxide and Mn dioxide coatings on coarse particles and gravel (for example, T-Fe_2O_3 and As; Figure 4). In this regard, relict quartz particles coated with Fe hydroxides are found in the Bungo Channel [26]. However, this explanation does not fully account for the enrichment of MgO, P_2O_5, Sc, TiO_2, and V. According to Okamura [19], the topographic highs in this region are formed from basement rocks of Miocene–Pliocene siltstone. These highs typically have a low sedimentation rate and are located in a region of erosion, due to the strong bottom flow associated with the Kuroshio Current [24]. The spar and knoll sediments are therefore assumed to have formed by denudation of the basement rocks (siltstone), which have a different lithology to the southern part of Shikoku Island. Therefore, we assume that basement rocks of siltstone might be influenced by mafic volcanic activity at Miocene-Pliocene age. Figure 8b shows the abundance of elements in coarse or gravelly spar sediments and knoll sediments (mainly fine sands), normalized to the stream sediments in the Pacific Ocean region. Despite the fact that Ashizuri Spar is more than 100 km away from Muroto Spar and Tosa-Bae, the abundance patterns of the coarse spar sediments are very similar. Furthermore, the fine sands collected around Ashizuri Knoll and Muroto Knoll have similar abundance patterns to those of the coarse spar sediments. As such, the unexpected cluster analysis result for coarse sediments in this region can be explained by mineral segregation under a strong tidal current unique to the Seto Inland Sea, and by a denudation of old basement rocks (Miocene–Pliocene siltstone) in the Pacific Ocean.

5.5. The Transfer of Silty and Clayey Sediments Influenced by Periodic Currents, Tidal Currents, and a Water Mass Boundary

5.5.1. Mahalanobis' Generalized Distances for Finding Outliers

Silty and clayey sediments supplied from rivers take a long time to reach the sea floor. Therefore, their spatial distribution is a result of conveyance and dispersion by coastal sea currents. Ohta and Imai [7] and Ohta et al. [8] simply focused on the spatial distribution patterns of high Cr and Ni concentrations in silty sediments, which are indicative of transport of fine particles from land to sea or marine environments. Their spatial distribution can be easily discriminated because they are extremely enriched in silty marine sediments derived from ultramafic rocks in the adjacent terrestrial area. Ohta et al. [42] tried to visualize the particle transfer process using the spatial distribution patterns of the other elements. However, many elements are enriched in finer sediments due to the particle size effect, and so in order to highlight the particle transfer process, it is useful to detect outliers using the relationships between elemental concentrations and median diameter or mud content [42].

Unfortunately, in this study, data of median diameter or mud content are available for only half of the samples. ANOVA analyses suggest that Cs, Hg and Th concentrations in marine sediments are determined only by particle size and are not sensitive at all to either regional differences or interaction effects ($\eta^2 < 0.01$) (Table 4). The particle size effect of Cs has the largest η^2 score of the three elements, suggesting that the particle size effect has the maximum effect on Cs concentrations. Although concentrations of 13 elements, including Cr, Cu, and La, in marine sediments are also controlled dominantly by particle size effects, they are further influenced weakly by regional difference effects and interaction effects ($0.01 \leq \eta^2 < 0.06$) (Table 4). In addition, Hg, Cu, and Cd concentrations in marine sediments might be influenced by metalliferous deposits and anthropogenic activity in the adjacent terrestrial area. For these reasons, we conveniently use Cs concentration as a proxy for the median diameter or mud content.

Figure 9 shows the relationships between Cr, Cu, Zn, Cd, Sb, and La concentrations and that of Cs. The concentrations of all six elements correlate positively and linearly with Cs, and it can be assumed that those samples plotting outside the linear trends are subject to influencing factors in addition to the particle size effect. Ohta et al. [42] detected outliers from a scatter diagram according to their best judgment. In this study, the outliers appearing in the scatter diagram are objectively obtained using Mahalanobis' generalized distance (D) [43]. This method presupposes that the data follow a normal distribution similar to ANOVA. Thus, the data transformation is given in Table C1. The obtained D values gradually increase from the inner part of the data cluster to the outer part, giving an onion-like structure (Figure 9). D values of $D \leq 1.117$, $D \leq 1.665$, and $D \leq 2.146$ indicate that 50%, 75%, and 90% of the total data points are included, respectively, and data points are defined as an outlier herein if $D > 2.146$, which includes the upper and lower 5% of multivariate outliers. The outliers were determined from all datasets, so silt and clay classified as outliers are expressed as cross symbols; while coarse sediments and fine sands classified as outliers are expressed as plus symbols in Figure 4.

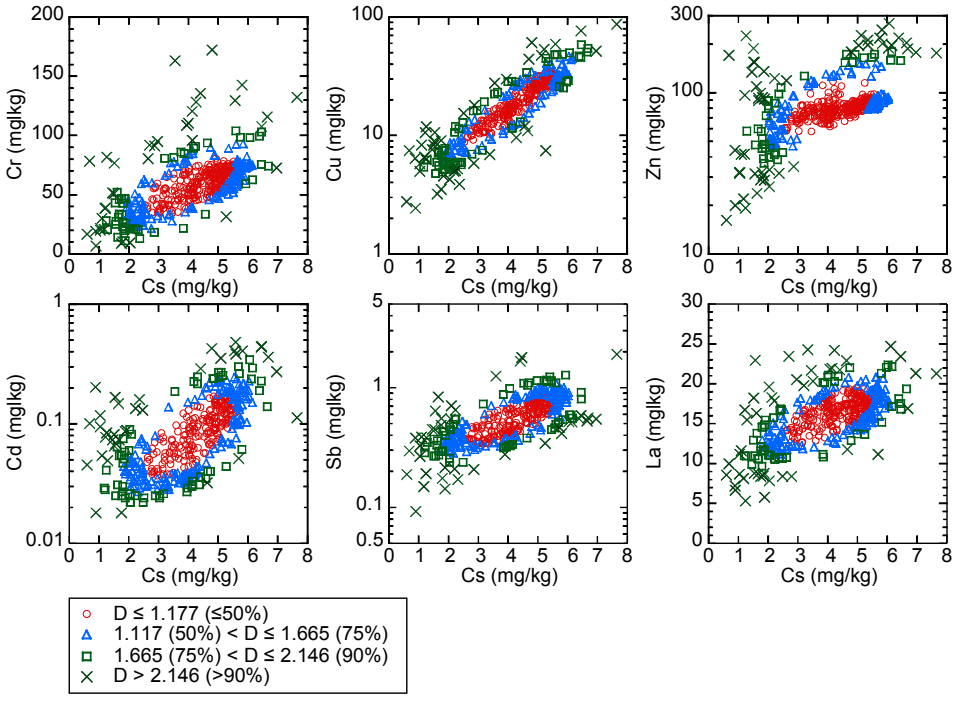

Figure 9. Relationship between elemental concentrations and Cs concentration. Mahalanobis' generalized distances (D) increase from the central part to the outer part of the plot in an onion-like structure. Values of $D \leq 1.117$, $D \leq 1.665$, and $D \leq 2.146$ indicate that 50%, 75%, and 90% of the total data points are included, respectively.

5.5.2. Transport of Elements in Silt Derived from the Parent Lithology

Figure 4 shows that the locations of the outliers calculated for Cr (cross symbols) correspond with a NNW-SSE distribution of silty-clayey sediments with high Cr concentrations in the Kii Channel. This distribution of Cr outliers indicates that silty particles that originated from ultramafic rocks are supplied through the Yoshino, Naka, and Kino Rivers to the Kii Channel, and are then widely dispersed by a periodic current, as Ohta and Imai [7] noted. Hiuchi-Nada also contains abundant silty sediments, however the distribution of outliers (corresponding to high concentration areas) for MgO, Cr, Co, and Ni is restricted to the vicinity of Shikoku Island (shown by Cr in Figure 4). This can be explained by the fact that the terrestrial sediment discharge yield to Hiuchi-Nada is minimal compared to the output of the Yoshino River, Naka River and Kino River systems (Table 1).

Y, Nb, Ln, Ta and Th are also enriched in the silty sediments of Hiuchi-Nada, especially in the eastern part (La in Figure 4). The differing distributions of La and Cr outliers suggest that Y, Nb, Ln, Ta and Th have a different origin from MgO, Cr, Co, and Ni. Minakawa et al. [44] reported that rare earth minerals, including allanite and monazite, occur within pegmatite veins of the Ryoke granitic rocks, which outcrop in northwest Shikoku Island, on the small islands in Aki-Nada and Bisan-Seto-Nada, and are partly exposed on the seafloor [12]. Yanagi [10] suggested that fine particles transported by periodic currents accumulate in eastern Hiuchi-Nada where the amplitude of the tidal current is small and a counterclockwise circulation occurs. Consequently, we assume that silt enriched in rare earth minerals has been swept toward the eastern side of Hiuchi-Nada by periodic currents and accumulated there over a long period of time.

In Tosa Bay, tongue-shaped distribution patterns of high MgO, Cr, Co, Ni, Nb, Y, Ln, Ta, and Th concentrations and their outliers are apparent (shown by Cr and La in Figure 4). MgO, Cr, Co, and Ni originated from ultramafic rocks, while the other elements are derived from greenstones wedged between the Sambagawa metamorphic rocks and accretionary complexes e.g., [45]. Ikehara [25] and Hoshino [46] reported that silty and clayey sediments are selectively deposited at the boundary between coastal waters with low salinity (due to River input) and the outer sea with higher salinity. This is supported by the fact that the water discharges from the Niyodo and Shimanto Rivers into Tosa Bay are among the largest in the region (Table A1). Thus, on the basis of this evidence, sedimentation at the boundary between water masses can explain this distinctive distribution [7]. In addition, the countercurrent of the Kuroshio Current, which flows in a counterclockwise direction on the continental shelf (Figure 1b), may also contribute to the transport of fine particles enriched in the elements mentioned above [21].

5.5.3. Transfer of Materials Related to Mineral Deposits and Anthropogenic Activity

A number of silty sediment samples in Hiuchi-Nada are abundant in Cu (40.6–86.6 mg/kg) and are classified as outliers (Figure 4); these reflect the mining activity at the nearby Besshi Cu mines over the past 240 years [47]. Similarly, the outlier observed within the Kii Channel sediments is related to activity at the Cu mine in the watershed of the Yoshino River. In addition, one outlier for Sb (1.89 mg/kg) is found near to the shore in southern Hiuchi-Nada. This enrichment of Sb suggests contamination from the Ichinose Sb mine, which is located close to the Besshi mine.

Osaka Bay is adjacent to Osaka City, which is the second largest city in Japan and has a long history of industrial development. Ohta et al. [32] found that Cu, Zn, Cd, Sn, Sb, Hg, and Pb are significantly enriched in stream sediments collected from the urban areas of Osaka Plain. Similarly, the silty sediments in Osaka Bay are highly enriched in Cr, Cu, Zn, As, Mo, Cd, Sn, Hg, Pb, and Bi (as shown by Cr, Cu, Zn, and As in Figure 4). Samples with the top 1% of concentrations for these elements, which are mostly classified as outliers, are found in Osaka Bay, and the area of high concentrations near the mouth of the Yodo and Yamato Rivers is clearly due to the discharge of contaminated sediments. Hoshika and Shiozawa [27], Hoshika et al. [48], and Manabe [49] reported the same results, showing large accumulations of Cr, Cu, Zn, Cd, Pb, and Hg in Osaka Bay.

A number of outliers of Cu, Zn, Cd, Sn, Pb, and Bi are also found in Harima-Nada, Hiroshima Bay and Suo-Nada (shown by Cu, Zn, and Cd in Figure 4). Their enrichment may be a result of the nearby metalliferous deposits and contamination by the coastal industrial zones [49,50]. In particular, Ikuno mine is considered a possible source for the elements abundant in Harima-Nada because it is one of the largest hydrothermal-type polymetallic mines, bearing Cu, Zn, As, Cd, Sb, Sn, Pb, and Bi [31] (Figure 2). However, the spatial distributions of the outliers are different for each enriched element. A likely explanation for this is that the rivers flowing through the mineralized zones are small and have much smaller sediment discharges. Alternatively, the elements may have been released in the water during the oxidation of sulfide ores, and have subsequently absorbed into the surface sediment of the coastal seas [51].

5.5.4. Geochemical Features of Silt and Clay in the Deep Sea Basins of the Pacific Ocean

Silt and clay deposited in deep Pacific basins are typically enriched in MnO, V, Ni, Co, Mo, Sb, Pb, and Bi, as a result of early diagenetic processes in an oxic environment [7,42]. In contrast, Cu, Sb, Cd, Hg, and U are enriched in deep-sea sediments during early diagenesis under anoxic conditions, as they are immobile in reducing waters [52]. In addition, Cu and Hg are taken up by living organisms, transported to sediments, and bound within residual organic matter in bottom sediments [53–55]. Results of this study reveal that Cu, Sb, Cd, Hg, and U are abundant in the silt and clay of the Tosa Basin, Hyuga Basin, and the Muroto Trough (shown by Cu, Sb and Cd in Figure 4). This suggests that these deep-sea basins are under anoxic conditions. However, outliers for these elements are scarce in the Pacific Ocean, in contrast to the Seto Inland Sea (Figure 4). Ikehara [25] reported that these deep-sea basins are hemi-pelagic and are partly associated with turbidites. Therefore, we assume that the enrichment of heavy metals is lost when gradual sedimentation is interrupted by turbidity flows, and that early diagenetic processes and the deposition of organic matter begin again after the turbidity flow event [56]. As a result, no significant enrichment of heavy metals is visible in the Pacific Ocean.

6. Conclusions

The composition and transfer processes of coastal sea sediments are analyzed using a comprehensive geochemical database of many elements from the Seto Inland Sea and the Pacific Ocean in western Japan. The geochemical features of fine sands and silty-clayey sediments reflect those of stream sediments in the adjacent terrestrial areas. This pattern is comparable to the potential sediment yield from terrestrial areas and its supply to the adjacent marine environment. The spatial distribution of anomalous elemental concentrations in silty and clayey sediments suggests horizontal dispersion by a periodic current, as well as precipitation processes occurring at the boundary between water masses. However, the geochemical features of coarse sands and gravels differ significantly from those of stream sediments in the adjacent terrestrial areas, and fractionation of the mineralogical composition due to strong tidal currents, in addition to the denudation of Miocene–Pliocene basement rocks of the underwater topographic highs are possible reason for this inconsistency in geochemistry. As such, comprehensive geochemical maps of both the land and the sea are demonstrated as being useful for determining the source of fine marine sediments, as well as for tracking the transfer and deposition of silty-clayey sediments.

Acknowledgments: The authors extend special thanks to Takashi Okai, Yutaka Kanai, Masumi Mikoshiba, and Ran Kubota (Geological Survey of Japan, AIST) for their useful suggestions, which have helped to improve the manuscript. We are grateful to the Japan Oceanographic Data Center (JODC) for providing data files.

Author Contributions: Noboru Imai conceived the study and organized the sampling on land; Ken Ikehara organized the sampling in the coastal seas; Yoshiko Tachibana measured elemental concentrations; and Atsuyuki Ohta analyzed the data and wrote the paper.

Conflicts of Interest: The authors declare no conflict of interest.

Appendix A

The sediment yield, drainage basin area, and river water discharge of 24 major rivers in the study area are summarized in Table A1. The abbreviation of each river name is shown in Figure 1b. The sediment yield of each river system is calculated using the drainage basin area and the average rate of erosion in each river basin after Akimoto et al. [16].

Table A1. Sediment yield and river water discharge data in each river system of the study area.

River System	Sediment Yield ($\times 10^3$ m^3/Year)	River Water Discharge [1] ($\times 10^6$ m^3/Year)	Discharged Area	Relative Rate to Total Sediment Yield
		Shikoku region		
Yoshino (Ys)	870	3202	Kii Channel	11%
Naka (Na)	510	1628	Kii Channel	7%
Toki (To)	83	(34) [2]	Ibi-Seto-Nada	1%
Shigenobu (Sg)	97	46	Iyo-Nada	1%
Hiji (H)	215	1111	Iyo-Nada	3%
Mononobe (M)	458	777	Tosa Bay	6%
Niyodo (Ni)	534	3101	Tosa Bay	7%
Shimanto (Sm)	699	4712	Tosa Bay	9%
		Chugoku region		
Yoshii (Yi)	290	(1125) [2]	Ibi-Seto-Nada	4%
Asahi (Ah)	238	1492	Ibi-Seto-Nada	3%
Takahari (Ta)	358	1605	Ibi-Seto-Nada	5%
Ashido (Ad)	142	187	Bingo-Nada	2%
Ohta (Ot)	(238) [3]	-	Hiroshima Bay	3%
Oze (Oz)	48	255	Hiroshima Bay	1%
Sanami (Sn)	95	261	Suo-Nada	1%
		Kinki region		
Ibo (I)	174	676	Harima-Nada	2%
Kako (Ka)	247	918	Harima-Nada	3%
Yodo (Yd)	1310	5376	Osaka Bay	17%
Yamato (Ym)	123	(426) [2]	Osaka Bay	2%
Kino (Ki)	377	1184	Kii Channel	5%
		Kyushu region		
Yamakuni (Yk)	99	418	Suo-Nada	1%
Ohita (Oi)	150	498	Beppu Bay	2%
Ohno (On)	240	1616	Beppu Bay	3%
Banjo (B)	89	392	Bungo Channel	1%

Notes: [1] River water discharge data in 2000, which are taken from [57]; [2] River water discharge data in 1994 [57]; [3] Average rate of sediment yield of Ohta River is missing [16], so the value is assumed to be the same as that of Oze River.

Appendix B

Ohta et al. [29] and Ohta et al. [32] assumed that when a specific rock type outcrops over more than half of the drainage basin area, it is representative of the surface rock types in the watershed and is the dominant control of elemental abundances in stream sediments. In the study area, there are seven rock types exposed in more than half of the river basin areas: sediments and sedimentary rocks (Sed); sedimentary rocks of accretionary complexes (Acc); granitic rocks (Gr); felsic volcanic rocks (Fv); mafic volcanic rocks (Mv); debris and pyroclastic rocks (Phy); and high-pressure type metamorphic rocks (Meta). We further separated those stream sediments collected in urban areas (Sed_u), from sediments and sedimentary rocks (Sed), using a land use map, because anthropogenic contamination significantly enhances certain elements in the sediments, including Cu, Zn and Cd [32]. Table B1 presents the median elemental concentrations of stream sediments classified by the above rock types. In this, "other" represents those cases in which no specific rock type occupies more than half of the catchment area, and is not used in the cluster analysis. The Sed_u and Phy categories are also excluded from cluster analysis because contaminated sediments reflect only local conditions, and debris and pyroclastic rocks represent a mixture of mafic and felsic eruptive products.

Table B1. Median elemental concentrations in stream sediments classified according to the dominant rock type in the drainage basin.

Element	Sed	Sed_u	Acc	Gr	Mv	Fv	Phy	Meta	Other
	***n* = 70**	***n* = 11**	***n* = 157**	***n* = 71**	***n* = 41**	***n* = 61**	***n* = 13**	***n* = 47**	***n* = 105**
wt %									
Na_2O	2.06	2.21	1.74	2.89	2.44	1.82	2.34	2.26	2.08
MgO	1.34	1.63	1.54	1.03	3.17	1.12	3.80	3.57	1.98
Al_2O_3	11.54	9.89	11.47	11.43	12.14	10.35	13.43	13.35	11.05
P_2O_5	0.109	0.157	0.093	0.098	0.156	0.085	0.181	0.148	0.103
K_2O	2.21	2.22	2.28	2.57	1.13	2.65	1.34	1.74	2.18
CaO	1.21	1.41	0.52	1.58	3.60	1.07	4.33	2.87	1.80
TiO_2	0.56	0.65	0.49	0.50	1.10	0.48	1.17	0.73	0.68
MnO	0.088	0.083	0.091	0.116	0.152	0.117	0.187	0.168	0.126
T-Fe_2O_3	3.94	4.59	4.13	3.82	7.00	4.10	9.42	7.21	5.19
mg/kg									
Li	35.2	32.5	42.7	30.4	25.5	38.4	24.2	37.3	37.6
Be	1.54	1.70	1.66	2.34	1.20	1.95	1.32	1.38	1.64
Sc	8.33	8.23	8.55	7.41	14.1	7.80	20.3	18.3	11.0
V	69	59	82	52	155	62	237	155	97
Cr	47.1	110	55.6	24.1	53.7	32.8	38.6	169	61.1
Co	9.05	11.9	10.4	7.1	18.5	8.6	22.7	23.8	13.1
Ni	18.7	38.4	26.2	9.3	17.2	13.0	12.6	59.5	25.3
Cu	29.5	67.7	35.9	25.2	27.0	27.7	31.9	62.3	35.2
Zn	108	194	101	114	130	137	131	122	130
Ga	16.3	16.8	16.6	19.2	17.9	17.8	18.8	17.9	17.1
As	6	7	8	7	4	22	8	8	13
Rb	102	109	102	121	39	153	49.8	73	104
Sr	110	97	90	100	254	91	301	144	122
Y	18.0	20.3	11.9	24.7	17.2	20.5	23.2	24.8	19.5
Nb	8.77	10.05	8.12	10.8	11.4	8.82	8.82	8.29	8.63
Mo	0.77	1.79	1.00	0.91	1.03	0.98	1.46	0.94	1.07
Cd	0.13	0.20	0.11	0.17	0.15	0.26	0.16	0.18	0.20
Sn	3.62	7.72	2.95	4.60	2.36	4.30	2.17	2.81	4.04
Sb	0.80	1.21	0.75	0.38	0.52	0.92	0.48	0.85	0.92
Cs	4.84	3.89	4.97	4.44	2.39	7.65	3.24	5.06	5.59
Ba	469	491	448	401	352	456	402	351	414
La	20.7	30.9	19.4	24.1	16.4	20.9	18.2	20.0	19.4
Ce	38.9	57.1	37.3	41.2	29.2	35.3	37.7	39.4	34.0
Pr	4.63	6.74	4.42	5.42	3.87	4.66	4.94	4.80	4.55
Nd	17.8	26.2	16.9	22.0	15.9	17.8	20.6	19.6	17.9
Sm	3.72	5.44	3.21	4.59	3.27	3.62	4.46	4.27	3.73
Eu	0.78	0.88	0.65	0.73	0.94	0.71	1.24	1.07	0.79
Gd	3.40	4.37	2.78	4.31	3.09	3.33	4.40	4.28	3.48
Tb	0.59	0.72	0.45	0.75	0.54	0.59	0.75	0.77	0.59
Dy	3.10	3.61	2.14	4.00	2.70	3.05	3.87	4.05	3.10
Ho	0.60	0.67	0.41	0.79	0.52	0.61	0.75	0.81	0.60
Er	1.77	1.89	1.14	2.34	1.56	1.81	2.24	2.29	1.80
Tm	0.28	0.29	0.18	0.40	0.25	0.30	0.36	0.36	0.29
Yb	1.75	1.74	1.11	2.58	1.53	1.89	2.23	1.97	1.82
Lu	0.26	0.27	0.16	0.39	0.24	0.28	0.33	0.27	0.26
Ta	0.77	0.87	0.73	1.11	0.80	0.70	0.72	0.71	0.68
Hg	0.06	0.12	0.12	0.03	0.06	0.04	0.06	0.07	0.04
Tl	0.63	0.62	0.58	0.69	0.33	0.85	0.47	0.44	0.64
Pb	26.0	37.1	24.2	32.4	22.6	44.1	19.0	20.6	29.6
Bi	0.23	0.32	0.28	0.40	0.17	0.52	0.25	0.25	0.39
Th	8.21	12.8	6.62	14.4	4.37	8.46	5.78	6.74	7.33
U	1.83	2.27	1.51	3.31	1.03	2.41	1.61	1.21	1.79

Appendix C

Statistical analysis assumes that the data follow a normal distribution. However, it is known that the elemental concentrations of minor elements follow a lognormal distribution, such that their logarithmic data follow a normal distribution. The Shapiro–Wilk test is applied to examine the data distribution for each data set at a confidence level of $p = 0.01$ [58,59]. When the estimated probability is

greater than 0.01, we conclude that the data follow a normal distribution. However, in this study, the estimated probabilities were all smaller than 0.01, and the geochemical data are concluded to follow neither a normal nor a lognormal distribution. This is because statistical tests with a large amount of data, such as the 463 sets used in this study, are highly sensitive to very small differences. Thus, we determine a probable distribution using the W-value of the Shapiro–Wilk statistic; the closer this value is to 1.0, the more closely it follows a normal distribution. As an alternative, Ohta et al. [8] and Ohta et al. [32] proposed that the data with skewness close to zero, which indicates a symmetrical distribution, is used for ANOVA. Both the Shapiro–Wilk statistics and skewness are summarized in Table C1. For example, K_2O data are unchanged for ANOVA because the Shapiro–Wilk statistics and the skewness of unaltered K_2O data are closer to 1.0 and zero, respectively, than those of log-transformed K_2O data (Table C1). On the basis of this analysis, data for 24 elements within the marine sediments were log-transformed, with the remaining data left unaltered for ANOVA (Table C1).

Table C1. The Shapiro–Wilk test applied to the unchanged and log-transformed data and their skewness.

Element	W-Value of Shapiro–Wilk Statistics		Skewness		Data Transformation
	Unchanged	Log-Transformed	Unchanged	Log-Transformed	
MgO	0.884	0.872	1.3	−1.3	Unchanged
Al_2O_3	0.971	0.869	−0.48	−2.0	Unchanged
P_2O_5	0.168	0.870	19	0.96	Log-transformed
K_2O	0.949	0.820	−0.78	−2.3	Unchanged
CaO	0.777	0.980	2.5	−0.34	Log-transformed
TiO_2	0.722	0.873	3.3	−0.80	Log-transformed
MnO	0.731	0.946	2.9	0.72	Log-transformed
T-Fe_2O_3	0.667	0.839	3.4	−0.32	Log-transformed
Li	0.924	0.975	1.1	−0.46	Log-transformed
Be	0.957	0.854	−0.60	−2.0	Unchanged
Sc	0.769	0.874	2.6	−0.84	Log-transformed
V	0.580	0.914	6.1	−0.19	Log-transformed
Cr	0.952	0.923	0.78	−1.2	Unchanged
Co	0.804	0.905	2.5	−0.55	Log-transformed
Ni	0.883	0.930	1.9	−1.0	Log-transformed
Cu	0.922	0.965	1.1	−0.44	Log-transformed
Zn	0.734	0.896	2.7	−0.02	Log-transformed
Ga	0.919	0.781	−1.2	−2.6	Unchanged
As	0.615	0.899	4.7	−0.98	Log-transformed
Rb	0.985	0.897	−0.44	−1.5	Unchanged
Sr	0.647	0.964	3.7	0.69	Log-transformed
Y	0.977	0.991	0.66	−0.29	Log-transformed
Nb	0.990	0.945	0.01	−0.93	Unchanged
Mo	0.378	0.961	11.22	0.85	Log-transformed
Cd	0.835	0.978	1.8	0.14	Log-transformed
Sn	0.519	0.936	6.8	0.53	Log-transformed
Sb	0.931	0.980	1.1	−0.27	Log-transformed
Cs	0.961	0.885	−0.42	−1.3	Unchanged
Ba	0.771	0.886	4.4	−1.2	Log-transformed
La	0.981	0.917	−0.45	−1.3	Unchanged
Ce	0.981	0.924	−0.38	−1.2	Unchanged
Pr	0.973	0.897	−0.61	−1.5	Unchanged
Nd	0.969	0.888	−0.64	−1.6	Unchanged
Sm	0.975	0.905	−0.44	−1.4	Unchanged
Eu	0.987	0.971	0.20	−0.64	Unchanged
Gd	0.983	0.942	0.01	−1.0	Unchanged
Tb	0.982	0.971	0.36	−0.62	Unchanged
Dy	0.981	0.982	0.48	−0.46	Log-transformed
Ho	0.980	0.989	0.56	−0.34	Log-transformed
Er	0.982	0.988	0.53	−0.36	Log-transformed
Tm	0.983	0.989	0.50	−0.36	Log-transformed
Yb	0.985	0.986	0.45	−0.42	Log-transformed
Lu	0.987	0.983	0.40	−0.50	Unchanged
Ta	0.986	0.948	0.10	−0.87	Unchanged
Hg	0.187	0.819	19	−1.6	Log-transformed
Tl	0.964	0.876	0.20	−1.6	Unchanged
Pb	0.637	0.893	4.3	1.2	Log-transformed
Bi	0.753	0.975	2.5	0.31	Log-transformed
Th	0.804	0.890	3.2	−1.0	Log-transformed
U	0.886	0.988	1.8	0.10	Log-transformed

Table C2 shows the two-way layout of ANOVA in this study. The table shows that the sample numbers are not equal for each condition, this is known as an "unbalanced sample size". Some methods have been proposed to calculate the sum of squares for an unbalanced two-way ANOVA [59,60]. Ohta et al. [8] suggested that a two-way ANOVA using the Type II method [60,61] is preferable for these data because our interest lies in understanding the effects of the two main factors.

Table C2. The two-way layout for ANOVA.

	Coarse Sediment	Fine Sand	Silt and Clay
Seto Inland Sea	$n = 26$	$n = 15$	$n = 47$
Pacific Ocean	$n = 75$	$n = 107$	$n = 193$

References

1. Imai, N.; Terashima, S.; Ohta, A.; Mikoshiba, M.; Okai, T.; Tachibana, Y.; Togashi, S.; Matsuhisa, Y.; Kanai, Y.; Kamioka, H. *Geochemical Map of Sea and Land of Japan*; Geological Survey of Japan, AIST: Tsukuba, Japan, 2010.
2. Webb, J.S.; Thornton, I.; Thompson, M.; Howarth, R.J.; Lowenstein, P.L. *The Wolfson Geochemical Atlas of England and Wales*; Clarendon Press: Oxford, UK, 1978.
3. Salminen, R.; Batista, M.J.; Bidovec, M.; Demetriades, A.; De Vivo, B.; De Vos, W.; Duris, M.; Gilucis, A.; Gregorauskiene, V.; Halamic, J.; et al. *Geochemical Atlas of Europe. Part 1—Background Information, Methodology and Maps*; Geological Survey of Finland: Espoo, Finland, 2005.
4. Caritat, P.D.; Cooper, M. *National Geochemical Survey of Australia: Data Quality Assessment*; Geoscience Australia Record 2011/21; p. 478. Available online: http://www.ga.gov.au/corporate_data/71971/Rec2011_021_Vol1.pdf (accessed on 17 November 2014).
5. Smith, D.B.; Cannon, W.F.; Woodruff, L.G.; Solano, F.; Ellefsen, K.J. *Geochemical and Mineralogical Maps for Soils of the Conterminous United States*; U.S. Geological Survey Open-File Report 2014-1082. Available online: http://pubs.usgs.gov/of/2014/1082/pdf/ofr2014-1082.pdf (accessed on 19 May 2014).
6. Xie, X.J.; Chen, H.X. Global geochemical mapping and its implementation in the Asia-Pacific region. *Appl. Geochem.* **2001**, *16*, 1309–1321.
7. Ohta, A.; Imai, N. Comprehensive survey of multi-elements in coastal sea and stream sediments in the island arc region of Japan: Mass transfer from terrestrial to marine environments. In *Advanced Topics in Mass Transfer*; El-Amin, M., Ed.; InTech: Rijeka, Croatia, 2011; pp. 373–398.
8. Ohta, A.; Imai, N.; Terashima, S.; Tachibana, Y.; Ikehara, K.; Okai, T.; Ujiie-Mikoshiba, M.; Kubota, R. Elemental distribution of coastal sea and stream sediments in the island-arc region of Japan and mass transfer processes from terrestrial to marine environments. *Appl. Geochem.* **2007**, *22*, 2872–2891. [CrossRef]
9. Kuwashiro, I. Submarine topography of Japanese Inlandsea Setonaikai. *Geogr. Rev. Jpn.* **1959**, *32*, 24–35. [CrossRef]
10. Yanagi, T. Currents and sediment transport in the Seto Inland Sea, Japan. In *Residual Currents and Long-Term Transport*; Cheng, R.T., Ed.; Springer: Beilin, Germany, 1990; Volume 38, pp. 348–355.
11. Sano, S.; Inouchi, Y.; Kanai, Y.; Maruoka, N. Geochemical properties of surface sediments in Seto Inland Sea part 1: Aki-nada surface sediments. *Mem. Fac. Educ. Ehime Univ. Ser. III Nat. Sci.* **2000**, *20*, 1–9.
12. Inouchi, Y. Distribution of bottom sediments in the Seto Inland Sea—The influence of tidal currents on the distribution of bottom sediments. *J. Geol. Soc. Jpn.* **1982**, *88*, 665–681. [CrossRef]
13. Yanagi, T.; Hagita, T.; Saino, T. Episodic outflow of suspended sediments from the Kii channel to the Pacific Ocean in winter. *J. Oceanogr.* **1994**, *50*, 99–108. [CrossRef]
14. Kawana, K.; Tanimoto, T. Turbid bottom water layer and bottom sediment in the Seto Inland Sea. *J. Oceanogr. Soc. Jpn.* **1984**, *40*, 175–183. [CrossRef]
15. Hoshika, A.; Shiozawa, T.; Kawana, K.; Tanimoto, T. Heavy metal pollution in sediment from the Seto Inland Sea, Japan. *Mar. Pollut. Bull.* **1991**, *23*, 101–105. [CrossRef]
16. Akimoto, T.; Kawagoe, S.; Kazama, S. Estimation of sediment yield in Japan by using climate projection model. *Proc. Hydraul. Eng.* **2009**, *53*, 655–660.
17. *Geological Map of Japan, 1:1,000,000*, 3rd ed.; Geological Survey of Japan, AIST: Tsukuba, Japan, 1992.

18. Kato, M. Recent foramininifera in the surface sediments in the inland sea of Japan. *Ann. Sci. Coll. Lib. Arts Kanazawa Univ.* **1995**, *19*, 63–73.
19. Okamura, Y. Geologic structure of the upper continental slope off Shikoku and Quaternary tectonic movement of the outer zone of southwest Japan. *J. Geol. Soc. Jpn.* **1990**, *96*, 223–237. [CrossRef]
20. Fujimoto, M. On the flow types and current stability in Tosa bay and adjacent seas. *Sea Sky* **1987**, *62*, 127–140.
21. Miyata, K.; Sakamoto, H.; Momota, M. Oceanographycal structure in the Tosa bay-1. On the tidal current. *Bull. Nansei Natl. Fish. Res. Inst.* **1980**, *12*, 115–124.
22. Imai, N.; Terashima, S.; Ohta, A.; Mikoshiba, M.; Okai, T.; Tachibana, Y.; Togashi, S.; Matsuhisa, Y.; Kanai, Y.; Kamioka, H.; et al. *Geochemical Map of Japan*, 1st ed.; Geological Survey of Japan, AIST: Tsukuba, Japan, 2004.
23. Mikoshiba, M.U.; Imai, N.; Tachibana, Y. Geochemical mapping in Shikoku, southwest Japan. *Appl. Geochem.* **2011**, *26*, 1549–1568. [CrossRef]
24. Arita, M.; Kinoshita, Y. Sedimentological map of cape Muroto. In *1:200,000 Marine Geology Map Series 37*; Geological Survey of Japan: Tsukuba, Japan, 1990.
25. Ikehara, K. Sedimentological map of Tosa Wan. In *1:200,000 Marine Geology Map Series 34*; Geological Survey of Japan: Tsukuba, Japan, 1988.
26. Ikehara, K. Sedimentological map south of Bungo channel. In *1:200,000 Marine Geology Map Series 51*; Geological Survey of Japan: Tsukuba, Japan, 1999.
27. Hoshika, A.; Shiozawa, T. Heavy metals and accumulation rates of sediments in Osaka bay, the Seto Inland Sea, Japan. *J. Oceanogr. Soc. Jpn.* **1986**, *42*, 39–52. [CrossRef]
28. Imai, N. Multielement analysis of rocks with the use of geological certified reference material by inductively coupled plasma mass spectrometry. *Anal. Sci.* **1990**, *6*, 389–395. [CrossRef]
29. Ohta, A.; Imai, N.; Terashima, S.; Tachibana, Y.; Ikehara, K.; Nakajima, T. Geochemical mapping in Hokuriku, Japan: Influence of surface geology, mineral occurrences and mass movement from terrestrial to marine environments. *Appl. Geochem.* **2004**, *19*, 1453–1469. [CrossRef]
30. Reimann, C. Geochemical mapping: Technique or art? *Geochem. Explor. Environ. Anal.* **2005**, *5*, 359–370. [CrossRef]
31. Ohta, A.; Imai, N.; Terashima, S.; Tachibana, Y. Investigation of elemental behaviors in Chugoku region of Japan based on geochemical map utilizing stream sediments. *Chikyukagaku (Geochemistry)* **2004**, *38*, 203–222.
32. Ohta, A.; Imai, N.; Terashima, S.; Tachibana, Y. Application of multi-element statistical analysis for regional geochemical mapping in central Japan. *Appl. Geochem.* **2005**, *20*, 1017–1037. [CrossRef]
33. Fritz, C.O.; Morris, P.E.; Richler, J.J. Effect size estimates: Current use, calculations, and interpretation. *J. Exp. Psychol. Gen.* **2012**, *141*, 2–18. [CrossRef] [PubMed]
34. Richardson, J.T. Eta squared and partial eta squared as measures of effect size in educational research. *Educ. Res. Rev.* **2011**, *6*, 135–147. [CrossRef]
35. Miller, J.C.; Miller, J.N. *Statistics for Analytical Chemistry*, 6th ed.; Pearson Education Canada: Don Mills, ON, USA, 2010.
36. Taylor, S.R.; McLennan, S.M. The geochemical evolution of the continental crust. *Rev. Geophys.* **1995**, *33*, 241–265. [CrossRef]
37. Togashi, S.; Imai, N.; Okuyama-Kusunose, Y.; Tanaka, T.; Okai, T.; Koma, T.; Murata, Y. Young upper crustal chemical composition of the orogenic Japan arc. *Geochem. Geophys. Geosyst.* **2000**, *1*, 2000GC000083. [CrossRef]
38. Aitchison, J. The statistical analysis of compositional data. *J. R. Stat. Soc. Ser. B* **1982**, *44*, 139–177.
39. Pawlowsky-Glahn, V.; Egozcue, J.J. Compositional data and their analysis: An introduction. In *Compositional Data Analysis in the Geosciences: From Theory to Practice*; Buccianti, A., Mateu-Figueras, G.H., Pawlowsky-Glahn, V., Eds.; Geological Society, Publishing House: Bath, UK, 2006; Volume 264, pp. 1–10.
40. Ward, J.H., Jr. Hierarchical grouping to optimize an objective function. *J. Am. Stat. Assoc.* **1963**, *58*, 236–244. [CrossRef]
41. Goldich, S.S. A study in rock-weathering. *J. Geol.* **1938**, *46*, 17–58. [CrossRef]
42. Ohta, A.; Imai, N.; Terashima, S.; Tachibana, Y.; Ikehara, K.; Katayama, H. Elemental distribution of surface sediments around Oki trough including adjacent terrestrial area: Strong impact of Japan Sea Proper Water on silty and clayey sediments. *Bull. Geol. Surv. Jpn.* **2015**, *66*, 81–101. [CrossRef]
43. Mahalanobis, P.C. On the generalized distance in statistics. *Proc. Natl. Inst. Sci.* **1936**, *2*, 49–55.

44. Minakawa, T.; Funakoshi, N.; Morioka, H. Chemical properties of allanite from the Ryoke and Hiroshima granite pegmatites in Shikoku, Japan. *Men. Fac. Sci. Ehime Univ.* **2001**, *7*, 1–13.
45. Nozaki, T.; Nakamura, K.; Osawa, H.; Fujinaga, K.; Kato, Y. Geochemical features and tectonic setting of greenstones from Kunimiyama, northern Chichibu belt, central Shikoku, Japan. *Resour. Geol.* **2005**, *55*, 301–310. [CrossRef]
46. Hoshino, M. On the muddy sediments of the continental shelf adjacent to Japan. *J. Geol. Soc. Jpn.* **1952**, *58*, 41–53.
47. Hoshika, A.; Shiozawa, T. Sedimentation rates and heavy metal pollution of sediments in the Seto Inland Sea. Part 3. Hiuchi-nada. *J. Oceanogr. Soc. Jpn.* **1984**, *40*, 334–342. [CrossRef]
48. Hoshika, A.; Tanimoto, T.; Mishima, Y. Sedimentation processes of particulate matter in the Osaka bay. *Oceanogr. Jpn.* **1994**, *3*, 419–425. [CrossRef]
49. Manabe, T. Distribution of sediments contamination in the eastern Seto Inland Sea. *Sea Sky* **1991**, *67*, 1–9.
50. Hoshika, A.; Shiozawa, T. Sedimentation rates and heavy metal pollution of sediments in the Seto Inland Sea. Part 4. Suo-nada. *J. Oceanogr. Soc. Jpn.* **1985**, *41*, 283–290. [CrossRef]
51. Hudson-Edwards, K.A.; Macklin, M.G.; Curtis, C.D.; Vaughan, D.J. Processes of formation and distribution of Pb-, Zn-, Cd-, and Cu-bearing minerals in the Tyne basin, northeast England: Implications for metal-contaminated river systems. *Environ. Sci. Technol.* **1996**, *30*, 72–80. [CrossRef]
52. Rosenthal, Y.; Lam, P.; Boyle, E.A.; Thomson, J. Authigenic cadmium enrichments in suboxic sediments: Precipitation and postdepositional mobility. *Earth Planet. Sci. Lett.* **1995**, *132*, 99–111. [CrossRef]
53. Mason, R.P.; Fitzgerald, W.F.; Morel, F.M.M. The biogeochemical cycling of elemental mercury: Anthropogenic influences. *Geochim. Cosmochim. Acta* **1994**, *58*, 3191–3198. [CrossRef]
54. Shaw, T.J.; Gieskes, J.M.; Jahnke, R.A. Early diagenesis in differing depositional environments: The response of transition metals in pore water. *Geochim. Cosmochim. Acta* **1990**, *54*, 1233–1246. [CrossRef]
55. Klinkhammer, G.P. Early diagenesis in sediments from the eastern equatorial pacific. II. Pore water metal results. *Earth Planet. Sci. Lett.* **1980**, *49*, 81–101. [CrossRef]
56. Wilson, T.R.S.; Thomson, J.; Colley, S.; Hydes, D.J.; Higgs, N.C.; Sorensen, J. Early organic diagenesis: The significance of progressive subsurface oxidation fronts in pelagic sediments. *Geochim. Cosmochim. Acta* **1985**, *49*, 811–822. [CrossRef]
57. Ministry of Land, Infrastructure, Transport and Tourism. Available online: http://www.mlit.go.jp/river/toukei_chousa/ (accessed on 19 November 2015).
58. Shapiro, S.S.; Wilk, M.B. An analysis of variance test for normality (complete samples). *Biometrika* **1965**, *52*, 591–611. [CrossRef]
59. Royston, P. A remark on algorithm as181: The w-test for normality. *Appl. Stat. J. R. Stat. Soc.* **1995**, *44*, 547–551.
60. Shaw, R.G.; Mitchell-Olds, T. ANOVA for unbalanced data: An overview. *Ecology* **1993**, *74*, 1638–1645. [CrossRef]
61. Littell, R.C.; Stroup, W.W.; Freund, R. *SAS for Linear Models*; SAS Institute: Cary, NC, USA, 2002.

water

MDPI

Article

Numerical Simulations of Suspended Sediment Dynamics Due to Seasonal Forcing in the Mekong Coastal Area

Vu Duy Vinh [1,*], Sylvain Ouillon [2,3], Nguyen Van Thao [1] and Nguyen Ngoc Tien [4]

1 Institute of Marine Environment and Resources, VAST, 246 Danang Street, Haiphong City 180000, Vietnam; thaonv@imer.ac.vn
2 UMR LEGOS, Université de Toulouse, IRD, CNES, CNRS, UPS, 14 avenue Edouard Belin, 31400 Toulouse, France; sylvain.ouillon@legos.obs-mip.fr
3 Department Water-Environment-Oceanography, University of Science and Technology of Hanoi, 18 Hoang Quoc Viet, Hanoi 100000, Vietnam
4 Institute of Marine Geology and Geophysics, VAST, 18 Hoang Quoc Viet, Hanoi 100000, Vietnam; nntien@imgg.vast.vn
* Correspondence: vinhvd@imer.ac.vn; Tel.: +84-912-799-629

Academic Editor: Y. Jun Xu
Received: 27 April 2016; Accepted: 9 June 2016; Published: 16 June 2016

Abstract: The Mekong River is ranked as the 8th in terms of water discharge and as the 10th in terms of sediment load in the world. During the last 4500 years, its delta prograded more than 250 km to the south due to a tremendous amount of sediments deposited, and turned from a "tide-dominated" delta into a "wave-and-tide dominated" delta. This study aims at completing our knowledge on the fate of sediments that may be stored in estuarine or coastal systems, or dispersed over the continental shelf and slope. Sediment transport in the Mekong River Delta (MRD) coastal area was studied by numerical simulations using the Delft3D model. The model configuration was calibrated and validated from data collected *in situ* during 4 periods from 2012 to 2014. Then, 50 scenarios corresponding to different wave conditions (derived from the wave climate) and river discharge values typical of low flow and flood seasons enabled us to quantify the dispersal patterns of fluvial sediments close to the mouths and along the coast. Sediments mostly settled in the estuary and close to the mouths under calm conditions, and suspended sediment with higher concentrations extend further offshore with higher waves. Waves from the Southeast enhanced the concentration all along the MRD coastal zone. Waves from the South and Southwest induced coastal erosion, higher suspended sediment concentrations in front of the southern delta, and a net transport towards the Northeast of the delta. Because of episodes of Southern and Southwestern waves during the low flow season, the net alongshore suspended sediment transport is oriented Northeastward and decreases from the Southwestern part of the coastal zone (~960 $\times$ 10^3 t yr^{-1}) to the Northeastern part (~650 $\times$ 10^3 t yr^{-1}).

Keywords: suspended sediment; sediment transport; coastal hydraulics; Mekong; river plume; monsoon; mathematical model

1. Introduction

Rivers originating from the Tibetan plateau and the Himalayas (Ganges, Brahmaputra, Yellow River, Yangtze, Mekong, Irrawady, Red River, Pearl River) are huge providers of sediments to the ocean at global scale [1]. However, recent human activities have severely altered their sediment discharge, mainly as a consequence of artificial impoundments, and also by activities such as groundwater pumping, irrigation, dredging, and deforestation [2]. At a global scale, around 53% of river sediment

flux is now potentially trapped in reservoirs [3], and this reduction dramatically affects deltas [4]. For example, in Asia, sediment discharge decreased by 87% (from 1200 to 150 $\times$ 10^6 t yr^{-1}) over a 40 year period in the Yellow River (Huanghe) [5,6] and by 61% (from 119 to 46 $\times$ 10^6 t yr^{-1}) in the Red River after the Hoa Binh dam settlement [7].

Sediment dynamics have considerable impacts, not only in terms of geomorphology but also in terms of geochemical cycles [8,9], biogeochemistry [10], microbiology [11], fate of metal contamination [12], benthic environment, coral reefs and seagrass communities ([13] and references therein). Sediment budgets are thus of interest for many interdisciplinary studies [14].

Seasonally, the sediment discharge, transport and deposition in the Asian deltas are strongly affected by the variations in precipitation, wind and waves induced by the monsoons [15,16]. The monsoons highly influence coastal geomorphology of these deltas, which experience rapid changing shorelines. Understanding the influences of monsoons is essential for predicting changes in sedimentary environment and coastal geomorphology [16].

The Mekong River delta (MRD) is amongst the third largest delta plain in the world, with 16–20 million inhabitants in its Vietnamese part (density of ~460 people km^{-2}, [17]). It covers an area of 62,500 km^2 between Phnom Penh in the Cambodian lowlands and the southern Vietnamese coast [18]. The MRD lies entirely within three meters above sea level.

Recent studies focused on sediment variability in the Mekong River [19,20], on sedimentation in the Lower Mekong River [21,22], within the distributaries [23], and along the MRD coast at depths > 5 m [24]. The concentration of surface suspended matter in the Mekong River plume was shown to decrease by ~5% per year during the period 2002–2012 from the analysis of MERIS satellite data [25]. However, little is known on the fate of sediments reaching the sea that may be stored in estuarine or coastal systems, or dispersed over the continental shelf and slope ([26] and references therein).

With a tidal range up to 3 m in spring tide, sediment dynamics within the Mekong distributaries is strongly affected by tidal oscillations. From *in situ* measurements, Wolanski *et al.* [27,28] sketched a conceptual model of the present-day sediment dynamics in the Bassac estuary (the southern main distributary of the Mekong River), completed by Hein *et al.* [29]: most of the sediment brought by the River is deposited in the shallow coastal waters of depth <20 m (corresponding to the subaqueous delta) in the flood season, while a net flux of particles occurs upstream in the estuary during the low flow season. Alongshore, numerical simulations by Hein *et al.* [29] have shown that deposition dominates over the annual cycle directly off the mouths of the Mekong branches, where erosion prevails throughout the year in shallow waters to the North and to the South (along the Cape), while erosion and deposition alternate further offshore with the seasonal cycle. Therefore, there are specific needs to quantitatively assess the dispersal patterns of fluvial sediments close to the mouths and along the coasts for management purposes.

This paper aims at complementing the previous studies in the coastal area along the Mekong River delta. The variability of sediment transport along the delta is examined during the low flow and flood seasons from numerical modeling, under 50 scenarios based on the wave climate (25 scenarios per season). The resulting numerical simulations are discussed in view of recent changes in sediment deposition and erosion along the delta coastline.

2. Materials and Methods

2.1. The Mekong River Delta (MRD)

2.1.1. The Mekong River

The Mekong River originates from the Tibetan plateau at elevations mostly >5000 m, then flows through six countries along a 4880-km course down to the South China Sea (East Sea of Vietnam), making it the 12th longest river in the world [22]. The Mekong River, which drains a basin area of ~795 $\times$ 10^3 km^2 [19], was ranked as the 8th in terms of water discharge with an average flow of

15,000 $m^3 \cdot s^{-1}$ [30] and as the 10th in terms of sediment load with an average value estimated to be 160×10^6 t yr^{-1} [31], corrected to $144 \pm 36 \times 10^6$ t yr^{-1} over the last 3 k yr by Ta *et al.* [32].

The Mekong River water and sediment discharges are distributed amongst a network of two main distributaries which divide near Phnom Penh: the Mekong—called the Tiền River after entering Vietnam—to the North, and the Bassac—called the Hậu River in Vietnam—to the South. The Mekong (Tien) distributary divides itself into three main estuaries with Tieu and Dai mouths for the further North, Ham Luong for the central branch, and Co Chien and Cung Hau mouths for the further South. The Bassac (Hau) River divides mainly into the Tran De mouth and the Dinh An mouth (see Figure 1).

The Dong Nai–Saigon River system flows to the South China Sea just to the North of the MRD. The Saigon River is called Soai Rap River in its lower basin. The Vamco River is a tributary that joins the Soai Rap River just upstream of its mouth (Figure 1a).

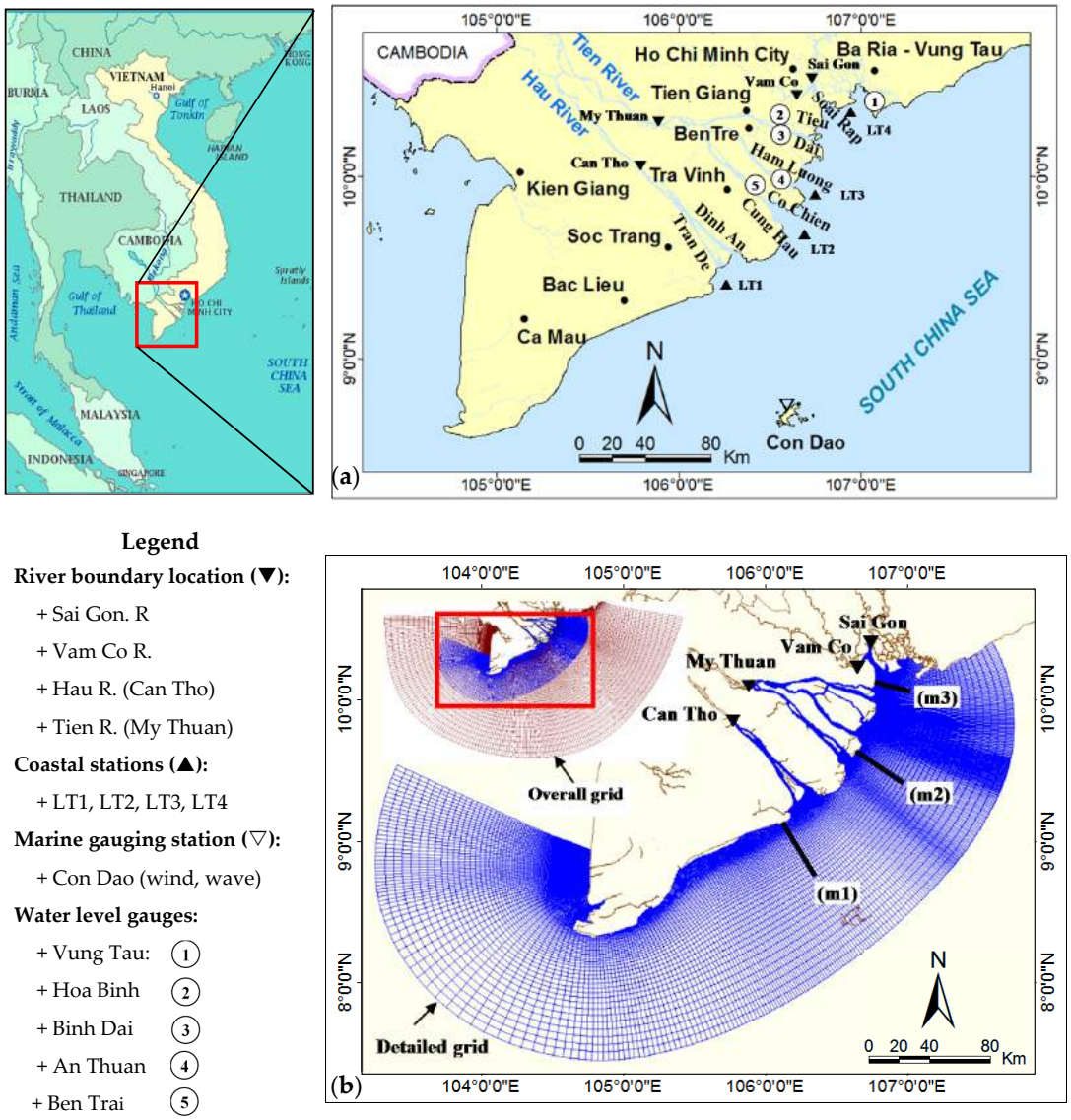

Figure 1. The Mekong River Delta and its region of freshwater influence. (**a**) General map with locations of measurements (coastal stations LT1, LT2, LT3 and LT4; marine gauging station of Con Dao; water level gauges); (**b**) The parent grid outside and the child grid over the study area, with locations of the river boundaries of the model, and cross sections (m1, m2 and m3) used in the calculations.

During the last 4500 years, the MRD prograded more than 250 km to the southeast [18]. Approximately 3000 years ago, the prodelta was located near Ben Tre and Tra Vinh cities (see [32],

their Figure 4). During this recent progradation (~3 k yr BP), the southern coast of the MRD became more sensitive to waves from the East and North-East during the dry season, and the MRD turned from a "tide-dominated delta" into a "tide-and-wave dominated" delta [32]. The continental shelf is very shallow (most of the plume flows over depths <10–15 m), the river mouths being located in a sedimental plain. Despite the low Coriolis number, the large freshwater discharge still creates a baroclinic coastal current flowing in the direction of the Kelvin wave [33].

2.1.2. Climate and Rainfall

The Mekong basin ranges from cool temperate to tropical climates. The Lower Mekong River basin is subject to a tropical climate that is characterized by a summer monsoon from the Southwest (from May to October) and a winter monsoon from the Northeast (from November to April). The wet season (from June to October) alternates with a dry season (November–May) and accounts for 85%–90% of the total yearly rainfall. In South Vietnam, the annual rainfall ranges between 1600 and 2000 mm [34,35]. Rainfall is higher (2000–2400 mm per year) in the Western region than in the Eastern (1600–1800 mm) and in the central delta (1200–1600 mm) [36]. According to the Vietnamese National Centre for Hydro-Meteorological Forecasts [37], 18 typhoons impacted on the MRD during the 52-year period of 1961–2012. Amongst them, 13 typhoons occurred recently, during the last 20 years (1992–2012).

2.1.3. Hydrological Regimes and Sediment Transport

The total water discharge of the Mekong is ~500 $km^3\ yr^{-1}$, of which 85% flows in flood season (from September to November) and 15% in low flow season (from December to August) [21,35]. In the delta, the flood season occurs later than the local rainy season, since the water flux mainly comes from the upper and central Mekong basin and is partially regulated by the dynamics of the Tonle Sap in Cambodia. Discharges at the Can Tho and My Thuan stations are almost the same, and vary between 25,000 $m^3 \cdot s^{-1}$ in September-October and a minimum in April (typically 2000 $m^3 \cdot s^{-1}$) [38]. The total suspended sediment discharge entering the delta is about 145×10^6 t yr^{-1}, and the average sediment concentration in the river is about 60 $mg \cdot L^{-1}$; maximum values can reach 500 $mg \cdot L^{-1}$ in the wet season [39].

The suspended sediments in the distributaries of the Mekong are mostly composed of fine silt with about 15% clay [27].

The coastal current along the MRD shifts with the monsoon forcing; it is oriented Southwestward during the Northeast (or winter) monsoon and Northeastward during the Southwest (or summer) monsoon [40].

2.1.4. Tides

The MRD is affected by tides of a mixed diurnal and semi-diurnal character. Semi-diurnal lunar tide M2 and solar tide S2 amplitudes are up to 0.9 m and 0.5, respectively, while diurnal solar tide K1 and lunar tide O1 amplitudes are up to 0.7 m and 0.5 m, respectively, along the MRD [41]. The resulting amplitude is gradually decreasing from 3.8 m in the Northeast (NE) area to approximately 2 m in the Southwest (SW) along the Ca Mau peninsula [26].

Tidal mechanisms are key processes acting on water distribution in deltas and on sediment transport in estuaries (e.g., [42–44]). In the middle and lower estuaries, deposition is mainly driven by the dynamics of the turbidity maximum zone, whose presence and dynamics are governed by the coupling between river discharge and tidal propagation (e.g., tidal pumping and/or density gradients; [27,28,45,46]). In this study, tidal propagation within the estuaries is included in the numerical model and the tide is taken into account through its boundary conditions in the river mouths.

2.2. Data

Data used to set up, calibrate and validate the model are the following.

Bathymetry and coastline in the MRD coastal area were digitized from topography maps in VN2000 coordinates (national coordinate system of Vietnam corresponding to UTM projection with a WGS84 reference ellipsoid and specified local parameters) with scale 1:50,000 in the coastal zone and 1:25,000 in the estuary. These maps were published by the Department of Survey and Mapping in 2004, now belonging to the Ministry of Natural Resources and Environment of Vietnam. Bathymetry offshore was extracted from GEBCO-1/8 with 30 arc-second interval grid [47].

River water discharge and suspended sediment concentration (SSC) measured in the period 2007–2014 at My Thuan (Tien River) and Can Tho (Hau River) were used to set-up river boundary condition in these rivers. In the absence of gauging station in the Vamco River and Soai Rap River (to the North of the MRD), the averaged river discharges and SSCs in low flow and flood seasons provided by a previous project [48] were used to set up the river boundary conditions in these rivers.

Wind and wave data measured at Con Dao Island and Vung Tau were analyzed and used in the simulations. Data measured with interval of 6 hours in 2012, 2013 and 2014 were considered in this study for calibration/validation. Wave and wind average values over 20 years (1992–2013) from the wave climate [49] were considered along the MRD coastal zone to setup different scenarios of simulations.

Sea level elevations measured at Vung Tau, Hoa Binh, Binh Dai, An Thuan and Ben Trai stations (Figure 1a) were used for model calibration and validation. Moreover, measured sea level near the coast was analyzed to determine the harmonic constants of 8 tidal constituents (M2, S2, K2, N2, O1, K1, P1, Q1) to be imposed at sea boundaries in the refined grid. The tidal harmonics constants imposed offshore were extracted from FES2014 [50,51]. The World Ocean Atlas [52] with 0.25 degree-grid resolution was used for open sea boundary transport condition of the parent model.

Current velocity, grain size of bottom sediment and SSC were measured in the framework of the project "Interaction between hydrodynamics of the Bien Dong (East Sea of Vietnam) and Mekong River water" at 4 *in situ* stations (LT1, LT2, LT3 and LT4, see Figure 1a) in September 2013 (flood season) and April 2014 (low flow season). These data were used for model calibration and validation.

2.3. Modelling Strategy

2.3.1. The Delft3D Model

In this study, hydrodynamics (resulting from tides, currents and waves) and suspended sediment transport were simulated using the Delft3D-Flow module and the Delft3D-Wave module (based on the SWAN model). The Delft3D-Flow model developed by Deltares (Delft, The Netherlands) is a 3D modeling suite to investigate hydrodynamics, sediment transport and morphology, and water quality for fluvial, estuarine and coastal environment [53]. Delft3D solves the Reynolds-averaged Navier-Stokes equations, including the k-ε turbulence closure model, and applies a horizontal curvilinear grid with σ-layers for vertical grid resolution.

SWAN is used as wave model [54–56]. In the action balance equation (see e.g., [57]), the JONSWAP expression [58] is chosen to express the bottom friction dissipation, with the parameter C_{jon} = 0.067 $m^2 \cdot s^{-3}$ proposed by Bouws and Komen [59] for fully developed wave conditions in shallow water. The model from Battjes and Janssen [60] is used to model the energy dissipation in random waves due to depth-induced breaking waves.

2.3.2. Model Setup

The NESTING method (Delft3D-NESTHD) was used to create sea boundaries condition for a refined (child) grid within a coarse (parent or overall) model. The parent model grid is orthogonal, curvilinear with 210 × 156 grid cells. Horizontal grid size changes from 166 to 22,666 m (Figure 1b). Along the vertical, 4 layers in σ-coordinate are considered, each of them accounting for 25% of the water depth. Open sea boundary conditions of the overall model are provided by FES2004 and the World Ocean Atlas 2013.

The grid of the detailed model is also orthogonal curvilinear. Curvilinear grids are applied in the models to provide a high grid resolution in the area of interest and a low resolution elsewhere, thus saving computational effort. The model frame includes all the coastal zone of Ba Ria-Vung Tau to Ca Mau cape (Figure 1a) along circa 485 km in the long-shore direction and 100 km in the cross-shore direction. The horizontal grid encompasses 424 × 296 points with grid size between 44 m and 11,490 m. Along the vertical, 4 layers in σ-coordinate are considered, similar to the parent model. The hydrodynamics model takes into account the influences by water temperature, salinity, sediment transport and wave actions.

The model was setup and run for different periods of time, with time steps of 0.2 min (12 s). Its calibration and validation were performed during 4 periods: March–May 2012 (low flow season), August–October 2012 (flood season), September 2013 (flood season) and April 2014 (low flow season).

There are four open river boundaries: Soai Rap, Vamco, My Thuan and Can Tho (Figure 1b). The Soai Rap and Vamco boundaries belong to the Dong Nai–Saigon River catchment. River water discharge measured every hour in Can Tho and My Thuan stations were imposed as river boundary conditions. Others river boundaries were set to 546.9 $m^3 \cdot s^{-1}$ (Soai Rap R.) and 52.5 $m^3 \cdot s^{-1}$ (Vamco R.) in low flow season; 1310 $m^3 \cdot s^{-1}$ in the Soai Rap River and 177.8 $m^3 \cdot s^{-1}$ in the Vamco River in flood season. The averaged SSC values during flood tide and ebb tide at Can Tho and My Thuan stations were imposed as boundary condition for these two distributaries. SSC in Vamco and Soai Rap rivers were almost the same and considered in this study to be worth 55 $mg \cdot L^{-1}$ in low flow season and 70 $mg \cdot L^{-1}$ in flood season. At each river boundary, the same SSC values were imposed from the surface to the bottom.

The averaged water temperature and salinity values in the low flow and flood seasons were imposed at the river boundaries (T = 27.5 °C in low flow season and 27.2 °C in flood season; S = 0). Wind velocity and direction, which were measured every 6 h in Con Dao in the period 2012–2014, were imposed on the model. The wave module was setup with online coupling with hydrodynamics and sediment transport. Sea boundary conditions of the wave model were extracted from the wave climate [49].

The bottom roughness was specified by a spatial distribution of Manning (n) coefficients with values in the range 0.018–0.023 $m^{-1/3} \cdot s$ [61,62]. The background horizontal eddy viscosity and horizontal eddy diffusivity were considered to be, after calibration, equal to 8 $m \cdot s^{-2}$. The Horizontal Large Eddy Simulation (HLES) sub-grid, which is integrated in Delf3D-Flow, is based on theoretical considerations presented by Uittenbogaard [63] and Van Vossen [64]. In this study, the HLES sub-grid was activated to add calculated results to background values. Two sediment fractions were simulated in the model: one non-cohesive and one cohesive.

Measured grain sizes of non-cohesive particles in the MRD coastal area range from 29 to 252 μm (average 113 μm) in flood season (September 2013) and from 15 to 262 μm (averaged 103 μm) in low flow season (April 2014). Therefore, median sand-sized particles of 113 μm and 103 μm were considered in our simulations in flood and low flow season, respectively. A specific density of 2650 $kg \cdot m^{-3}$ and dry bed density of 1600 $kg \cdot m^{-3}$ were considered; all other sand transport calibration parameters were kept at the default values proposed by Delft3D. Sand fraction transport was modeled with the van Rijn TR2004 formulation [65], which has been shown to successfully represent the movement of non-cohesive sediment ranging in size from 60 μm to 600 μm.

Previous observational studies in the Mekong estuary indicated that most of Mekong sediments are flocculated fine particles. In low flow season, measured flocsize was 30–40 μm with about 20%–40% of clay content in volume [28]. In the flood season, the flocsize was 50–200 μm with a 20%–30% clay content in volume [27]. For the cohesive sediments, if the bed shear stress is larger than a critical value, erosion is modeled following the Partheniades' formulation [66], whereas if the bed shear stress is less than a critical value for deposition, Krone's formula [67] is used to quantify the deposition flux. The parameters required to simulate the cohesive sediment transport include critical bed shear stresses for erosion τ_{cre} and deposition τ_{crd}, the erosion parameter M and the particle settling velocity w_s [68]. After

calibration, τ_{crd} was set to 1000 N· m^{-2}, which effectively implied that deposition was a function of concentration and fall velocity [69]. τ_{cre} was set to 0.2 N· m^{-2}, and M was set to 2 × 10^{-5} kg· m^{-2}· s^{-1}.

In salt water, cohesive sediments flocculate, the degree of flocculation depending on salinity. Flocs are much larger than the individual sediment particles and settle at a faster rate. In order to model this salinity dependency, Delft3D-Flow considers two settling velocities and a maximum salinity. The velocity $w_{s,f}$ is the settling velocity of the sediment fraction in fresh water (salinity S = 0), while the velocity $w_{s,max}$ is the settling velocity of the cohesive fraction in water having a salinity equal to salmax (S = 30 over our area). For the Mekong River plume and based on Stoke's law, Hung *et al.* [70] reported that grain size in the range of 29.4–40 μm has settling velocities in the range 0.9–1.7 mm· s^{-1}. Manh *et al.* [23], considering an extended range of grain sizes from 2.5 to 80 μm, evaluated a calibration range of settling velocities between 0.01 and 7 mm· s^{-1}. Portela *et al.* [71] reported settling velocities increasing by a factor of 6.5 between freshwater conditions (S = 0) and marine conditions (S = 30). In this study, the settling velocity of the cohesive sediments was set to 0.05 mm· s^{-1} in fresh water and to 0.325 mm· s^{-1} at S = 30.

In our simulations, we chose to set the input of sand concentration into suspension to 0 at the river boundaries (inside the delta, where the slope is almost flat) and specified the values of SSC for the cohesive suspended sediments. Simulations in the lower estuary and coastal areas are not sensitive to the sand concentrations at the upper river boundary since sand particles settle very fast; the sand profile is in equilibrium over very short distances, depending on the local capacity of transport and the available particles at the bed [72,73]. Sand particles can be eroded within the model area, in the estuary and along the coast as well, under the combined action of waves and currents.

The bottom-boundary layer calculation accounts for the interaction of wave and current over a moveable bed [65,74–76].

2.3.3. Calibration and Validation Process

Model calibration and validation were conducted simulating low flow and flood seasons of 2012, flood of 2013 and low flow season 2014. The discrepancy between results and measurements was quantified, for each simulation, using the Nash-Sutcliffe efficiency number E [77], calculated as follows:

$$E = 1 - \frac{\sum (obs - calc)^2}{\sum (obs - mean)^2} \quad (1)$$

in which the sum of the absolute squared differences between the predicted and observed values is normalized by the variance of the observed values during the period under investigation. E varies from 1.0 (perfect fit) to $-\infty$, a negative value indicating that the mean value of the observed time series would have been a better predictor than the model [78].

2.3.4. Scenario Simulation

In order to describe characteristics of sediment transport in the MRD coastal area, scenarios were set up with different conditions of wave, wind and river discharge. Initial conditions of the scenarios result from a previous simulation (either August for flood season or March for low flow season). At the river boundaries, temperature was fixed at 27.5 °C in the low flow season and at 27.2 °C in the flood season, and salinity was fixed to 0 (there is no income of seawater at the upstream boundaries). The average temperatures do not differ considerably since the low flow season includes both hot months (April to August) and cool months (December, January). The resulting average value is close to the water temperature in the flood season (September, October and November). Temperature and salinity at the open sea boundaries vary from one scenario to another following the climatology.

The average values of river discharge and SSC measured at Can Tho and My Thuan stations during the period 2007–2014 were imposed as boundary conditions. Two groups of scenarios were then considered, referred to as md (low flow season, mostly dry) and mf (flood season):

- during the low flow season (from December to August), the average water river discharges of 3054 $m^3 \cdot s^{-1}$ at My Thuan in the Tien River, 3739 $m^3 \cdot s^{-1}$ at Can Tho in the Hau River, 52.5 $m^3 \cdot s^{-1}$ in the Vamco River and 546.9 $m^3 \cdot s^{-1}$ in the Soai Rap River were imposed, with SSC = 50 $mg \cdot L^{-1}$ at Can Tho, 53.6 $mg \cdot L^{-1}$ at My Thuan, 55 $mg \cdot L^{-1}$ in the Vamco and Soai Rap rivers (Table 1);
- during the flood season (from September to November), the average water river discharges of 12,530 $m^3 \cdot s^{-1}$ at My Thuan, 13,130 $m^3 \cdot s^{-1}$ at Can Tho, 177.8 $m^3 \cdot s^{-1}$ in the Vamco River and 1310 $m^3 \cdot s^{-1}$ in the Soai Rap River were considered, with SSC = 67.8 $mg \cdot L^{-1}$ at Can Tho, 86.5 $mg \cdot L^{-1}$ at My Thuan and 70 $mg \cdot L^{-1}$ at Vamco and Soai Rap (Table 2).

Table 1. Scenario simulations in the low flow season (December to August).

Scenario	Wave Direction	Duration (Days)	Wave		Wind Velocity ($m \cdot s^{-1}$)
			H_s (m)	T_p (s)	
md0		29.87			
md1	NE	0.27	0.5	6.5	4.5
md2		5.48	2	8.5	7.5
md3		1.10	4	10.5	10.5
md4	E	1.64	0.5	6.5	4.5
md5		23.29	2	8.5	8
md6		11.78	4	10.5	12.5
md7		4.38	6	11.5	14.5
md8		0.55	8	12.5	16.5
md9	SE	1.64	0.5	6.5	4.5
md10		18.36	2	8.5	7.5
md11		9.59	4	10.5	10.5
md12		3.29	6	11.5	12.5
md13		0.27	8	12.5	14.5
md14	S	2.47	0.5	6.5	4.5
md15		25.21	2	8.5	6.5
md16		14.80	4	10.5	9.5
md17		7.67	6	11.5	12.5
md18		1.10	8	12.5	14.5
md19	SW	3.29	0.5	6.5	4.5
md20		45.76	2	8.5	7.5
md21		31.51	4	10.5	10.5
md22		21.65	6	11.5	12.5
md23		6.30	8	12.5	14.5
md24		2.74	10.5	13.5	16.5

Table 2. Scenario simulations in the flood season (September to November).

Scenario	Wave Direction	Duration (Days)	Wave		Wind Velocity ($m \cdot s^{-1}$)
			H_s (m)	T_p (s)	
mf0		13.01			
mf1	NE	0.09	0.5	6.5	4.5
mf2		2.82	2	9	7.5
mf3		0.55	4	10.5	9.5
mf4		0.09	6	11.5	12.5
mf5	E	0.46	0.5	6.5	4.5
mf6		7.74	2	9	7.5
mf7		4.64	4	10.5	10.5
mf8		2.00	6	11.5	12.5
mf9		0.09	8	12.5	14.5
mf10	SE	0.09	0.5	6.5	4.5
mf11		6.19	2	9	7.5
mf12		4.55	4	10.5	11
mf13		1.00	6	11.5	12.5

Table 2. Scenario simulations in the flood season (September to November).

Scenario	Wave Direction	Duration (Days)	Wave		Wind Velocity ($m \cdot s^{-1}$)
			H_s (m)	T_p (s)	
mf14	S	0.18	0.5	6.5	4.5
mf15		7.46	2	9	7.5
mf16		5.92	4	10.5	11.5
mf17		2.09	6	11.5	13
mf18		0.46	8	12.5	15
mf19	SW	0.27	0.5	6.5	4.5
mf20		12.56	2	9	7.5
mf21		11.01	4	10.5	11.5
mf22		6.28	6	11.5	13
mf23		1.18	8	12.5	15
mf24		0.27	10.5	13.5	17

The variation in SSC values at My Thuan and Can Tho between low flow and flood seasons is not large since these values are constrained by erosion, transport, deposition all along the Mekong River, and by storage and release by the Tonle Sap. However, the seasonal variations of suspended sediment discharge are higher than the seasonal variations of the flow.

The wave and wind conditions were derived from the wave climate obtained over the 22-year period of 1992–2013 by the BMT ARGOSS [49]. For each class of wave direction (NE, E, SE, S, SW) and significant wave height (0.5–1 m, 1–3 m, 3–5 m, 5–7 m, above 7 m), the average durations during the 274 days of the low flow season (from December to August) and the 91 days of the flood season (from September to November) were defined. Adding periods of calm weather (*i.e.*, with significant wave height <0.5 m), we obtained 25 typical scenarios for the low flow season (Table 1) and 25 typical scenarios for the flood season (Table 2). For each scenario, significant wave heights H_s representative of the above described classes were defined as: 0.5 m, 2 m, 4 m, 6 m, 8 m, respectively. Wave peak periods T_p were determined from statistics established over 20 years of measurements, available online at the BMT group website. In each scenario, we assumed that wind was coming from the same direction as the waves, which is mostly the case since the gauging station is located offshore.

Each of the above-defined scenarios was run for a 14.75-day period corresponding to one full neap-spring tide cycle [79]. Each simulation considered real tidal boundary conditions from one typical cycle, which was chosen as the period 11–25 September, 2012.

3. Results

3.1. Model Validation from Field Measurements

Water elevation at hydrometeorological stations of Vung Tau, Binh Dai, An Thuan and Ben Trai (e.g., Figure 2a,b) was used to calibrate (e.g., for the choice of the Manning coefficient) and then validate the model. After calibration, comparisons show good agreement between model results and measurements with *E* coefficients between 0.68 and 0.85. Current velocity measured in LT1 (Figure 2c), LT2 (Figure 2d), LT3 and LT4 in September 2013 and April 2014 were analyzed to provide horizontal velocity components U and V, which were compared with model simulations. The comparison showed an acceptable agreement between model and measurements with *E* coefficients between 0.65 and 0.89. Comparisons between measured SSC in LT1 (Figure 2e), LT2 (Figure 2f), LT3, LT4 and modeled SSC also resulted in acceptable *E* coefficients in the range 0.66–0.78.

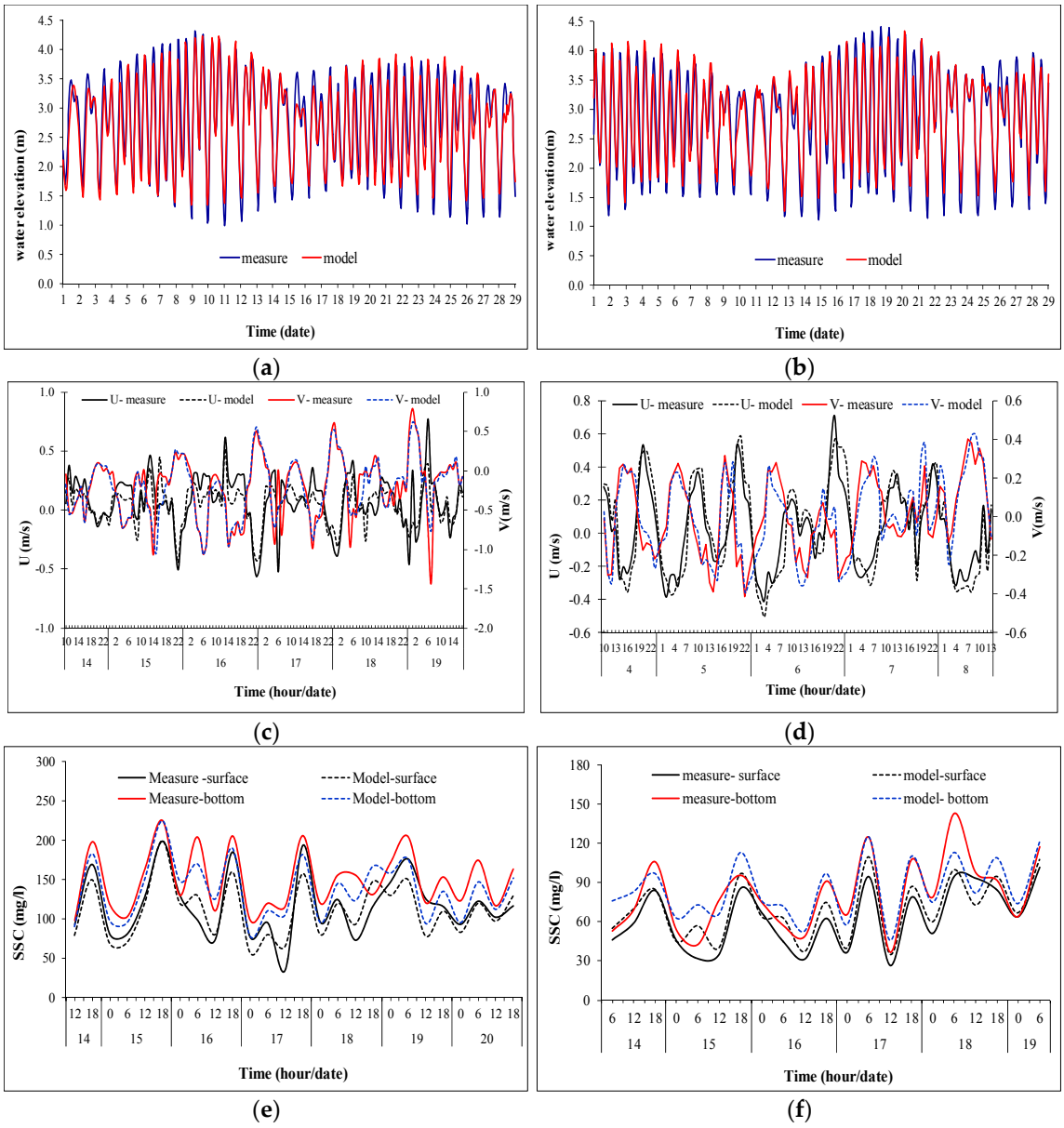

Figure 2. Comparison between simulations and measurements: (**a**) water elevation at Bền Trại (Cồ Chiên mouth) in April 2012; (**b**) water elevation at Bền Trại (Cồ Chiên mouth) in September 2012; (**c**) current components in the surface layer at LT1, flood season (14–19 September 2013); (**d**) current components in the middle of water column at LT2, low flow season (4–8 April 2014); (**e**) SSC at LT1, flood season (14–20 September 2013); (**f**) SSC at LT2, flood season (14–19 September 2013).

3.2. Spatial Distribution of SSC with or without Waves

Figure 3 (in low flow season) and Figure 4 (in flood season) show the distribution of SSC below the surface in the absence of wind and waves (Figures 3a and 4a), and with waves of significant height of 2 m, coming from 5 different directions from NE to SW. These distributions are provided in Figures 3 and 4 one hour before low tide, which correspond to the maximum extent of the plume to the ocean.

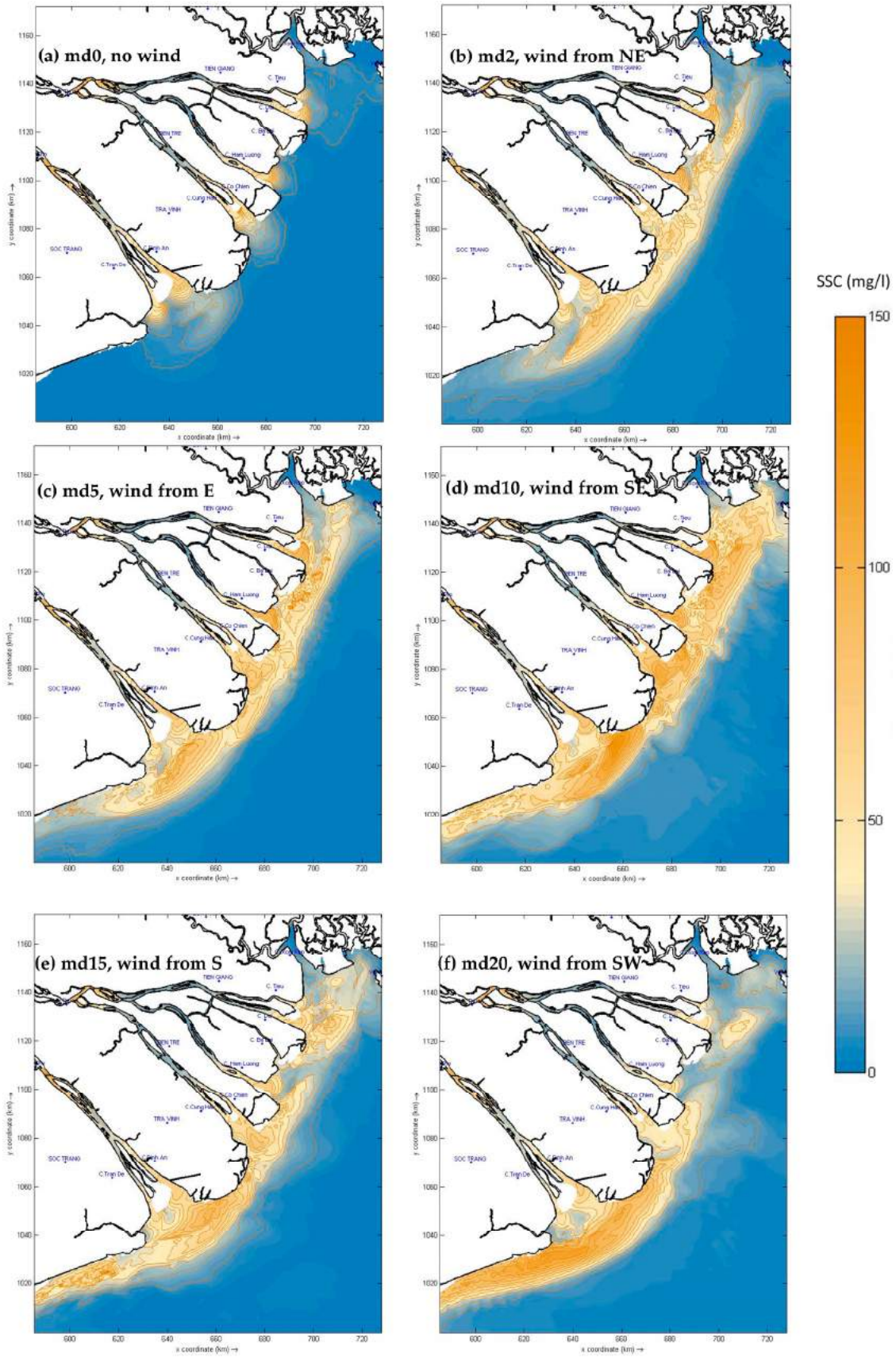

Figure 3. Distribution of suspended sediment concentration in the surface layer in the low flow season in the MRD coastal area (1 h before low tide), with no wave or wave heights = 2 m from different directions.

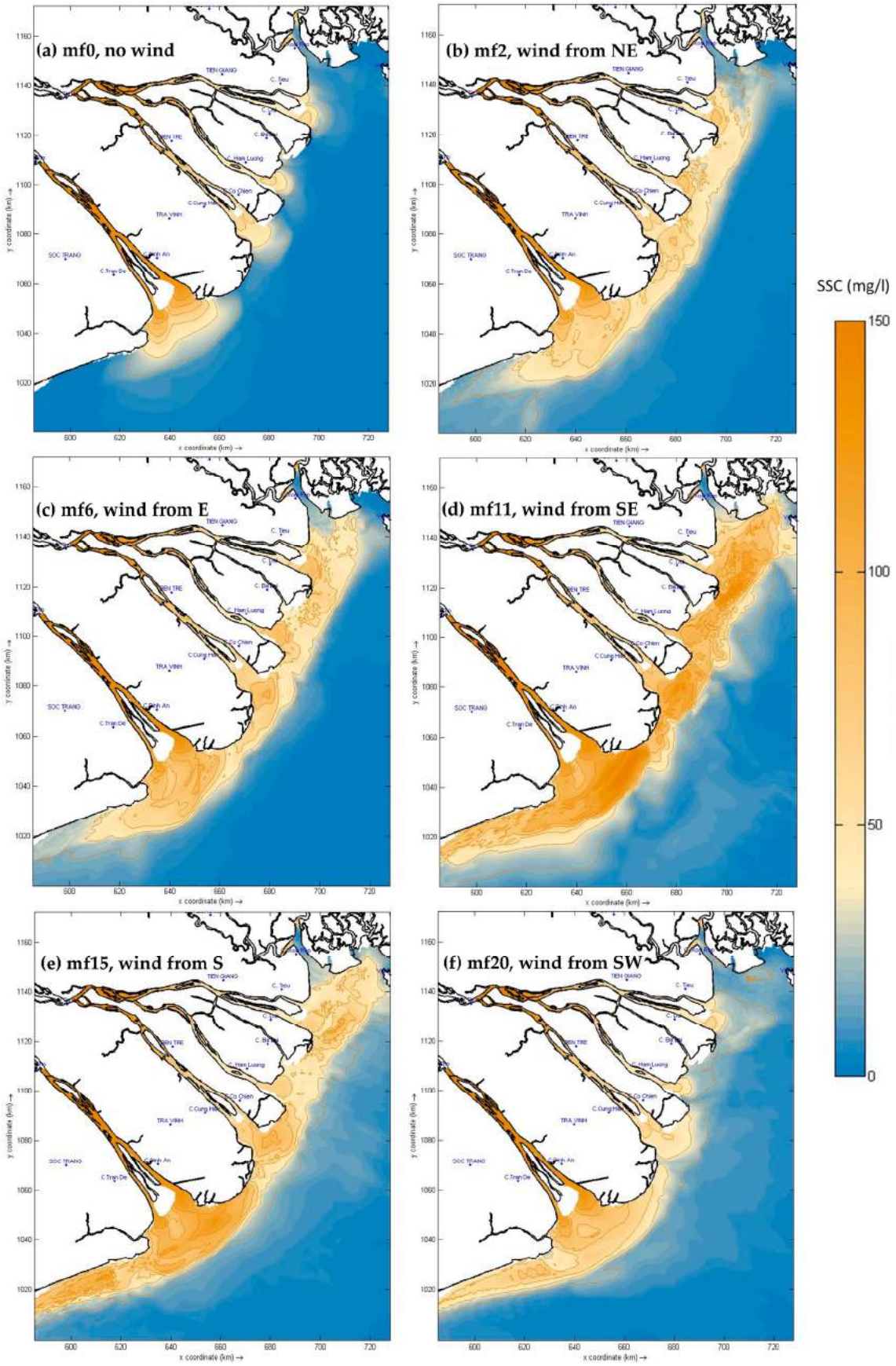

Figure 4. Distribution of suspended sediment concentration in the surface layer in the flood season in the MRD coastal area (1 h before low tide), with no wave or wave heights = 2 m from different directions.

3.2.1. Without Waves

It appears from the wave climate [49] that calm weather conditions (without wave) in the MRD coastal area occurs about 25.2% of the year (14.3% during the flood season and 10.9% during the low flow season). Therefore, annually, there are about 43 days without waves (13 days in flood season and 30 days in the low flow season; see Tables 1 and 2).

In this case with no waves, the distribution of suspended sediment concentration derives from the interaction between sediments originating from the river and tidal oscillation. In the low flow season, sediments from the river settle in the estuary or very close to the mouths (not further than 10–15 km seawards from the estuaries) with SSC in the range 40–60 mg· L^{-1} (Figure 3a). There are relevant differences amongst SSC values along the delta: SSC is higher in Southwestern estuaries (Tran De, Dinh An mouths) than in Northeastern estuaries (Tieu, Dai, Ham Luong mouths). In the flood season, SSC varies between 40 and 80 mg· L^{-1}, with higher values in the Southwestern estuaries and river mouth area as well (Figure 4a).

3.2.2. With Waves

With increasing wave height, the combination of waves and tides strengthens resuspension over increasing depths along the delta. As a result, SSC values increase locally and high SSCs also extend further offshore. However, their distribution strongly depends on wave height and direction.

Low flow season. In the low flow season, NE waves extend the plume up to around 15 km from the coast with SSC values of 30–50 mg· L^{-1} inside and <10 mg· L^{-1} further offshore with the md2 scenario (Figure 3b). Higher SSC values due to erosion are observed with higher waves (md3 scenario), but the plume pattern remains the same (and its time evolution during the tidal cycle—not shown in this paper—is very similar as well). In the case of waves coming from the East, the turbid plume is slightly less extended offshore than with NE waves but with sensitively higher SSC values (scenario md5, SSC about 40–60 mg· L^{-1}, Figure 3c). SSC values and the plume extent increase with increasing wave height (scenarios md6-md8). Waves from SE have the highest impact on suspended sediment transport because they travel perpendicularly toward the coast. With wave height in the 1–3 m range (scenario md10, Figure 3d), higher SSC values (40–70 mg· L^{-1}) covered the all coastal zones up to 15–20 km from the coast. Outside of 20 km from the coast, SSC decreases to below 20 mg· L^{-1}. Waves from the South have a higher impact on Southwestern estuaries (Dinh An, Tran De, Cung Hau) which experienced higher SSC values (30–50 mg· L^{-1}) than on the Northeastern estuaries (with SSC values in the range 20–40 mg· L^{-1}) (scenario md15, Figure 3e). This trend remains the same with higher waves. Waves from the SW direction cause strong erosion in the southern part of the delta, near Tran De and Dinh An mouths. As a result, SSC is higher (about 60–120 mg· L^{-1}) in the Southwestern part than in the Northeastern coastal area with values almost below 30 mg· L^{-1} (scenario md20, Figure 3f).

Flood season. During the flood season, mean water river discharge increased about 4 times compared to the low flow season, and SSC in the river increased by 30%–60%. The general patterns of the turbid plume are similar to the ones observed in the low flow season, with almost the same shape and horizontal extension, but with higher SSC values. With waves from the NE, the highest SSC values reach 70–100 mg· L^{-1} in the Southwestern estuaries (scenario mf2, Figure 4b). With waves from the East, the sediment distribution is quite similar but exhibits slightly higher SSC values around the Northeastern mouths (scenario mf6, Figure 4c). Waves from SE have the higher impact on resuspension and SSC values range from 80 and 150 mg· L^{-1} all along the delta (scenario mf11, Figure 4d). Waves from the South and the SW induce higher SSC values in the Southwestern estuaries up to 80–120 mg· L^{-1} (scenario mf15, Figure 4e). High SSC values (80–100 mg· L^{-1}) are also observed around the Southwestern delta when waves originate from the SW, with lower values in the Northern coastal zone (scenario mf20, Figure 4f). Surprisingly, the impact of waves from the SW seems strongly reduced by fresh water flux in the flood season, through the interaction of waves and fresh water (see Figures 3f and 4f). We observed one noticeable difference between the low flow and flood seasons: except for waves from the SE, the highest values of SSC were observed in the Southern estuaries in the

case of SW waves in the low flow season (Figure 3f) and in the case of Southern waves in the flood season (Figure 4e).

Globally, the river plume is very narrow and its extent is reduced throughout the year (as also shown by Loisel *et al.* [25]) for two reasons: (1) most of the particles carried by the river settle in the lower estuary or around the river mouths; (2) the plume is constrained along a baroclinic coastal current as demonstrated by Hordoir *et al.* [33]. Differences between low flow and flood seasons are small because the turbidity patterns are driven by wave action, more than by the river flow.

3.3. Temporal Variation of SSC

For a given river discharge, temporal variation of SSC in the MRD coastal area depends on tidal oscillation and wave conditions. Figure 5 shows the water elevation and SSC values at two stations during 11 days over 14.75 of the full spring-neap tide cycle (for readability purpose). The highest SSC values are observed at low tide or at the beginning of the flood. The lowest SSC values are seen 2–3 h after the high tide, during the ebb period (Figure 5). SSC values are also higher during the spring tide (days 18–22) than the neap tide (day 23 and after), but the difference is quite small: less than 10 mg· L^{-1} at the Northeastern coastal station (Figure 5a), and less than 20 mg· L^{-1} at the Southwestern coastal station (Figure 5b).

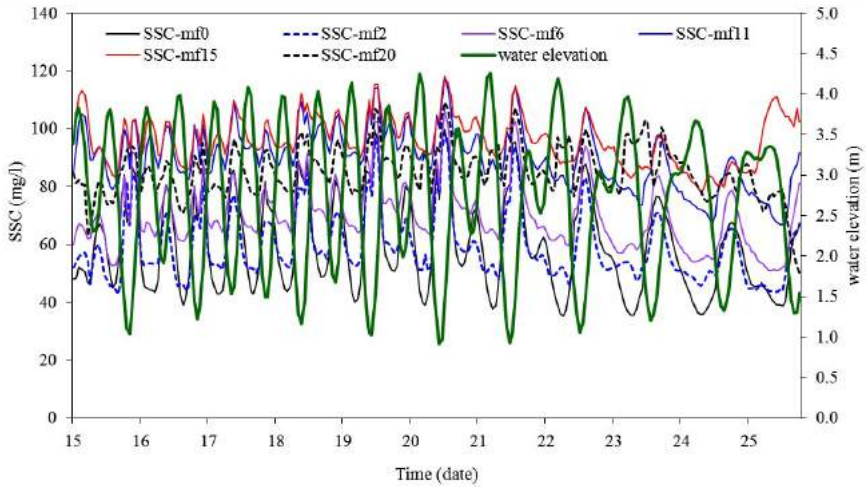

(**a**)

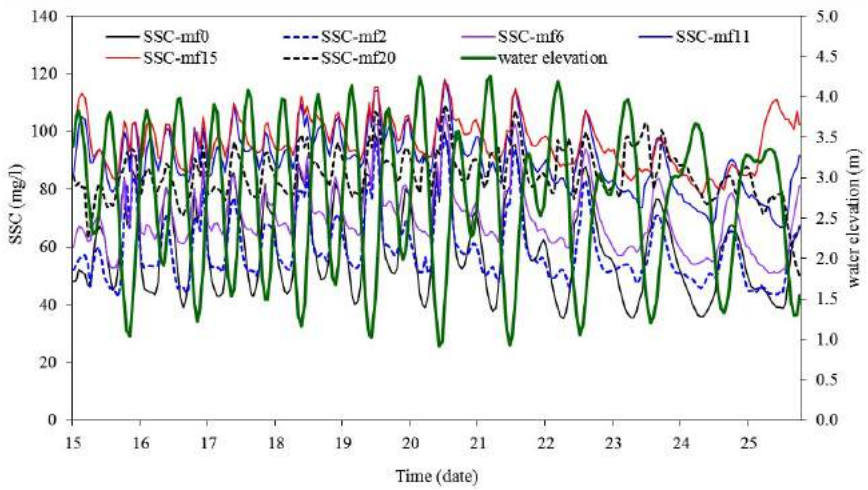

(**b**)

Figure 5. Temporal variation of SSC under some scenario simulations during 11 days of the 14.75 neap-spring cycle, in the flood season: (**a**) at station LT3 to the NE; (**b**) at station LT1 to the SW.

The temporal variation in SSC is similar with or without waves, but SSC values are much higher with waves. In the Northeastern coastal zone, waves from E and SE directions (scenarios mf6 and mf11) induce SSC values 3–4 times higher than under calm conditions, and higher than any other wave direction (Figure 5a). In the Southwestern coastal zone, the highest SSC values occur when waves originate from the S and SW (scenarios mf15 and mf20), 20%–50% higher than when waves come from other directions (Figure 5b).

3.4. Alongshore Sediment Transport

3.4.1. Without Waves

Under calm conditions, a net sediment transport occurs from NE to SW in the low flow season with fluxes across sections m3, m2 and m1 of 0.15, 0.65 and 2.32 $\times$ 10^3 tons, respectively, during a spring-neap tide cycle (Table 3). In the flood season, with a much higher river discharge, the sediment flux to the Southwest across the Southern transect m1 more than doubled (5.04 $\times$ 10^3 tons) as compared to the low flow season, the sediment flux across section m2 decreased by about 40%, and a flux of 0.71 $\times$ 10^3 tons was generated towards the Northeastern direction across section m3 directly North to the Northern mouths (Table 3).

Table 3. Total sediment flux (10^3 tons) transported across the sections under the 50 scenarios. (Positive values represent sediment transport from the SW to NE, negative values from the NE to SW).

Low Flow Season					Flood Season				
Scenario	**Wave Direction**	**Cross Section**			**Scenario**	**Wave Direction**	**Cross Section**		
		m1	**m2**	**m3**			**m1**	**m2**	**m3**
md0		−2.32	−0.65	−0.15	mf0		−5.04	−0.37	0.71
md1	NE	−0.05	−0.02	−0.01	mf1	NE	−0.07	−0.01	0.00
md2		−7.02	−4.44	−1.52	mf2		−7.28	−3.04	−0.89
md3		−6.38	−4.43	−1.23	mf3		−3.65	−2.19	−0.49
md4	E	−0.30	−0.10	−0.06	mf4		−1.50	−1.00	−0.21
md5		−39.60	−15.97	−5.49	mf5	E	−0.31	−0.04	0.01
md6		−117.58	−51.71	−5.98	mf6		−21.38	−6.11	−1.54
md7		−81.66	−37.03	−3.30	mf7		−38.83	−15.98	−1.35
md8		−16.91	−7.61	−0.80	mf8		−29.81	−13.39	0.26
md9	SE	−0.39	−0.07	−0.07	mf9		−0.02	−1.08	0.02
md10		−24.16	2.63	11.12	mf10	SE	−0.08	0.00	0.00
md11		−53.18	17.96	37.14	mf11		−19.14	1.47	6.24
md12		−36.69	15.49	26.06	mf12		−41.88	13.45	27.64
md13		−5.53	2.12	3.23	mf13		−15.00	5.97	10.29
md14	S	−0.23	0.02	0.01	mf14	S	−0.07	0.01	0.02
md15		2.02	9.39	3.83	mf15		1.89	0.29	3.79
md16		30.21	47.87	32.25	mf16		38.13	6.13	41.94
md17		62.96	80.14	67.92	mf17		23.29	22.69	25.24
md18		38.93	44.46	36.71	mf18		10.61	12.48	9.27
md19	SW	−0.13	0.02	0.05	mf19	SW	−0.06	0.01	0.03
md20		67.09	23.05	6.33	mf20		10.42	6.02	2.51
md21		229.37	125.38	51.66	mf21		85.28	55.33	19.94
md22		361.55	201.51	95.72	mf22		95.57	58.32	21.96
md23		234.97	128.43	63.25	mf23		37.57	20.87	8.62
md24		187.43	104.88	54.69	mf24		15.46	8.40	3.65

3.4.2. Sensitivity to Wave Height and Direction

Low flow season. Waves from the NE cause a net alongshore sediment transport to the SW (Table 3). This flux increases over each cross section from the Northern estuaries to the Southern ones, with net transports of 2.76 × 10^3 tons across m3, 8.89 across m2 and 13.45 across m1 (Table 4). They are mainly due to waves higher than 2 m (scenarios md2 and md3, Table 3). Waves from the East globally induce a higher sediment flux Southwestward, which also increases from across section m3 (15.6 × 10^3 tons), to m2 (112 × 10^3 tons) and m1 (256 × 10^3 tons). These fluxes are higher than with NE waves by a factor of 20 in m1, 12 in m2 and 5 in m3 (Table 4). In the low flow season, with waves from the SE (*i.e.*, perpendicular to the coastline), the alongshore sediment transport is globally oriented to the NE direction in the Northern and central area (m3 and m2), and to the SW in the Southern area (1). The global flux to the SW across m1 is much lower than when waves come from the East (120 × 10^3 tons instead of 256 × 10^3 tons, see Table 4). Waves coming from the S or SW globally induce alongshore sediment fluxes in a Northwestward direction. When waves come from the South, the flux is higher in the central zone (m2, 182 × 10^3 tons), while it is higher in the South (m1, 1080 × 10^3 tons) in the case of SW waves. The highest values of sediment flux occur when waves come from SW, with decreasing fluxes from the Southwest to the Northeastern area (1080 × 10^3 tons across m1, 583 across m2 and 272 across m3). A total of 89% of the total flux of sediment across m1 section is due to SW waves. This percentage drops to 73% and 55% across sections m2 and m3, respectively.

Table 4. Total sediment flux (10^3 tons) transported across sections per year. (Positive values represent sediment transport from the SW to NE, negative values from the NE to SW).

Wave Direction	Low Flow Season			Flood Season			Total Year		
	Cross Section			Cross Section			Cross Section		
	m1	m2	m3	m1	m2	m3	m1	m2	m3
calm	−2.32	−0.65	−0.15	−5.04	−0.37	0.71	−7.356	−1.013	0.555
NE	−13.45	−8.89	−2.76	−12.51	−6.24	−1.59	−25.95	−15.12	−4.35
E	−256.06	−112.43	−15.64	−90.35	−36.59	−2.59	−346.41	−149.02	−18.24
SE	−119.95	38.13	77.48	−76.11	20.90	44.18	−196.06	59.03	121.66
S	133.88	181.88	140.72	73.84	41.61	80.26	207.73	223.49	220.98
SW	1080.28	583.25	271.69	244.25	148.95	56.70	1324.53	732.20	328.39
NEward	1214.52	803.34	489.96	318.22	211.45	182.13	1532.26	1014.72	671.59
SWward	−392.13	−122.03	−18.62	−184.14	−43.20	−4.47	−575.78	−165.15	−22.58
Net transport	822.39	681.31	471.34	134.08	168.25	177.66	956.48	849.57	649.01

Flood season. Although the river discharge is much higher than in the low flow season, the alongshore sediment transport qualitatively occurs in the same way in both seasons. In the case of waves from the NE, the net alongshore sediment transport is still oriented to the Southwest, with increasing values from the North to the South: 1.59 × 10^3 tons across m3, 6.24 × 10^3 tons across m2, and 12.51 × 10^3 tons across m1 (Table 4). When waves come from the East, sediment is mainly transported alongshore to the SW, with increasing values from m3 to m1. However, we observe that the net transport is oriented Northeastward at m3 (in the North) in case of wave height less than 2.0 m or higher than 4.0 m (Table 3). Similar to the low flow season, waves from the SE induce alongshore sediment transport Northeastward in the Northern (m3) and central delta (m2), and Southwestward in the South (m1) in the flood season. The highest flux occurs across section m1 from the NE to SW with about 76 × 10^3 tons (Table 4). With waves from the South, the net alongshore sediment transport is significantly higher in the Northeast (80 × 10^3 tons across m3, see Table 4) and Southwest (74 × 10^3 tons across m1) than in the middle delta (42 × 10^3 tons across m2). Sediment transport is oriented to the NE, except across section m1 with waves less than 0.5 m (Table 3). The same behavior is observed in the case of waves from the SW, with decreasing flux from the South to the North: ~244 × 10^3 tons (m1), 146 × 10^3 tons (m2) and 57 × 10^3 tons (m3). In the Southwestern estuaries of Dinh An-Tran De, the net sediment transport is oriented Southwestward in the case of small waves, and Northeastward with

waves higher than 0.5 m (Table 3). In that case, the net alongshore sediment flux is thus a consequence of resuspension of sediment along the Southern delta, along the Ca Mau peninsula.

Globally, the net alongshore sediment transport is oriented to the Northeast of the MRD coastal area in both seasons (Table 4). In the MRD coastal area, the flood season lasts about 3 months. Even if the instantaneous sediment discharge is much higher, the net alongshore sediment transport is much higher in the low flow season than in the flood season: 86% of the net annual alongshore transport across m1 occurs in the low flow season (822×10^3 tons *vs.* 134, see Table 4), 80% across m2 and 73% across m3. Much of the sediment brought by the river settle and is deposited in the estuaries and close to the river mouths.

In the Southwestern area (across section m1), the annual alongshore sediment transport to the Northeast (1532×10^3 tons, Table 4) is due to the waves coming from the S and SW and thus to resuspension along the Ca Mau peninsula. Waves from the NE, E and SE, as well as calm conditions, induce a sediment transport of about 575×10^3 tons to the Southwest.

In the middle coastal part (across section m2 between the Tien River mouth and Hau River mouth), waves from the SE, S and SW generate an annual sediment transport to the Northeast of 1014×10^3 tons, while calm conditions and waves from the NE and E generate alongshore transport of 165×10^3 tons.

In the Northern coastal part (across section m3), the total flux to the Northeast of 672×10^3 tons is generated in the case of waves from the SE, S and SW, while the sediment transport to the Southwest (in case of waves from NE and E) is restricted to about 23×10^3 tons.

As the net alongshore sediment transport decreases from the Southwest (m1) to the Northeast (m3), it shows that the source of global alongshore sediment transport along the MRD is double, generated both by the sediments settling from the river plume, and by erosion, which seems to occur mainly along the Ca Mau peninsula to the Southwest, while a net deposition occurs to the North of section m1.

4. Discussion and Conclusions

In this study, the cumulative alongshore transport of suspended sediments across three sections was estimated to be less than 1.5×10^6 tons per year in a given direction. A comment is necessary since the average sediment load of the Mekong River was estimated to be around 145×10^6 t yr^{-1} over the last 3 k yr [32,39]. In fact, using a detailed numerical model of sediment transport, erosion and deposition within the Mekong delta, Manh *et al.* [23] reported that total sediment load to the coast was about 50%–60% of the sediment flux at the gauging station of Kratie in Cambodia during a year of low flow (like 2010) or normal condition (like 2009), and that this percentage was about 48% during a year with extreme flooding (like in 2011). In a normal flood year, they estimated that the sediment load to the coast was about 42×10^6 tons per year [23]. A complementary study by Xue *et al.* [24] reported that 86.9% of the sediment coming from the Mekong River system was trapped in the MRD estuaries and nearshore area. As a result, in normal years, around 5.5×10^6 tons of sediments are transported alongshore and seaward. As most of these sediments seem to settle and deposit very near to the mouths, the estimations obtained for the cumulated alongshore transports in this study are thus consistent with previous studies.

The present study underlined the role of waves in the sediment redistribution along the delta. Under the present configuration and shoreline, the main alongshore flux is not due to the fate of the river plume but to the action of waves coming from the SW and S, which induce resuspension along the Southern delta and sediment transport to the Northeast. Under small wave conditions, the highest SSC values are seen in the estuaries or very close to the mouths. With increasing wave height, SSC values increase and zones with high SSC values extend a little bit offshore. However, the plume never extends further than 20 km from the coast, which is the limit of the subaqueous delta. Our results are consistent with those from Hordoir *et al.* [33], who showed that the plume of the Mekong River is dominated by geostrophy from a dynamical perspective, with freshwater advected by a coastally

trapped baroclinic current. This behavior was confirmed by a Rossby number less than 1 throughout the year, due to the large freshwater discharge.

Waves from the SW direction (and to a lesser extent waves from the South) are mainly responsible of the net alongshore transport to the Northeast of the delta. Waves from the SW generate about 86% of the Northeastward flux in the Southern delta (1324×10^3 tons over 1532 across section m1), 72% along the central delta (m2) and 49% in the Northern part (across m3).

A companion paper [80] provided the maps of deposition and erosion (in mm) in the study area, per season, and per year. It showed that: (1) deposition occurs in the lower estuary at a rate reaching 40–50 mm yr^{-1}; (2) deposition is decreasing fast with decreasing water depth in front of the mouths up to 5 m depth; (3) patches of erosion are found along the MRD in water between 5 and 10 m depth; (4) further offshore at 10–15 m depths, deposition occurs at rates <10 mm yr^{-1}. These values are consistent with the accumulation rates determined by Ta *et al.* [32] in front of the MRD for the most recent period. Erosion zones and rates differ slightly from these given by Xue *et al.* [25] over water depth between 5 and 10 m since their study did not take into account the action of the highest waves.

The net sediment transport to the Northeast observed in the Southern part of the delta (along Ca Mau cape) is the main original result of our calculations. This trend is consistent with simulations of the Mekong shelf circulation and sediment transport and dispersal performed for 2005 by Xue *et al.* [22], who reported that the Southwestern part of the MRD (between Tran De mouth and Ca Mau Cape) receives very few sediments from the Mekong River. Deposition in that area should almost result from a slow but persistent deposition process occurring over a much longer (millennial) time scale. Regardless, the sediment deficit along the Southern coastal area of the delta, which results mainly from the action of waves coming from the S and SW in low flow season, is consistent with the geological studies and with the severe erosion along the Ca Mau peninsula, estimated to be an average of 1.1 km^2 yr^{-1} since 1885 [81].

Remote sensing data can be used in complement to numerical simulations to study the river plume dynamics and sediment transport [82–86]. Satellite data are available under clear sky conditions only; such data are numerous during the dry season but less abundant during the wet and mostly cloudy season, which makes it difficult to estimate sediment budgets from remote sensing alone. Continuous and costly measurements or modeling (after validation from *in situ* data) are the two ways to estimate annual fluxes such as given in this study (Table 4). However, such estimates could greatly benefit from the available remote sensing data (e.g., [25]) to offer a synoptic view to complement local measurements and further constraint the model. Such a coupling between modeling, satellite data analysis and field measurements may be envisaged in a future step over the Mekong coastal zone.

Acknowledgments: This work was financed by the science and technological cooperation program between the Vietnam Academy of Sciences and Technology (VAST) and the French Institut de Recherche pour le Développement (IRD) within the space science and technological program, through the VT/CB-01/14-15 project: "Study on method for analyzing, assessing and monitoring coastal water quality by using the high and average resolution and multi-temporal remote sensing data; testing the VNRedsat–1", by the project "Interaction between hydrodynamic processes of the Bien Dong (East Sea of Vietnam) and water Mekong River", by the project VAST.ĐLT.06/15-16, and by the project VIETNAMINS from the University of Science and Technology of Hanoi.

Author Contributions: V.D.V. and N.V.T. conceived the study; V.D.V. and N.N.T. organized the field trip and designed the numerical experiments; V.D.V. performed the simulations; V.D.V., N.V.T. and S.O. analyzed the data and simulations; V.D.V. and S.O. wrote the paper.

Conflicts of Interest: The authors declare no conflict of interest.

References

1. Liu, J.P.; Xue, Z.; Ross, K.; Wang, H.J.; Yang, Z.S.; Li, A.C.; Gao, S. Fate of sediments delivered to the sea by Asian large rivers: Long-distance transport and formation of remote alongshore clinothems. *Sediment. Rec.* **2009**, *7*, 4–9.

2. Saito, Y.; Chaimanee, N.; Jarupongsakul, T.; Syvitski, J.P.M. Shrinking megadeltas in Asia: Sea-level rise and sediment reduction impacts from case study of the Chao Phraya delta. *Newsl. IGBP/IHDP Land Ocean Interact. Coast. Zone* **2007**, *2*, 3–9.
3. Vörösmarty, C.J.; Meybeck, M.; Fekete, B.; Sharma, K.; Green, P.; Syvitski, J.P.M. Anthropogenic sediment retention: Major global impact from registered river impoundments. *Glob. Planet. Chang.* **2003**, *39*, 169–190. [CrossRef]
4. Syvitski, J.P.M.; Saito, Y. Morphodynamics of Deltas under the Influence of Humans. *Glob. Planet. Chang.* **2007**, *57*, 261–282. [CrossRef]
5. Wang, H.J.; Yang, Z.S.; Saito, Y.; Liu, J.P.; Sun, X. Interannual and seasonal variation of the Huanghe (Yellow River) water discharge over the past 50 years: Connections to impacts from ENSO events and dams. *Glob. Planet. Chang.* **2006**, *50*, 212–225. [CrossRef]
6. Wang, H.J.; Yang, Z.S.; Wang, Y.; Saito, Y.; Liu, J.P. Reconstruction of sediment flux from the Changjiang (Yangtze River) to the sea since the 1860s. *J. Hydrol.* **2008**, *349*, 318–332. [CrossRef]
7. Vinh, V.D.; Ouillon, S.; Tanh, T.D.; Chu, L.V. Impact of the Hoa Binh dam (Vietnam) on water and sediment budgets in the Red River basin and delta. *Hydrol. Earth Syst. Sci.* **2014**, *18*, 3987–4005. [CrossRef]
8. Schlünz, B.; Schneider, R.R. Transport of terrestrial organic carbon to the oceans by rivers: Re-estimating flux- and burial rates. *Int. J. Earth Sci.* **2000**, *88*, 599–606. [CrossRef]
9. Viers, J.; Dupré, B.; Gaillardet, J. Chemical composition of suspended sediments in World Rivers: New insights from a new database. *Sci. Total Environ.* **2009**, *407*, 853–868. [CrossRef] [PubMed]
10. Rochelle-Newall, E.J.; Chu, V.T.; Pringault, O.; Amouroux, D.; Arfi, R.; Bettarel, Y.; Bouvier, T.; Bouvier, C.; Got, P.; Nguyen, T.M.; *et al.* Phytoplankton diversity and productivity in a highly turbid, tropical coastal system (Bach Dang Estuary, Vietnam). *Mar. Pollut. Bull.* **2011**, *62*, 2317–2329. [CrossRef] [PubMed]
11. Mari, X.; Torréton, J.P.; Chu, V.T.; Lefebvre, J.P.; Ouillon, S. Seasonal aggregation dynamics along a salinity gradient in the Bach Dang estuary, North Vietnam. *Estuar. Coast. Shelf Sci.* **2012**, *96*, 151–158. [CrossRef]
12. Navarro, P.; Amouroux, D.; Duong, T.N.; Rochelle-Newall, E.; Ouillon, S.; Arfi, R.; Chu, V.T.; Mari, X.; Torréton, J.P. Butyltin and mercury compounds fate and tidal transport in waters of the tropical Bach Dang estuary (Haiphong, Vietnam). *Mar. Pollut. Bull.* **2012**, *64*, 1789–1798. [CrossRef] [PubMed]
13. Syvitski, J.P.M.; Vörösmarty, C.J.; Kettner, A.J.; Green, P. Impact of Humans on the Flux of Terrestrial Sediment to the Global Coastal Ocean. *Science* **2005**, *308*, 376. [CrossRef] [PubMed]
14. Ouillon, S. Erosion and sediment transport: Width and stakes. *Houille Blanche* **1998**, *53*, 52–58. [CrossRef]
15. Clift, P.D.; Plumb, R.A. *The Asian Monsoon: Causes, History and Effects*; Cambridge University Press: Cambridge, UK, 2008; p. 288. [CrossRef]
16. Tamura, T.; Horaguchi, K.; Saito, Y.; Nguyen, V.L.; Tateishi, M.; Ta, T.K.O.; Nanayama, F.; Watanabe, K. Monsoon-influenced variations in morphology and sediment of a mesotidal beach on the Mekong River Delta coast. *Geomorphology* **2010**, *116*, 11–23. [CrossRef]
17. Eastham, J.; Mpelasoka, F.; Mainuddin, M.; Ticehurst, C.; Dyce, P.; Hodgson, G.; Ali, R.; Kirby, M. *Mekong River Basin Water Resources Assessment: Impacts of Climate Change*; CSIRO National Research Flagship, Water for a Healthy Country: Canberra, Australia, 2008.
18. Nguyen, V.L.; Ta, T.K.O.; Tateishi, M. Late Holocene depositional environments and coastal evolution of the Mekong River Delta, Southern Vietnam. *J. Asian Earth Sci.* **2000**, *18*, 427–439. [CrossRef]
19. Walling, D.E. The changing sediment load of the Mekong River. *AMBIO* **2008**, *37*, 150–157. [CrossRef]
20. Xue, Z.; Liu, J.P.; Ge, Q. Changes in hydrology and sediment delivery of the Mekong River in the last 50 years: Connection to damming, monsoon, and ENSO. *Earth Surf. Process. Landf.* **2011**, *36*, 296–308. [CrossRef]
21. Le, T.V.H.; Nguyen, H.N.; Wolanski, E.; Tran, T.C.; Haruyama, S. The combined impact on the flooding in Vietnam's Mekong River Delta of local man-made structures, sea level rise, and dams upstream in the river catchment. *Estuar. Coast. Shelf Sci.* **2007**, *71*, 110–116. [CrossRef]
22. Wang, J.J.; Lu, X.X.; Kummu, M. Sediment load estimates and variations in the lower Mekong River. *River Res. Appl.* **2011**, *27*, 33–46. [CrossRef]
23. Manh, N.V.; Dung, N.V.; Hung, N.N.; Merz, B.; Apel, H. Large-scale suspended sediment transport and sediment deposition in the Mekong delta. *Hydrol. Earth Syst. Sci.* **2014**, *18*, 3033–3053. [CrossRef]
24. Xue, Z.; He, R.; Liu, J.P.; Warner, J.C. Modeling transport and deposition of the Mekong River sediment. *Cont. Shelf Res.* **2012**, *37*, 66–78. [CrossRef]

25. Loisel, H.; Mangin, A.; Vantrepotte, V.; Dessailly, D.; Dinh, N.D.; Garnesson, P.; Ouillon, S.; Lefebvre, J.P.; Mériaux, X.; Phan, M.T. Analysis of the suspended particulate matter concentration variability of the coastal waters under the Mekong's influence: A remote sensing approach. *Remote Sens. Environ.* **2014**, *150*, 218–230. [CrossRef]
26. Szczuciński, W.; Jagodziński, R.; Hanebuth, T.J.J.; Stattegger, K.; Wetzel, A.; Mitręga, M.; Unverricht, D.; Phach, P.V. Modern sedimentation and sediment dispersal pattern on the continental shelf off the Mekong River delta, South China Sea. *Glob. Planet. Chang.* **2013**, *110*, 195–213. [CrossRef]
27. Wolanski, E.; Ngoc Huan, N.; Trong Dao, L.; Huu Nhan, N.; Ngoc Thuy, N. Fine sediment dynamics in the Mekong River Estuary, Vietnam. *Estuar. Coast. Shelf Sci.* **1996**, *43*, 565–582. [CrossRef]
28. Wolanski, E.; Nhan, N.H.; Spagnol, S. Sediment dynamics during low flow conditions in the Mekong River Estuary, Vietnam. *J. Coast. Res.* **1998**, *14*, 472–482.
29. Hein, H.; Hein, B.; Pohlmann, T. Recent dynamics in the region of Mekong water influence. *Glob. Planet. Chang*. **2013**, *110*, 183–194. [CrossRef]
30. Mekong River Commission (MRC). *State of the Basin Report: 2003*; MRC: Phnom Penh, Cambodia, 2003.
31. Milliman, J.D.; Meade, R.H. World-wide delivery of river sediment to the oceans. *J. Hydrol.* **1983**, *91*, 1–21. [CrossRef]
32. Ta, K.T.O.; Nguyen, V.L.; Tateishio, M.; Kobayashi, I.; Tanabe, S.; Saito, Y. Holocene delta evolution and sediment discharge of the Mekong River, southern Vietnam. *Quat. Sci. Rev.* **2002**, *21*, 1807–1819. [CrossRef]
33. Hordoir, R.; Nguyen, K.D.; Polcher, J. Simulating tropical river plumes, a set of parametrizations based on macroscale data: A test case in the Mekong Delta region. *J. Geophys. Res.* **2006**, *111*, C09036. [CrossRef]
34. Snidvongs, A.; Teng, S.K. *Global International Waters Assessment, Mekong River GIWA Regional Assessment 55*; University of Kalmar: Kalmar, Sweden, 2006.
35. Unverricht, D.; Szczuciński, W.; Stattegger, K.; Jagodziński, R.; Le, X.T.; Kwong, L.L.W. Modern sedimentation and morphology of the subaqueous Mekong delta, Southern Vietnam. *Glob. Planet. Chang.* **2013**, *110*, 223–235. [CrossRef]
36. Deltares. *Mekong Delta Water Resources Assessment Studies*; Report of the Vietnam-Netherlands Mekong Delta Masterplan Project; Deltares: Delft, The Netherlands.
37. Vietnamese National Centre for Hydro-Meteorological Forecasts. Statistics on Typhoon Occurrence in Vietnam. 2016. Available online: http://ttnh.vnea.org (accessed on 20 April 2016).
38. Tri, V.K. Hydrology and hydraulic infrastructure systems in the Mekong delta, Vietnam. In *The Mekong Delta System*; Renaud, F.G., Kuenzer, C., Eds.; Springer: Dordrecht, Germany, 2012; pp. 49–82. [CrossRef]
39. Lu, X.X.; Siew, R.Y. Water discharge and sediment flux changes over the past decades in the Lower Mekong River: Possible impacts of the Chinese dams. *Hydrol. Earth Syst. Sci.* **2006**, *10*, 181–195. [CrossRef]
40. Kubicki, A. Large and very large subaqueous delta dunes on the continental shelf off southern Vietnam, South China Sea. *Geo-Mar. Lett.* **2008**, *28*, 229–238. [CrossRef]
41. Nguyen, C.T. Processes and Factors Controlling and Affecting the Retreat of Mangrove Shorelines in South Vietnam. Ph.D. Thesis, Kiel University, Kiel, Germany, 2012.
42. Allen, G.P.; Salomon, J.C.; Bassoulet, P.; du Penhoat, Y.; de Grandpre, C. Effects of tides on mixing and suspended sediment transport in macrotidal estuaries. *Sediment. Geol.* **1980**, *26*, 69–90. [CrossRef]
43. Dyer, K.R. *Coastal and Estuarine Sediment Dynamics*; Wiley: Chichester, UK, 1986; p. 342. [CrossRef]
44. Dronkers, J. Tide-induced residual transport of fine sediment. In *Physics of Shallow Estuaries and Bays*; van de Kreeke, J., Ed.; Lecture Notes Coastal Estuarine Studies, Volome 16; Springer: Berlin, Germany, 1986; pp. 228–244. [CrossRef]
45. Sottolichio, A.; Le Hir, P.; Castaing, P. Modeling mechanisms for the turbidity maximum stability in the Gironde estuary, France. *Proc. Mar. Sci.* **2001**, *3*, 373–386. [CrossRef]
46. Lefebvre, J.P.; Ouillon, S.; Vinh, V.D.; Arfi, R.; Panche, J.Y.; Mari, X.; Van Thuoc, C.; Torréton, J.P. Seasonal variability of cohesive sediment aggregation in the Bach Dang-Cam Estuary, Haiphong (Vietnam). *Geo-Mar. Lett.* **2012**, *32*, 103–121. [CrossRef]
47. Weatherall, P.; Marks, K.M.; Jakobsson, M.; Schmitt, T.; Tani, S.; Arndt, J.E.; Rovere, M.; Chayes, D.; Ferrini, V.; Wigley, R. A new digital bathymetric model of the world's oceans. *Earth Space Sci.* **2015**, *2*, 331–345. [CrossRef]

48. Lanh, D.T. *Integrated Water Resources Management and Sustainable Use for the Dong Nai River System*; Technical Report of the Project KC.08.18/06-10; The Southern Institute of Water Resources Research: Ho Chi Minh City, Vietnam, 2010. (In Vietnamese)
49. Groenewoud, P. *Overview of the Service and Validation of the Database*; Reference: RP_A870; BMT ARGOSS: Marknesse, The Netherlands, 2011.
50. Lefevre, F.; Lyard, F.; Le Provost, C.; Schrama, E.J.O. FES99: A global tide finite element solution assimilating tide gauge and altimetric information. *J. Atmos. Ocean. Technol.* **2002**, *19*, 1345–1356. [CrossRef]
51. Lyard, F.; Lefevre, F.; Letellier, T.; Francis, O. Modelling the global ocean tides: Modern insights from FES2004. *Ocean Dyn.* **2006**, *56*, 394–415. [CrossRef]
52. World Ocean Atlas 2013 Version 2 (WOA13 V2). Available online: https://www.nodc.noaa.gov/OC5/woa13/ (accessed on 20 April 2016).
53. Deltares Systems. *Delft3D-FLOW User Manual: Simulation of Multi-Dimensional Hydrodynamic Flows and Transport Phenomena, including Sediments*; Technical Report; Deltares: Delft, The Netherlands, 2014.
54. Booij, N.; Ris, R.C.; Holthuijsen, L.H. A third-generation wave model for coastal regions: 1. Model description and validation. *J. Geophys. Res.* **1999**, *104*, 7649–7666. [CrossRef]
55. Ris, R.C.; Holthuijsen, L.H.; Booij, N. A third-generation wave model for coastal regions: 2. Verification. *J. Geophys. Res.* **1999**, *104*, 7667–7681. [CrossRef]
56. Deltares Systems. *Delft3D-WAVE User Manual: Simulation of Short-Crested Waves with SWAN*; Technical Report; Deltares: Delft, The Netherlands, 2014.
57. Jouon, A.; Lefebvre, J.P.; Douillet, P.; Ouillon, S.; Schmied, L. Wind wave measurements and modelling in a fetch-limited semi-enclosed lagoon. *Coast. Eng.* **2009**, *56*, 599–608. [CrossRef]
58. Hasselmann, K.; Barnett, T.P.; Bouws, E.; Carlson, H.; Cartwright, D.E.; Enke, K.; Ewing, J.; Gienapp, H.; Hasselmann, D.E.; Kruseman, P.; *et al. Measurements of Wind Wave Growth and Swell Decay during the Joint North Sea Wave Project (JONSWAP). Deutsche Hydrographische Zeitschrift 8 (12)*; Deutsches Hydrographisches Institut: Hamburg, Germany, 1973.
59. Bouws, E.; Komen, G. On the balance between growth and dissipation in an extreme, depth-limited wind-sea in the southern North Sea. *J. Phys. Oceanogr.* **1983**, *13*, 1653–1658. [CrossRef]
60. Battjes, J.; Janssen, J. Energy loss and set-up due to breaking of random waves. In Proceedings of the 16th International Conference Coastal Engineering, ASCE, Hamburg, Germany, 26 August–6 September 1978; pp. 569–587.
61. Arcement, G.J., Jr.; Schneider, V.R. Guide for Selecting Manning's Roughness Coefficients for Natural Channels and Flood Plains. U.S. Geological Survey Water Supply Paper 2339; 1989. Available online: http://www.fhwa.dot.gov/bridge/wsp2339.pdf (accessed on 20 April 2016).
62. Simons, D.B.; Senturk, F. *Sediment Transport Technology—Water and Sediment Dynamics*; Water Resources Publications: Littleton, CO, USA, 1992.
63. Uittenbogaard, R.E. *Model for Eddy Diffusivity and Viscosity Related to Sub-Grid Velocity and Bed Topography*; Technical Report; WL Delft Hydraulics: Delft, The Netherlands, 1998.
64. Van Vossen, B. *Horizontal Large Eddy Simulations; Evaluation of Computations with DELFT3D-FLOW*; Report MEAH-197; Delft University of Technology: Delft, The Netherlands, 2000.
65. Van Rijn, L.C. Unified view of sediment transport by currents and waves, Part II: Suspended transport. *J. Hydraul. Eng.* **2007**, *133*, 668–689. [CrossRef]
66. Partheniades, E. Erosion and deposition of cohesive soils. *J. Hydraul. Div.* **1965**, *91*, 105–139.
67. Krone, R.B. *Flume Studies of the Transport of Sediment in Estuarial Shoaling Processes*; Hydraulic Engineering Laboratory and Sanitary Engineering Research Laboratory, University of California: Berkeley, CA, USA, 1962.
68. Douillet, P.; Ouillon, S.; Cordier, E. A numerical model for fine suspended sediment transport in the south-west lagoon of New-Caledonia. *Coral Reefs* **2001**, *20*, 361–372. [CrossRef]
69. Winterwerp, J.C.; van Kesteren, W.G.M. *Introduction to the Physics of Cohesive Sediment in the Marine Environment*; Elsevier: Amsterdam, The Netherlands, 2004; pp. 1–466.
70. Hung, N.N.; Delgado, J.M.; Güntner, A.; Merz, B.; Bárdossy, A.; Apel, H. Sedimentation in the floodplains of the Mekong Delta, Vietnam Part II: Deposition and erosion. *Hydrol. Process.* **2004**, *28*, 3145–3160. [CrossRef]
71. Portela, L.I.; Ramos, S.; Rexeira, A.T. Effect of salinity on the settling velocity of fine sediments of a harbour basin. *J. Coast. Res.* **2013**, *2*, 1188–1193. [CrossRef]

72. Van Rijn, L.C. Mathematical modeling of suspended sediment in non-uniform flows. *J. Hydraul. Eng.* **1986**, *112*, 433–455. [CrossRef]
73. Ouillon, S.; Le Guennec, B. Modelling non-cohesive suspended sediment transport in 2D vertical free surface flows. *J. Hydraul. Res.* **1996**, *34*, 219–236. [CrossRef]
74. Van Rijn, L. *Principles of Sediment Transport in Rivers, Estuaries and Coastal Seas*; Aqua Publications: Amsterdam, The Netherlands, 1993.
75. Madsen, O.S. Spectral wave–current bottom boundary layer flows. In Proceedings of the 24th International Conference on Coastal Engineering Research Council, Kobe, Japan, 23–28 October 1994; pp. 384–398. [CrossRef]
76. Walstra, D.J.R.; Roelvink, J.A. 3D Calculation of Wave Driven Cross-shore Currents. In Proceedings of the 27th International Conference on Coastal Engineering, Sydney, Australia, 16–21 July 2000; pp. 1050–1063. [CrossRef]
77. Nash, J.E.; Sutcliffe, J.V. River flow forecasting through conceptual models, Part I—A discussion of principles. *J. Hydrol.* **1970**, *10*, 282–290. [CrossRef]
78. Krause, P.; Boyle, D.P.; Bäse, F. Comparison of different efficiency criteria for hydrological model assessment. *Adv. Geosci.* **2005**, *5*, 89–97. [CrossRef]
79. Kvale, E.P.; Archer, A.W.; Johnson, H.R. Daily, monthly, and yearly tidal cycles within laminated siltstones of the Mansfield Formation (Pennsylvanian) of Indiana. *Geology* **1989**, *17*, 365–368. [CrossRef]
80. Vinh, V.D.; Lan, T.D.; Tu, T.A.; Anh, N.K.; Tien, N.N. Influence of dynamic processes on morphological change in the coastal area of Mekong river mouth. *J. Mar. Sci. Technol.* **2016**, *16*, 32–45. [CrossRef]
81. Saito, Y. Deltas in Southeast and East Asia: Their evolution and current problems. In *APN/SURVAS/LOICZ Joint Conference on Coastal Impact of Climate Change and Adaption in the Asia-Pacific Region*; Mimura, N., Yokoki, H., Eds.; APN: Kobe, Japan, 2000; pp. 185–191.
82. Durand, N.; Fiandrino, A.; Fraunie, P.; Ouillon, S.; Forget, P.; Naudin, J.J. Suspended matter dispersion in the Ebro ROFI: An integrated approach. *Cont. Shelf Res.* **2002**, *22*, 267–284. [CrossRef]
83. Ouillon, S.; Douillet, P.; Andréfouët, S. Coupling satellite data with *in situ* measurements and numerical modeling to study fine suspended sediment transport: A study for the lagoon of New Caledonia. *Coral Reefs* **2004**, *23*, 109–122. [CrossRef]
84. Stroud, J.R.; Lesht, B.M.; Schwab, D.J.; Beletsky, D.; Stein, M.L. Assimilation of satellite images into a sediment transport of Lake Michigan. *Water Resour. Res.* **2009**, *45*, W02419. [CrossRef]
85. Carniello, L.; Silvestri, S.; Marani, M.; D'Alpaos, A.; Volpe, V.; Defina, A. Sediment dynamics in shallow tidal basins: *In situ* observations, satellite retrievals, and numerical modeling in the Venice Lagoon. *J. Geophys. Res. Earth Surf.* **2014**, *119*, 802–2015. [CrossRef]
86. Yang, X.; Mao, Z.; Huang, H.; Zhu, Q. Using GOCI retrieval data to initialize and validate a sediment transport model for monitoring diurnal variation of SSC in Hangzhou Bay, China. *Water* **2016**, *8*, 108. [CrossRef]